

Science and Technology of Nuclear Installations

Advanced Computational Models for Accelerator-Driven Systems

Guest Editors: Alberto Talamo, Piero Ravetto,
and Wacław Gudowski





Advanced Computational Models for Accelerator-Driven Systems

Science and Technology of Nuclear Installations

Advanced Computational Models for Accelerator-Driven Systems

Guest Editors: Alberto Talamo, Piero Ravetto,
and Waclaw Gudowski



Copyright © 2012 Hindawi Publishing Corporation. All rights reserved.

This is a special issue published in “Science and Technology of Nuclear Installations.” All articles are open access articles distributed under the Creative Commons Attribution License, which permits unrestricted use, distribution, and reproduction in any medium, provided the original work is properly cited.

Editorial Board

Nusret Aksan, Switzerland
Antonio C. Marques Alvim, Brazil
Won Pil Baek, Korea
Stephen M. Bajorek, USA
George Bakos, Greece
Jozsef Banati, Sweden
Ricardo Barros, Brazil
Anis Bousbia Salah, Belgium
Giovanni B. Bruna, France
Nikola Čavlina, Croatia
Xu Cheng, China
Leon Cizelj, Slovenia
Alejandro Clausse, Argentina
Francesco D' Auria, Italy
Marcos P. de Abreu, Brazil
Giovanni Dell'Orco, France
Juan Carlos Ferreri, Argentina
Nikolay Fil, Russia
Cesare Frepoli, USA
Giorgio Galassi, Italy
Regina Galetti, Brazil

Michel Giot, Belgium
Valerio Giusti, Italy
Horst Glaeser, Germany
Satish Kumar Gupta, India
Ali Hainoun, Syria
Keith E. Holbert, USA
Kostadin Ivanov, Germany
Yacine Kadi, Republic of Korea
Ahmed Khedr, Egypt
Tomasz Kozłowski, USA
Tomoaki Kunugi, Japan
Mike Kuznetsov, Germany
H.-Y. Lee, Republic of Korea
Bundit Limmeechokchai, Thailand
Jiri Macek, Czech Republic
Annalisa Manera, USA
Borut Mavko, Slovenia
Oleg Melikhov, Russia
Rafael Miró, Spain
Josef Misak, Czech Republic
Rahim Nabbi, Germany

Manmohan Pandey, India
Yuriy Parfenov, Russia
Yves Pontillon, France
Nik Popov, Canada
Piero Ravetto, Italy
Francesc Reventos, Spain
Enrico Sartori, France
Carlo Sborchia, France
Massimo Sepielli, Italy
Arkady Serikov, Germany
James F. Stubbins, USA
Iztok Tiselj, Slovenia
Rizwan Uddin, USA
Eugenijus Ušpuras, Lithuania
Richard Wright, Norway
Chao Xu, China
Yanko Yanev, Bulgaria
Zhiwei Zhou, China
Enrico Zio, Italy
Massimo Zucchetti, Italy

Contents

Advanced Computational Models for Accelerator-Driven Systems, Alberto Talamo, Piero Ravetto, and Waclaw Gudowski

Volume 2012, Article ID 376164, 1 page

Investigation of the Energy Correlations of Spallation Neutrons by Monte Carlo Simulations,

Máté Szieberth and Gábor Radócz

Volume 2012, Article ID 373979, 9 pages

Monte Carlo Calculation of Fragment Distributions in Nuclear Reactions, A. Deppman, E. Andrade-II,

P. C. R. Rossi, F. Garcia, and J. R. Maiorino

Volume 2012, Article ID 480343, 9 pages

Solutions without Space-Time Separation for ADS Experiments: Overview on Developments and Applications, B. Merk and V. Glivici-Cotruță

Volume 2012, Article ID 140946, 11 pages

Two-Group Theory of the Feynman-Alpha Method for Reactivity Measurement in ADS,

Lénárd Pál and Imre Pázsit

Volume 2012, Article ID 620808, 14 pages

Interpretation of Local Flux Measurements in Subcritical Systems and Reactivity Determination,

S. Dulla and P. Ravetto

Volume 2012, Article ID 629039, 13 pages

Study of an ADS Loaded with Thorium and Reprocessed Fuel, Graiciany de Paula Barros, Claubia Pereira,

Maria A. F. Veloso, and Antonella L. Costa

Volume 2012, Article ID 934105, 12 pages

Subcritical Multiplication Parameters of the Accelerator-Driven System with 100 MeV Protons at the Kyoto University Critical Assembly, Jae-Yong Lim, Cheol Ho Pyeon, Takahiro Yagi, and Tsuyoshi Misawa

Volume 2012, Article ID 395878, 9 pages

Nuclear Level Density Parameters of $^{203-209}\text{Pb}$ and $^{206-210}\text{Bi}$ Deformed Target Isotopes Used on Accelerator-Driven Systems in Collective Excitation Modes, Şeref Okuducu, Nisa N. Aktı,

Sabahattin Akbaş, and M. Orhan Kansu

Volume 2012, Article ID 915496, 9 pages

Detector Dead Time Determination and Optimal Counting Rate for a Detector Near a Spallation Source or a Subcritical Multiplying System, V. Bécares and J. Blázquez

Volume 2012, Article ID 240693, 7 pages

Development of a Secondary SCRAM System for Fast Reactors and ADS Systems, Simon Vanmaercke, Gert Van den Eynde, Engelbert Tijsskens, and Yann Bartosiewicz

Volume 2012, Article ID 351985, 9 pages



Advanced Method for Calculations of Core Burn-Up, Activation of Structural Materials, and Spallation Products Accumulation in Accelerator-Driven Systems, A. Stankovskiy and G. Van den Eynde

Volume 2012, Article ID 545103, 12 pages

A Fast Numerical Method for the Calculation of the Equilibrium Isotopic Composition of a Transmutation System in an Advanced Fuel Cycle, F. Álvarez-Velarde and E. M. González-Romero

Volume 2012, Article ID 149089, 6 pages

Editorial

Advanced Computational Models for Accelerator-Driven Systems

Alberto Talamo,¹ Piero Ravetto,² and Waclaw Gudowski³

¹ Argonne National Laboratory, Chicago, IL, USA

² Politecnico di Torino, Turin, Italy

³ Royal Institute of Technology (KTH), Stockholm, Sweden

Correspondence should be addressed to Alberto Talamo, alby@anl.gov

Received 17 May 2012; Accepted 17 May 2012

Copyright © 2012 Alberto Talamo et al. This is an open access article distributed under the Creative Commons Attribution License, which permits unrestricted use, distribution, and reproduction in any medium, provided the original work is properly cited.

In the nuclear engineering scientific community, Accelerator Driven Systems (ADSs) have been proposed and investigated for the transmutation of nuclear waste, especially plutonium and minor actinides. These fuels have a quite low effective delayed neutron fraction relative to uranium fuel, therefore the subcriticality of the core offers a unique safety feature with respect to critical reactors. The intrinsic safety of ADS allows the elimination of the operational control rods, hence the reactivity excess during burnup can be managed by the intensity of the proton beam, fuel shuffling, and eventually by burnable poisons. However, the intrinsic safety of a subcritical system does not guarantee that ADSs are immune from severe accidents (core melting), since the decay heat of an ADS is very similar to the one of a critical system. Normally, ADSs operate with an effective multiplication factor between 0.98 and 0.92, which means that the spallation neutron source contributes little to the neutron population. In addition, for 1 GeV incident protons and lead-bismuth target, about 50% of the spallation neutrons has energy below 1 MeV and only 15% of spallation neutrons has energies above 3 MeV. In the light of these remarks, the transmutation performances of ADS are very close to those of critical reactors.

This contributes to different research topics, including the following:

(i) analyses of subcritical research assemblies:

- (a) the analytical solution of the P_1 neutron transport equation without the space-time separation;
- (b) the comparison between numerical and experimental results;

- (c) the investigation of the kinetic and local neutron parameters;
 - (d) the neutron detector dead time;
 - (e) the two-group theory of the Feynman-alpha method;
- (ii) fuel cycles for actinides incineration and ^{233}U production from thorium;
 - (iii) new computational software to analyze the in-core and out-of-core fuel cycles, the activation of structural materials, and the accumulation of spallation products;
 - (iv) safety studies and the design of the SCRAM system;
 - (v) studies on nuclear level density parameters of target isotopes, energy correlation of spallation neutrons, and fragments production.

*Alberto Talamo
Piero Ravetto
Waclaw Gudowski*

Research Article

Investigation of the Energy Correlations of Spallation Neutrons by Monte Carlo Simulations

Máté Szieberth and Gábor Radócz

Institute of Nuclear Techniques, Budapest University of Technology and Economics, Műegyetem rkp. 3-9, Budapest 1111, Hungary

Correspondence should be addressed to Máté Szieberth, szieberth@reak.bme.hu

Received 29 December 2011; Accepted 8 April 2012

Academic Editor: Alberto Talamo

Copyright © 2012 M. Szieberth and G. Radócz. This is an open access article distributed under the Creative Commons Attribution License, which permits unrestricted use, distribution, and reproduction in any medium, provided the original work is properly cited.

Earlier works have suggested that the energy correlations in a spallation source may influence the neutron noise measurements in an ADS. For the calculation of this effect not only the generally known and used one-particle spectrum is needed but also the so-called two particle spectrum, which describes also the energy correlations. Since measured data are not available for the energy correlation of the neutrons from a single spallation event, the physical models of the MCNPX code have been used to investigate the effect. The calculational model has been successfully validated with measurements of the number distribution of spallation neutrons. The simulated one- and two-particle energy distributions and spectra proved that the energy correlations exist and have an important effect in low multiplicity spallation events and in thin targets. On the other hand, for thick targets this effect appears negligible and the factorization of the two-particle spectrum seems an acceptable approximation. Further investigations are in hand to quantify the actual effect of the energy correlations on the neutron noise measurements.

1. Introduction

Spallation sources are considered as neutron sources for Accelerator-Driven Subcritical Systems (ADSs). In an ADS an accelerator is supposed to provide a high-energy (~ 1 GeV) proton beam, which produces neutrons in a heavy metal (e.g., lead) target through the spallation process. Besides the high neutron energies (up to the energy of the proton) the spallation neutron source is also distinguished from other neutron sources by its high multiplicity: one proton can produce up to 40–50 neutrons. The high multiplicity increases the importance of the source in a subcritical system, especially in case of deeper subcriticality. Therefore, the precise description of the spallation source is inevitable for the modeling of an ADS.

A special case is the modeling of the neutron fluctuations in an ADS (e.g., neutron noise measurements for reactivity determination) as this requires also the description of the higher moments of the probability distributions. While one can easily find measured data about spallation sources for the average values (the first moment) in the literature, the higher moments are not available due to the smaller interest and

the difficulties of such measurements. This paper makes an attempt to reproduce the higher moments and correlations needed for the accurate simulation of the neutron fluctuations in an ADS with the help of the physical models of the spallation process implemented in the MCNPX [1] high-energy Monte Carlo particle transport code.

2. Effect of the Spallation Source on the Neutron Fluctuations

2.1. Effect of the Multiplicity of the Source. The distribution of the number of neutrons q from a single source event can be described by the probability distribution $p(q)$, which by definition has to fulfill the following criteria:

$$\sum_{q=0}^{\infty} p(q) = 1. \quad (1)$$

Yamane and Pázsit et al. investigated the effect of the high multiplicity of the spallation source on different neutron noise measurement methods [4–6]. Let us take the variance-to-mean ratio or Feynman- α measurement as an example.

According to the well-known formula, if a Poisson neutron source (e.g., Pu-Be) is placed into a subcritical core, the ratio of the variance and the mean value of the number of counts N in a detector during a certain measuring time Δt will be the following [6]:

$$\frac{\sigma^2(N(\Delta t))}{\langle N(\Delta t) \rangle} = 1 + Y(\Delta t) = 1 + \frac{\epsilon D_{\nu_p}}{(\rho - \beta)^2} \left(1 - \frac{1 - e^{-\alpha \Delta t}}{\alpha \Delta t} \right), \quad (2)$$

where ϵ is the detector efficiency, ρ is the reactivity of the subcritical system, β is the delayed neutron fraction, α is the prompt decay constant, and D_{ν_p} is the so-called Diven-factor for the prompt neutrons, which can be calculated from the first and second factorial moments of the number distribution of prompt neutrons from fission (ν_p):

$$D_{\nu_p} = \frac{\langle \nu_p (\nu_p - 1) \rangle}{\langle \nu_p \rangle^2}. \quad (3)$$

As it is shown in [4, 5] in case of a multiplicative source a $(1 + \delta)$ factor has to be introduced in (2):

$$Y(\Delta t) = \frac{\epsilon D_{\nu_p}}{(\rho - \beta)^2} (1 + \delta) \left(1 - \frac{1 - e^{-\alpha \Delta t}}{\alpha \Delta t} \right). \quad (4)$$

δ is defined as:

$$\delta = -\rho \frac{\langle q \rangle D_q}{\langle \nu_p \rangle D_{\nu_p}}, \quad (5)$$

where D_q is the Diven factor for the number of the neutrons from a source event q and can be calculated analogously to D_{ν_p} :

$$D_q = \frac{\langle q(q-1) \rangle}{\langle q \rangle^2}. \quad (6)$$

A similar formula with the same $(1 + \delta)$ correction factor can be derived for the Rossi- α or autocorrelation measurement, too [6]. From (5) one can arrive at the trivial conclusion that the higher the multiplicity of the source compared to the multiplicity from fission and the deeper the subcriticality, the more important the effect of the source on the neutron fluctuations.

The importance of this fact comes if one calculates the typical values of δ for a spallation source. The Diven-factor for spallation sources is somewhat higher than for fission. For example, for the number distribution in [3] measured for 35 cm thick Pb target (see in Section 5.1 in details) $D_q \approx 1.4$ can be obtained. Taking typical values for ^{235}U fission as in [4] one arrives at $D_q/D_{\nu_p} \approx 1.75$. The more important effect comes from the source multiplicity since in the same measurement as above $\langle q \rangle \approx 20$ was found for a spallation source, which gives $\langle q \rangle / \langle \nu_p \rangle \approx 8.3$. Assuming these data $\delta \approx -14.5\rho$, which means $\delta \approx 0.76$ in case of a subcritical system with $k_{\text{eff}} = 0.95$. If one considers a deep subcriticality with $k_{\text{eff}} = 0.7$ then $\delta \approx 6.2$ is obtained. These high values

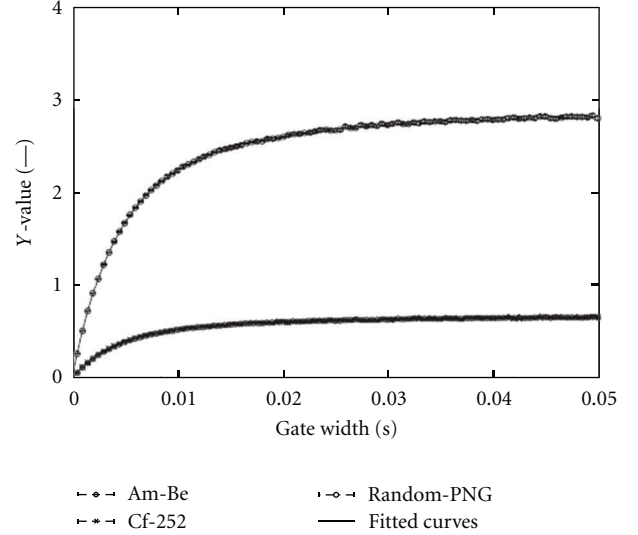


FIGURE 1: Feynman- α curves measured with different neutron sources [2].

for δ emphasize the importance of the spallation source in the neutron fluctuations.

The importance of the source multiplicity has been confirmed by experimental results from Kitamura et al. [2, 6]. In Figure 1 one can see the results of Feynman- α measurements in a subcritical system of $k_{\text{eff}} = 0.9874$ with different neutron sources. The curves obtained with the Am-Be source (which is a Poisson source) and with the ^{252}Cf source cover each other due to the fact that the multiplicity of the ^{252}Cf source is about the same as the fission multiplicity, which results in a small δ value. On the other hand, when a randomly triggered pulsed D-T neutron generator (Random-PNG) is applied, despite the relatively small negative reactivity, the effect of the higher δ value can be observed due to the high number of neutrons from a pulse.

2.2. Effect of the Energy Correlations of the Source. The above-shown importance of the spallation source indicates that minor effects may be worthwhile for deeper investigation, as well, such is the energy correlation between the neutrons from a spallation source. Neutron fluctuations are often handled in an energy independent one-group theory, but the high-energy spectrum assumed in an ADS seeks for energy dependent multigroup treatment. Such treatment requires also the description of the energy distribution of the source neutrons. This can be described in full detail by giving the $f_q(E_1, E_2, \dots, E_q)$ energy distribution of the q -particle emission event for each q . Being conditional probability density functions, these functions also have to be normalized to unity:

$$\int f_q(E_1, E_2, \dots, E_q) dE_1 dE_2 \dots dE_q = 1. \quad (7)$$

One can also define n -particle distributions (where $n < q$) by averaging over the remaining energy coordinates:

$$f_n(E_1, E_2, \dots, E_n) = \int f_q(E_1, E_2, \dots, E_q) dE_{n+1} \dots dE_q. \quad (8)$$

In practice the $f_q(E)$ one- and the $f_q(E_1, E_2)$ two-particle distributions have relevance, since they are sufficient for the determination of the first and second moments. If the energies of the neutrons originating from a single source event are totally independent from each other, the q -particle distribution can be factorized and substituted by the one-particle distribution:

$$f_q(E_1, E_2, \dots, E_q) \equiv \prod_{i=1}^q f_q(E_i), \quad (9)$$

which obviously also means that:

$$f_q(E_1, E_2) \equiv f_q(E_1)f_q(E_2). \quad (10)$$

In some cases the energy independence can be a good approximation but generally it cannot be assumed. The spectrum of the neutrons from the source $\chi(E)$ can be calculated by averaging the one-particle distribution $f_q(E)$ weighted by the expected number of neutrons from a q -particle emission event $qp(q)$:

$$\chi(E) = \frac{\sum_q qp(q)f_q(E)}{\sum_q qp(q)} = \frac{1}{\langle q \rangle} \sum_q qp(q)f_q(E). \quad (11)$$

This spectrum is known from experiments for both fission and spallation sources. However, Pázsit et al. showed [7] that in an energy-dependent approach the calculation of the second moment of the neutron fluctuations requires also the two-particle spectrum $\chi(E_1, E_2)$, which involves the energy correlations between the source neutrons. This can be expressed with the help of the two-particle energy distributions:

$$\chi(E_1, E_2) = \frac{\sum_q q(q-1)p(q)f_q(E_1, E_2)}{\sum_q q(q-1)p(q)}. \quad (12)$$

This function is usually unknown. In the case of fission it is generally replaced by the one-particle spectrum assuming that $\chi(E_1, E_2) = \chi(E_1)\chi(E_2)$. However, from (12) one can conclude that this assumes not only that (10) is valid but also the independence of $f_q(E)$ from q :

$$f_q(E) \equiv \chi(E). \quad (13)$$

This approximation is often used (e.g., in [8] where a general theory of neutron noise measurements is derived assuming different neutron sources), although the conditions in (10) and (13) do not apply for a spallation source. In order to decide on the applicability of this approximation the determination of the two-particle spectrum $\chi(E_1, E_2)$ is needed. As measurement data are not available for this purpose, one possibility is to use the physical models describing spallation and calculate a Monte Carlo estimation of $\chi(E_1, E_2)$.

3. Modeling of Spallation

The spallation process is modeled in high-energy particle transport codes (e.g., MCNPX, LAHET [9], FLUKA [10],

and HERMES [11]). Such codes use Monte Carlo methods both in the physical models to determine the outcome of nuclear interactions and for the transport of particles between interactions. The transport between interactions is done in the conventional way except that total cross-sections are calculated from physical models. Whenever a collision site is sampled, physical models are used to calculate the outcome of the interaction.

The physical models are composed of two basic parts. The first part is the so-called intranuclear cascade (INC) model. This describes the nuclear interaction as series of nucleon-nucleon collisions inside the nucleus. During this process secondary particles are generated as “knocked-out” nucleons. The process is followed while a thermal equilibrium of the nucleons is achieved, and the nucleus is left in an excited state. The second part of the model describes the deexcitation of the nucleus, which leads to either evaporation (simultaneous emission of several particles) or fission.

It is important to note that the modeling of the spallation process is fully analogous. Therefore, one can expect that these models provide good estimation not only for the mean values of the distributions but also for the higher moments, which are important for the simulation of neutron fluctuations.

4. Computational Methods

The MCNPX code has been chosen for the calculation. Geometry and parameters of a published measurement of spallation neutron yields have been used in the simulation in order to validate the physical models. In the experiments performed by Hilscher et al. [3] a lead target of variable thickness was bombarded by 1.22 GeV protons. The target was surrounded by a 4π neutron detector, the so-called Berlin Neutron Ball (BNB) (see Figure 2). This is a spherical shell filled with liquid scintillator and 0.4 weight% of Gd in order to make it sensitive to neutrons. 24 photomultiplier tubes are attached to the outer surface of the shell to detect the scintillation events.

In the simulation only the target has been modeled as a natural lead ($\rho = 11.34 \text{ g/cm}^3$) cylinder with a diameter of 15 cm and a height of 0.2 cm, 5 cm, and 35 cm, respectively. The proton beam arrives axially at the middle of the cover plane of the target.

The MCNPX code includes the Bertini [12], the Isabel [13], the INCL4 [14] and the CEM03 [15] INC models, and the ABLA and Dresner [16] deexcitation models. CEM03 consists of an intranuclear cascade model, followed by a preequilibrium model and an evaporation model. For Bertini and ISABEL and the INCL4 the Dresner evaporation model with Rutherford Appleton Laboratory (RAL) fission has been used. The transport of protons, neutrons, and pions was followed in the simulations.

During the simulations data have been collected about neutrons leaving the target with the help of the PTRAC event file of the MCNPX, in which (upon user request) data are recorded about certain events. A program has been developed to process this PTRAC file, extract the energy of the neutrons escaping the target, and reconstruct

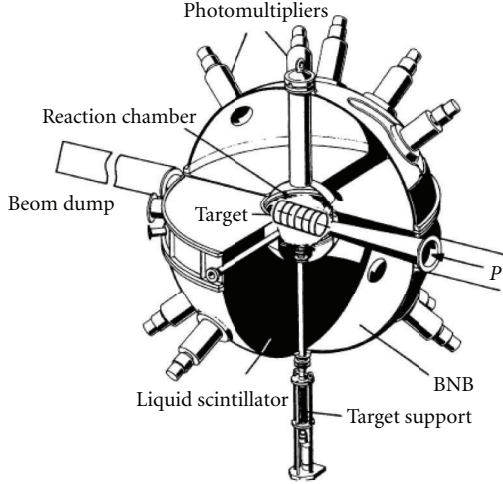


FIGURE 2: The experimental set up of the neutron multiplicity measurements performed by Hilscher et al. [3].

the requested distributions. It has to be noted again that in this way fully analogous estimators have been used, which do not bias the higher moments of the distributions. The number of simulated source events has been chosen large enough to arrive at acceptable statistics with a few percent of relative error.

5. Results

5.1. Validation to the Measured Number Distributions. In order to validate the applied models, first the $p(q)$ number distributions have been calculated. For this purpose the number of source events producing q neutrons leaving the target (N_q) has been determined from the PTRAC event file and divided by the total number of source events (N):

$$p(q) = \frac{N_q}{N}. \quad (14)$$

In [3] fitted functions are given for the differential cross-section of the source protons of the neutron multiplicity $d\sigma/dn$, where multiple reactions initiated by the same source proton are counted as one. This quantity needs to be converted to probability distribution per incident particle in order to be comparable with the simulated results:

$$p(q) = \frac{P_{\text{reac}}}{\sigma_{\text{tot}}} \frac{d\sigma}{dn} \Big|_{n=q}, \quad (15)$$

where P_{reac} is the probability that a source proton enters a nuclear interaction in the target, while σ_{tot} is the microscopic total cross-section of the source protons for entering a nuclear interaction in the lead target. $p(0)$ needs to be increased by the survival probability of source protons $1 - P_{\text{reac}}$. All parameters have been taken from [3]. The fitted function is the sum of an exponential and a Gaussian distribution:

$$p(q) = \frac{S_G}{s\sqrt{2\pi}} e^{-(q-M_n^{\text{max}})^2/2s^2} + \frac{S_E}{T_n} e^{-q/T_n}, \quad (16)$$

where the parameters are the ratio of the exponential and the Gaussian part (S_E and S_G , resp.), the mean value of the exponential and the Gaussian distribution (T_n and M_n^{max} , resp.), and the spread s of the Gaussian term.

Comparison of the measured and simulated data using four different physical models can be seen in Figures 3, 4 and 5 for the target thickness of 0.2 cm, 5 cm, and 35 cm, respectively. The main conclusion of the comparison is that the simulated results give good approximation of the measured ones and follow the same behavior: the thicker the target, the lower the exponential part, the wider the Gaussian distribution, and more neutrons are produced. This effect is due to the increasing number of secondary reactions.

One can also observe that there is a systematic over-estimation of the number of neutrons produced compared to the measured values. This is most probably due to the fact that during the evaluation of the measurements an average efficiency of 85% was used for the neutron detection efficiency, which had been measured by a ^{252}Cf source, although the spallation source emits also much higher energy neutrons for which the efficiency is lower [3]. Concerning the different models one can observe that the very similar Bertini and Isabel provide approximately the same results. CEM03 also provides a similar distribution but with higher probabilities in the Gaussian part. The distribution obtained from INCL4 is shifted toward smaller multiplicities. The results prove that the physical models are suited to reproduce the distributions in all details and therefore they preserve not only the mean values but also the higher moments. The MCNPX default option Bertini model has been chosen for the detailed investigation of the energy correlations.

5.2. Calculation of the One-Particle Energy Distribution and Spectrum. For the calculation of the one-particle energy distributions an energy group structure (E_i) has been set up and the number of neutrons from source events producing q neutrons has been determined in each energy bin (M_q^i). The one-particle energy distribution $f_q(E)$ can be estimated as:

$$f_q(E_i) = \frac{M_q^i}{M_q(E_i - E_{i-1})}, \quad (17)$$

where $M_q = N_q q$ is the sum of the neutrons from source events producing q neutrons. The average one-particle neutron spectrum $\chi(E)$ has also been determined:

$$\chi(E_i) = \frac{\sum_q M_q^i}{M(E_i - E_{i-1})}, \quad (18)$$

where $M = \sum_q M_q$ is the total number of neutrons produced. One can see in Figures 6, 7, and 8. the results of the simulations for the 0.2 cm, the 5 cm, and the 35 cm thick targets, respectively. It is obvious from the figures that the condition (13) does not stand for a spallation source and the energy distribution of the neutrons clearly depends on the number of neutrons produced. The explanation of this effect is related to the energy conservation: the fewer the number of neutrons produced, the higher the average excitation energy per one neutron is. This is the reason why at low neutron

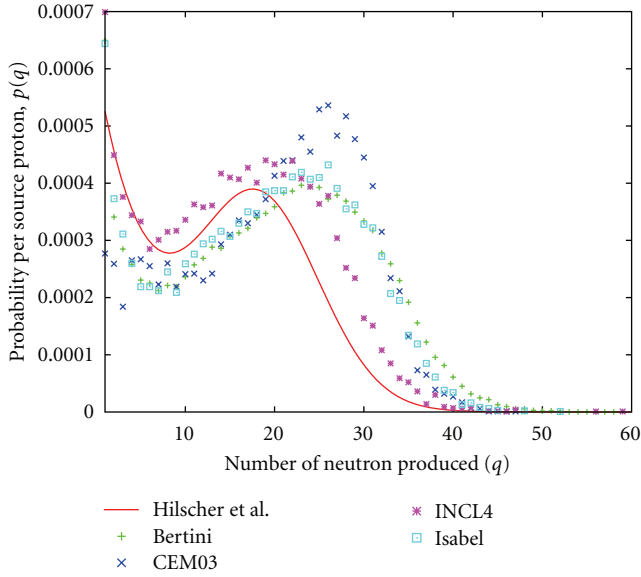


FIGURE 3: Comparison of measured and simulated distribution of the number of neutrons produced by a source proton for the 0.2 cm thick target.

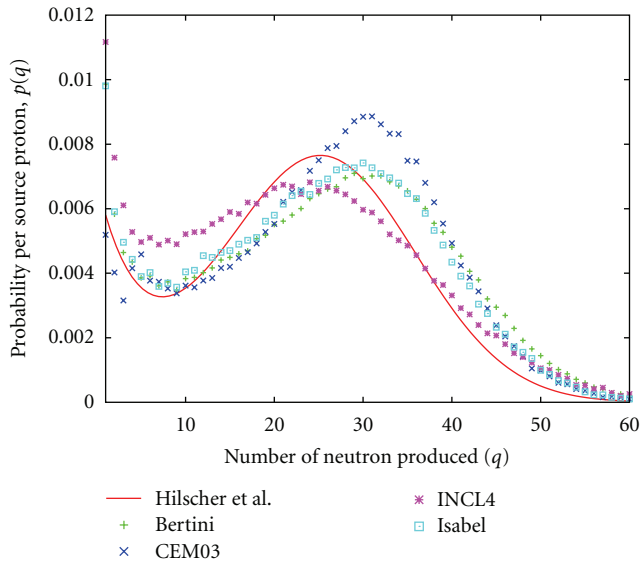


FIGURE 4: Comparison of measured and simulated distribution of the number of neutrons produced by a source proton for the 5 cm thick target.

numbers ($q < 10$) the probability of a high energy neutron is much higher than at higher neutron numbers.

The comparison of the results obtained with different target thicknesses shows that in case of the thicker targets the difference between the one-particle energy distributions for low q and for high q decreases. In the case of the 35 cm thick target (see Figure 8) for neutron numbers higher than 25, there is no difference between the distributions, which are very close to the average spectrum $\chi(E)$. This can also be seen in Figure 9 where the portion of the low-energy

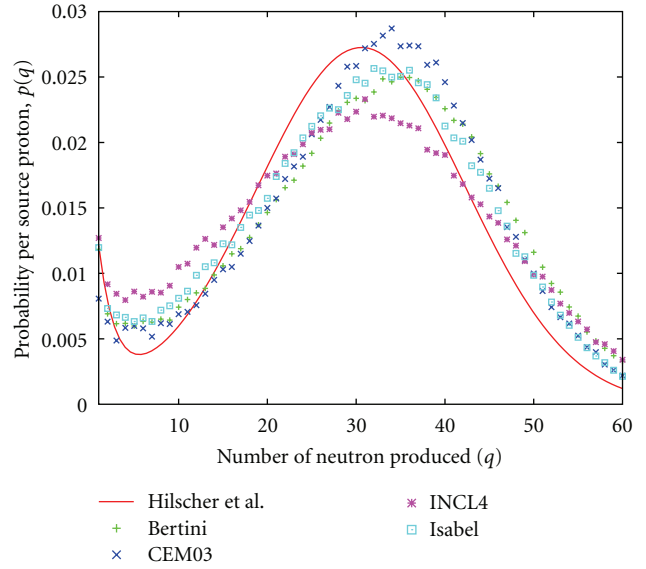


FIGURE 5: Comparison of measured and simulated distribution of the number of neutrons produced by a source proton for the 35 cm thick target.

(<100 MeV) neutrons can be seen compared to the high-energy (>100 MeV) neutrons for the different targets. Up to about 25 neutrons/proton this ratio goes together in the three cases, and the spectrum becomes softer as the number of neutrons increases. But above this value it steeply increases for the thin ($d = 0.2$ cm) target while saturates for the thick ones. This is due to the fact that in the thin target all the neutrons come from one single nuclear interaction while in the thick targets the higher multiplicity is the result of secondary reactions and an average spectrum is produced. This averaging effect of the secondary reactions reduces the differences between the energy distributions for high neutron numbers in thick targets.

5.3. Calculation of the Two-Particle Energy Distribution and Spectrum. It has been shown above that the condition formulated in (13) does not stand for a spallation source, and therefore the factorization of the two-particle spectrum $\chi(E_1, E_2)$ is not possible. Now it is also important to investigate whether the energies of the neutrons from a source event are independent from each other and approximations (9) and (10) can be used. For this purpose all the $q(q-1)/2$ possible pairs have been created from the q neutrons escaping the target after a single source event and collected into energy bins according to the two energies E_i and E_j to determine the number of neutrons in each bin ($M_q^{i,j}$). In this way the two-particle energy distribution for q outgoing neutrons can be obtained as:

$$f_q(E_i, E_j) = \frac{2M_q^{i,j}}{q(q-1)M_q(E_i - E_{i-1})(E_j - E_{j-1})}, \quad (19)$$

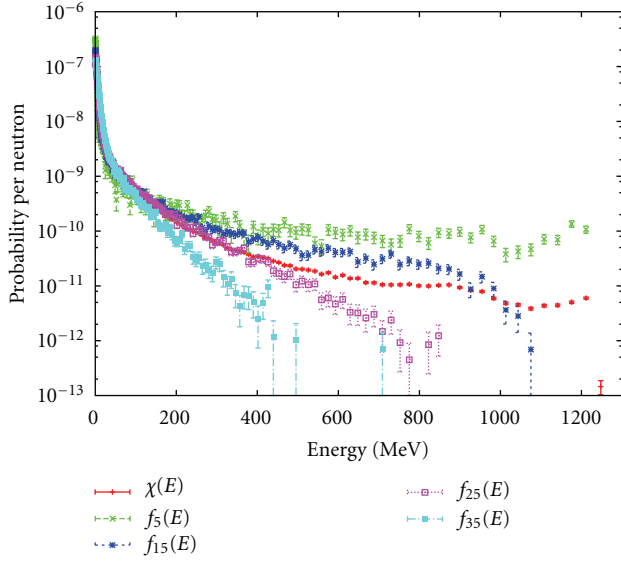


FIGURE 6: One-particle energy distributions $f_q(E)$ for different number of produced neutrons q and average spectrum $\chi(E)$ calculated for the 0.2 cm thick target.

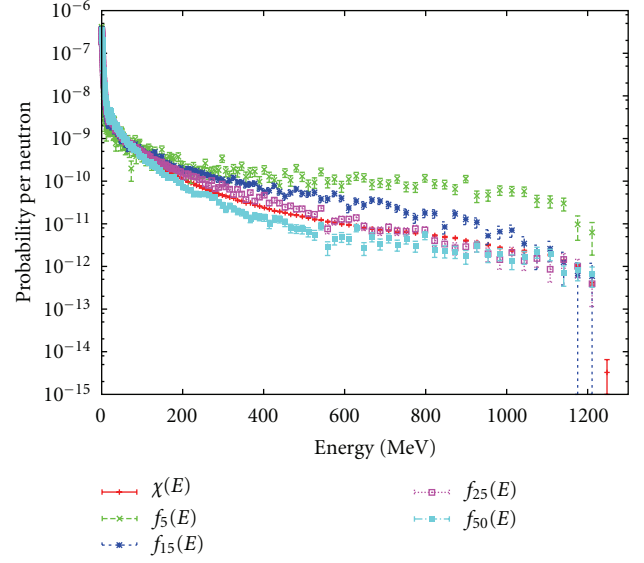


FIGURE 8: One-particle energy distributions $f_q(E)$ for different number of produced neutrons q and average spectrum $\chi(E)$ calculated for the 35 cm thick target.

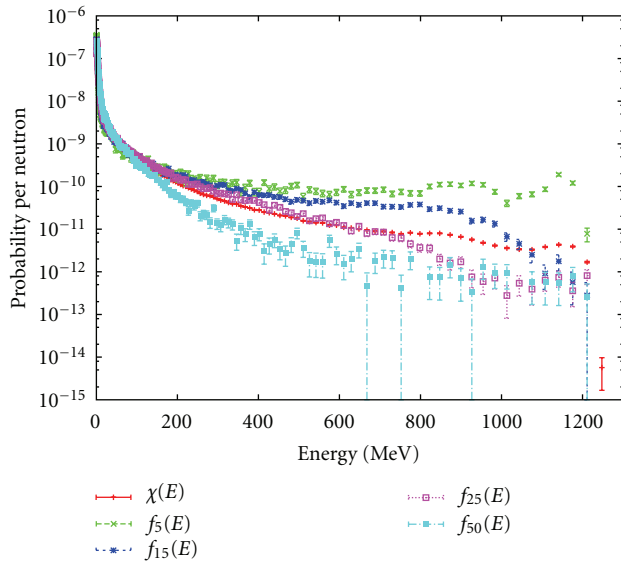


FIGURE 7: One-particle energy distributions $f_q(E)$ for different number of produced neutrons q and average spectrum $\chi(E)$ calculated for the 5 cm thick target.

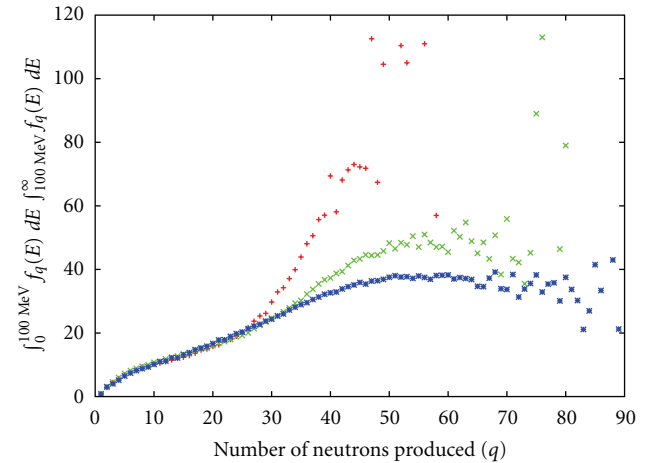


FIGURE 9: Portion of the low-energy (<100 MeV) neutrons compared to the high-energy (>100 MeV) neutrons for the different targets.

while the two-particle spectrum is given as:

$$\chi(E_i, E_j) = \frac{2 \sum_q M_q^{i,j}}{q(q-1)M(E_i - E_{i-1})(E_j - E_{j-1})}. \quad (20)$$

In order to express the deviation of the above functions from the case when conditions (9), (10), and (13) are valid, the following covariance functions have also been calculated:

$$\begin{aligned} C_{f_q}(E_1, E_2) &= f_q(E_1, E_2) - f_q(E_1)f_q(E_2), \\ C_\chi(E_1, E_2) &= \chi(E_1, E_2) - \chi(E_1)\chi(E_2). \end{aligned} \quad (21)$$

In Figure 10 one can see the two-energy distributions $f_q(E_i, E_j)$ for different neutron numbers q and the corresponding covariance functions $C_{f_q}(E_1, E_2)$ for the thin target. It can be observed that for low neutron numbers the condition (10) is not valid as the distributions are clearly antisymmetric for the $E_1 = E_2$ axis. This represents an ‘‘anti-correlation’’ of the neutron pairs: if a neutron is emitted with higher energy, then the other one tends to have lower energy. This effect diminishes at higher neutron numbers, due to the much higher degree of freedom the neutron energies become independent from each other. The same effect can be

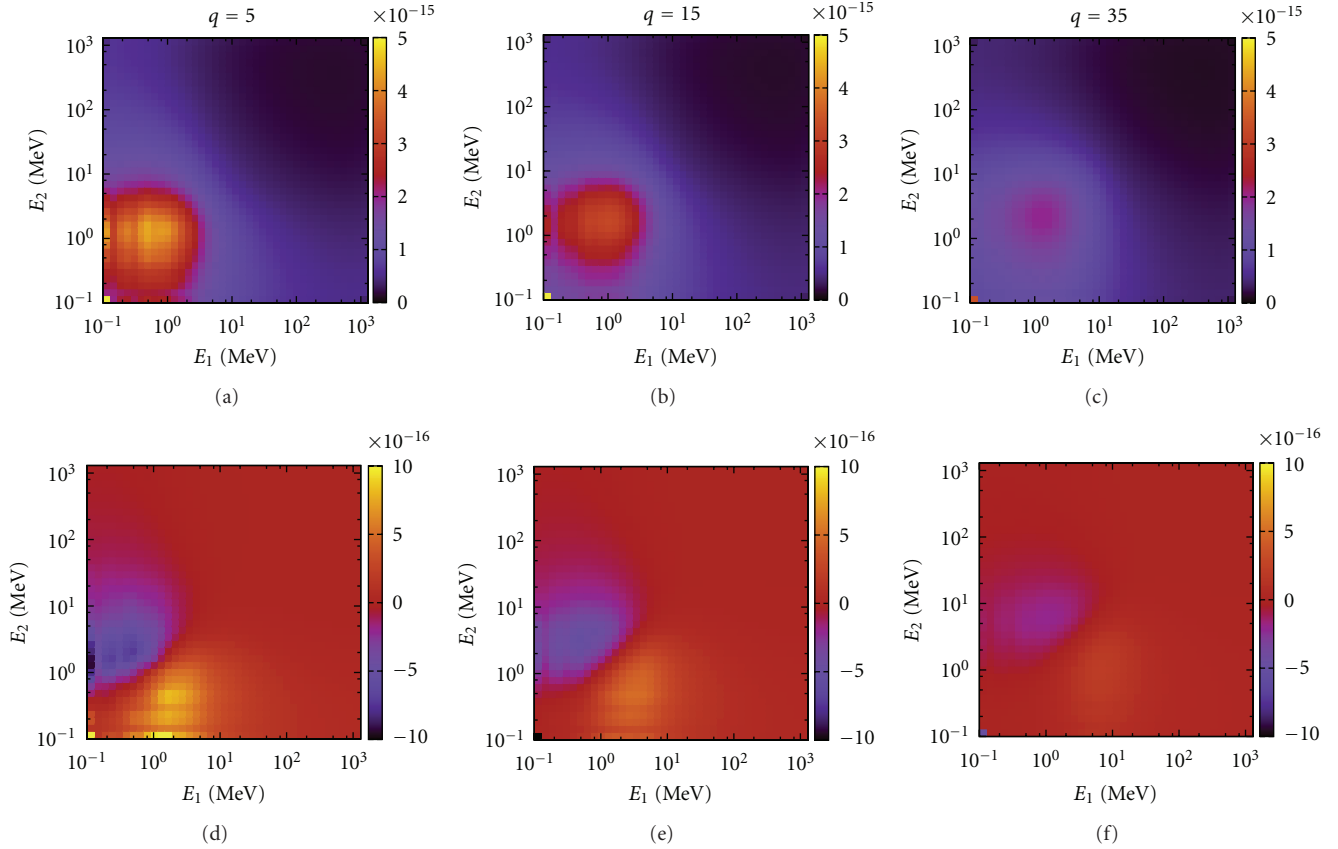


FIGURE 10: Two-energy distributions $f_q(E_i, E_j)$ (a)–(c) for different neutron numbers (q) and the corresponding covariance functions $C_{f_q}(E_1, E_2)$, (d)–(f) for the thin target ($d = 0.2$ cm).

observed for the thick targets, but due to the averaging effect of the secondary particles the “anti-correlation” diminishes even faster.

Concerning the two-particle spectra in Figure 11 one can see that the correlation observed in Figure 10 influences also the spectrum. In the case of the thin target the two-particle spectrum $\chi(E_1, E_2)$ is also asymmetric. This is demonstrated by the spectral covariance function $C_\chi(E_1, E_2)$, as well. For the thick targets this asymmetry is not obvious, but the covariance functions show that the effect exists, although in a much smaller extent than for the thin target. This is again due to the many more secondary particles produced in thicker targets.

6. Method to Investigate the Effect on Noise Measurements

As it was shown above, energy correlations between spallation neutrons exist, although the effect is very small and seems diminishing as the target thickness increases. Therefore, it is important to quantify the effect of these energy correlations on actual noise measurements in order to decide whether this effect needs to be considered or can be neglected by the assumption in (13). In the followings a simulation method is proposed for this investigation.

Noise measurements can be simulated by Monte Carlo calculations as described in, for example, [17]. In such calculations the data of the produced neutrons recorded during the above simulations can be used as the neutron source. In order to distinguish the effect of the different approximations, the calculations need to be performed by modified source data also, where the neutrons are redistributed between the source events:

- (i) by preserving the number distribution $p(q)$ but sampling the neutron energies from the one-energy distributions $f_q(E)$ to investigate the effect of the assumption in (9), that is, the independence of the energy distribution of the neutrons from the same source event;
- (ii) by preserving the number distribution $p(q)$ but sampling the neutron energies from the one-energy spectrum $\chi(E)$ to investigate the effect of the assumption in (13), that is, the independence of the energy spectrum of the produced neutrons from the number of neutrons produced in a source event;
- (iii) by preserving the number distribution $p(q)$ but sampling the neutron energies from the two-energy spectrum $\chi(E_1, E_2)$ to investigate whether the second moments are fully preserved in this way.

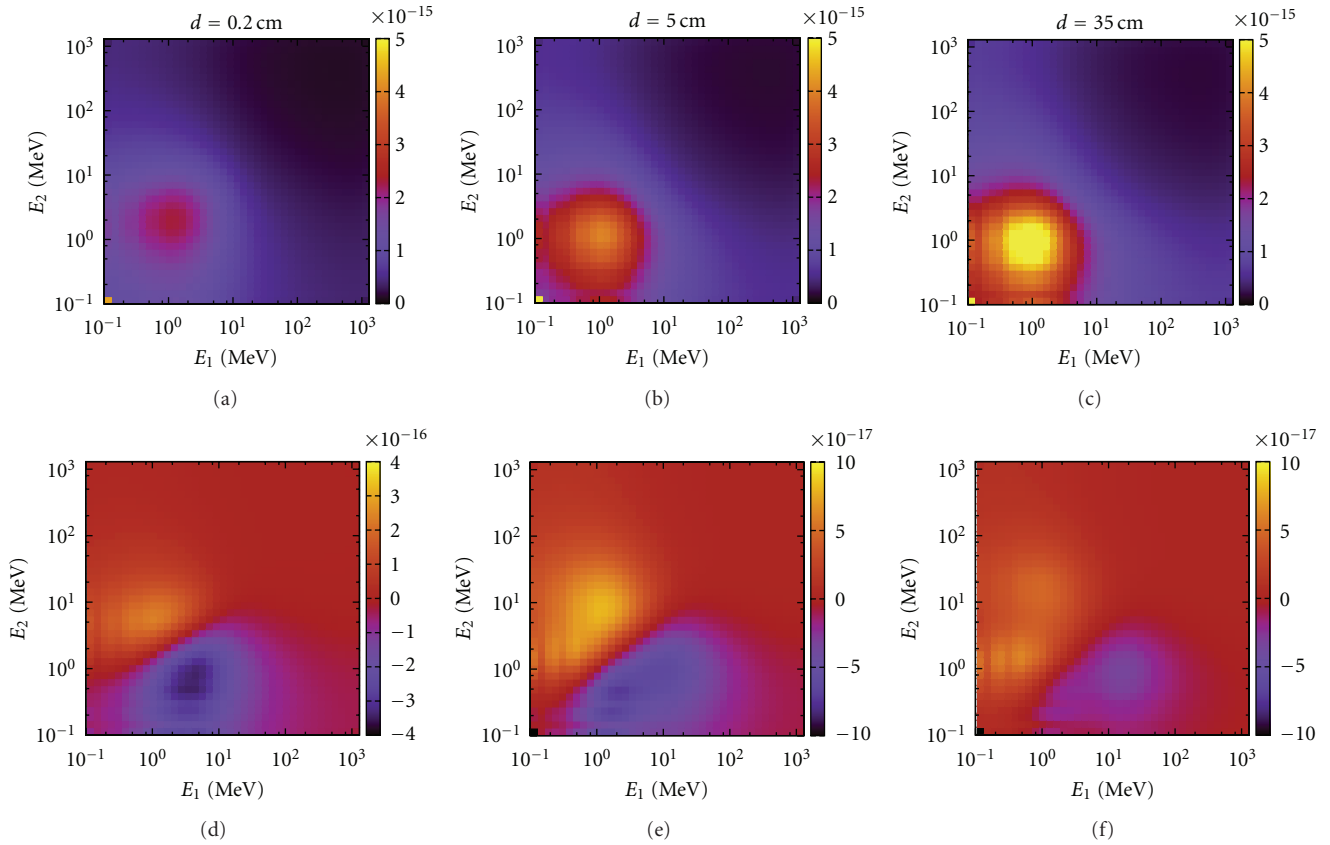


FIGURE 11: Two-particle neutron spectra $\chi(E_1, E_2)$ (a)–(c) and neutron spectrum covariance functions $C_\chi(E_1, E_2)$, (d)–(f) for different target thicknesses d .

Calculations are in hand with the above described method for a typical lead cooled ADS design to quantify the effect of the energy correlation on neutron noise measurements.

7. Conclusions

In the present paper the physical models implemented in the MCNPX code have been used for the investigation of the energy correlation in a spallation neutron source. After a successful validation of the model with a neutron multiplicity measurement, the one- and two-particle energy distributions and spectra of the spallation neutrons have been determined. It has been shown that the one-particle energy distributions highly depend on the number of neutrons produced in a source event. Fewer neutrons result in a higher probability of high-energy neutrons as the excitation energy per neutron is higher. It has also been observed that the averaging effect of the large number of secondary reactions in thick targets reduces this effect. The energy correlation between the neutrons from low multiplicity spallation events has been demonstrated also by the two-energy distributions. Finally, one can conclude that the energy correlation is an important effect in a thin spallation target and for the complete description of the neutron fluctuations the two-energy spectrum $\chi(E_1, E_2)$ has to be used. On the other hand this effect reduces in thick targets and the factorization of the two-energy spectrum $\chi(E_1, E_2) = \chi(E_1)\chi(E_2)$ appears

as an acceptable approximation. Further investigations are in hand to quantify the actual effect of the observed energy correlations on the higher moments of the neutron fluctuations in a subcritical system.

Acknowledgments

This work is connected to the scientific program of the “Development of quality-oriented and harmonized R+D+I strategy and functional model at BME” project. This project is supported by the New Széchenyi Plan (Project ID: TÁMOP-4.2.1/B-09/1/KMR-2010-0002).

References

- [1] D. B. Pelowitz, Ed., “MCNPX user’s manual, version: 2.6.0,” Tech. Rep. LA-CP-07-1473, Los Alamos National Laboratory, Los Alamos, NM, USA, 2008.
- [2] Y. Kitamura, T. Misawa, A. Yamamoto, Y. Yamane, C. Ichihara, and H. Nakamura, “Feynman-alpha experiment with stationary multiple emission sources,” *Progress in Nuclear Energy*, vol. 48, no. 6, pp. 569–577, 2006.
- [3] D. Hilscher, U. Jahnke, F. Goldenbaum, L. Pienkowski, J. Galin, and B. Lott, “Neutron production by hadron-induced spallation reactions in thin and thick Pb and U targets from 1 to 5 GeV,” *Nuclear Instruments and Methods in Physics Research A*, vol. 414, no. 1, pp. 100–116, 1998.

- [4] Y. Yamane and I. Pázsit, “Theory of neutron fluctuations in source-driven subcritical systems,” *Nuclear Instruments and Methods in Physics Research A*, vol. 403, no. 2-3, pp. 431–441, 1998.
- [5] Y. Yamane and I. Pázsit, “Heuristic derivation of Rossi-alpha formula with delayed neutrons and correlated source,” *Annals of Nuclear Energy*, vol. 25, no. 17, pp. 1373–1382, 1998.
- [6] I. Pázsit and L. Pál, *Neutron Fluctuations*, Elsevier, Oxford, UK, 2008.
- [7] I. Pázsit, N. G. Sjöstrand, and V. Fhager, “On the significance of the energy correlations of spallation neutrons on the neutron fluctuations in accelerator-driven subcritical systems,” *Nuclear Instruments and Methods in Physics Research A*, vol. 452, no. 1, pp. 256–265, 2000.
- [8] J.-L. Muñoz-Cobo, C. Berglöf, J. Peña, D. Villamarín, and V. Bournos, “Feynman- α and Rossi- α formulas with spatial and modal effects,” *Annals of Nuclear Energy*, vol. 38, no. 2-3, pp. 590–600, 2011.
- [9] R. E. Prael and H. Liechtenstein, “User guide to LCS: the LAHET code system,” Tech. Rep. LA-UR-89-3014, Los Alamos National Laboratory, Los Alamos, NM, USA, 1989.
- [10] A. Fassó, A. Ferrari, J. Ranft, P. R. Sala, G. R. Stevenson, and J. M. Zazula, “A comparison of FLUKA simulations with measurements of fluence and dose in calorimeter structures,” *Nuclear Instruments and Methods in Physics Research A*, vol. 332, no. 3, pp. 459–468, 1993.
- [11] P. Cloth, D. Filges, R. D. Neef et al., “KFA report Jülich 2203,” Tech. Rep., Forschungszentrum Jülich, Berlin, Germany, 1988.
- [12] H. W. Bertini, “Low-energy intranuclear cascade calculation,” *Physical Review*, vol. 131, no. 4, pp. 1801–1821, 1963.
- [13] Y. Yariv and Z. Fraenkel, “Intranuclear cascade calculation of high energy heavy ion collisions: effect of interactions between cascade particles,” *Physical Review C*, vol. 24, no. 2, pp. 488–494, 1981.
- [14] J. Cugnon, C. Volant, and S. Vuillier, “Improved intranuclear cascade model for nucleon-nucleus interactions,” *Nuclear Physics A*, vol. 620, no. 4, pp. 475–509, 1997.
- [15] S. Mashnik, K. Gudima, A. Sierk, M. Baznat, and N. Mokhov, “CEM03.01 user manual,” Tech. Rep. LA-UR-05-7321, Los Alamos National Laboratory, Los Alamos, NM, USA, 2005.
- [16] L. Dresner, “EVAP—a FORTRAN program for calculating the evaporation of various particles from excited compound nuclei,” Tech. Rep. ORNL-TM-196, Oak Ridge National Laboratory, Oak Ridge, Tenn, USA, 1962.
- [17] M. Szieberth and J. L. Kloosterman, “Estimation of coincidence and correlation in non-analogous Monte Carlo particle transport,” in *Proceedings of the Advances in Reactor Physics to Power the Nuclear Renaissance (PHYSOR '10)*, Pittsburgh, Pa, USA, 2010.

Research Article

Monte Carlo Calculation of Fragment Distributions in Nuclear Reactions

A. Deppman,¹ E. Andrade-II,¹ P. C. R. Rossi,² F. Garcia,³ and J. R. Maiorino⁴

¹Instituto de Física, Universidade de São Paulo (IFUSP), Rua do Matão, Travessa R 187, 05508-900 São Paulo, SP, Brazil

²Divisão de Reatores, Instituto de Pesquisas Energéticas e Nucleares (IPEN/CNEN-SP), Rua do Matão, Travessa R 400, 05508-900 São Paulo, SP, Brazil

³Centro de Pesquisas em Ciências e Tecnologia das Radiações (CPqCTR), Universidade Estadual de Santa Cruz, Road Ilhéus-Itabuna km 16, Ilhéus, BA, Brazil

⁴Centro de Engenharia, Modelagem e Ciências Sociais Aplicadas, Universidade Federal do ABC, Rua Santa Adélia, 166, 09210-170-Santo Andre, SP, Brazil

Correspondence should be addressed to A. Deppman, adeppman@gmail.com

Received 13 December 2011; Revised 5 March 2012; Accepted 5 March 2012

Academic Editor: Alberto Talamo

Copyright © 2012 A. Deppman et al. This is an open access article distributed under the Creative Commons Attribution License, which permits unrestricted use, distribution, and reproduction in any medium, provided the original work is properly cited.

The fragments produced in nuclear reactions for accelerator driven systems (ADS) operation form elements that can have effects on the structure of the reactor. In this regard, the calculation of fragment distributions gives important information for the development of ADS. To obtain those distributions, the Monte Carlo (MC) method is an important tool, and in this work we describe calculations of fragment distributions through a MC code for reactions initiated by intermediate- and high-energy protons and photons on actinide and preactinide nuclei. We study the production of fragments through spallation and fission reactions. The results show good qualitative agreement with experimental data.

1. Introduction

The accelerator driven system (ADS) is an innovative reactor which is being developed as a dedicated burner in a double strata fuel Cycle to incinerate nuclear waste [1–4]. The ADS system consists of a subcritical assembly driven by accelerator delivering a proton beam on a target to produce neutrons by a spallation reaction. The spallation target constitutes at the same time the physical and the functional interface between the accelerator and the subcritical reactor. For this reason it is probably the most innovative component of the ADS, and its design is a key issue to develop ADS. The performance of the reactor is characterized by the number of neutrons emitted for incident proton, the mean energy deposited in the target for neutron produced, the neutron spectrum, and the spallation product distribution [5].

The detailed design of spallation neutron sources or accelerator-driven systems (ADS) requires reliable computational tools in order to optimize their performance in terms of useful neutron production and to properly assess specific

problems likely to happen in such systems. Among those problems are the radioactivity induced by spallation reaction and the problem of shielding [6] the radiation due to energetic particles generated in the reaction, the changes in the chemical composition and radiation damage in target, window, or structure materials [7], and induced radiotoxicity within the target [8] due the production of several nuclides. Radiation damage can arise from gas production that causes embrittlement of structural materials and from atomic displacements (DPA) which fragilize the various components of the spallation source. Modifications of the chemical composition of these materials possibly result into problems of corrosion or alloy cohesion and modification of mechanical properties because of the appearance of compounds not existing initially in the materials.

It is important to emphasize that, at the present status in the development of ADS, it is still necessary to study the best technological options for variables such as the material used for the target and the energy of incident particles. For this reason the most important aspect in the calculations of yields

of nuclides is the confidence one has on the results obtained. More important than accuracy, at this moment, may be the reliability of the calculation method. One should consider more important methods which take into consideration the correct mechanisms of reactions, than those methods that have many free parameters to fit experimental data. These are of great importance to interpolate experimental data, when they are available, but are of restrict use when there is not any data.

This paper is organized as follows: Section 2 describes the main mechanisms for fragments production in nuclear reactions and gives a short description of the intranuclear cascade process, which is relevant for the description of the residual nucleus formation. In Section 3 the evaporation mechanism is described. This is the most important mechanism for the study of spallation. In Section 4 the fission process is described, this decay channel being relevant for the formation of fission fragments. In Section 5 we present and discuss the results obtained with the CRISP code, and in Section 6 we show our conclusions.

2. Production of Nuclide in Nuclear Reactions

The production of nuclide is associated to the different mechanisms through which the nuclear reaction evolves. Depending on the target, on the probe and on the energy, different mechanisms are more or less relevant. On the other hand, the distribution of fragments generated when the reaction finishes is strongly dependent on the channels, open to the system and on the respective branching ratios.

As the reaction energy increases, more channels are available and the complexity of the reaction increases. This high complexity is the main reason to adopt Monte Carlo (MC) methods in calculations of nuclear reactions results. Indeed the large number of particles, the large number of available channels and the fact that the reaction may be understood as a Markovian sequence of steps are features that perfectly match the characteristics of Monte Carlo calculations. In this work we adopt the MC method and use the implementation for nuclear reaction calculations developed in the CRISP code [12], which has been already used in ADS studies [13–15]. This implementation is described in some details below.

It is well established that intermediate- and high-energy reactions follow a two-step mechanism, as proposed by Bohr. In the first one, usually called intranuclear cascade, the energy and momentum of the incident particle is distributed among a few nucleons through baryon-baryon reactions which are mainly elastic, but at sufficiently high energies nucleonic degrees of freedom can be excited. This step finishes when there is not any nucleons with kinetic energy that is high enough to escape from the nuclear binding. Thereafter the collisions among nucleons lead only to the system thermalization.

The second step depends on the excitation of the residual nucleus formed at the end of the intranuclear cascade. If the nuclear excitation energy is $E/A \leq 3$ MeV, a statistical competition between evaporation and fission takes place. For heavy-nuclei ($A > 230$) fission is the dominant channel, and in most of the cases the reaction ends with the formation of

two fragments [16]. For nuclei with $A < 230$, fission is much less probable, and in most cases the nucleus evaporates until there is not energy for evaporation of any particle (neutrons, protons, and alpha particles are the most frequent). Then a spallation product is formed which is characterized by its mass and atomic numbers.

If the nuclear excitation energy is $E \geq 3$ MeV/A an entirely different process may occur, namely, the nuclear multifragmentation [17–19]. This process is much faster than the evaporation/fission competition, and it is characterized by the simultaneous production of a large number of fragments with very different mass and atomic numbers. In the following we give a brief description of each process mentioned above.

2.1. Intranuclear Cascade. We now describe the nuclear mechanisms relevant in nuclear reactions at intermediate and high energies, which have been implemented in the CRISP code. The first thing we have to deal with is the intranuclear cascade (IC). As the incident particle enters the nucleus region, IC is the first mechanism of the reaction which is triggered by the collision of the probe with one of the nucleons in inelastic scattering. This collision, called elementary collision, will always generate secondary particles, which can be two nucleons in the case of elastic scattering, mesons, or resonance states of the nucleon. These secondaries have energies relatively high compared to the other nucleons in the Fermi sea and occupy high-energy single-state levels in the system [20–23]. We call them cascade particles.

The secondary particles generated in an elementary collision will propagate inside the nucleus and may interact with other particles, increasing the number of cascade particles or may reach the nuclear surface. In this case, if it has energy higher than the nuclear binding energy, it escapes from the nucleus, otherwise it is reflected back and keeps its propagation inside the nucleus. In this way, as the intranuclear cascade continues, the number of cascade particles increases. The decision to stop the intranuclear cascade and start the second step of the reaction is based on energetic criteria, namely, when there is not any bound particle that is in an excited state or has kinetic energy greater than its binding energy [21, 22, 24].

There are several important aspects in the intranuclear cascade calculations with the CRISP code. The first one is that it is a multicolisional simulation of the cascade, with all nucleons moving simultaneously. The time-ordered sequence of elementary collisions considers the probability of interactions among all those particles based on their respective cross sections. This is an important difference with respect to other Monte Carlo codes where only one cascade particle is considered, while all others are kept frozen in their initial state.

The multicolisional approach is an important improvement in the simulation of intranuclear cascade in respect to the MC method used in well-known codes like those from Barashenkov et al. or Bertini et al. [25, 26], since dynamical aspects as nuclear density modifications or the evolution of occupancy numbers during the cascade are naturally taken into account in the former method but not in the last [24].

Another important aspect is the Pauli blocking mechanism, responsible for keeping track of possible violations of the Pauli Principle. With the multicollisional method it is possible to adopt a very precise method for verifying the availability of single-particle states for the fermions generated in the elementary collisions, eliminating possible violations of this important principle of quantum mechanics. It is because we use this method for Pauli blocking that we can use the energetic criteria to decide to end the intranuclear cascade [27].

After the cascade finishes there is not any particle with energy high enough to escape from the nucleus. Then a sequence of elementary collisions will distribute the excitation energy remaining in the nucleus among all nucleons. This is called thermalization process. The main characteristics of the nucleus do not change during this step, and the mass number, the atomic number, and the excitation energy at the end of the thermalization step are the same as in the end of the intranuclear cascade.

In a CRISP simulation, the reactions can be initiated by intermediate- and high-energy protons [21] or photons [21, 22, 27, 28]. It has been used for energies up to 3.5 GeV [24], where it was shown that CRISP code can give good results for total photonuclear absorption cross sections from approximately 50 MeV, where the quasi-deuteron absorption mechanism is dominant, up to 3.5 GeV, where the so-called photon-hadronization mechanism is dominant, leading to a shadowing effect in the cross-section. Recently the CRISP code has been used to study final state interactions for the nonmesonic weak decay of hypernucleus [29]. The results show that it can be used even for light nuclei, as ^{12}C , and relatively low energies, as in the case of hypernucleus decay.

3. Evaporation

The thermalization is followed by the evaporation process, when nucleons or small clusters are emitted carrying part of the nuclear excitation energy. This process continues while there is energy enough in the nucleus to allow the evaporation of any particle. It consists of a sequence of emissions of particles by a nucleus, each one governed by the Weisskopf theory. Here the evaporation regime is governed by the relative probabilities of different particle emission channels [27, 28, 30].

These probabilities are obtained from the particle emission width, Γ_k , calculated according to the well-known Weisskopf evaporation model [31] in such a way that for proton emission we have

$$\frac{\Gamma_p}{\Gamma_n} = \frac{E_p}{E_n} \exp\left\{2\left[(a_p E_p)^{1/2} - (a_n E_n)^{1/2}\right]\right\}, \quad (1)$$

and for alpha particle emission,

$$\frac{\Gamma_\alpha}{\Gamma_n} = \frac{2E_\alpha}{E_n} \exp\left\{2\left[(a_\alpha E_\alpha)^{1/2} - (a_n E_n)^{1/2}\right]\right\}, \quad (2)$$

TABLE 1: Values for the relevant parameters in semiempirical mass formula.

Parameter	Value
a_v	-15.0175 ± 0.000013
a_{sf}	15.5981 ± 0.000032
a_{sym}	-7.09740 ± 0.00067
a_{ss}	144.764 ± 0.0022

TABLE 2: Values for the relevant parameters in Dostrovsky's empirical formulas.

Parameter	Value
a_1	18.81302 ± 0.000097
a_2	1.30001 ± 0.000097
a_3	18.670295 ± 0.000097
a_4	4.23501 ± 0.000097
a_5	18.89 ± 0.19
a_6	24.82 ± 2.18

where E_k corresponds to the nuclear excitation energy after the emission of a particle of kind k , with $k = p, n, \alpha$, which are calculated by

$$\begin{aligned} E_n &= E - B_n, \\ E_p &= E - B_p - V_p, \\ E_\alpha &= E - B_\alpha - V_\alpha, \end{aligned} \quad (3)$$

where B_n , B_p , and B_α are the separation energy of neutrons, protons, and alpha particles, and V_p and V_α are the Coulomb potentials for protons and alpha particles, respectively.

These Coulomb potentials are given by the expressions:

$$\begin{aligned} V_p &= C \frac{K_p(Z-1)e^2}{r_0(A-1)^{1/3} + R_p}, \\ V_\alpha &= C \frac{2K_\alpha(Z-2)e^2}{r_0(A-4)^{1/3} + R_\alpha}, \end{aligned} \quad (4)$$

where $K_p = 0.70$ and $K_\alpha = 0.83$ are the Coulomb barrier penetrabilities for protons and alpha particles. Also, $R_p = 1.14$ fm is the proton radius, $R_\alpha = 2.16$ fm is the alpha particle radius, and $r_0 = 1.18$ fm. C is the charged particle Coulomb barrier correction and is calculated according to

$$C = 1 - \frac{E}{B}, \quad (5)$$

B being the nuclear binding energy.

The level density parameters a_k are calculated from the Dostrovsky's empirical formulas [32]:

$$\begin{aligned} a_n &= \frac{A}{a_1} \left(1 - a_2 \frac{A - 2Z}{A^2}\right)^2, \\ a_p &= \frac{A}{a_3} \left(1 + a_4 \frac{A - 2Z}{A^2}\right)^2, \\ a_\alpha &= \frac{A}{a_5} \left(1 - \frac{a_6}{Z}\right)^2. \end{aligned} \quad (6)$$

TABLE 3: Values for some of the relevant parameters in the multimode formula for the fission-fragment mass distributions.

Parameter	Low-energy	Parameter	²⁴¹ Am	²³⁷ Np	²³⁸ U	²⁰⁸ Pb
Γ_S	10.0 ± 2	K_S (mb)	2970.0 ± 20.5	2590.0 ± 23.3	—	—
A_1^H	135.0 ± 1	K_1 (mb)	45.8 ± 0.2	49.0 ± 0.3	—	—
Γ_1^H	3.75 ± 2	K_2 (mb)	220.5 ± 1.5	252.0 ± 1.3	—	—
A_2^H	141.0 ± 2	μ_1	4.1	4.1	4.1	0.97
Γ_2^H	5.0 ± 1	μ_2	0.38	0.38	0.38	0.413
		γ_1	0.92	0.92	0.92	0.5
		γ_2	0.003	0.003	0.003	0.008

TABLE 4: Values of the relevant parameters found for the best agreement between simulated and experimental data for the fission of ²⁰⁸Pb induced by 500 MeV protons. Errors indicated represent superior limit for uncertainties.

Parameter	Value
b_1	0.01 ± 0.05
b_2	121.68 ± 0.05
b_3	0.23 ± 0.05
b_4	125.66 ± 0.05
b_5	14.93 ± 0.05
a_6	3.97 ± 0.05
b_7	5.21 ± 0.05

For the mass formula it was considered the semiempirical one proposed in [33] for the nuclear binding energy so that the nuclear masses are calculated according to

$$M(A, Z) = Zm_p + Nm_n + a_v A + a_{sf} A^{2/3} + \frac{3e^2}{5r_0} \frac{Z^2}{A^{1/3}} + (a_{sym} + a_{ss} A^{-1/3}) \frac{(N - Z)^2}{A}, \quad (7)$$

N being the number of neutrons. Formula (7) was fitted to compilation of Audi et al. [34] by the method of least squares with the MINUIT package [35]. The values for each parameter corresponding to the best fit are shown in Table 1.

To evaluate the evaporation probability one assumes that it is proportional to the corresponding width, that is, [15, 30]

$$P_k = \frac{\Gamma_k}{\Gamma_n + \Gamma_p + \Gamma_\alpha}. \quad (8)$$

While enough energy is available for particle evaporation other emissions are processed. The evaporation phase ends when the excitation energy of the nucleus is smaller than all the separation energies B_n , B_p , and B_α . At this point a nucleus that can be completely different from the initial one is formed. This nucleus is called spallation product.

4. Fission

The CRISP code can also evaluate the fission probability [36]. Fission is a process that competes with evaporation in the sense that each nucleus in the evaporation sequence can

undergo fission, forming two fragments with masses around one-half of the fissioning nucleus. This process can be easily included in the frame of the evaporation process by including the fission branching ratio, Γ_f , in formula (8), in such a way that it now reads

$$P_k = \frac{\Gamma_k}{\Gamma_n + \Gamma_p + \Gamma_\alpha + \Gamma_f}. \quad (9)$$

The fission branching ratio is calculated according to the Bohr-Wheeler fission model [37], by

$$\frac{\Gamma_f}{\Gamma_n} = K_f \exp\left\{2\left[\left(a_f E_f\right)^{1/2} - \left(a_n E_n\right)^{1/2}\right]\right\}, \quad (10)$$

where,

$$K_f = K_0 a_n \frac{\left[2\left(a_f E_f\right)^{1/2} - 1\right]}{\left(4A^{2/3} a_f E_n\right)}, \quad (11)$$

$$E_f = E - B_f,$$

$$a_f = r_f a_n,$$

B_f being the fission barrier calculated according to the Nix model [38], $K_0 = 14.39$ MeV and r_f an adjustable parameter.

With formula (9) it is now possible to calculate the probability of fission, P_f , at each step of the evaporation/fission competition process. Whenever the fission channel is chosen, two fragments are formed [39, 40], the heaviest one having mass and atomic numbers, A^H and Z^H , respectively, is sorted according to a probability distribution given by the statistical scission model (SSM) from Brosa et al. [41]. The lighter fragment has mass and atomic numbers given, respectively, by $A^L = A^F - A^H$ and $Z^L = Z^F - Z^H$.

The Brosa's model takes into account the collective effects of nuclear deformation during fission through a liquid-drop model and includes single-particle effects through microscopic shell-model corrections. The microscopic corrections create valleys in the space of elongation and mass number, each valley corresponding to one different fission mode. Fission cross section results from the incoherent sum of

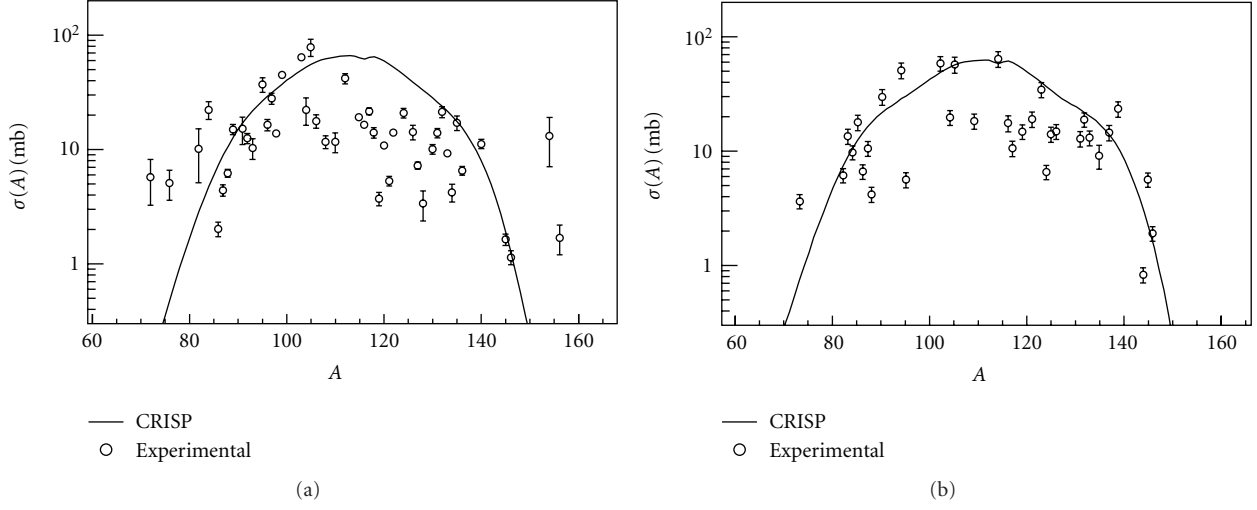


FIGURE 1: Cross section of fragments produced in the fission of ^{241}Am (a) and ^{237}Np as a function of fragment mass (b) induced by 660 MeV protons. Values from the systematic study of [9] for the parameters corresponding to the three fission modes considered in this work (—) were used. Open symbols (\circ) are the experimental data [10].

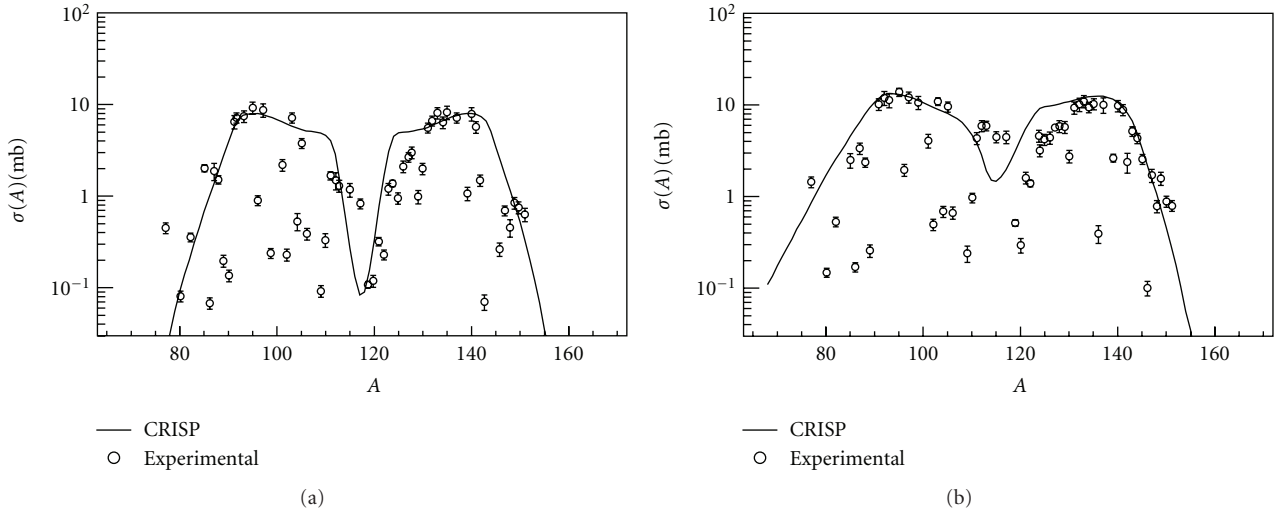


FIGURE 2: Cross sections for fragments produced in the fission of ^{238}U induced by bremsstrahlung of 50 MeV (a) and 3500 MeV (b) endpoint energies as a function of fragment mass. Open circles (\circ) are experimental results [11].

the contributions of each channel, $\sigma_i(A, Z)$, which are usually written in the form

$$\sigma(A, Z) = \left\{ \sum_{i=1,2} \left[\frac{K_i^L}{\sqrt{2\pi}\Gamma_i^L} \exp\left(-\frac{(A-A_i^L)^2}{2(\Gamma_i^L)^2}\right) + \frac{K_i^H}{\sqrt{2\pi}\Gamma_i^H} \exp\left(-\frac{(A-A_i^H)^2}{2(\Gamma_i^H)^2}\right) \right] + \frac{K_S}{\sqrt{2\pi}\Gamma_S} \exp\left(-\frac{(A-A_S)^2}{2(\Gamma_S)^2}\right) \right\} \times \frac{1}{\sqrt{2\pi}\Gamma_Z} \exp\left(-\frac{(Z-Z_f)^2}{2\Gamma_Z^2}\right), \quad (12)$$

where the summation runs over the asymmetric modes. The parameters for the symmetric mode are K_S , A_S , and Γ_S , while $K_i^{H(L)}$, $A_i^{H(L)}$, and $\Gamma_i^{H(L)}$ are the parameters for the heavy (light) fragment produced in the asymmetric mode i . For the atomic number distribution the parametrization used is

$$Z_f = \mu_1 + \mu_2 A, \quad (13)$$

for the most probable atomic number of the fragment, and

$$\Gamma_Z = \nu_1 + \nu_2 A, \quad (14)$$

for the width of the atomic number distribution. μ_1 , μ_2 , ν_1 and ν_2 are fitting parameters.

It is important to stress that the evaporation process has as input the distribution of nuclei obtained at the end

of the intranuclear cascade, therefore the fissioning nucleus may be different from the cascade residual nucleus because some neutrons, protons, and/or alpha-particles are allowed to evaporate before fission takes place. The effects of mass and energy distribution of the fissioning nucleus have been discussed elsewhere [40].

It is important to notice that all the parameters used in the CRISP code are fitted to a large number of experimental data for many different nuclei in different energy ranges. Also the probes can be as different as protons, tagged photons, Bremsstrahlung photons, or electrons. In this way, the method is reliable because it is not an *ad hoc* fitting to specific nucleus, reaction, or energy.

5. Results and Discussions

We used the CRISP code to calculate cross sections for the formation of fragments in nuclear reactions. As explained above, the main sources of fragments in the reactions studied here are spallation and fission processes, and in this section we show the cross sections for fission fragments and for spallation products.

5.1. Fission Reactions. The relevant parameters in Dostrovsky's empirical formulas (see (6)) for evaporation process are shown in Table 2. This set of parameters were used for all reactions studied in this work. The parameters for fission fragments calculations in formula (12) are shown in Table 3. For ^{241}Am , ^{237}Np , and ^{238}U cases, the values for width and position (Table 3, first column) of the fission modes were taken from a low-energy systematics [9]. The relative intensities of each fission mode for ^{241}Am and ^{237}Np were considered fixed, with their values given in Table 3. In the case of ^{238}U the relative intensities were calculated according to gaussian expressions depending on the fissioning system mass numbers.

There is not any systematic study of the multimodal parameters in the mass region of Pb. To obtain those parameters, we used a sigmoid fit for K_5 and gaussian fits for K_1 and K_2 , all depending on the mass of the fissioning system. For heavy fragment distributions the peak for the asymmetric modes are obtained by:

$$\begin{aligned} A_1^H &= b_1 A_f + b_2, \\ A_2^H &= b_3 A_f + b_4, \end{aligned} \quad (15)$$

while the width for each mode is assumed to be constant:

$$\begin{aligned} \Gamma_5 &= b_5, \\ \Gamma_1^H &= b_6, \\ \Gamma_2^H &= b_7. \end{aligned} \quad (16)$$

The values for each of these parameters corresponding to the best fit are presented in Table 4.

In Figure 1 we show results obtained for proton-induced fission. We observe that the results obtained with the CRISP code give a good description of the experimental data, although the data are spread over a large range.

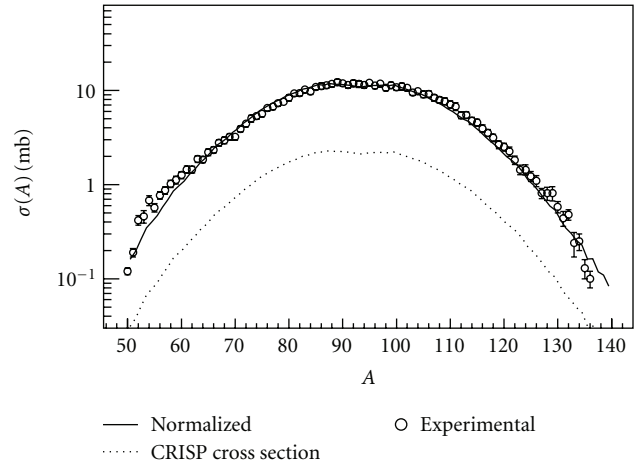


FIGURE 3: Cross sections for fragments produced in the fission of ^{208}Pb induced by 500 MeV protons as a function of mass.

Since CRISP can be used also for photon-induced reactions, we calculated the mass distributions of fragments for fission induced in ^{238}U by Bremsstrahlung photons with endpoint energies at 50 MeV and 3500 MeV. The results are presented in Figure 2. Also in this case the data do not show good resolution, but we can observe that the results with CRISP give a good general description of the experimental data.

A more precise experiment was performed for proton-induced fission on ^{208}Pb . In this case the experimental results are very precise. In Figure 3 we show the experimental data compared to the calculation results. We observe a very good agreement between experiment and calculation with the CRISP code, especially about the overall form of the distribution. Such an agreement is better attested when the result is normalized to the data.

For all results shown in Figures 1, 2, and 3, the evaporation of fragments were performed. This was achieved by using the already presented expression (12) to obtain the mass and atomic numbers of heavy and light fragments. By first approximation, the calculated excitation energy of the fissioning system was divided between the fragments which continued the evaporation process till the stopping criterion is reached again, as explained in Section 3.

5.2. Spallation Reactions. Nuclei with mass number $A < 220$ present low fission probabilities. In these cases the most probable reaction channel is the spallation, when the evaporation continues till the residual nucleus is cold, without fissioning. The nucleus at the end of the evaporation is then called spallation product.

With the CRISP code, using the parameters for evaporation and fission competition as described above, we can calculate also spallation product distributions. In Figure 4 we show our results and compare them to experimental data. In general we observe a fair agreement with data, since the well-known spallation parabola as calculated by us show position and width in good agreement with experimental results. For the most probable products, also the absolute cross sections, are in good agreement with data, although for

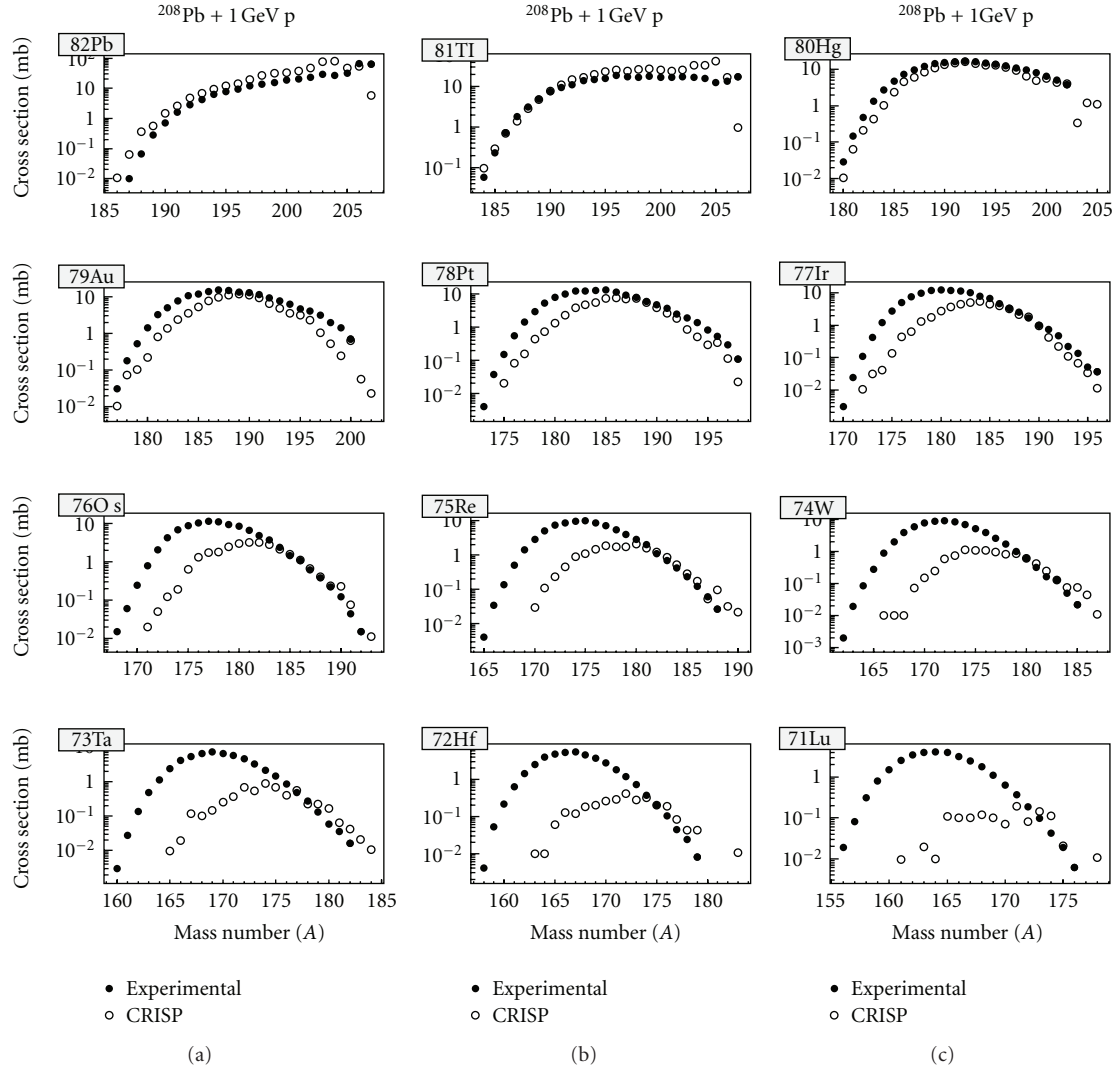


FIGURE 4: Cross section for fragments produced in spallation of ^{208}Pb induced by 1 GeV protons.

some spallation products the agreement is not good. Similar behaviour occurs for the case of spallation on ^{147}Au , shown in Figure 5.

In fact, these results show that it is extremely difficult to obtain good results simultaneously for several different reactions on a wide range of target mass numbers and for quite different energies. The main difficulty comes from the fact that, at the end of the intranuclear cascade, we have in general excited residual nuclei that may be far from the line of stability. Since most of the nuclear models and their parameters are determined for cold stable nuclei, we do not have precise information on the structure of all nuclei that are formed during nuclear reactions at intermediate and high energies. Improvements on mass formula and on shell effects can lead to better agreement between calculations and experiments.

6. Conclusion

In this work we addressed the problem of fragment production in nuclear reactions. This is a relevant issue in the

development of ADS, as it is directly related to the study of damage induced in materials used in ADS.

We discussed the importance of reliability of calculation, and show that the model implemented in the CRISP code is developed with reduced number of free parameters and care in reproducing accurately the physical process that occurs during the nuclear reaction. The parameters appearing in the mass formula were obtained by fittings to the nuclear mass data. The parameters for evaporation and fission were fitted simultaneously to several results for fission and spallation cross sections on several nuclei and with different probes at many different energies. For these reasons, the code can be used to calculate several observables in different reactions induced by probes like photons, electrons, protons, and neutrons in a large energy range on nuclei with mass from $A \approx 12$ to $A \approx 240$.

We use the CRISP code for calculating the production of nuclide in nuclear reactions induced by intermediate- or high-energy probes. Proton and photon reactions on actinide and preactinide nuclei were considered. The most important

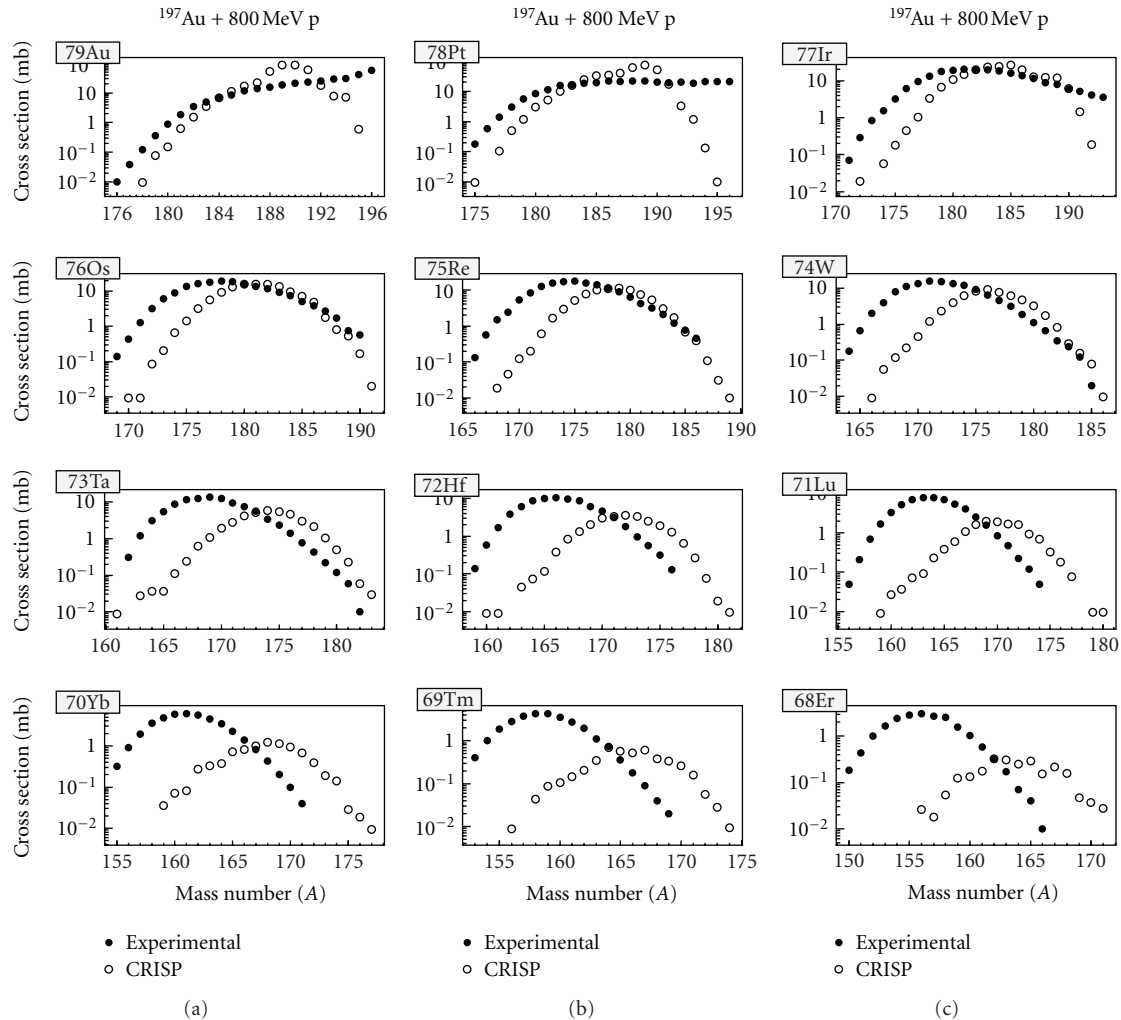


FIGURE 5: Cross section for fragments produced in spallation of ^{197}Au induced by 800 MeV protons.

mechanisms of fragments production, spallation, and fission were studied in details. We show that the results are in qualitative good agreement with experimental data available.

References

- [1] W. Gudowski, "Accelerator-driven transmutation projects. The importance of nuclear physics research for waste transmutation," *Nuclear Physics A*, vol. 654, no. 1-2, pp. 436–457, 1999.
- [2] E. Birgersson, S. Oberstedt, A. Oberstedt et al., "Light fission-fragment mass distribution from the reaction $251\text{Cf}(\text{nth}, \text{f})$," *Nuclear Physics A*, vol. 791, no. 1-2, pp. 1–23, 2007.
- [3] Department of Nuclear Energy Research Advisory Committee and the Generation IV International Forum, A Technology Roadmap for Generation IV Nuclear Energy Systems, GIF-002-00, 2002.
- [4] C. Rubbia et al., "Conceptual design of a fast neutron operated high power energy amplifier," CERN, Report CERN/AT/95-44(ET), 1995.
- [5] S. T. Mongelli, J. R. Maiorino, S. Anéfalos, A. Deppman, and T. Carluccio, "Spallation physics and the ADS target design," *Brazilian Journal of Physics*, vol. 35, no. 3 B, pp. 894–897, 2005.
- [6] S. Leray, "Long term needs for nuclear data development," IAEA report indc-nds-0428, 2001.
- [7] Villagrasa et al., "AccApp'03 Accelerator Applications in a Nuclear Renaissance," San Diego, Calif, USA, Stats-Unis d'Amerique.
- [8] T. Aoust, E. M. Malambu, and H. A. Abderrahim, "Importance of nuclear data for windowless spallation target design," in *Proceedings of the International Conference on Nuclear Data for Science and Technology*, vol. 769, pp. 1572–1575, October 2004.
- [9] C. Böckstiegel, S. Steinhäuser, K.-H. Schmidt et al., "Nuclear-fission studies with relativistic secondary beams: analysis of fission channels," *Nuclear Physics A*, vol. 802, pp. 12–25, 2008.
- [10] G. S. Karapetyan, A. R. Balabekyan, N. A. Demekhina, and J. Adam, "Multimode approach to 241Am and 237Np fission induced by 660-MeV protons," *Physics of Atomic Nuclei*, vol. 72, no. 6, pp. 911–916, 2009.
- [11] N. A. Demekhina and G. S. Karapetyan, "Multimode approximation for 238U photofission at intermediate energies," *Physics of Atomic Nuclei*, vol. 71, no. 1, pp. 27–35, 2008.
- [12] A. Deppman, S. B. Duarte, G. Silva et al., "The CRISP package for intermediate- and high-energy photonuclear reactions," *Journal of Physics G*, vol. 30, no. 12, pp. 1991–2002, 2004.

- [13] S. Anefalos, A. Deppman, G. Da Silva, J. R. Maiorino, A. Dos Santos, and F. Garcia, "The utilization of crisp code in hybrid reactor studies," *Brazilian Journal of Physics*, vol. 35, pp. 912–914, 2005.
- [14] S. Anefalos, A. Deppman, J. D. T. Arruda-Neto et al., "The CRISP code for nuclear reactions," in *Proceedings of the International Conference on Nuclear Data for Science and Technology*, vol. 769, pp. 1299–1302, 2004.
- [15] S. A. Pereira, "Spallation product distributions and neutron multiplicities for accelerator-driven system using the CRISP code," *Nuclear Science and Engineering*, vol. 159, pp. 102–105, 2008.
- [16] M. L. Terranova and O. A. P. Tavares, "Total nuclear photoabsorption cross section in the range 0.2–1.0 GeV for nuclei throughout the periodic table," *Physica Scripta*, vol. 49, pp. 267–279, 1994.
- [17] J. P. Bondorf, R. Donangelo, I. N. Mishustin, C. J. Pethick, H. Schulz, and K. Sneppen, "Statistical multifragmentation of nuclei. (I). Formulation of the model," *Nuclear Physics, Section A*, vol. 443, no. 2, pp. 321–347, 1985.
- [18] J. Bondorf, R. Donangelo, I. N. Mishustin, and H. Schulz, "Statistical multifragmentation of nuclei. (II). Application of the model to finite nuclei disassembly," *Nuclear Physics, Section A*, vol. 444, no. 3, pp. 460–476, 1985.
- [19] C. E. Aguiar, R. Donangelo, and S. R. Souza, "Nuclear multifragmentation within the framework of different statistical ensembles," *Physical Review C*, vol. 73, no. 2, Article ID 024613, pp. 1–8, 2006.
- [20] J. Cugnon, "Proton-nucleus interactions at high energy," *Nuclear Physics A*, vol. 462, p. 751, 1987.
- [21] M. Gonçalves, S. De Pina, D. A. Lima, W. Milomen, E. L. Medeiros, and S. B. Duarte, "Many-body cascade calculation for photonuclear reactions," *Physics Letters Section B*, vol. 406, no. 1–2, pp. 1–6, 1997.
- [22] S. De Pina, E. C. De Oliveira, E. L. Medeiros, S. B. Duarte, and M. Gonçalves, "Photonuclear K⁺ production calculation near threshold," *Physics Letters Section B*, vol. 434, no. 1–2, pp. 1–6, 1998.
- [23] J. Cugnon, C. Volant, and S. Vuillier, "Improved intra-nuclear cascade model for nucleon-nucleus interactions," *Nuclear Physics A*, vol. 620, p. 475, 1997.
- [24] A. Deppman, G. Silva, S. Anefalos et al., "Photofission and total photoabsorption cross sections in the energy range of shadowing effects," *Physical Review C*, vol. 73, no. 6, Article ID 064607, 2006.
- [25] V. S. Barashenkov, F. G. Geregghi, A. S. Iljinov, G. G. Jonsson, and V. D. Toneev, "A cascade-evaporation model for photonuclear reactions," *Nuclear Physics, Section A*, vol. 231, no. 3, pp. 462–476, 1974.
- [26] H. W. Bertini, "Low-energy intranuclear cascade calculation," *Physical Review*, vol. 131, no. 4, pp. 1801–1821, 1963.
- [27] A. Deppman, O. A. P. Tavares, S. B. Duarte et al., "The MCEF code for nuclear evaporation and fission calculations," *Computer Physics Communications*, vol. 145, no. 3, pp. 385–394, 2002.
- [28] A. Deppman, O. A. P. Tavares, S. B. Duarte et al., "Photofissibility of heavy nuclei at intermediate energies," *Physical Review C*, vol. 66, no. 6, pp. 676011–676014, 2002.
- [29] I. Gonzales, "Many-body cascade calculation of final state interactions in 12 nonmesonic weak decay," *Journal of Physics G*, vol. 38, no. 11, Article ID 115105, 2011.
- [30] A. Deppman, O. A. P. Tavares, S. B. Duarte et al., "A Monte Carlo method for nuclear evaporation and fission at intermediate energies," *Nuclear Instruments and Methods in Physics Research Section B*, vol. 211, no. 1, pp. 15–21, 2003.
- [31] V. Weisskopf, "Statistics and nuclear reactions," *Physical Review*, vol. 52, no. 4, pp. 295–303, 1937.
- [32] I. Dostrovsky, P. Rabinowitz, and R. Bivins, "Monte Carlo calculations of high-energy nuclear interactions. I. Systematics of nuclear evaporation," *Physical Review*, vol. 111, no. 6, pp. 1659–1676, 1958.
- [33] J. M. Pearson, "The quest for a microscopic nuclear mass formula," *Hyperfine Interactions*, vol. 132, no. 1–4, pp. 59–74, 2001.
- [34] G. Audi, A. H. Wapstra, and C. Thibault, "The Ame2003 atomic mass evaluation—(II). Tables, graphs and references," *Nuclear Physics A*, vol. 729, no. 1, pp. 337–676, 2003.
- [35] F. James, "Minuit: Function Minimization and Error Analysis-Reference Manual Version 94.1," CERN Program Library Long Writup D506.
- [36] A. Deppman, O. A. P. Tavares, S. B. Duarte et al., "Photofissibility of actinide nuclei at intermediate energies," *Physical Review Letters*, vol. 87, no. 18, Article ID 182701, pp. 1827011–1827014, 2001.
- [37] N. Bohr and J. A. Wheeler, "The mechanism of nuclear fission," *Physical Review*, vol. 56, no. 5, pp. 426–450, 1939.
- [38] J. R. Nix, "Calculation of fission Barriers for heavy and super-heavy nuclei," *Annual Review of Nuclear Science*, vol. 22, pp. 65–120, 1972.
- [39] E. Andrade II, E. Freitas, O. A. P. Tavares, S. B. Duarte, A. Deppman, and F. Garcia, "Monte Carlo simulation of heavy nuclei photofission at intermediate energies," in *Proceedings of the 31st Workshop on Nuclear Physics*, vol. 1139, pp. 64–69, American Institute of Physics, 2009.
- [40] E. Andrade II, J. C. M. Menezes, S. B. Duarte et al., "Fragment mass distributions in the fission of heavy nuclei by intermediate- and high-energy probes," *Journal of Physics G*, vol. 38, no. 8, Article ID 085104, 2011.
- [41] U. Brosa, S. Grossmann, and A. Müller, "Nuclear scission," *Physics Report*, vol. 197, no. 4, pp. 167–262, 1990.

Research Article

Solutions without Space-Time Separation for ADS Experiments: Overview on Developments and Applications

B. Merk and V. Glivici-Cotruță

Helmholtz-Zentrum Dresden-Rossendorf, Institut für Sicherheitsforschung, Postfach 51 01 19, 01314 Dresden, Germany

Correspondence should be addressed to B. Merk, b.merk@hzdr.de

Received 13 December 2011; Accepted 17 March 2012

Academic Editor: Alberto Talamo

Copyright © 2012 B. Merk and V. Glivici-Cotruță. This is an open access article distributed under the Creative Commons Attribution License, which permits unrestricted use, distribution, and reproduction in any medium, provided the original work is properly cited.

The different analytical solutions without space-time separation foreseen for the analysis of ADS experiments are described. The SC3A experiment in the YALINA-Booster facility is described and investigated. For this investigation the very special configuration of YALINA-Booster is analyzed based on HELIOS calculations. The results for the time dependent diffusion and the time dependent P_1 equation are compared with the experimental results for the SC3A configuration. A comparison is given for the deviation between the analytical solution and the experimental results versus the different transport approximations. To improve the representation to the special configuration of YALINA-Booster, a new analytical solution for two energy groups with two sources (central external and boundary source) has been developed starting from the Green's function solution. Very good agreement has been found for these improved analytical solutions.

1. Introduction

Different current and planned experiments (MUSE [1], YALINA [2], GUINEVERE [3]) are designed to study the zero power neutron physical behavior of accelerator-driven systems (ADSs). The detailed analysis of the kinetic space-time behavior of the neutron flux is important for the evaluation of these ADS experiments. Current analysis for all these experiments is based on the standard methods [4]—Sjöstrand method [5] and Slope method [6]—both are based on the point kinetics equations [7]. The point kinetics equations are developed from different approximations to the transport equation. Nevertheless, all these partial differential equations of the transport equation are solved by the separation of space and time to derive the point kinetics equations. The separation of space and time does not provide useful results for cases with strongly space-time dependent external source [8]. In recent years, two big projects have been launched to solve the problem of subcriticality determination in ADS experiments and during ADS operation for the future. In the 6th European Framework program in the integrated project EUROTRANS, the domain 2, ECATS [9] has been dedicated to ADS experiments and the analysis

methods for the experiments. In the same time frame, the IAEA has launched the coordinated research project “Analytical and Experimental Benchmark Analyses of Accelerator Driven Systems (ADS)” [10]. Different correction methods based on Monte Carlo Results for the YALINA-Booster system have been derived for the Sjöstrand method as well as for the Slope method in EUROTRANS/ECATS [11, 12]. Good results have been achieved with this correction method for the analysis of the detectors in the thermal zone [13]. Nevertheless, there is still a problem that exists in the fast zone, which is the really important zone, since the follow-up experiment GUINEVERE will be a pure fast system. The results for the analysis of the fast zone of YALINA-Booster are still not convincing, even with the use of correction factors. Good results, but once more only for the thermal and the reflector positions, have been shown in the IAEA CRP by the US American group, especially. These results rely on the use of correction factors from deterministic calculations [14]. The conclusion of the IAEA meeting suggests for further activities, maybe a further CRP among others, the following two topics: “Online Reactivity Monitoring and Control of Sub-critical System”; “Determination of Sub-criticality Level and Uncertainties Analyses” [15].

2. Developed Analytical Solutions for the Analysis of ADS Experiments

To overcome the problems in the analysis of the fast zone in YALINA-Booster and in GUINEVERE as completely fast system, it has been proposed from Helmholtz-Zentrum Dresden-Rossendorf to solve a more elaborate approximation of the transport equation—either the diffusion equation itself (1) or even the time-dependent Telegrapher's equation (2) [16] without separation of space and time. The Telegrapher's equation and the diffusion equation without delayed neutron production are solved completely analytically by using the Green's function method [17, 18]:

$$\frac{1}{\nu} \frac{\partial \phi}{\partial t} = D \frac{\partial^2 \phi}{\partial x^2} - \Sigma_a \phi + S, \quad (1)$$

$$\frac{3D}{\nu^2} \frac{\partial^2 \phi}{\partial t^2} + \frac{1}{\nu} (1 + 3D\Sigma_a) \frac{\partial \phi}{\partial t} = D \frac{\partial^2 \phi}{\partial x^2} - \Sigma_a \phi + S. \quad (2)$$

Solutions for the Telegrapher's equation have already been provided for a Dirac type pulsed external source [19], for the start-up [20, 21], and for the switch-off [8] of an external source, even with consideration of the delayed neutron production. For the comparison with the experimental results, obtained at the YALINA-Booster facility, a special external source (switch-on followed by a switch-off after a finite time period) has been used for the determination of the analytical solution for the neutron flux [22–25]. The derived solutions for the space-time dependent neutron flux were compared to the detector responses at different locations in the fast area of the YALINA-Booster core [26, 27]. Major results of these comparisons were a good agreement for the spatial distributions during the pulse and only small differences between time-dependent diffusion and time-dependent P_1 transport using identical cross-sections and coefficients [23, 25]. The analysis of the specifics of the YALINA facility forced to extend the analytical solution of the diffusion equation using two energy groups, (3) [28]:

$$\begin{aligned} \frac{1}{\nu_1} \frac{\partial \phi_1}{\partial t} &= D_1 \frac{\partial^2 \phi_1}{\partial x^2} - \Sigma_{a1} \phi_1 + \chi_1 (\nu \Sigma_{f1} \phi_1 + \nu \Sigma_{f2} \phi_2) \\ &\quad - \Sigma_{1-2} \phi_1 + \Sigma_{2-1} \phi_2 + \chi_{s1} S, \\ \frac{1}{\nu_2} \frac{\partial \phi_2}{\partial t} &= D_2 \frac{\partial^2 \phi_2}{\partial x^2} - \Sigma_{a2} \phi_2 + \chi_2 (\nu \Sigma_{f1} \phi_1 + \nu \Sigma_{f2} \phi_2) \\ &\quad + \Sigma_{1-2} \phi_1 - \Sigma_{2-1} \phi_2 + \chi_{s2} S. \end{aligned} \quad (3)$$

For a better representation, especially for the experiments in the GUINEVERE facility [3, 29], analytical solutions for one energy group for a two-region system, consisting of a multiplicative core with source and a reflective, only absorbing surrounding (reflector), (4) [30], were calculated:

$$\begin{aligned} \frac{1}{\nu_1} \frac{\partial \phi_1}{\partial t} &= D_1 \frac{\partial^2 \phi_1}{\partial x^2} - \Sigma_{a1} \phi_1 + \nu \Sigma_{f1} \phi_1 + S, \\ \frac{1}{\nu_2} \frac{\partial \phi_2}{\partial t} &= D_2 \frac{\partial^2 \phi_2}{\partial x^2} - \Sigma_{a1} \phi_2. \end{aligned} \quad (4)$$

For all problems symmetry of the system was assumed and the solutions were derived for a half of the region. Reflective boundary conditions are used in the center of the system, as well as at the outer boundary. In order to connect two regions, continuous neutron flux and neutron current were used for the two-region solution.

The derived Green's functions $G_i(\xi, \tau | \xi_0, \tau_0)$ are universal solutions for the solved equation, which are still independent of the definition of the external source in space and time.

The analytical solution for the time-dependent one- and two-group diffusion equation with initial and boundary conditions (1) to (4) is expressed by a double integral in terms of the corresponding Green's functions and the external source, which has to be defined:

$$\begin{aligned} \Phi_i(\xi, \tau) &= \int_{\tau_a}^{\tau} \int_{\xi_0=0}^R G_i(\xi, \tau | \xi_0, \tau_0) [S(\xi_0, \tau_0)] d\xi_0 d\tau_0, \\ &\quad i = I \text{ or } I, II. \end{aligned} \quad (5)$$

$G_i(\xi, \tau | \xi_0, \tau_0)$, $i = I \text{ or } I, II$ are the Green's functions. A Green's function is a solution for the problem associated with the given problem (one-group diffusion, one-group P_1 , two-group diffusion, or two-region one-group diffusion) with the same boundary and initial conditions, in which the nonhomogeneous contribution—in our case the external neutron source $S(\xi_0, \tau_0)$ —is replaced by the unit impulse function $\delta(\xi - \xi_0)\delta(\tau - \tau_0)$. In a following step after the determination of the Green's functions, the different kinds of external sources have to be defined. In this way, solutions for a Dirac type pulsed external source [19], for the start-up [20, 21], and for the switch-off [8] of an external source for the time-dependent one-group diffusion and the time-dependent one-group P_1 equation were determined. For the comparison with the YALINA-Booster experiment the external neutron source like it is used in the experiment has to be included and the flux has to be determined by solving (5).

For the described YALINA-Booster experiment with the switch on of an external source followed by a switch off after a finite time step, a Heaviside function \mathbf{H} was used to model a source function. This Heaviside function is locally concentrated at the center part of the system (see Figure 1). In the figure the normalized spatial coordinate points to the front, the normalized time coordinate points to the right, and the source amplitude points upwards. The mathematical definition of the described external source is given by

$$S(\xi_0, \tau_0) \equiv \begin{cases} \frac{s(\mathbf{H}(\tau_0 - \tau_i) - \mathbf{H}(\tau_0 - \tau_a))}{\Delta \xi}, & 0 \leq \xi_0 \leq \Delta \xi, \\ 0, & \Delta \xi \leq \xi_0 \leq R. \end{cases} \quad (6)$$

This source was used for the already mentioned comparisons of the one energy group time-dependent diffusion and P_1 solution with the YALINA-Booster experiments [22, 23, 25].

To improve the reproduction of the special experimental conditions with the influences described in Specificity of

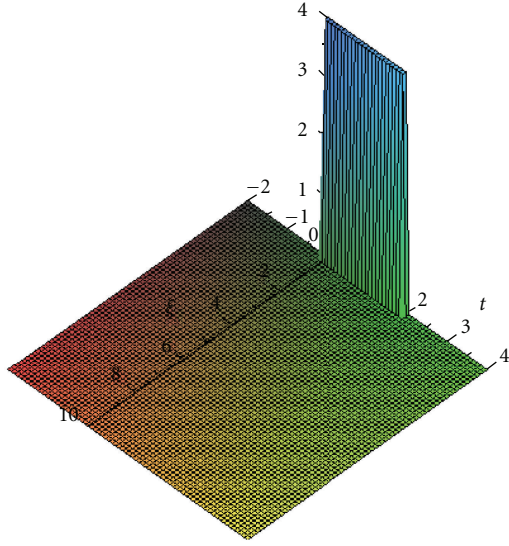


FIGURE 1: Illustrative sketch of the external neutron source used for the one-group analysis.

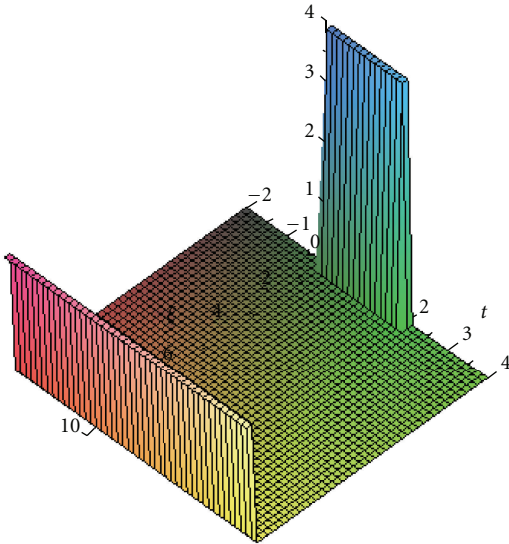


FIGURE 2: Illustrative sketch for the combination of the space-time dependent external neutron sources for the two-energy group solution.

YALINA-Booster section an additional source has been introduced into the two-group solution to represent the streaming of neutrons from the fast area into the thermal area:

$$S_b(\xi_0, \tau_0) \equiv \begin{cases} 0, & 0 \leq \xi_0 \leq R - \Delta\xi_b, \\ \frac{s_b \mathbf{H}(\tau_0 - \tau_b)}{\Delta\xi_b}, & R - \Delta\xi_b \leq \xi_0 \leq R. \end{cases} \quad (7)$$

Using the sources, defined in (6) and (7), a combined source is created for the two-energy group analytic solution, as it is sketched in Figure 2. It has to be mentioned that the different contributions of the central source and the boundary source can vary independently for the location and

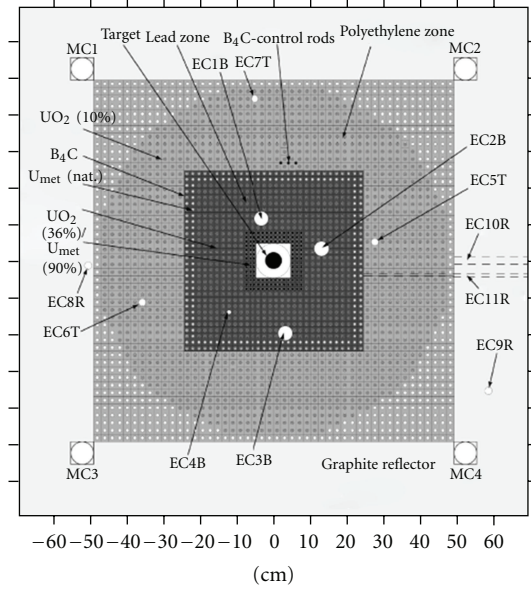


FIGURE 3: General configuration of the YALINA-Booster core.

for both energy groups. Thus for the experiments the central neutron source in the thermal group is set to zero, since the external source produced via the D-T reaction provides mono-energetic neutrons with 14 MeV. For the time behavior of the boundary source, a simple approximation has been used. The source has been used as constant, since the start-up of the source is not of interest for the analysis and the decay of the neutron flux in the thermal area is significantly slower than in the fast area, due to the strong difference in the neutron generation time.

3. Specificity of YALINA-Booster

The core of the YALINA-Booster facility, located in Belarus, consists of the central target region, surrounded by the region with 90% enriched uranium metal ($U_{\text{met}} 90\%$) or 36% enriched uranium oxide ($UO_2 36\%$) rods in a lead matrix. This central region is surrounded by another fast region consisting of a lead matrix with 36% enriched uranium oxide ($UO_2 36\%$) rods. In this region the three experimental channels (EC1B, EC2B, and EC3B) are located (see Figure 3). The fast region is decoupled from the surrounding thermal region by the so-called “valve,” consisting of one row of natural uranium metal (U_{met}) rods and one row of boron carbide (B_4C) rods. The thermal region consists of a polyethylene matrix with holes, which are filled either with 10% enriched UO_2 fuel or with air. The core is surrounded by a graphite reflector.

The SC3A configuration (see the HELIOS model in Figure 4) of the YALINA-Booster facility is used for the comparison with the different analytical solutions. The configuration has been modeled in all details in HELIOS for the determination of the one- and two-group cross-section sets [23, 24]. In the SC3A configuration the 90% enriched uranium metal fuel of the inner fast zone is replaced by 36%

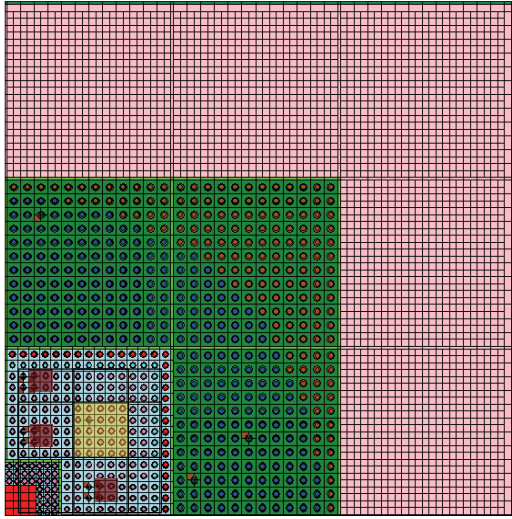
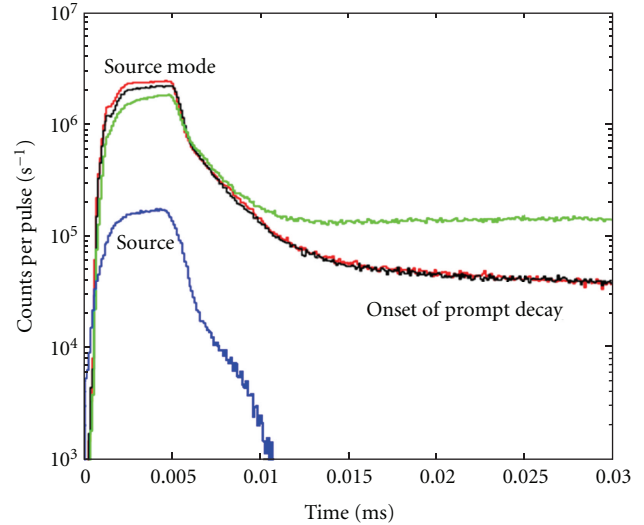


FIGURE 4: SC3A configuration of the YALINA-Booster core in the HELIOS model for XS preparation.

enriched uranium oxide fuel (tight rows of bright pink rods, which surround the red target zone). The thermal region in green contains the rods in deep blue and the empty positions in brown, respectively. The graphite reflector is shown in rose. The critical 2D HELIOS calculation has been corrected with a leakage term (defined in the HELIOS input by using the input buckling B^2 option) in the third dimension to reach a comparable result to a 3D MCNP calculation for a critical problem [31]. This is used to correct for the really small depth of the YALINA-Booster core ~ 0.5 m. The k_{eff} of the system with the above-mentioned leakage correction is 0.949090.

For the comparison of the space-time dependent analytical solutions with the real experiment a cross-section set is needed. This cross-section set is calculated with the licensing grade code module HELIOS 1.9 [26]. One-quarter of the YALINA-Booster facility is reproduced in a two-dimensional model in all details in unstructured mesh. The experimental channels are all relocated into the modeled core quarter, but only with the weight of 25%. The microscopic cross-sections are taken from the HELIOS internal library with 190 energy groups. A two-dimensional 190 energy group neutron flux solution is calculated using this library and the above-given geometry with the SC3A material configuration. These neutron flux solutions are used to produce condensed one- and two-group cross-section sets for the yellow overlaid reference element for the YALINA-Booster core in SC3A configuration.

The external source is not taken into account in the HELIOS calculation for the cross-section preparation. The absence of the external source neutrons with 14 MeV from the D-T reaction has the potential to influence the neutron spectrum slightly in the very center of the system. Nevertheless it has to be kept in mind that the amount of external source neutrons is small $< 5\%$ and the slowing down to “reactor energies” occurs after some collisions in the lead matrix.



- SC3a: CR ln, EC1B, U-235 (500 mg), bin:0.1 μs
- SC3a: CR ln, EC2B, U-235 (500 mg), bin:0.1 μs
- SC3a: CR ln, EC3B, U-235 (500 mg), bin:0.1 μs
- SC3a: CR ln, 180 deg, BC501A, bin:0.1 μs

FIGURE 5: Detector responses in the pulsed neutron source experiment at three different detector positions in the fast area of the SC3A configuration of YALINA-Booster [31].

The YALINA-Booster facility has a very specific and unusual design. The basic idea was to produce a small fast subcritical reactor experiment for ADS study. The thermal part around the fast system in the lead matrix was introduced to reduce the leakage out of the fast system and to reach an acceptable criticality level in a small facility; the overall core size is below one by one meter. To create the possibility of doing fast system measurements the “valve” was inserted. In theory, the rows consisting of B_4C and natural uranium should prevent the thermal neutrons from the thermal zone from entering the fast zone.

Figure 5 shows the detector responses at the three detector positions in the fast zone of the YALINA-Booster experiment induced by a finite source pulse. The neutron generator was operated in pulse mode. The detector’s signals were registered after each pulse. In Figure 5 the histograms of pulses were produced by adding data from all pulses to each other. For a more detailed analysis, the response of the source monitor (blue line) is added to create an insight into the time behavior of the external neutron source. The responses at the two innermost detectors show the expected results, but the response of the outer detector (EC3B in green) shows an unexpected behavior. After the prompt exponential die out of the neutron pulse, all curves should end at approximately the same delayed neutron level. The stable level of the detector response, which is significantly higher at the EC3B even after 0.03 ms, has to be explained. The most convenient explanation for the high detector response after the die out of the prompt pulse in the fast area is the inflow of neutrons from the thermal system. Since the neutron generation time in the thermal area is significantly longer, there is still a high

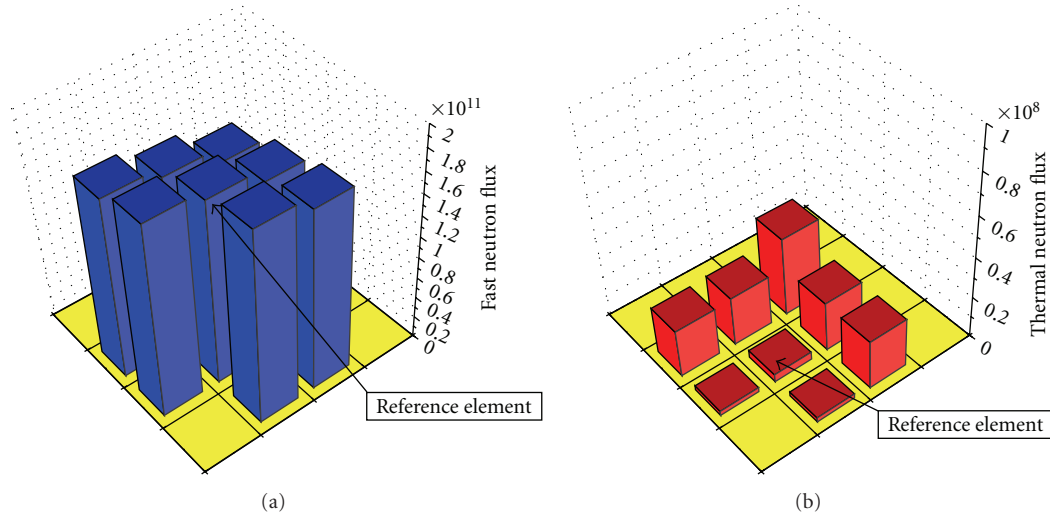


FIGURE 6: Fast neutron flux (a) and thermal neutron flux, (b) in the different relevant fuel elements in the fast part of YALINA-Booster for SC3A.

neutron flux available. The inflow of neutrons from the thermal area should be suppressed by the design using the “valve,” the combination of one row of B_4C and one row of natural uranium. The “valve” is more efficient for thermal neutrons, since the absorption coefficient of B-10 for thermal neutrons is high, but fission neutrons can penetrate the “valve” since they are definitely not all well thermalized before they appear at the “valve.” A conclusion of the described effect of the insufficient die out of the detector response is that fast fission neutrons born in the thermal area can influence at least the outermost detector in the fast area. Thus, “EC3B is affected by the thermal zone” [31].

A detailed analysis has been performed on the basis of the HELIOS model, developed for the cross-section preparation to explain the unexpected results in the cross-section sets [22] and to confirm the thesis of the inflow of neutrons from the thermal area.

The 190 energy group neutron flux calculated with HELIOS is condensed for the detailed analysis of the spatial neutron flux distributions on the basis of the fuel element-like structures, marked in Figure 4. The relevant fast and the thermal neutron flux (cutoff energy is $6.2506 \cdot 10^{-1}$ eV) distributions are shown in Figure 6. The spatial distribution of the fast neutron flux (Figure 6(a)) shows the expected cosine-like distribution. An influence of the neutrons penetrating through the “valve” is not explicitly visible here. The result for the thermal neutron flux (Figure 6(b)) is in strong contrast to the result for the fast neutron flux. In the fast area the thermal flux has to be very low due to the lead matrix in the fast zone of the YALINA-Booster core. The thermal neutron flux shows a distribution which is neither expected nor typical for a reactor core. In contrast to the cosine distribution of the fast neutron flux, the thermal neutron flux grows exponentially with increasing distance from the center. The thermal neutron flux is the highest in the corner of the fast zone, which is surrounded by the thermal zone on both sides. This kind of distribution can be explained only by

the ingress of thermal neutrons from the moderated outer, thermal area through the “valve” into the fast area. The comparison of the thermal neutron flux shows an 18 times higher thermal neutron flux in the corner element compared to the elements in the inner row. This significantly higher thermal neutron flux in the outer fuel elements has strong influence on the production of the cross-section set for all kinds of deterministic calculations for YALINA-Booster. The influence of the thermal neutrons on the cross-section preparation is very strong, since the microscopic cross-section, for example, fission of U-235, is more than hundred times higher than for fast neutrons. The macroscopic production cross-section $\nu\Sigma_f$ is roughly a factor of 3 higher in the corner element than in the elements of the inner row. The effect is only a spectral effect, since the materials in all elements are completely identical. In the standard cross-section preparation a fuel element is calculated in infinite grid, where this spectral effect is lost. Thus an adequate flux weighting of the cross-sections requires a simulation of the full YALINA-Booster core. Due to the strong differences in the thermal flux distribution, the cross-sections for identical material at different positions will vary significantly [22].

4. Comparison with the Experiment

4.1. One Group P_1 and Diffusion Solution. The experimental results, shown in Figure 5, are compared with the developed analytical approximation solutions for the first 0.01 ms on a logarithmic scale for a qualitative comparison in Figure 7. The results for the analytical solution for the different detector positions are given as lines, and the experimental results are given as diamonds in the identical color. This graph already shows one of the major problems. The mathematical representation of the external neutron source by two Heaviside functions is only an approximation of the detected pulse of the external source. In the experiment the external neutron source is created by a D-T reaction in the target

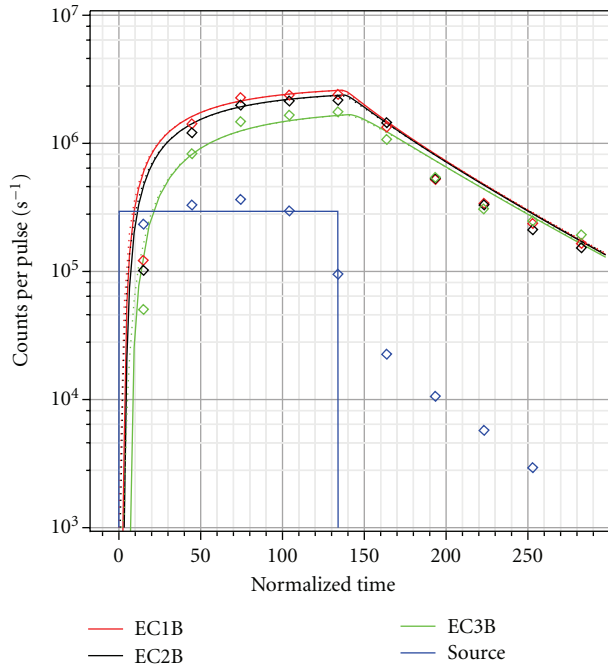


FIGURE 7: Comparison of the analytical results for the space-time dependent neutron flux (full line— P_1 transport; dotted line—diffusion) with the results for the SC3A experiment at the YALINA-Booster facility on logarithmic scale.

in the center of the YALINA-Booster facility. Unfortunately, switch on as well as switch off of the accelerator, which provides the source with deuterium ions, takes some finite time. With this limitation it is impossible to create really sharp pulse fronts for the external neutron source.

Additionally, the source detector is located in another room with a distance of roughly 4 meters from the target, and the signal, taken from the source monitor, follows another chain of electronics which might have other time properties. Both facts cause some time delay in the source counts compared to the counts in the core. These effects have been taken into account by an estimated time correction of $2 \mu\text{s}$ for the source.

Nevertheless, a good qualitative agreement between the analytic approximation solutions (P_1 transport—solid line, diffusion—dotted line) and the experimental data is observable. Especially, the spatial distribution in the plateau phase shows a good agreement. This exactly confirms the need and demonstrates the progress of the developed analytic approximation solutions derived without separation of space and time in contrast to the currently used methods based on point kinetics.

The detailed comparison of the developed analytical solutions with the SC3A experimental results at the YALINA-Booster facility on linear scale is shown in Figure 8. It is once more observable that the response of the source detector in the experiment (blue diamonds) does not have the sharp rectangular time behavior like it is used in the development of the analytical solutions. The switch on of the accelerator as well as the switch off of the accelerator cannot be performed

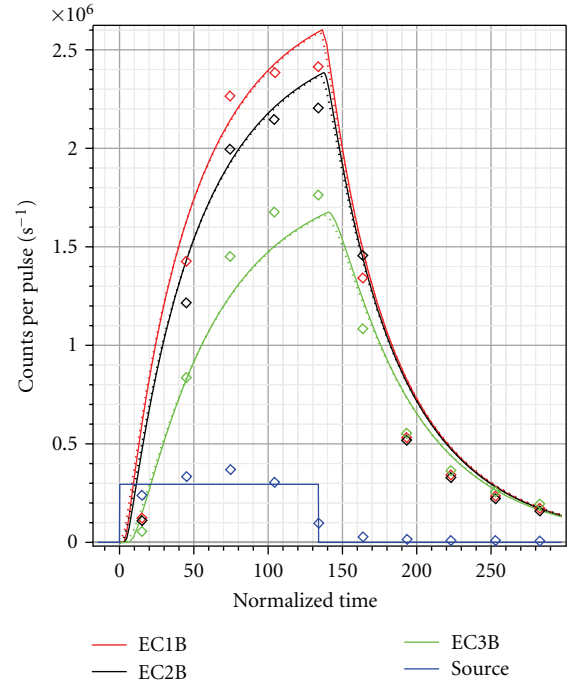


FIGURE 8: Comparison of the analytical results for the space-time dependent neutron flux (full line— P_1 transport; dotted line—diffusion) with the results for the SC3A experiment at the YALINA-Booster facility on linear scale.

in sharp way like it is defined in the mathematical way. This fact causes observable differences in the results for the experiment and the analytical solution on the linear scale. Nevertheless, there is a good agreement between the analytical results with the experimental results. The detector response for the three different detector positions EC1B red, EC2B black, and EC3B green is given at different time points of the experiment by diamonds. The time behavior of the neutron flux at the different positions of the detectors calculated with the analytical solution for the time-dependent P_1 transport solution is given by the full-lines and the results obtained with the analytical solution for the time-dependent diffusion solution with the dotted line: EC1B-red; EC2B-black; EC3B-green. Both analytical solutions show similar behavior with only minor differences in a short time period after the step change in the external source, for the switch on as well as for the switch off. The comparison with the experiment demonstrates that the developed solutions without separation of space and time can reproduce the behavior of the neutron flux at the different detector positions. A small overestimation for the diffusion solution in comparison with the time-dependent P_1 solution is observable in the initiation phase of the transient. The neutron flux grows rapidly after the switch on of the source. After roughly 10 neutron generations the neutron production exceeds due to multiplication of the external neutron source. The calculated neutron flux rises as long as the external source is in operation and would reach a steady state value if the external source would be operated long enough.

The neutron flux decays very rapidly in an exponential manner after the switch off of the external source. The response at the outermost detector is somewhat lower in the calculation. This difference can be once more explained by the ingress of neutrons from the thermal area.

The effect of the fast neutrons, which travel from the thermal into the fast area, is the starting point for the discussion of another important fact. Currently, the analytic approximation is only for one region and one energy group and it has only been applied to the fast area of the system. However, the k_{eff} for the fast area is not known and even a prediction is very problematic, since, on the one hand, the fast area is heavily influenced by the thermal area and the “neutron valve,” and on the other hand, the model for the cross-sections is only two-dimensional. These two facts make it nearly impossible to draw a reliable balance between neutron gains and losses for the fast region. Additional problems are caused by the definition of the boundary, since including or excluding of the strong absorber in the “valve” influences the result significantly. A rough estimation of the k_{eff} has given a value around 0.6 for the fast region. This value has finally been used for the calculations with the analytic approximation solutions. This means an analytic solution for two or more regions would be needed to overcome this problem at least partly. Ideally the solution for the thermal area should be additionally expanded to two-energy group. Summing up all mentioned above, we can conclude that a really complicated experiment like YALINA-Booster is not the ideal test case for the development of a new analysis method. A system like Guinevere [3], consisting of only two regions, a pure lead region containing the fuel, and another pure lead region, acting as reflector, will simplify the problem. Nevertheless, at least an analytical solution for two regions would be needed even for this kind of system to determine the real multiplication factor for the system.

4.2. Diffusion versus P_1 Transport. The decision for either the time-dependent P_1 transport equation or the time-dependent diffusion equation for the further development of the analytic approximation solutions is very important. It is required to solve a second-order equation for the development of the analytic approximation solution for the P_1 transport equation. To solve only the time-dependent diffusion equation would lead to a significantly reduced complexity in the solution, since there is only a first-order partial differential equation in time to solve. This reduced complexity offers the possibility to invest more into the spatial or energetic domain of the problem by tracking a system with two or more regions or more than one energy group [28].

It has already been demonstrated that there is a visible deviation between the results for the time-dependent P_1 transport equation and the time-dependent diffusion equation [8, 20, 21]. An evaluation of the deviation Figure 9(a) and the difference Figure 9(b) between the P_1 transport and the diffusion solution for the three different detector positions in YALINA-Booster is shown in Figure 9. The structure of the deviations is identical for all three detector positions. The major deviations occur certainly in the moments directly after the change in the external neutron source. The

deviation in the beginning is rather high since the neutron flux used for normalization is comparably low. This deviation dies out after roughly 50 neutron generations for the case of a constant operating source. Following the switch off of the source the deviation rises once more but only to roughly 3% and dies out rapidly during the fade away of the neutron flux. The deviation in the beginning is strongly dependent on the distance from the source. The reason for this deviation is the infinite velocity of a perturbation in the diffusion equation compared to the finite velocity of the spreading of the perturbation in the P_1 transport solution. Due to this fact, the time delay of the reduction of the deviation increases with increasing distance from the external source.

The difference between the time-dependent P_1 result and the time-dependent diffusion result is normalized on an average plateau value of $2 \cdot 10^6$ counts per pulse. This way of evaluation avoids the weighting of the difference by different flux values, which leads, especially in cases of very low neutron flux, to tremendously high deviation. The evaluation of the difference gives a good overview on the quality of the result independent of the actual flux level. The difference during the whole transient is below 4% with peaks at the points of the changes of the external source. Negative difference indicates overestimation by the diffusion result.

Both evaluations show significant differences between the diffusion and the P_1 result, but these differences are low in comparison with the differences between the experimental results and the calculations. The major reasons for the differences between experiment and calculation are the limited representation of the real external source in the experiment and the difficulties to represent the complicated geometric structure (three different regions, three dimensions) of the experimental facility by one energy group, one region, and one-dimensional analytical solution.

The comparison of the time-dependent diffusion and the time-dependent P_1 solutions, both without separation of space and time, shows that already the diffusion solution provides good results for the evaluated finite source pulse experiment. The limitation for the recalculation of the experiment is given by the incomplete representation of the character of the source pulse. Unfortunately, the pulses are not as sharp as it would be needed for a detailed analysis of pulsed source experiments based on a Heaviside step function.

4.3. Two-Energy Group Solution. The results of the analytic approximation solutions for the time-dependent one- and two-group diffusion equation for three different detector positions (EC1B, EC2B, and EC3B) are compared to the detector response in the experiment SC3A in Figure 10. First of all, the same conditions (difference in the temporal source shape, influence of the thermal zone. . .) exist, but the observed time period has been extended for the analysis of the delayed neutron level. The detector response for the three different detector positions—EC1B (red), EC2B (black), and EC3B (green)—is given once more by diamonds at different time points of the experiment. The time behavior of the neutron flux is calculated in this case with the analytical time-dependent one group diffusion solution (Figure 10(a)). The neutron flux at the different positions of the detector is

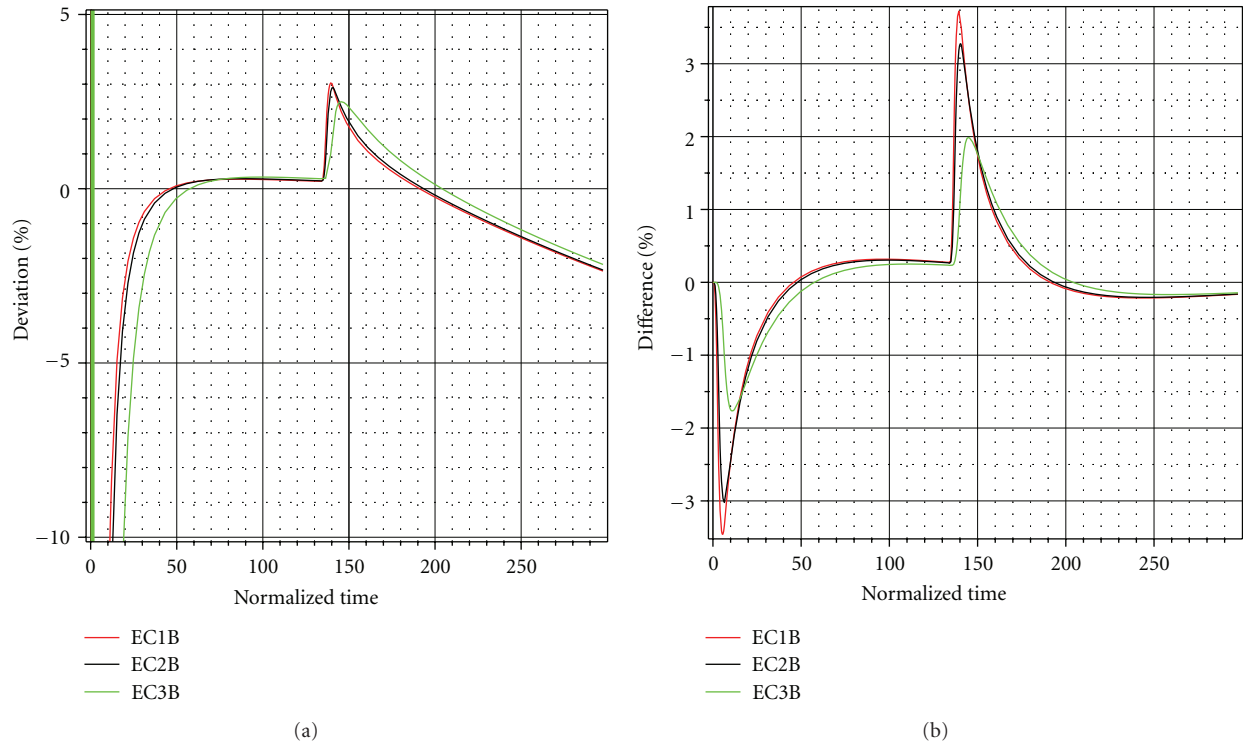


FIGURE 9: Evaluation of the deviation (a) ($\text{deviation} = (\Phi_{P_1}/\Phi_{\text{diffusion}} - 1) * 100$) and difference, (b) ($\text{difference} = \Phi_{P_1} - \Phi_{\text{diffusion}}$) between the time dependent P_1 transport solution and the time dependent diffusion solution at the different detector positions.

given by the full lines: EC1B-red; EC2B-black; EC3B-green. The comparison with the experiment demonstrates that the developed one group solution without space and time separation can reproduce the behavior of the neutron flux at the different positions of the detectors, like it was demonstrated before. The neutron flux decays very rapidly in an exponential manner after the switch off of the external source. Two points show deviations which have to be discussed: first, the response at the outermost detector (green) is somewhat lower in the calculation. This difference can be explained by the location close to the thermal area position. Second, the steady state value of the neutron flux after the switch off of the source is in the experiment significantly higher at the outermost position than in the calculation. This difference indicates once more that there is an influence from the thermal area to the fast area. The neutrons have a significantly longer lifetime in the thermal area; thus there is still a high neutron density available in the thermal area, while the neutron density in the fast area has already decreased significantly. This gradient between the fast and the thermal area leads to the possibility of a neutron inflow to the fast area.

The results of the improved mathematical model, which uses the time-dependent two-group diffusion equation and an adopted source, are shown in the right part of Figure 10. The external source is a combination of the central external source pulse and the time independent boundary source (to reproduce the incoming neutrons from the thermal area),

like it is shown in Figure 2. The first significant difference can be seen in the values after the die out of the pulse. The adopted solution shows a very good agreement when the effect of the pulse has died out and the neutrons are still streaming from the thermal area into the fast area due to the significantly slower decay of the prompt flux in the thermal area. Thus the influence of the thermal area on the fast area can be represented with the new model. With the knowledge of having captured this effect, a close look on the peaks is of our interest. In the one group analysis without caring for the neutrons streaming into the fast area, an increased deviation was visible in the outermost detector EC3B. Now this deviation has vanished nearly completely. The representation of all peaks is good and reflects a good reproduction of the spatial distribution of the neutron flux during the pulse. Additionally, the time shape of the pulses at all detector positions has improved and comes closer to the experiment. This improvement can be explained with the use of two different neutron velocities, or neutron generation times, in the two energy group solution, which is simply a better approximation of the real continuous energy flux. The change in the horizontal axis is caused by the different, in the two-group case averaged, neutron generation times.

Overall, the comparison of the results of the different analytic approximations with experimental ones from the YALINA-Booster facility has been successful for the SC3A. The extended solution has only been required due to the very special design of the YALINA-Booster facility.

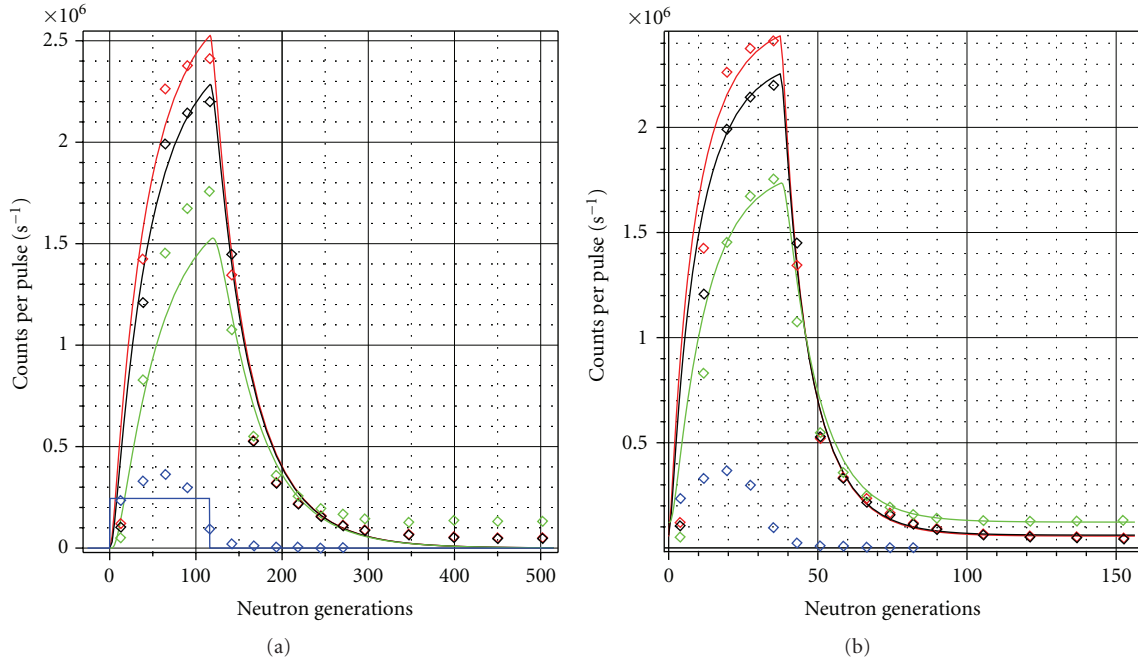


FIGURE 10: Comparison of the analytical results gained with the analytical solution of the time dependent diffusion equation (one-group—(a), two-group—(b)) with the experimental results for the SC3A configuration of the YALINA-Booster facility.

4.4. Two-Spatial Region-Solution. The final idea is to use a solution with two spatial regions, especially for the analysis of the experiments in the GUINEVERE facility [3, 29]. The two-region solution without separation of space and time for the coupled system of a multiplying core with external source and a reflecting surrounding has been derived recently. The flux and the current density are continuous across the interface between two media, and the outer boundaries are reflecting. The exact analytical solution is expressed in terms of a Green's function. The solution is developed by the application of the Laplace transformation [30]. The problems that occur for the one-region solution in YALINA, where the multiplication factor has been calculated only for the region, which is simulated, should be eliminated with this solution for GUINEVERE, where only two regions exist.

The solution will not be applied to YALINA, since two regions would not be sufficient for this complicated configuration. The experiments in the GUINEVERE facility are planned in the beginning of 2012. The successful coupling of the GENEPI accelerator with subcritical VENUS reactor has been announced on October 28, 2011. Early in December an official start-up is scheduled and the first experiments start.

5. Conclusion

A newly developed methodology for reaching a deeper understanding of ADS experiments has been presented as basis for a new method for the analysis of ADS experiments. In the last years at the Helmholtz-Zentrum Dresden-Rossendorf the developed method for the solution of the time-dependent P_1 transport equation, avoiding separation

of space and time and based on Green's functions, is promising. Further solutions for the time-dependent diffusion equation for one region and one- and two-energy groups have been used and compared with the YALINA experiments. A special solution for a finite pulse of the localized external neutron source has been developed for all analytical solutions. As an input for the new methodology, a cross-section set has to be created. This is performed with the HELIOS code with a detailed two-dimensional model for the whole core of the YALINA-Booster facility. This detailed two-dimensional transport model has been used to get a deeper insight into the specificity of the YALINA-Booster experimental setup. The detailed analysis of the fast and the thermal neutron flux distribution in the fast area has shown a strong influence of the thermal area on the fast area. This strong influence requires a significantly increased effort for the cross-section preparation. A full model should be used instead of the standard method, which uses a fuel element in reflective surrounding, to catch the effect of the neutron ingress from the thermal to the fast area.

The first comparison of the results of the analytic approximation solutions with experiments from the YALINA-Booster facility has been successful. Good agreement between the experiment and the calculation was obtained in space as well as in time. The comparison of the time-dependent P_1 results with the time-dependent diffusion results has shown that the differences between the modeling and the experiment cause in the case of YALINA significantly stronger differences than the use of different transport approximations. For a better representation of the specifics of the YALINA-Booster setup, a two-energy group solution with

a special arrangement of the sources has been developed which leads to improved results. Since the complicated YALINA-Booster system cannot be represented by a one-region solution the analysis had to be concentrated on the fast zone only. A drawback of this reduction is the limitation of the k_{eff} calculation only to the fast zone. For a prediction of the k_{eff} for the SC3A configuration of the YALINA-Booster facility a calculation for the full system would be essential (at least 3 regions). To overcome this problem for the future experiment GUINEVERE a two region solution has already been developed for the full representation of the GUINEVERE configuration.

Generally, it has to be mentioned that the advantage of the analytical solution over the numerical method lies in the following: the analytical solution is an exact solution, which gives dependences on variables; the numerical method is only an approximation to the problem, which causes an inaccuracy, if a large region is considered. Additionally, the numerical method does not give a continuous solution and, in some cases, can be time and resource consuming due to the number of iterations.

Overall, very promising results have been obtained, and a good agreement between the experiment and the calculation has been met in space, as well as in time by using analytical solutions developed without separation of space and time. The flexibility of the analytical solutions for the complicated experimental settings has been demonstrated. Thus, analytical solutions without separation of space and time are a very promising tool to develop a new method for the analysis of ADS experiments.

References

- [1] R. Soule, W. Assal, P. Chaussonnet et al., "Neutronic studies in support of accelerator-driven systems: the MUSE experiments in the MASURCA facility," *Nuclear Science and Engineering*, vol. 148, no. 1, pp. 124–152, 2004.
- [2] A. I. Kievitskaia et al., "Experimental and theoretical research on transmutation of long-lived fission products and minor actinides in a subcritical assembly driven by a neutron generator," in *Proceedings of the 3rd International Conference on ADTTA*, Praha, Czech Republic, 1999.
- [3] H. Ait Abderrahim and P. Baeten, "The GUINEVERE-project at VENUS, project status," in *ECATS Meeting*, Cadarache, France, Januray 2008.
- [4] C. M. Persson, P. Seltborg, A. Åhlander et al., "Analysis of reactivity determination methods in the subcritical experiment Yalina," *Nuclear Instruments and Methods in Physics Research, Section A*, vol. 554, no. 1–3, pp. 374–383, 2005.
- [5] N. G. Sjöstrand, "Measurements on a subcritical reactor using a pulsed neutron source," *Arkiv för Fysik*, vol. 11, p. 13, 1956.
- [6] B. E. Simmons and J. S. King, "A pulsed neutron technique for reactivity determination," *Nuclear Science and Engineering*, vol. 3, p. 595, 1958.
- [7] K. Ott and R. Neuhold, *Introductory Nuclear Reactor Dynamics*, American Nuclear Society, La Grange Park, Ill, USA, 1985.
- [8] B. Merk and F. P. Weiß, "A three-scale expansion solution for a time-dependent P_1 neutron transport problem with external source," *Nuclear Science and Engineering*, vol. 163, no. 2, pp. 152–174, 2009.
- [9] G. Granget et al., "EUROTRANS/ECATS or neutronic experiments for the validation of XT-ADS and EFIT monitoring: status, progress and first assessments," in *OECD Nuclear Energy Agency International Workshop on Technology and Components of Accelerator Driven Systems*, Karlsruhe, Germany, March 2010.
- [10] Analytical and Experimental Benchmark Analyses of Accelerator Driven Systems (ADS), <http://www.iaea.org/inisnkm/nkm/aws/fnss/crp/crp7.html>.
- [11] P. Gajda, "Pulsed neutron source measurement in YALINA-subcritical facility," in *Proceedings of the 3rd Environmental Compatible Air Transport System Progress Meeting (ECATS' 10)*, Mol, Belgium, March 2010.
- [12] V. Bécares, "Analysis of pulsed neutron source experiments," in *Proceedings of the 3rd Environmental Compatible Air Transport System Progress Meeting (ECATS' 10)*, Mol, Belgium, March 2010.
- [13] V. Bécares, D. Villamarín, M. Fernández-Ordóñez, E. M. González-Romero, and Y. Fokov, "Correction methods for reactivity monitoring techniques in Pulsed Neutron Source (PNS) measurements," in *Proceedings of the International Conference on the Physics of Reactors (PHYSOR '10)*, pp. 914–928, Pittsburgh, Pa, USA, May 2010.
- [14] Y. Gohar et al., "Argonne analyses of YALINA-booster, YALINA-thermal, and LEU YALINA-booster," in *IAEA Meeting*, Mumbai, India, February 2010.
- [15] Summary of the Technical Meeting on, "Use of Low Enriched Uranium (LEU Fuel in Accelerator Driven Sub-Critical Assembly (ADS Systems), and 3rd RCM of the CRP on 'Analytical and Experimental Benchmark Analyses of Accelerator Driven Systems,'" Mumbai, India, February 2010.
- [16] A. M. Weinberg and E. P. Wigner, *The Physical Theory of Neutron Chain Reactors*, University of Chicago Press, Chicago, Ill, USA, 1958.
- [17] D. G. Duffy, *Green's Functions with Application*, Chapman & Hall/CRC, 2001.
- [18] M. N. Özişik and B. Vick, "Propagation and reflection of thermal waves in a finite medium," *International Journal of Heat and Mass Transfer*, vol. 27, no. 10, pp. 1845–1854, 1984.
- [19] B. Merk, "Time dependent analytical approximation solutions for a pulsed source problem: P_1 transport versus diffusion," in *IEEE Nuclear Science Symposium*, Dresden, Germany, 2008.
- [20] B. Merk, "An analytical solution for a one dimensional time-dependent neutron transport problem with external source," *Transport Theory and Statistical Physics*, vol. 37, no. 5–7, pp. 535–549, 2008.
- [21] B. Merk, "An analytical approximation solution for a time-dependent neutron transport problem with external source and delayed neutron production," *Nuclear Science and Engineering*, vol. 161, no. 1, pp. 49–67, 2009.
- [22] B. Merk, V. Glivici-Cotruță, and F. P. Weiß, "A solution for the telegrapher's equation with external source: application to Yalina—SC3A and SC3B," in *International Conference on the Physics of Reactors (PHYSOR '10)*, pp. 3053–3065, Pittsburgh, Pa, USA, May 2010.
- [23] B. Merk, V. Glivici-Cotruța, and F. P. Weiß, "A solution for Telegrapher's equation with external source: development and first application," *Nuovo Cimento della Societa Italiana di Fisica B*, vol. 125, no. 12, pp. 1547–1559, 2010.
- [24] B. Merk, V. Glivici-Cotruță, and F.-P. Weiß, "Application of a two energy group analytical solutions to the YALINA experiment SC3A," in *Proceedings of the International Conference on Mathematics and Computational Methods Applied to Nuclear Science and Engineering (MC '11)*, Rio de Janeiro, Brazil, 2011.

- [25] B. Merk, V. Glivici-Cotruța, and F.-P. Weiß, “A three scale expansion solution for the Telegrapher’s equation with external source: development and first application,” in *Proceedings of the 21st International Conference on Transport Theory*, Torino, Italy, 2009.
- [26] HELIOS Methods, Studsvik Scandpower, 2003.
- [27] V. Bécares Palacios et al., “Analysis of PNS measurements at the YALINA-Booster subcritical facility,” in *Proceedings of the 2nd EUROTRANS ECATS Progress Meeting*, Aix-en-Provence, France, January 2009.
- [28] B. Merk and F. P. Weiß, “A two group analytical approximation solution for an external source problem without separation of space and time,” *Annals of Nuclear Energy*, vol. 37, no. 7, pp. 942–952, 2010.
- [29] FREYA: Fast Reactor Experiments for hYbrid Applications, <http://freya.sckcen.be/en>.
- [30] V. Glivici-Cotruta and B. Merk, “An analytical solution of the time dependent diffusion equation in a composite slab,” submitted to: *Transport Theory and Statistical Physics*.
- [31] C. Berglöf, “YALINA-booster: pulsed neutron source characterization,” in *Proceedings of the 2nd EUROTRANS ECATS Progress Meeting*, Aix-en-Provence, France, 2009.

Research Article

Two-Group Theory of the Feynman-Alpha Method for Reactivity Measurement in ADS

Lénárd Pál¹ and Imre Pázsit²

¹Centre for Energy Research, Hungarian Academy of Sciences, P.O. Box 49, 1525 Budapest, Hungary

²Department of Nuclear Engineering, Chalmers University of Technology, SE 412 96 Göteborg, Sweden

Correspondence should be addressed to Imre Pázsit, imre@chalmers.se

Received 30 December 2011; Accepted 21 February 2012

Academic Editor: Alberto Talamo

Copyright © 2012 L. Pál and I. Pázsit. This is an open access article distributed under the Creative Commons Attribution License, which permits unrestricted use, distribution, and reproduction in any medium, provided the original work is properly cited.

The theory of the Feynman-alpha method, which is used to determine the subcritical reactivity of systems driven by an external source such as an ADS, is extended to two energy groups with the inclusion of delayed neutrons. This paper presents a full derivation of the variance to mean formula with the inclusion of two energy groups and delayed neutrons. The results are illustrated quantitatively and discussed in physical terms.

1. Introduction

Methods of online measurement of subcritical reactivity, in connection with ADS, have been studied over a decade by now. Both deterministic methods, such as the area ratio or Sjöstrand method [1] (pulsed measurements), and stochastic or fluctuation-based methods (Feynman- and Rossi-alpha methods) have been investigated. What regards the latter class of methods, the theory of classical systems, based on a stationary source with Poisson statistics, had to be extended to the case of nonstationary (pulsed) source with compound Poisson statistics (spallation source, generating several neutrons simultaneously in one source emission event). Regarding the pulsed sources, both narrow (instantaneous) as well as finite width pulses with various pulse shapes were considered, both with “deterministic” (synchronised between source emission and counting interval) and stochastic (nonsynchronised) pulse injection. An overview of the field can be found in [2]. The most general treatment of all the above mentioned cases is found in Degweker and Rana [3] and Rana and Degweker [4, 5].

In this paper, we will discuss another aspect of stochastic reactivity measurement methods, which is related more to the system properties than those of the source. The new aspect is to take into account the energy dependence of the neutrons by the use of a two-group approach. All work so

far in which compact analytical results could be obtained in this area (calculation of the Feynman- and Rossi-alpha formulae) was made by the use of one-group theory. This is justified by the fact that the methods were used in thermal systems, where the neutron population and hence its dynamics is dominated by thermal neutrons. However, many of the planned ADS concepts will use a core with a fast spectrum, in which the dominance of thermal neutrons will be significantly reduced. In terms of a two-group approach, unlike in a thermal system where there is one time or decay constant in a pulsed experiment, there will be two components in the temporal response with two different time constants and with comparable amplitudes. One indication for this possibility comes from the area of nuclear safeguards, where such effects have already been investigated, as it will be described below.

Actually there have been experiments, such as in the EU-supported project MUSE [6] and the Yalina experiment [7–9], where the fitting of Feynman- and Rossi-alpha measurements required more than one exponentials. Although the appearance of more than one decay constant may have also other reasons (e.g., the presence of a reflector, i.e., a multiregion system), the energy aspect is clearly one possibility to lead to the occurrence of two different decay constants. In the theoretical work so far on the explanation of the multiple exponentials or multiple alpha modes, the

emphasis was on the spatial effects as being the reason for the appearance of the multiple alpha modes [10–12]. In [10, 11] a general energy dependent framework was used which, in order to arrive to explicit expressions, requires the possession of the fundamental and higher order alpha-eigenfunctions of the space-energy dependent transport equation. However, due to the continuous energy treatment, no discrete modes can be attributed to the energy dependence.

The purpose of the present paper is the elaboration of the two-group theory of the Feynman-alpha method, based on the backward master equation approach. Such an energy-dependent extension of the existing theory might have a relevance also to on-going and future ADS experiments, such as the European FP7 project FREYA. This work has actually been started already by the present authors, although in a different setting. In nuclear safeguards, identification of fissile material can be achieved by detecting the temporal decay of fast neutrons from an unknown sample, following irradiation by a pulse of fast neutrons. Appearance of a second decay constant is an indication of the presence of fissile material. This is the so-called differential die-away analysis (DDAA) method. A stochastic generalisation of this method, to the use of a stationary (intrinsic) source and the measurement of the time correlations, the so-called DDSI (differential die-away self interrogation) method, was recently suggested by Menlove et al. [13]. The theory of the DDSI method, by way of the extension of the Rossi-alpha method to two energy groups, without delayed neutrons, was recently given by the present authors based on both the backward [14] and the forward master equation approach [15].

In the present paper, we extend the treatment by the inclusion of delayed neutrons in the formalism. Understandably, the calculations get quite involved. Although a full analytical treatment is possible, many expressions in the final results become too extensive to be quoted explicitly. Hence these will not be given and analysed in this paper. Likewise, the question of how to extract the subcritical reactivity from the measurement of the two time constants will not be discussed here, rather it will be given in a subsequent communication. Instead, here we focus on the formulation of the problem and the full derivation sequence until arriving to the final result. The intermediate and final results will be discussed in physical terms.

2. General Principles

As usual in the context, we shall assume a homogeneous infinite medium with properties constant in space. We shall use a two-group theory model, that is, describe the neutron population with two type of neutrons: fast and thermal. One group of delayed neutron precursors will be assumed. The possible neutron reactions are absorption of both the fast and thermal neutrons, downscattering (“removal”) of neutrons from the fast group to the thermal, and thermal fission, which produces a random number of fast neutrons according to a probability distribution function. At such a thermal fission also at most one delayed neutron precursor

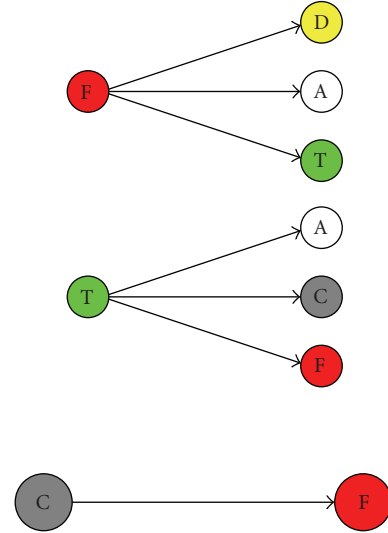


FIGURE 1: The possible reactions which the three different particles can undergo. Fast neutrons (red circle) can be detected (yellow), absorbed (white), and thermalized (green). Thermal neutrons (green) can be absorbed, and through fission lead to a random number of delayed neutron precursors (grey) and fast neutrons (red). Delayed neutron precursors decay into a fast neutron.

can be generated with a certain probability. The decay of this precursor will lead to the appearance of one fast neutron. For simplicity, fast fission will be neglected. It can be easily incorporated into the model, at the expense of some further complication of the calculations, but without any essential problem. Figure 1 illustrates the possible reactions induced by the fast and thermal neutrons and the delayed neutron precursors, respectively.

A word on the notations used is in order here. In a two-group model of reactor physics, the indices 1 and 2 are used to denote the fast and the thermal group, respectively. This notation will be used also in this paper, whenever it will not lead to confusion. For practical reasons, the delayed neutron precursors will be taken as group 3. However, often it will be simpler and more practical to refer to the fast and thermal neutrons and the precursors with the notations F , T , and C , as it is seen also in Figure 1. In traditional reactor physics texts, short-hand notations are used for denoting the first factorial moments of the neutron population and that of the fission neutron distribution, such as ν and the Diven factor D_ν , for the latter. In the literature on neutron fluctuations, the transition probabilities (more correctly, transition intensities) are usually denoted by λ_i , where the subscript i stands for the type of reaction (capture, absorption, removal, and fission) (see, e.g., [2, Part II]). These transition intensities are related to the corresponding macroscopic cross sections of the particular reactions and the neutron speed.

However, in this paper we will keep a more general mathematical system of notations for the factorial moments and transition intensities. This is partly because the purpose of this paper is to describe the formalism used in a general setting, and partly in order to relate the work reported here

to our preceding paper, where the two-group generalisation of the Feynman- and Rossi-alpha methods was introduced [14]. Accordingly, the transition probabilities will be denoted in a way similar to that in [14], that is, for the fast neutrons one has

$$Q_F = Q_{FA} + Q_{FT}, \quad (1)$$

where Q_{FA} and Q_{FT} are the intensities of the absorption and thermalization of fast neutrons, respectively. Similar, self-obvious notations are used for the thermal neutrons. In the numerical work, there will be no attempt to relate these reaction intensities to cross-sections of a real reactor in this paper; such a coupling to realistic systems will be made in a subsequent work.

The final quantity we need in order to formulate a probability balance equation is the number distribution of fast neutrons and delayed neutron precursors in a thermal fission event. Denote by $f(k, \ell)$ the probability that a thermal neutron produces $k \geq 0$ fast neutrons and $\ell \geq 0$ delayed neutron precursors, that is, particles of type C. Suppose that

$$f(k, \ell) = f_p(k) f_d(\ell), \quad (2)$$

that is, the numbers fast neutrons and delayed neutron precursors created in one reaction are independent. Further, let $f_d(\ell)$ be given by

$$f_d(\ell) = \begin{cases} 1 - q_1^{(d)}, & \text{if } \ell = 0, \\ q_1^{(d)}, & \text{if } \ell = 1, \\ 0, & \text{if } \ell > 1, \end{cases} \quad (3)$$

where $q_1^{(d)} \leq 1$. The probability that a delayed neutron precursor produced at time $t = 0$ decays to a fast neutron during the time interval not larger than $t \geq 0$ is given by

$$T_d = 1 - e^{-\lambda t}, \quad \lambda \geq 0. \quad (4)$$

With this all quantities that are needed to formulate the problem are defined.

3. Description of the Basic Process with One Starting Particle

Since we are going to use the backward master equation approach, first we will need the neutron and precursor distributions, generated by one single starting particle (a fast or thermal neutron or a delayed neutron precursor). First the number distribution of generated particles will be studied and explicit results derived for the first two moments. In the next section the detection process will also be accounted for, and in the last section the variance and the mean of the number of neutrons detected in a time interval, induced by a stationary external source of fast neutrons, will be calculated from the results of the preceding two sections.

Let us introduce the random functions $\mathbf{n}_F(t)$, $\mathbf{n}_T(t)$, and $\mathbf{n}_C(t)$, giving the numbers of particles of types **F**, **T**, and

C, respectively, at the time moment $t \geq 0$. Define the probabilities:

$$\begin{aligned} \mathcal{P} \{ \mathbf{n}_F(t) = n_1, \mathbf{n}_T(t) = n_2, \mathbf{n}_C(t) = n_3 \mid S_j \} \\ = p(n_1, n_2, n_3, t \mid S_j), \end{aligned} \quad (5)$$

where the conditions S_j , $j = \{1, 2, 3\}$, $\{S_j\} = \{F, T, C\}$, indicating the type of particle starting the process, are defined as

$$S_1 \equiv F = \{ \mathbf{n}_F(0) = 1, \mathbf{n}_T(0) = 0, \mathbf{n}_C(0) = 0 \},$$

$$S_2 \equiv T = \{ \mathbf{n}_F(0) = 0, \mathbf{n}_T(0) = 1, \mathbf{n}_C(0) = 0 \}, \quad (6)$$

$$S_3 \equiv C = \{ \mathbf{n}_F(0) = 0, \mathbf{n}_T(0) = 0, \mathbf{n}_C(0) = 1 \},$$

respectively. Introduce also the corresponding generating functions:

$$\begin{aligned} g(z_1, z_2, z_3, t \mid S_j) \\ = \sum_{n_1=0}^{\infty} \sum_{n_2=0}^{\infty} \sum_{n_3=0}^{\infty} p(n_1, n_2, n_3, t \mid S_j) z_1^{n_1} z_2^{n_2} z_3^{n_3}. \end{aligned} \quad (7)$$

With these notations, based on the probabilities of the mutually exclusive events of the starting particle not having or having a reaction within the time interval $(0, t)$, and the summing up of the probabilities of the mutually exclusive events generated by the respective reactions, one can write that

$$\begin{aligned} g(z_1, z_2, z_3, t \mid F) = e^{-Q_F t} z_1 + Q_{FA} \int_0^t e^{-Q_F(t-t')} dt' \\ + Q_{FT} \int_0^t e^{-Q_F(t-t')} g(z_1, z_2, z_3, t' \mid T) dt', \end{aligned} \quad (8)$$

$$\begin{aligned} g(z_1, z_2, z_3, t \mid T) = e^{-Q_T t} z_2 + Q_{TA} \int_0^t e^{-Q_T(t-t')} dt' \\ + Q_{TF} \int_0^t e^{-Q_T(t-t')} q_p [g(z_1, z_2, z_3, t' \mid F)] \\ \times q_d [g(z_1, z_2, z_3, t' \mid C)] dt', \end{aligned} \quad (9)$$

as well as

$$\begin{aligned} g(z_1, z_2, z_3, t \mid C) \\ = e^{-\lambda t} z_3 + \lambda \int_0^t e^{-\lambda(t-t')} g(z_1, z_2, z_3, t' \mid F) dt', \end{aligned} \quad (10)$$

where

$$q_p(z) = \sum_{k=0}^{\infty} f_p(k) z^k, \quad q_d(z) = \sum_{\ell=0}^{\infty} f_d(\ell) z^\ell = 1 - q_1^{(d)} + q_1^{(d)} z. \quad (11)$$

For later use, we note that

$$\left[\frac{d^j q_p(z)}{dz^j} \right]_{z=1} = q_j^{(p)}, \quad \left[\frac{d^j q_d(z)}{dz^j} \right]_{z=1} = q_j^{(d)} = \delta_{j1} q_1^{(d)} \quad (12)$$

are the factorial moments of the number of prompt and delayed neutrons in a fission event. The relationship with the traditional notations is given by

$$q_1^{(p)} = \nu_p = (1 - \beta)\nu, \quad q_1^{(d)} = \nu_d = \beta\nu, \quad (13)$$

with $\nu = \nu_p + \nu_d$, and $\beta = \nu_d/(\nu_p + \nu_d)$.

3.1. Expectations of the Numbers of Particles of Different Types. By using (8)–(10), one can derive equations for the expectations of the numbers of fast and thermal neutrons and the delayed neutron precursors, that is, particles of types **F**, **T**, and **C**, respectively. With obvious notations, for the expectation (first moment) $m_1^{(F)}(t | S_j)$ of the number of fast neutrons, induced by one starting fast neutron, thermal neutron and delayed neutron precursor, respectively, one obtains the equations:

$$\begin{aligned} m_1^{(F)}(t | F) &= \left[\frac{\partial g(z_1, z_2, z_3, t | F)}{\partial z_1} \right]_{z_1=z_2=z_3=1} \\ &= e^{-Q_F t} + Q_{FT} \int_0^t e^{-Q_F(t-t')} m_1^{(F)}(t' | T) dt', \\ m_1^{(F)}(t | T) &= \left[\frac{\partial g(z_1, z_2, z_3, t | T)}{\partial z_1} \right]_{z_1=z_2=z_3=1} \\ &= Q_{TF} \int_0^t e^{-Q_T(t-t')} \\ &\quad \times \left[q_1^{(p)} m_1^{(F)}(t' | F) + q_1^{(d)} m_1^{(F)}(t' | C) \right] dt', \\ m_1^{(F)}(t | C) &= \left[\frac{\partial g(z_1, z_2, z_3, t | C)}{\partial z_1} \right]_{z_1=z_2=z_3=1} \\ &= \lambda \int_0^t e^{-\lambda(t-t')} m_1^{(F)}(t' | F) dt'. \end{aligned} \quad (14)$$

Equations for the quantities $m_1^{(T)}(t | S_j)$ and $m_1^{(C)}(t | S_j)$ can be derived in a completely similar manner; these will not be given here, for brevity.

The arising integral equation system can be readily solved by Laplace transform methods. Introduce the Laplace transforms:

$$\tilde{m}_1^{(S_j)}(s | S_i) = \int_0^\infty e^{-st} m_1^{(S_j)}(t | S_i) dt, \quad (15)$$

then, from (14) one obtains

$$\begin{aligned} \tilde{m}_1^{(F)}(s | F) &= \frac{1}{s + Q_F} + \frac{Q_{FT}}{s + Q_F} \tilde{m}_1^{(F)}(s | T), \\ \tilde{m}_1^{(F)}(s | T) &= \frac{Q_{TF}}{s + Q_T} \left[q_1^{(p)} \tilde{m}_1^{(F)}(s | F) + q_1^{(d)} \tilde{m}_1^{(F)}(s | C) \right], \\ \tilde{m}_1^{(F)}(s | C) &= \frac{\lambda}{s + \lambda} \tilde{m}_1^{(F)}(s | F). \end{aligned} \quad (16)$$

After elementary algebra one obtains

$$\tilde{m}_1^{(F)}(s | F) = \frac{(s + Q_T)(s + \lambda)}{\mathcal{N}(s)}, \quad (17)$$

where

$$\begin{aligned} \mathcal{N}(s) &= (s + Q_F)(s + Q_T)(s + \lambda) \\ &\quad - Q_{FT} Q_{TF} \left[q_1^{(p)}(s + \lambda) + q_1^{(d)} \lambda \right] \end{aligned} \quad (18)$$

is a third-order polynomial of s . It can be proven that the roots of the equation:

$$\begin{aligned} \mathcal{N}(s) &= s^3 + (Q_F + Q_T + \lambda)s^2 \\ &\quad + \left[Q_F Q_T + \lambda(Q_F + Q_T) - q_1^{(p)} Q_{FT} Q_{TF} \right] s \\ &\quad + \lambda \left[Q_F Q_T - Q_{FT} Q_{TF} (q_1^{(p)} + q_1^{(d)}) \right] = 0 \end{aligned} \quad (19)$$

are all real. Hence, introducing the notation $s_i = -\omega_i$, $i = 1, 2, 3$, one can write that

$$\mathcal{N}(s) = (s + \omega_1)(s + \omega_2)(s + \omega_3). \quad (20)$$

Clearly, the system is subcritical, if none of the ω_1 , ω_2 , and ω_3 is zero or negative. For the sake of illustration in Figure 2 the dependence of the characteristic function $\mathcal{N}(s)$ on s is shown (for the calculations, the following parameter values were used: $Q_{FA} = 1/3$, $Q_{FT} = 2/3$, $Q_F = 1$, $Q_{TA} = 14/10$, $Q_{TF} = 3/5$, $Q_T = 2$, $q_1^{(p)} = 3$, $q_1^{(d)} = 0.02$, and $\lambda = 0.1$). The right hand side figure is an enlargement of the $\mathcal{N}(s)$ in the interval $(-0.4, 0)$.

The algebraic solutions for the Laplace transforms $\tilde{m}_1^{(T)}(s | S_j)$ and $\tilde{m}_1^{(C)}(s | S_j)$ can be obtained in a similar manner. Here we only list these solutions, which for $\tilde{m}_1^{(T)}(s | S_j)$ are given by

$$\begin{aligned} \tilde{m}_1^{(T)}(s | F) &= \frac{Q_{FT}(s + \lambda)}{\mathcal{N}(s)}, \\ \tilde{m}_1^{(T)}(s | T) &= \frac{(s + Q_F)(s + \lambda)}{\mathcal{N}(s)}, \\ \tilde{m}_1^{(T)}(s | C) &= \frac{Q_{FT}\lambda}{\mathcal{N}(s)}. \end{aligned} \quad (21)$$

and for $\tilde{m}_1^{(C)}(s | S_j)$ as

$$\begin{aligned} \tilde{m}_1^{(C)}(s | F) &= q_1^{(d)} \frac{Q_{FT} Q_{TF}}{\mathcal{N}(s)}, \\ \tilde{m}_1^{(C)}(s | T) &= q_1^{(d)} \frac{Q_{TF}(s + Q_F)}{\mathcal{N}(s)}, \\ \tilde{m}_1^{(C)}(s | C) &= q_1^{(d)} \frac{(s + Q_F)(s + Q_T) - q_1^{(p)} Q_{FT} Q_{TF}}{\mathcal{N}(s)}. \end{aligned} \quad (22)$$

The expectations can be obtained in a rather simple way by inversion of these Laplace transforms. All solutions consist of the sum of three exponential functions, namely,

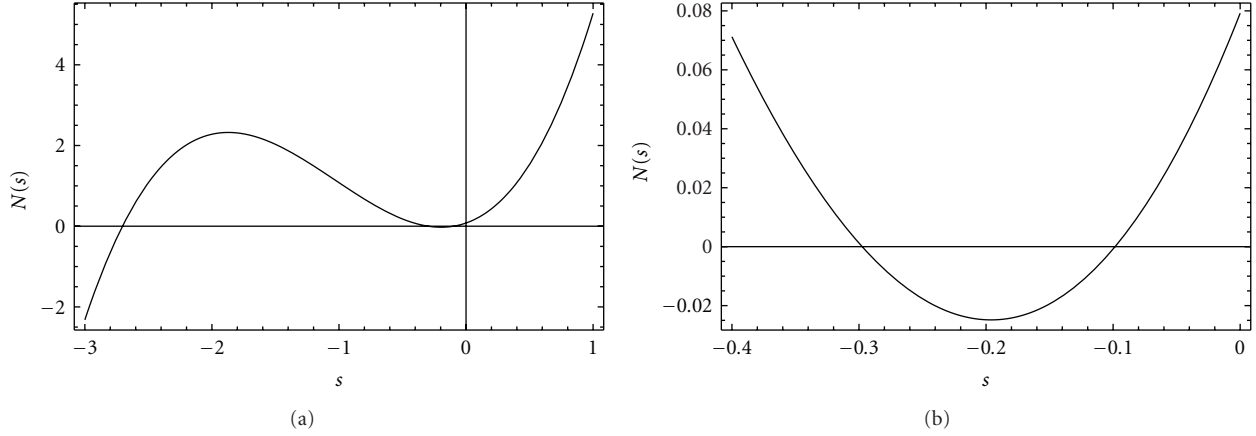


FIGURE 2: Characteristic function $\mathcal{N}(s)$. The right-hand figure shows the two largest roots of the equation.

of $e^{-\omega_1 t}$, $e^{-\omega_2 t}$ and $e^{-\omega_3 t}$. As an illustration, we give the expectation $m_1^{(F)}(t | F)$ of the number of fast neutrons, generated by one initial fast neutron injected into the system. One obtains

$$\begin{aligned} m_1^{(F)}(t | F) &= \frac{\omega_1^2 - (Q_T + \lambda)\omega_1 + Q_T\lambda}{(\omega_1 - \omega_2)(\omega_1 - \omega_3)} e^{-\omega_1 t} \\ &\quad - \frac{\omega_2^2 - (Q_T + \lambda)\omega_2 + Q_T\lambda}{(\omega_1 - \omega_2)(\omega_2 - \omega_3)} e^{-\omega_2 t} \\ &\quad + \frac{\omega_3^2 - (Q_T + \lambda)\omega_3 + Q_T\lambda}{(\omega_1 - \omega_3)(\omega_2 - \omega_3)} e^{-\omega_3 t}. \end{aligned} \quad (23)$$

The other expectations are obtained in a similar form, that is, as a sum of three exponentials, and they will not be given here. Some quantitative examples of the expectations are shown in Figure 3. The figure shows the expectations of the numbers of fast and thermal neutrons and the delayed neutron precursors versus time, assuming that the starting particle was either a fast or a thermal neutron (for the calculations the following parameter values were used: $Q_{FA} = 1/3$, $Q_{FT} = 2/3$, $Q_F = 1$, $Q_{TA} = 14/10$, $Q_{TF} = 3/5$, $Q_T = 2$, $q_1^{(p)} = 3$, $q_1^{(d)} = 0.02$, and $\lambda = 0.1$).

It is to be mentioned that the above results could also be obtained directly from deterministic equations, namely, from the two-group point kinetic equations with one group of delayed neutrons.

3.2. Variances of the Numbers of Particles of Different Types.

As it follows from the definitions and formulae in the previous section, the variance of the numbers of, say, fast neutrons at the time $t \geq 0$, induced by an initial fast neutron, is given by the formula:

$$\mathbf{D}^2\{\mathbf{n}_1(t) | F\} = m_2^{(F)}(t | F) + m_1^{(F)}(t | F)[1 - m_1^{(F)}(t | F)]. \quad (24)$$

Similar expressions can be derived for the other 8 variances.

3.2.1. Second Factorial Moments. It is seen that for the determination of variances, one needs the second factorial

moments which can be obtained from the generating function (8)–(10). Introducing the notations:

$$\begin{aligned} m_2^{(F)}(t | F) &= \left[\frac{\partial^2 g(z_1, z_2, z_3, t | F)}{\partial z_1^2} \right]_{z_1=z_2=z_3=1}, \\ m_2^{(F)}(t | T) &= \left[\frac{\partial^2 g(z_1, z_2, z_3, t | T)}{\partial z_1^2} \right]_{z_1=z_2=z_3=1}, \\ m_2^{(F)}(t | C) &= \left[\frac{\partial^2 g(z_1, z_2, z_3, t | C)}{\partial z_1^2} \right]_{z_1=z_2=z_3=1}, \end{aligned} \quad (25)$$

one can derive the following equations:

$$m_2^{(F)}(t | F) = Q_{FT} \int_0^t e^{-Q_F(t-t')} m_2^{(F)}(t' | T) dt', \quad (26)$$

$$\begin{aligned} m_2^{(F)}(t | T) &= \\ &Q_{TF} \int_0^t e^{-Q_T(t-t')} \times \left\{ q_1^{(p)} m_2^{(F)}(t' | F) \right. \\ &\quad + q_2 [m_1^{(F)}(t' | F)]^2 + 2 q_1^{(p)} q_1^{(d)} m_1^{(F)}(t' | F) \\ &\quad \left. \times m_1^{(F)}(t' | C) + q_1^{(d)} m_2^{(F)}(t' | C) \right\} dt', \end{aligned} \quad (27)$$

$$m_2^{(F)}(t | C) = \lambda \int_0^t e^{-\lambda(t-t')} m_2^{(F)}(t' | F) dt'. \quad (28)$$

Analogous definitions can be introduced for $m_2^{(T)}(t | S_j)$, and $m_2^{(C)}(t | S_j)$ and similar equations can be readily derived for these.

For the solution of the arising system of integral equations, again the method of the Laplace transform is used. Before performing the transforms, it is practical to introduce short-hand notations for the functions appearing in (27)

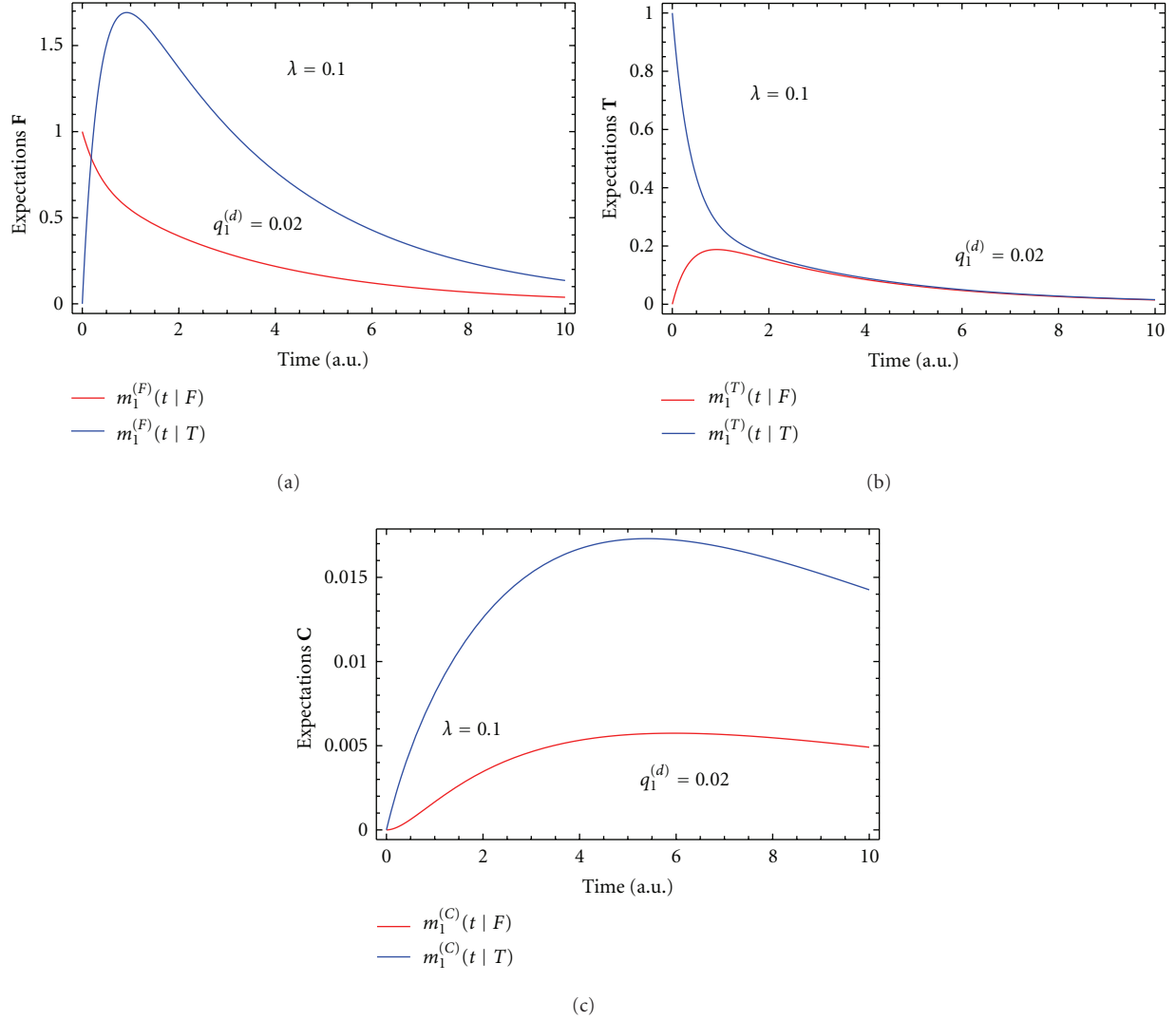


FIGURE 3: Dependence of the expectations of the numbers of particles of types F, T, and C on the time, assuming that the starting particle was either F or T.

and in the corresponding equations for $m_2^{(T)}(t | S_j)$ and $m_2^{(C)}(t | S_j)$ as

$$\begin{aligned}
 A_F(t') &= q_2 \left[m_1^{(F)}(t' | F) \right]^2 \\
 &\quad + 2q_1^{(p)} q_1^{(d)} m_1^{(F)}(t' | F) m_1^{(F)}(t' | C), \\
 A_T(t') &= q_2 \left[m_1^{(T)}(t' | F) \right]^2 \\
 &\quad + 2q_1^{(p)} q_1^{(d)} m_1^{(T)}(t' | F) m_1^{(T)}(t' | C), \\
 A_C(t') &= q_2 \left[m_1^{(C)}(t' | F) \right]^2 \\
 &\quad + 2q_1^{(p)} q_1^{(d)} m_1^{(C)}(t' | F) m_1^{(C)}(t' | C).
 \end{aligned} \tag{29}$$

These functions are known at this stage, since they contain only the expectations of the numbers of the particles. Applying the notation for the Laplace transforms defined already, one obtains

$$\begin{aligned}
 \tilde{m}_2^{(F)}(s | F) &= \frac{Q_{FT}}{s + Q_F} \tilde{m}_2^{(F)}(s | T), \\
 \tilde{m}_2^{(F)}(s | T) &= \frac{Q_{TF}}{s + Q_T}, \\
 &\quad \times \left[q_1^{(p)} \tilde{m}_2^{(F)}(s | F) + q_1^{(d)} \tilde{m}_2^{(F)}(s | C) + \tilde{A}_F(s) \right], \\
 \tilde{m}_2^{(F)}(s | C) &= \frac{\lambda}{s + \lambda} \tilde{m}_2^{(F)}(s | F),
 \end{aligned} \tag{30}$$

and similar equations for $\tilde{m}_2^{(T)}(s | S_j)$ and $\tilde{m}_2^{(C)}(s | S_j)$. After simple algebra the solutions can be written in the following form:

$$\begin{aligned}\tilde{m}_2^{(F)}(s | F) &= Q_{TF} \frac{Q_{FT}(s + \lambda)}{\mathcal{N}(s)} \\ \tilde{A}_F(s) &= Q_{TF} \tilde{m}_1^{(T)}(s | F) \tilde{A}_F(s), \\ \tilde{m}_2^{(F)}(s | T) &= Q_{TF} \frac{(s + Q_T)(s + \lambda)}{\mathcal{N}(s)} \\ \tilde{A}_F(s) &= Q_{TF} \tilde{m}_1^{(T)}(s | T) \tilde{A}_F(s), \\ \tilde{m}_2^{(F)}(s | C) &= Q_{TF} \frac{Q_{FT}\lambda}{\mathcal{N}(s)} \\ \tilde{A}_F(s) &= Q_{TF} \tilde{m}_1^{(T)}(s | C) \tilde{A}_F(s).\end{aligned}\quad (31)$$

Similar solutions are found for the other two groups of factorial moments.

Based on the form of the solutions in the Laplace domain, one notices that the solutions in the time domain can be written in the form a convolution as follows:

$$\begin{aligned}m_2^{(F)}(t | F) &= Q_{TF} \int_0^t m_1^{(T)}(t - t' | F) A_F(t') dt', \\ m_2^{(F)}(t | T) &= Q_{TF} \int_0^t m_1^{(T)}(t - t' | T) A_F(t') dt', \\ m_2^{(F)}(t | C) &= Q_{TF} \int_0^t m_1^{(T)}(t - t' | C) A_F(t') dt',\end{aligned}\quad (32)$$

and similarly for the second factorial moments of the thermal neutrons and the delayed neutron precursors. Equations (32) express the fact, known from the backward theory of branching processes [2], that the first moments of the single-particle generated distributions play the role of the Green's function for the higher-order moments (and also for all order moments of the distributions of the detected neutrons). This is because the higher-order moment equations have the same form as those for the first moment, except that the Dirac delta function in the first moment equations, representing the starting particle, is replaced by some products of known first moments quantities, which play the role of the inhomogeneous r.h.s. of the second- and higher-order moments. These inhomogeneous right hand sides, or "source functions" depend on the problem at hand and the type of the moment to be calculated. In the present case they are given by the functions $A_F(t)$, and so forth of (29).

The convolution integrals over these known functions can be performed analytically and closed form analytical solutions can be obtained for the second factorial moments. However, in the present case these explicit forms are extremely long and complicated expressions containing the exponential functions $e^{-\omega_1 t}$, $e^{-\omega_2 t}$, and $e^{-\omega_3 t}$ in various combinations. These will not be given here since there is very little insight one could gain from the analytical form of the coefficients multiplying the exponentials.

3.3. Covariances of the Numbers of Particles of Different Types. Although not needed explicitly for the calculation of the two-group version of the Feynman-alpha formula, it might give some insight to calculate the covariances of the numbers of particles of different types at a given time moment, provided that at the time instant $t = 0$, only one particle was in the system. This will be done in this subsection. If the starting particle was a fast neutron, then the following covariances have to be calculated:

$$\begin{aligned}\mathbf{Cov}\{\mathbf{n}_1(t), \mathbf{n}_2(t) | S_F\} &= m_2^{(FT)}(t | F) \\ &\quad - m_1^{(F)}(t | F) m_1^{(T)}(t | F), \\ \mathbf{Cov}\{\mathbf{n}_1(t), \mathbf{n}_3(t) | S_F\} &= m_2^{(FC)}(t | F) \\ &\quad - m_1^{(F)}(t | F) m_1^{(C)}(t | F), \\ \mathbf{Cov}\{\mathbf{n}_2(t), \mathbf{n}_3(t) | S_F\} &= m_2^{(TC)}(t | F) \\ &\quad - m_1^{(T)}(t | F) m_1^{(C)}(t | F).\end{aligned}\quad (33)$$

Along the same lines, the other 6 covariances can also readily be written down. However, for the sake of the simplicity only the above covariances will be calculated.

3.3.1. Mixed Second Moments. In order to determine the covariance between two different random functions at a given time moment, one should calculate first the mixed second moments. In the present case, one needs the following moments:

$$\begin{aligned}m_2^{(FT)}(t | F) &= \left[\frac{\partial^2 g(z_1, z_2, z_3, t | F)}{\partial z_1 \partial z_2} \right]_{z_1=z_2=z_3=1}, \\ m_2^{(FC)}(t | F) &= \left[\frac{\partial^2 g(z_1, z_2, z_3, t | F)}{\partial z_1 \partial z_3} \right]_{z_1=z_2=z_3=1}, \\ m_2^{(TC)}(t | F) &= \left[\frac{\partial^2 g(z_1, z_2, z_3, t | F)}{\partial z_2 \partial z_3} \right]_{z_1=z_2=z_3=1}.\end{aligned}\quad (34)$$

The calculations are straightforward and similar to the calculation of the second factorial moments of the previous section, but rather involved and lengthy. Hence the details of the calculations will not be given here. We only note that similar to the case of the second factorial moments, it is practical to introduce a shorthand notation for the functions

$$\begin{aligned}A_{FT}(t') &= q_2 m_1^{(F)}(t' | F) m_1^{(T)}(t' | F) \\ &\quad + q_1^{(p)} q_1^{(d)} \left[m_1^{(F)}(t' | F) m_1^{(T)}(t' | C) \right. \\ &\quad \left. + m_1^{(T)}(t' | F) m_1^{(F)}(t' | C) \right],\end{aligned}\quad (35)$$

and similarly for $A_{FC}(t')$ and $A_{TC}(t')$ which play the role of the inhomogeneous part of the mixed moment equations and hence appear in the convolution expressions for the solutions. Without going into details, by using the convolution theorem, the formal solutions for the three

mixed moments of the distributions of particles induced by one starting fast neutron are quoted as follows:

$$\begin{aligned} m_2^{(FT)}(t | F) &= Q_{TF} \int_0^t m_1^{(T)}(t-t' | F) A_{FT}(t') dt', \\ m_2^{(FC)}(t | F) &= Q_{TF} \int_0^t m_1^{(T)}(t-t' | F) A_{FC}(t') dt', \\ m_2^{(TC)}(t | F) &= Q_{TF} \int_0^t m_1^{(T)}(t-t' | F) A_{TC}(t') dt'. \end{aligned} \quad (36)$$

By using the formulae (36), one can immediately calculate the covariances (33).

Figure 4 shows the time dependence of the covariances between the numbers of fast and thermal neutrons, as well as between fast neutrons and delayed neutron precursors and also between the thermal neutrons and the precursors, assuming that the starting particle was a fast neutron. It is remarkable that each of them changes sign, but the absolute values of the covariances are very small. One can also show that the variation of the mean decay time λ^{-1} influences only slightly the values of covariances.

The reason for the initially negative value of the covariances can be explained in the same way as for the covariance between the fast and thermal neutrons without the presence of delayed neutrons, as was discussed in [14]. Namely, the process is started by one single fast neutron, which is the only particle in the system at $t = 0$, hence the joint expectation of having any two particles is zero at the beginning. The expectation of having a thermal neutron or a delayed neutron precursor is also zero at the beginning, but with the thermalization of the initial fast neutron the expectation of having a thermal neutron starts to deviate from zero, whereas the joint expectation of finding both a fast and a thermal neutron is negligible until the thermal neutron induces fission. Before the branching starts with first thermalisation and then a thermal fission, the covariance is negative. When the branching starts, the joint expectation of any two particles starts to increase, so the covariance starts to increase after having reached a local minimum and thereafter becomes positive.

4. Moments of the Detection of Neutrons

In order to calculate the variance to mean of detected particles, induced by a stationary extraneous source, two steps remain. One is the introduction of the detection process, which is treated in this section. The second is the introduction of a stationary source, which will be treated in the next section.

For brevity, in the forthcoming only the detection of the fast neutrons will be discussed. For the application of the Feynman-alpha method, even in a fast system, presumably the detection of the thermal neutrons will be more practical. However, the calculation goes exactly along the same lines, hence for illustration it is sufficient to discuss the detection of fast neutrons.

Denote by $Q_{FD} dt + o(dt)$ the probability that a fast neutron is detected in the time interval $(t, t + dt)$. Obviously,

the detected neutron is also absorbed, that is, removed from the branching process. Let $\mathbf{N}(t, u)$ denote the number of fast neutrons detected in the time interval $[t - u, t]$. If $t < u$, then $\mathbf{N}(t)$ stands for the number of fast neutron detections in the time interval $[0, t]$.

4.1. *Detection in Time Interval* $[0, t]$. Define the probabilities:

$$\begin{aligned} \mathcal{P}\{\mathbf{N}(t) = n | F\} &= p_F(n, t), \\ \mathcal{P}\{\mathbf{N}(t) = n | T\} &= p_T(n, t), \\ \mathcal{P}\{\mathbf{N}(t) = n | C\} &= p_C(n, t), \end{aligned} \quad (37)$$

and introduce the generating functions:

$$\begin{aligned} \mathbf{E}\{z^{\mathbf{N}(t)} | F\} &= \sum_{n=0}^{\infty} p_F(n, t) z^n = g_F(z, t), \\ \mathbf{E}\{z^{\mathbf{N}(t)} | T\} &= \sum_{n=0}^{\infty} p_T(n, t) z^n = g_T(z, t), \\ \mathbf{E}\{z^{\mathbf{N}(t)} | C\} &= \sum_{n=0}^{\infty} p_C(n, t) z^n = g_C(z, t). \end{aligned} \quad (38)$$

The equations determining the generating function can be easily written down. One obtains

$$\begin{aligned} g_F(z, t) &= e^{-Q_F t} + Q_{FA} \int_0^t e^{-Q_F(t-t')} dt' + z Q_{FD} \int_0^t e^{-Q_F(t-t')} dt' \\ &\quad + Q_{FT} \int_0^t e^{-Q_F(t-t')} g_T(z, t') dt', \\ g_T(z, t) &= e^{-Q_T t} + Q_{TA} \int_0^t e^{-Q_T(t-t')} dt' \\ &\quad + Q_{FT} \int_0^t e^{-Q_T(t-t')} q_p [g_F(z, t')] q_d [g_C(z, t')] dt', \end{aligned} \quad (39)$$

$$g_C(z, t) = e^{-\lambda t} + \lambda \int_0^t e^{-\lambda(t-t')} g_F(z, t') dt'. \quad (40)$$

Taking into account the second formula in (11), one has

$$q_d [g_C(z, t')] = 1 - q_1^{(d)} + q_1^{(d)} g_C(z, t'). \quad (41)$$

The notation applied does not show that the delayed neutrons also participate in the process.

4.1.1. *Expectations.* The expectations of detected number of F type particles can be easily calculated by using the formulae:

$$\begin{aligned} \mathbf{E}\{\mathbf{N}(t) | F\} &= \left[\frac{\partial g_F(z, t)}{\partial z} \right]_{z=1} = n_1^{(F)}(t), \\ \mathbf{E}\{\mathbf{N}(t) | T\} &= \left[\frac{\partial g_T(z, t)}{\partial z} \right]_{z=1} = n_1^{(T)}(t), \\ \mathbf{E}\{\mathbf{N}(t) | C\} &= \left[\frac{\partial g_C(z, t)}{\partial z} \right]_{z=1} = n_1^{(C)}(t). \end{aligned} \quad (42)$$

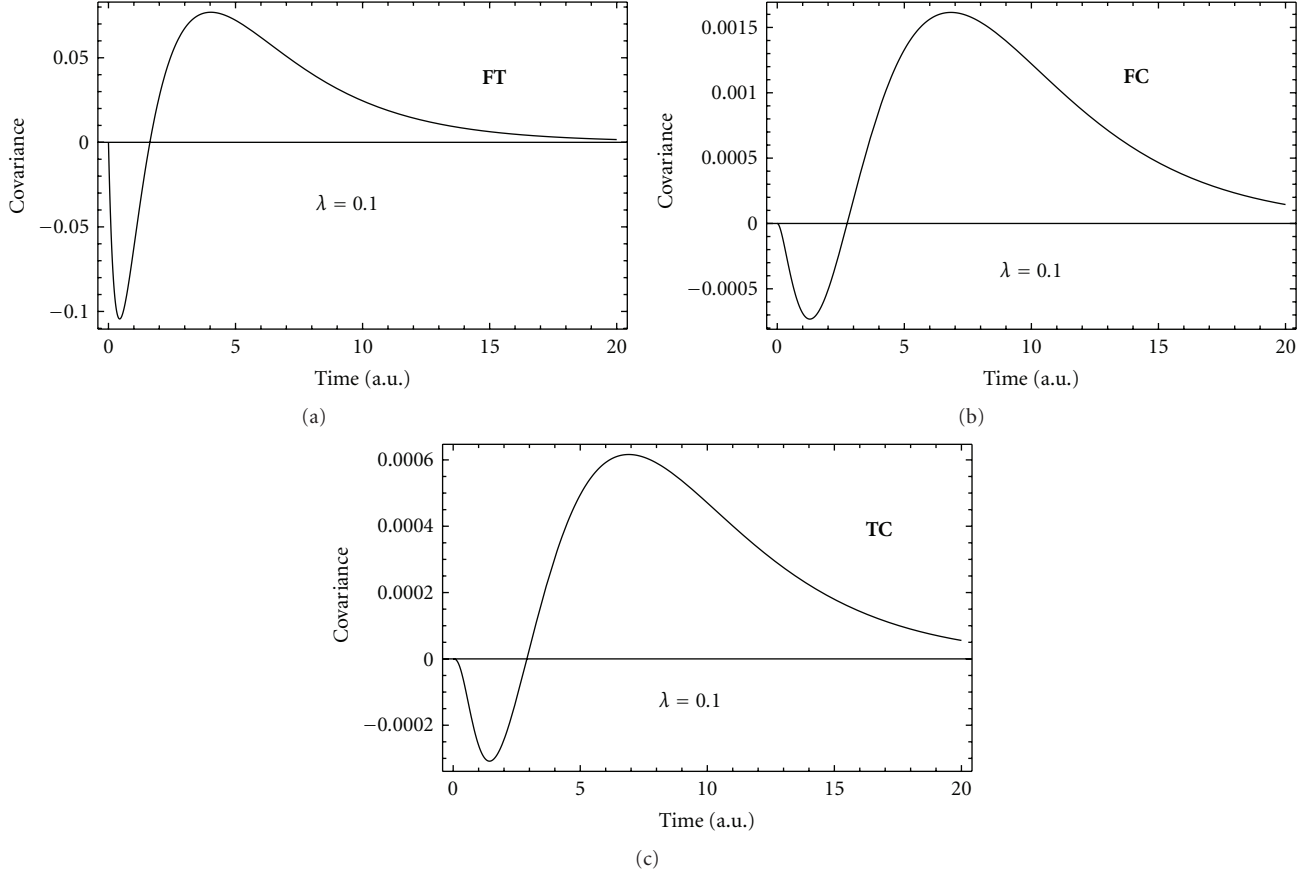


FIGURE 4: Dependence of the covariances between the numbers of particles of types F and T, as well as F and C, and also between the numbers of particles of types T and C on the time, assuming that the starting particle was F type.

After simple considerations one obtains the Laplace transforms of the expectations given by

$$\begin{aligned}\tilde{n}_1^{(F)}(s) &= Q_{FD} \frac{(s + Q_T)(s + \lambda)}{s\mathcal{N}(s)}, \\ \tilde{n}_1^{(T)}(s) &= Q_{FD} \frac{Q_{FT} [q_1^{(p)}(s + \lambda) + q_1^{(d)}\lambda]}{s\mathcal{N}(s)}, \\ \tilde{n}_1^{(C)}(s) &= Q_{FD} \frac{\lambda(s + Q_T)}{s\mathcal{N}(s)},\end{aligned}\quad (43)$$

where $\mathcal{N}(s)$ is defined by (20). Clearly, these expressions are the Laplace transforms of the following integrals:

$$\begin{aligned}n_1^{(F)}(t) &= Q_{FD} \int_0^t m_1^{(F)}(t' | F) dt', \\ n_1^{(T)}(t) &= Q_{FD} \int_0^t m_1^{(F)}(t' | T) dt', \\ n_1^{(C)}(t) &= Q_{FD} \int_0^t m_1^{(F)}(t' | C) dt' .\end{aligned}\quad (44)$$

By using the well-known Tauberian theorem [16], from (43) one obtains immediately the expectations of the number of F

type particles detected in time interval $[0, \infty]$. They are given by

$$\begin{aligned}n_1^{(F)}(\infty) &= Q_{FD} \frac{Q_T \lambda}{\omega_1 \omega_2 \omega_3}, \\ n_1^{(T)}(\infty) &= Q_{FD} \lambda \frac{q_1^{(p)} + q_1^{(d)}}{\omega_1 \omega_2 \omega_3}, \\ n_1^{(C)}(\infty) &= Q_{FD} \frac{Q_T \lambda}{\omega_1 \omega_2 \omega_3},\end{aligned}\quad (45)$$

where

$$\omega_1 \omega_2 \omega_3 = \lambda [Q_F Q_T - Q_{FT} Q_{TF} (q_1^{(p)} + q_1^{(d)})]. \quad (46)$$

It is worth to note that the total number of detected fast neutrons is the same whether the starting particle is a fast neutron or a delayed neutron precursor. However, if the starting particle is a thermal neutron, then, as expected, one obtains a different expectation for the number of detected fast neutrons.

4.1.2. Second Factorial Moments and the Variances. For the characterization of the detecting process, one needs the variances of the number of the fast neutrons, counted in the

time interval $[0, t]$, for the three different types of starting particles. In order to determine the variances, one has to calculate the second factorial moments. From equations (9) and (40), it follows that

$$\begin{aligned} n_2^{(F)}(t) &= Q_{FT} \int_0^t e^{-Q_F(t-t')} n_2^{(T)}(t') dt', \\ n_2^{(T)}(t) &= Q_{TF} \int_0^t e^{-Q_F(t-t')} [q_1^{(p)} n_2^{(F)}(t') + q_1^{(d)} n_2^{(C)}(t')] dt' \\ &\quad + Q_{TF} \int_0^t e^{-Q_F(t-t')} \\ &\quad \times \left\{ q_2 [n_1^{(F)}(t')]^2 + 2 q_1^{(p)} q_1^{(d)} n_1^{(F)}(t') n_1^{(C)}(t') \right\} dt', \\ n_2^{(C)}(t) &= \lambda \int_0^t e^{-\lambda(t-t')} n_2^{(F)}(t') dt'. \end{aligned} \quad (47)$$

Introducing the notation

$$B_{FC}(t') = q_2 [n_1^{(F)}(t')]^2 + 2q_1^{(p)} q_1^{(d)} n_1^{(F)}(t') n_1^{(C)}(t'), \quad (48)$$

and performing a Laplace transformation on (47), after the usual algebraic manipulations including the application of the convolution theorem, one obtains the solutions as

$$n_2^{(F)}(t) = Q_{TF} \int_0^t m_1^{(T)}(t-t' | F) B_{FC}(t') dt', \quad (49)$$

$$n_2^{(T)}(t) = Q_{TF} \int_0^t m_1^{(T)}(t-t' | T) B_{FC}(t') dt', \quad (50)$$

$$n_2^{(C)}(t) = Q_{FT} \int_0^t m_1^{(T)}(t-t' | C) B_{FC}(t') dt', \quad (51)$$

With the help of these expressions, the variances of the number of fast neutron detections for the three starting particle types are given by

$$\begin{aligned} \mathbf{D}^2 \{ \mathbf{N}(t) | F \} &= n_2^{(F)}(t) + n_1^{(F)}(t, | F) [1 - n_1^{(F)}(t, | F)], \\ \mathbf{D}^2 \{ \mathbf{N}(t) | T \} &= n_2^{(T)}(t) + n_1^{(F)}(t, | T) [1 - n_1^{(F)}(t, | T)], \\ \mathbf{D}^2 \{ \mathbf{N}(t) | C \} &= n_2^{(C)}(t) + n_1^{(F)}(t, | C) [1 - n_1^{(F)}(t, | C)]. \end{aligned} \quad (52)$$

4.2. Detection in the Time Interval $[t-u, t]$, $t > u$. Since the detection in the time interval $[0, t-u]$ is excluded and only in the time interval $[t-u, t]$ is permitted, one can write that

$$\begin{aligned} \mathcal{P} \{ \mathbf{N}(t, u) = n | S_F \} \\ &= p_F(n, t, u) \\ &= \sum_{j+k+\ell=n} \sum_{n_1=0}^{\infty} \sum_{n_2=0}^{\infty} \sum_{n_3=0}^{\infty} p(n_1, n_2, n_3, t-u | F) \\ &\quad \times Z^{(1)}(j, u | n_1) Z^{(2)}(k, u | n_2) Z^{(3)}(\ell, u | n_3), \end{aligned} \quad (53)$$

provided that at the time moment $t = 0$ one fast neutron was in the system. It is easy to prove that the probabilities $Z^{(1)}(j, u | n_1)$, $Z^{(2)}(k, u | n_2)$, and $Z^{(3)}(\ell, u | n_3)$ are given by the following formulae:

$$\begin{aligned} Z^{(1)}(j, u | n_1) &= \sum_{j_1+\dots+j_{n_1}=j} \prod_{i=1}^{n_1} p_F(j_i, u), \\ Z^{(2)}(k, u | n_2) &= \sum_{k_1+\dots+k_{n_2}=k} \prod_{i=1}^{n_2} p_T(k_i, u), \\ Z^{(3)}(\ell, u | n_3) &= \sum_{\ell_1+\dots+\ell_{n_3}=\ell} \prod_{i=1}^{n_3} p_C(\ell_i, u), \end{aligned} \quad (54)$$

where $p_F(j, u)$, $p_T(k, u)$, and $p_C(\ell, u)$ are defined by (37). From (54) one can immediately see that

$$\begin{aligned} \sum_{j=0}^{\infty} Z^{(1)}(j, u | n_1) z^j &= [g_F(z, u)]^{n_1}, \\ \sum_{k=0}^{\infty} Z^{(2)}(k, u | n_2) z^k &= [g_T(z, u)]^{n_2}, \\ \sum_{\ell=0}^{\infty} Z^{(3)}(\ell, u | n_3) z^\ell &= [g_C(z, u)]^{n_3}. \end{aligned} \quad (55)$$

Thus, the generating function

$$g_F(z, t, u) = \sum_{n=0}^{\infty} p_F(n, t, u) z^n, \quad t > u \quad (56)$$

can be written in the form:

$$g_F(z, t, u) = g[g_F(z, u), g_T(z, u), g_C(z, u), t-u | S_F]. \quad (57)$$

Since, as it is seen from (8)

$$g(z_1, z_2, z_3, 0 | F) = z_1, \quad (58)$$

from (57), one obtains

$$g_F(z, u, u) = g[g_F(z, u), g_T(z, u), g_C(z, u), 0 | S_F] = g_F(z, u), \quad (59)$$

which corresponds to the condition

$$\lim_{t \rightarrow u} g_F(z, t, u) = g_F(z, u). \quad (60)$$

Expressions similar to (57) can be obtained for the cases when the starting particle is a fast neutron or a delayed neutron precursor.

4.2.1. Expectation and Second Factorial Moment. For later use, let us determine the expectation:

$$n_1^{(F)}(t, u) = \left[\frac{\partial g_F(z, t, u)}{\partial z} \right]_{z=1} \quad (61)$$

of the number of fast neutron detections in the time interval $[t - u, t]$, where $t > u$, provided that the starting particle was also a fast neutron. By using (57) one obtains

$$n_1^{(F)}(t, u) = m_1^{(F)}(t - u | F)n_1^{(F)}(u) + m_1^{(T)}(t - u | F)n_1^{(T)}(u) + m_1^{(C)}(t - u | F)n_1^{(C)}(u), \quad (62)$$

where $n_1^{(F)}(u)$, $n_1^{(T)}(u)$, and $n_1^{(C)}(u)$ are defined by (44).

The calculation of the second factorial moment:

$$n_2^{(F)}(t, u) = \left[\frac{\partial^2 g_F(z, t, u)}{\partial z^2} \right]_{z=1} \quad (63)$$

is straightforward, but rather tedious. One finds

$$\begin{aligned} n_2^{(F)}(t, u) &= m_1^{(F)}(t - u | F)n_2^{(F)}(u) + m_1^{(T)}(t - u | F) \\ &\quad \times n_2^{(T)}(u) + m_1^{(C)}(t - u | F)n_2^{(C)}(u) + m_2^{(F)} \\ &\quad \times (t - u | F)[n_1^{(F)}(u)]^2 + m_2^{(T)}(t - u | F) \\ &\quad \times [n_1^{(T)}(u)]^2 + m_2^{(C)}(t - u | F)[n_1^{(C)}(u)]^2 \\ &\quad + 2m_2^{(FT)}(t - u | F)n_1^{(F)}(u)n_1^{(T)}(u) + 2m_2^{(FC)} \\ &\quad \times n_1^{(F)}(u)n_1^{(C)}(u) + 2m_2^{(TC)}(t - u | F)n_1^{(T)}(u)n_1^{(C)}(u). \end{aligned} \quad (64)$$

In this expression, the second factorial moments $n_2^{(F)}(u)$, $n_2^{(T)}(u)$, and $n_2^{(C)}(u)$ have been determined already by (49), (50), and (51) respectively hence they are already known. With the substitution of all the known functions, an explicit expression can be obtained which will contain three exponentials with the known exponents. The coefficients multiplying the exponents would take too much space to display and hence will not be shown here.

5. Process with Randomly Injected Particles

The last step in the derivation of the variance to mean or Feynman-alpha formula is to calculate the first two factorial moments of the detected fast neutrons, induced in a subcritical reactor by a stationary source of fast neutrons. Suppose that at the time instant $t = 0$ there are no particles present in the system, but as time passes fast neutrons appear randomly with a given intensity and initiate branching processes independently of one another. The theory of injection of particles is expounded in the book by Pázsit and Pál [2] for particles of one type. The generalization for particles of three types is straightforward.

5.1. Joint Distribution of the Numbers of Particles. In this work we assume that the source events constitute a Poisson point process, that is, that the random time interval

between two consecutive injections of fast neutrons follows an exponential distribution with parameter s_F . This corresponds to the case of an ADS driven by a DD or DT neutron generator in continuous mode. Neutron sources of future ADS will operate with spallation sources and/or in pulsed mode, which have a non-Poisson character. However, the generalisation of the treatment below to non-Poisson processes has been already done in other context (see, e.g., [2, 4, 5]), and the treatment presented in this paper can also be extended to the case of non-Poisson sources in a straightforward way.

For the case of a Poisson source, it can be easily shown that the generating function of the probability $P(n_1, n_2, n_3, t; F)$ of the event:

$$\{\mathbf{n}_1(t) = n_1, \mathbf{n}_2(t) = n_2, \mathbf{n}_3(t) = n_3\}, \quad (65)$$

provided that at time $t = 0$ there were no particles present in the system, is given by

$$G(z_1, z_2, z_3, t; F) = \exp \left\{ s_F \int_0^t [g(z_1, z_2, z_3, t' | F) - 1] dt' \right\}. \quad (66)$$

In general, if the injected particles are of type i , and if the intensity of the injection of particle type i is s_i , then one has

$$G(z_1, z_2, z_3, t; S_i) = \exp \left\{ s_i \int_0^t [g(z_1, z_2, z_3, t' | S_i) - 1] dt' \right\}. \quad (67)$$

5.1.1. Calculation of the Expectations and the Variances. By using the logarithm of the generating function, one can write the formulae:

$$\begin{aligned} M_1^{(F)}(t; F) &= \left[\frac{\partial \ln G(z_1, z_2, z_3, t; F)}{\partial z_1} \right]_{z_1=z_2=z_3=1} \\ &= s_F \int_0^t m_1^{(F)}(t' | F) dt', \\ M_1^{(T)}(t; F) &= \left[\frac{\partial \ln G(z_1, z_2, z_3, t; F)}{\partial z_2} \right]_{z_1=z_2=z_3=1} \\ &= s_F \int_0^t m_1^{(T)}(t' | F) dt', \\ M_1^{(C)}(t; F) &= \left[\frac{\partial \ln G(z_1, z_2, z_3, t; F)}{\partial z_3} \right]_{z_1=z_2=z_3=1} \\ &= s_F \int_0^t m_1^{(C)}(t' | F) dt', \end{aligned} \quad (68)$$

giving the expectations of the numbers of fast and thermal neutrons and delayed neutron precursors, respectively, at the time moment $t \geq 0$, provided that the type of the particles injected into the system was fast neutrons. Similar formulae can be derived for the other six expectations.

In the subcritical state, that is, if ω_1 , ω_2 and ω_3 , are positive real numbers, then the process is asymptotically stationary, consequently one has

$$\begin{aligned} M_1^{(F)}(\infty; F) &= s_F \frac{Q_T \lambda}{\mathcal{N}_{st}}, \\ M_1^{(T)}(\infty; F) &= s_F \frac{Q_{FT} \lambda}{\mathcal{N}_{st}}, \\ M_1^{(C)}(\infty; F) &= s_F q_1^{(d)} \frac{Q_{FT} Q_{TF}}{\mathcal{N}_{st}}, \end{aligned} \quad (69)$$

where

$$\mathcal{N}_{st} = \omega_1 \omega_2 \omega_3 = \lambda \left[Q_F Q_T - (q_1^{(p)} + q_1^{(d)}) Q_{FT} Q_{TF} \right]. \quad (70)$$

The rest of the stationary expectations are given by the following formulae:

$$\begin{aligned} M_1^{(F)}(\infty; T) &= s_T (q_1^{(p)} + q_1^{(d)}) \frac{Q_T \lambda}{\mathcal{N}_{st}}, \\ M_1^{(T)}(\infty; T) &= s_T \frac{Q_F \lambda}{\mathcal{N}_{st}}, \\ M_1^{(C)}(\infty; T) &= s_T q_1^{(d)} \frac{Q_F Q_{TF}}{\mathcal{N}_{st}}, \\ M_1^{(F)}(\infty; C) &= s_C \frac{Q_T \lambda}{\mathcal{N}_{st}}, \\ M_1^{(T)}(\infty; C) &= s_C \frac{Q_{FT} \lambda}{\mathcal{N}_{st}}, \\ M_1^{(C)}(\infty; C) &= s_C q_1^{(d)} \frac{Q_F Q_T - q_1^{(p)} Q_{FT} Q_{TF}}{\mathcal{N}_{st}}. \end{aligned} \quad (71)$$

For the determination of variances of the number of fast neutrons, generated by the three different possible starting particles, one obtains the expressions:

$$\begin{aligned} V_F(t; S_i) &= \left[\frac{\partial^2 \ln G(z_1, z_2, z_3, t; S_i)}{\partial z_1^2} \right]_{z_1=z_2=z_3=1} \\ &+ \left[\frac{\partial \ln G(z_1, z_2, z_3, t; S_i)}{\partial z_1} \right]_{z_1=z_2=z_3=1} \\ &= s_i \int_0^t \left[m_2^{(F)}(t' | S_i) + m_1^{(F)}(t' | S_i) \right] dt'. \end{aligned} \quad (72)$$

5.2. Distribution of the Number of Fast Neutrons Detected in a Given Time Interval. If the injection of fast neutrons into the medium is performed by a stationary source emitting particles according to a Poisson process defined by the intensity parameter s_F , then applying the procedure described in [2], one can prove that generating function of the probability mass function:

$$\mathcal{P} \{ \mathbf{N}(t, u) = n \mid \mathbf{n}_1 = \mathbf{n}_2 = \mathbf{n}_3 = 0 \} = P_F(n, t) \quad (73)$$

is given by

$$\begin{aligned} \mathbb{G}_F(z, t, u) &= \mathbb{G}_F(z, u) \exp \left\{ s_F \int_u^t [g_F(z, t', u) - 1] dt' \right\} \quad \text{if } t > u, \\ \mathbb{G}_F(z, t) &= \exp \left\{ s_F \int_0^t [g_F(z, t') - 1] dt' \right\} \quad \text{if } t \leq u, \end{aligned} \quad (74)$$

where

$$g_F(z, t', u) = g[g_F(z, u), g_T(z, u), g_C(z, u), t' - u \mid F]. \quad (75)$$

By using the method described in [2, pages 85-86], one can prove that the improper integral:

$$\lim_{t \rightarrow \infty} \int_u^t [g_F(z, t', u) - 1] dt' \quad (76)$$

exists, consequently the stationary generating function:

$$\lim_{t \rightarrow \infty} \mathbb{G}_F(z, t, u) = \mathbb{G}_F^{(st)}(z, u) \quad (77)$$

also exists, if the three roots of the characteristic function (18) are nonnegative. In this case the random function $\mathbf{N}(t, u)$ converges in distribution to a random function $\mathbf{N}^{(st)}(u)$, if $t \rightarrow \infty$. Hence, $\mathbb{G}_F^{(st)}(z, u)$ is the generating function of $\mathbf{N}^{(st)}(u)$, that is,

$$\mathbb{G}_F^{(st)}(z, u) = \mathbf{E} \{ z^{\mathbf{N}^{(st)}(u)} \}. \quad (78)$$

It is useful to rewrite the stationary generating function in the following form:

$$\begin{aligned} \ln \mathbb{G}_F^{(st)}(z, u) &= s_F \int_0^u [g_F(z, t) - 1] dt \\ &+ s_F \int_u^\infty [g_F(z, t, u) - 1] dt. \end{aligned} \quad (79)$$

Thus one finds

$$\begin{aligned} \ln \mathbb{G}_F^{(st)}(z, u) &= s_F \int_0^u [g_F(z, t) - 1] dt \\ &+ s_F \int_0^\infty \{ g[g_F(z, u), g_T(z, u), g_C(z, u), t \mid S_F] - 1 \} dt. \end{aligned} \quad (80)$$

If the injected particles are thermal neutrons, then the corresponding formula reads as

$$\begin{aligned} \ln \mathbb{G}_T^{(st)}(z, u) &= s_T \int_0^u [g_T(z, t) - 1] dt \\ &+ s_T \int_0^\infty \{ g[g_F(z, u), g_T(z, u), g_C(z, u), t \mid S_T] - 1 \} dt. \end{aligned} \quad (81)$$

In the continuation, we will only deal with the case of fast neutron injection.

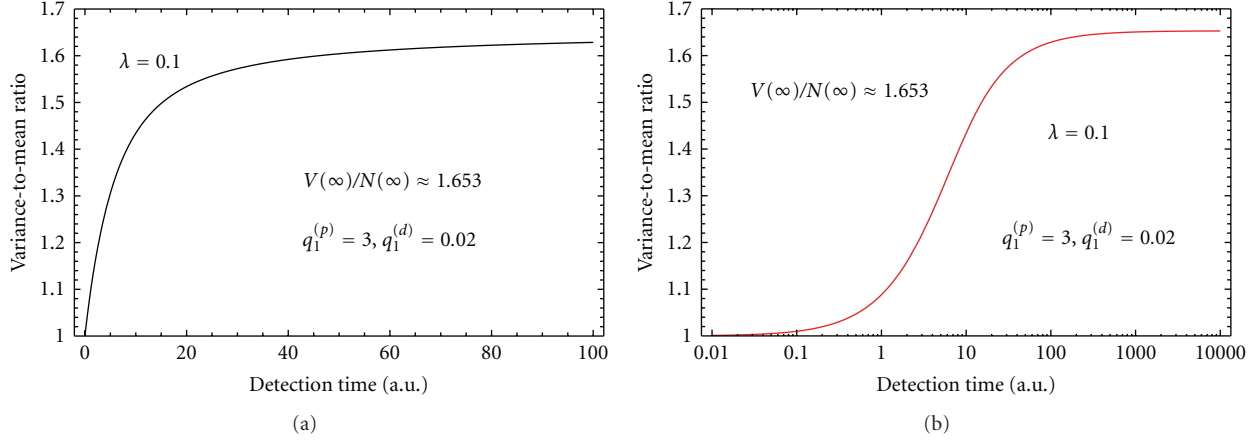


FIGURE 5: Dependence of the ratio of the variance to mean of the number of **F** types particle detections on the detection time u . The left-hand side figure shows the linear-linear, while the right-hand side one the log-linear plot.

5.2.1. *Calculation of the Expectation and the Variance to Mean in Stationary Case.* In the stationary case the expectation of the number of the detection of fast neutrons in the time interval u is given by

$$\begin{aligned} \mathbb{N}_F^{(st)}(u) &= \left[\frac{\partial \ln \mathbb{G}_F^{(st)}(z, u)}{\partial z} \right]_{z=1} \\ &= s_F \int_0^u n_1^{(F)}(t') dt' + s_F \int_u^\infty n_1^{(F)}(t', u) dt'. \end{aligned} \quad (82)$$

By using (79), one can write

$$\begin{aligned} \int_u^\infty n_1^{(F)}(t', u) dt' &= n_1^{(F)}(u) \int_0^\infty m_1^{(F)}(t | F) dt \\ &+ n_1^{(T)}(u) \int_0^\infty m_1^{(T)}(t | F) dt \\ &+ n_1^{(C)}(u) \int_0^\infty m_1^{(C)}(t | F) dt, \end{aligned} \quad (83)$$

where

$$\begin{aligned} \int_0^\infty m_1^{(F)}(t | F) dt &= \frac{\lambda Q_T}{\mathcal{N}_{st}}, \\ \int_0^\infty m_1^{(T)}(t | F) dt &= \frac{\lambda Q_{FT}}{\mathcal{N}_{st}}, \\ \int_0^\infty m_1^{(C)}(t | F) dt &= q_1^{(d)} \frac{Q_{FT} Q_{TF}}{\mathcal{N}_{st}}. \end{aligned} \quad (84)$$

After a lengthy algebra, one obtains

$$\mathbb{N}_F^{(st)}(u) = s_F \frac{Q_{FD} Q_T}{Q_F Q_T - Q_{FT} Q_{TF} (q_1^{(p)} + q_1^{(d)})} u, \quad (85)$$

which does not contain the delayed neutron precursor decay constant λ .

By using the logarithmic generation function $\ln \mathbb{G}_F^{(st)}(z, u)$, one can write down the ratio of the variance to mean of the number of **F** types particles detected in the time interval u in the form:

$$\begin{aligned} \frac{\mathbf{D}^2 \{ \mathbf{N}^{(st)}(u) \}}{\mathbf{E} \{ \mathbf{N}^{(st)}(u) \}} &= \frac{\mathbb{V}_F^{(st)}(u)}{\mathbb{N}_F^{(st)}(u)} \\ &= 1 + \frac{1}{\mathbb{N}_F^{(st)}(u)} \left[\frac{\partial^2 \ln \mathbb{G}_F^{(st)}(z, u)}{\partial z^2} \right]_{z=1} \\ &= 1 + Y(u), \end{aligned} \quad (86)$$

where

$$\begin{aligned} \left[\frac{\partial^2 \ln \mathbb{G}_F^{(st)}(z, u)}{\partial z^2} \right]_{z=1} &= s_F \int_0^u n_2^{(F)}(t') dt' \\ &+ s_F \int_u^\infty n_2^{(F)}(t', u) dt', \end{aligned} \quad (87)$$

and $n_2^{(F)}(t', u)$ is given by (64). The Feynman $Y(u)$ function can be written in the traditional form as

$$Y(u) = \sum_{i=1}^3 Y_i \left(1 - \frac{1 - e^{-\omega_i u}}{\omega_i u} \right). \quad (88)$$

The coefficients Y_i are rather involved functions of the roots ω_i as well as the various reaction intensities and the first and second factorial moments of the number of fast neutrons and the delayed neutron precursors per fission. Due to their very extensive character, they are not given here.

Figure 5 shows a quantitative illustration of the dependence of the variance to mean of the number of fast neutron detections on the detection time u . The left-hand side figure shows the linear-linear, while the right-hand side one shows a log-linear plot (for the calculations the following parameter values were used: $Q_{FD} = 1/10$, $Q_{FA} = 7/30$, $Q_{FT} = 2/3$, $Q_{TA} = 14/10$, $Q_{TF} = 3/5$, $q_1^{(p)} = 3$, $q_1^{(d)} = 0.02$, $\lambda = 0.1$).

In view of the fact that there are three decay constants ω_i , $i = 1, 2, 3$ one could expect a more complicated structure for the variance to mean than what is seen in the left-hand side figure, with for example, two or three different plateaus. Such is the case with the traditional (one-group) Feynman-alpha formula with delayed neutrons, which displays two different plateaus.

However, the Feynman-alpha formula will show the different plateaus if the decay constants are sufficiently different and differ by orders of magnitude from each other. Even the traditional (one-group) Feynman formula demonstrates this, since even if six different delayed neutron precursor types are accounted for, there are only two plateaus distinguishable: one corresponding to the prompt neutrons and only one more for all the six delayed neutron groups [17]. In the present two-group treatment, there will be two decay constants associated with the prompt neutrons, and one with the delayed neutrons. As discussed already in [14], quantitatively these two prompt neutron decay constants are not separated sufficiently from each other to make the two decay constants easily observable in the lin-lin plot, for example, by displaying two plateaus. The decay constant corresponding to the delayed neutrons, on the other hand, deviates sufficiently from the prompt decay constants. The plateau corresponding to the delayed neutrons is visible on the plot with logarithmic scale on the time axis (right-hand side figure).

6. Conclusions

The variance to mean formula was derived in a two-group treatment with one group of delayed neutrons with the use of the backward master equation technique. The temporal behaviour of both the first and second factorial moment of the detected particles is determined by three exponentials. The various factorial moments can be fully determined analytically; however, the expressions in most cases are too lengthy to write them out. Qualitatively, the form of the solutions is the same as in the traditional case, but the two decay constants associated with the prompt response of the system, are not distinguishable in the plots. The relationship between the decay constants and the subcritical reactivity of the system will be investigated in future communications.

Acknowledgments

This work was supported by the Hungarian Academy of Sciences and the FP7 EU Collaborative Research Project FREYA, Grant Agreement no. FP7-269665.

References

- [1] N. G. Sjöstrand, "Measurements on a subcritical reactor using a pulsed neutron source," *Arkiv för Fysik*, vol. 11, no. 13, pp. 233–246, 1956.
- [2] I. Pázsit and L. Pál, *Neutron Fluctuations: A Treatise on the Physics of Branching Processes*, Elsevier, 2008.
- [3] S. B. Degweker and Y. S. Rana, "Reactor noise in accelerator driven systems II," *Annals of Nuclear Energy*, vol. 34, no. 6, pp. 463–482, 2007.
- [4] Y. S. Rana and S. B. Degweker, "Feynman-alpha and Rossi-alpha formulas with delayed neutrons for subcritical reactors driven by pulsed non-Poisson sources," *Nuclear Science and Engineering*, vol. 162, no. 2, pp. 117–133, 2009.
- [5] Y. S. Rana and S. B. Degweker, "Feynman-alpha and Rossi-alpha formulas with delayed neutrons for subcritical reactors driven by pulsed non-Poisson sources with correlation between different pulses," *Nuclear Science and Engineering*, vol. 169, pp. 98–109, 2011.
- [6] R. Soule, W. Assal, P. Chaussonnet et al., "Neutronic studies in support of accelerator-driven systems: the MUSE experiments in the MASURCA facility," *Nuclear Science and Engineering*, vol. 148, no. 1, pp. 124–152, 2004.
- [7] H. Kiyavitskaya et al., "YALINA-Booster Benchmark Specifications for the IAEA Coordinated Research Projects on Analytical and Experimental Benchmark Analysis on Accelerator Driven Systems and Low Enriched Uranium Fuel Utilization in Accelerator Driven Sub-Critical Assembly Systems," IAEA, 2007.
- [8] Y. Gohar and D. L. Smith, "YALINA Facility, A Sub-Critical Accelerator-Driven System (ADS) for Nuclear Energy Research. Facility Description and Overview of the Research Program," Argonne National Laboratory, ANL-10/05, 2010.
- [9] A. Talamo and Y. Gohar, "Deterministic and Monte Carlo Modeling of YALINA Thermal Subcritical Assembly," Argonne National Laboratory, ANL-10/17, 2010.
- [10] J.-L. Munoz-Cobo, C. Berglöf, J. Pena, D. Villamarin, and V. Bournos, "Feynman- and Rossi- formulas with spatial and modal effects," *Annals of Nuclear Energy*, vol. 38, p. 590, 2011.
- [11] C. Berglöf, M. Fernandez-Ordonez, D. Villamarin et al., "Auto-correlation and variance-to-mean measurements in a subcritical core obeying multiple alpha-modes," *Annals of Nuclear Energy*, vol. 38, p. 194, 2011.
- [12] T. Yamamoto, "Higher order mode analyses in Feynman- α method," *Annals of Nuclear Energy*, vol. 38, p. 1231, 2011.
- [13] H. O. Menlove, S. H. Menlove, and S. J. Tobin, "Fissile and fertile nuclear material measurements using a new differential die-away self-interrogation technique," *Nuclear Instruments and Methods in Physics Research A*, vol. 602, no. 2, pp. 588–593, 2009.
- [14] L. Pál and I. Pázsit, "A special branching process with two particle types," *The European Physical Journal Plus*, vol. 126, no. 2, p. 20, 2011.
- [15] J. Anderson, L. Pál, I. Pázsit, D. Chernikova, and S. A. Pozzi, "Derivation and quantitative analysis of the differential self-interrogation Feynman-alpha method," *The European Physical Journal Plus*, vol. 127, no. 2, p. 21, 2012.
- [16] D. V. Widder, "The Laplace Transform," Princeton University Press, Princeton, NJ, USA, 1946.
- [17] L. Pál, "On the theory of stochastic processes in nuclear reactors," *Nuovo Cimento*, vol. 7, no. 1, pp. 25–42, 1958.

Research Article

Interpretation of Local Flux Measurements in Subcritical Systems and Reactivity Determination

S. Dulla and P. Ravetto

Dipartimento Energia, Politecnico Di Torino, Corso Duca degli Abruzzi, 24-10129 Torino, Italy

Correspondence should be addressed to S. Dulla, sandra.dulla@polito.it

Received 9 January 2012; Accepted 28 February 2012

Academic Editor: Alberto Talamo

Copyright © 2012 S. Dulla and P. Ravetto. This is an open access article distributed under the Creative Commons Attribution License, which permits unrestricted use, distribution, and reproduction in any medium, provided the original work is properly cited.

The determination of the subcriticality level constitutes an important issue in the assessment of the accelerator-driven system technology. For this purpose, the interpretation of flux measurements requires a lumped-parameter model employed in an inverse fashion. This paper addresses the drawbacks of point kinetics in performing such a task. In particular, the problem of the generation of integral parameters is considered, in connection with the use of a shape function and of a projection weight tailored to the neutron flux detector. Furthermore, the question of the generation of the effective source is analysed, and some proposals to modify the time dependence of such a function to account for the time delay at the flux detector are presented and discussed.

1. Introduction

The assessment of the feasibility of subcritical accelerator-driven systems requires the performance of experiments to verify the kinetic response features and the determination of the integral parameters that characterize the physical multiplying structure. Typical experiments involve the measurements of flux signals during source or reactivity-induced transients, either in pulsed or oscillated modes. Several experimental campaigns have been conducted in the past years [1, 2], and new more ambitious and advanced experiments are programmed in the near future.

An issue that is particularly important is the monitoring of the subcriticality level of the reactor. It is, therefore, required to establish efficient procedures to interpret flux measurements retrieved from detectors localized in various positions of the structure. This constitutes a basic and challenging inverse problem in reactor physics since the early times of nuclear energy and various approaches have been developed [3–5]. The interpretation of local measurements may be carried out only through suitable physico-mathematical models. The inverse procedure can be easily implemented if a lumped-parameter model, such as classic

point kinetics, is adopted. However, usually only localized values of the neutron flux are available from the detectors. Hence, the flux interpretation scheme needs unavoidably to account for spectral and spatial effects. It has been shown [6] by numerical simulations that the point model with integral kinetic parameters may be inadequate when local flux signals are used in a point framework to reconstruct the global system reactivity in an inverse fashion, while it may perform rather well for the analysis of the full power evolution, which is, however, seldom available from the direct experimental information. This aspect is also confirmed by real experimental analyses [7].

From the theoretical point of view, to construct integral kinetic parameters a projection involving the neutronic shape over a weighting function is always required. While for critical systems the mathematically consistent and physically meaningful choice for the weighting function is unique, as the reference steady-state system adjoint (neutron importance) [8], for source-driven systems the necessity of a definition of the adjoint source introduces a certain degree of freedom [9]. It has been shown [10] that the effect of the choice of the weighting function may be quite significant. The freedom of the choice may be used to suit the objectives

of the analysis. To be more specific, the adjoint source can be assumed as a cross section characterizing the physical properties of the local detector where the flux measurement is taken. The present paper shall discuss the effectiveness of the weighting to simulate in a point-like manner the evolution of local flux signals, therefore envisaging the possibility of devising tailored point models to interpret experimental measurements and establish the limits of the technique.

Another aspect that plays an important role in the interpretation procedure for source transients is the suitable time-shape of the neutron source that is assumed in the lumped-parameter model [11]. It is obvious that a time delay needs to be introduced when analyzing the signal from detectors away from the source region. This aspect is also discussed in the following.

2. The Factorization-Projection Procedure for the Neutronic Equations

A lumped-parameter model is derived from the most general balance equations involving both neutrons and delayed neutron precursors. By indicating with $n(\mathbf{x}, t)$ the neutron density at phase point \mathbf{x} at time t , the balance equations can be written as:

$$\begin{aligned} \frac{\partial n}{\partial t} &= \hat{L}n + \hat{F}_p n + \lambda C + S, \\ \frac{\partial C}{\partial t} &= -\lambda C + \hat{F}_d n, \end{aligned} \quad (1)$$

where only one family of delayed neutron precursors is considered, being the extension to any number of families just trivial. The symbols \hat{L} , \hat{F}_p , and \hat{F}_d denote the leakage, prompt neutron production, and delayed neutron production operators, respectively. They may take appropriate forms consistent with the neutronic model adopted (e.g., discrete ordinate approach, spherical harmonics, diffusion) to treat the transport process. The quantity S indicates the external neutron source. A factorization is now introduced according to the classical procedure [12]:

$$n(\mathbf{x}, t) = A(t)\varphi(\mathbf{x}, t). \quad (2)$$

A projection step leads to the required model, introducing integral parameters that are constant in time if the shape function and the system properties are assumed to be constant. The operation involves the multiplication of each equation by a proper weighting function followed by integration over phase space. When treating initially critical systems, the importance function, solution of the adjoint homogeneous equation [13], is used. For subcritical systems, the weighting function can be chosen according to the solution of an adjoint source-driven problem [10]:

$$\hat{L}_0^\dagger \phi_S^\dagger + \hat{F}_0^\dagger \phi_S^\dagger + S^\dagger = 0, \quad (3)$$

where \hat{L}_0^\dagger and \hat{F}_0^\dagger are the adjoint destruction and production operators for the reference (initial) system, respectively.

The factorization followed by a projection operation upon a general weighting function ψ leads to the following system of first-order differential equations in time:

$$\begin{aligned} \frac{dA}{dt} &= \frac{\langle \psi | \hat{L}\varphi \rangle}{\langle \psi | \varphi \rangle} A + \frac{\langle \psi | \hat{F}_p \varphi \rangle}{\langle \psi | \varphi \rangle} A + \lambda \frac{\langle \psi | C \rangle}{\langle \psi | \varphi \rangle} + \frac{\langle \psi | S \rangle}{\langle \psi | \varphi \rangle}, \\ \frac{d}{dt} \frac{\langle \psi | C \rangle}{\langle \psi | \varphi \rangle} &= \frac{\langle \psi | \hat{F}_d \varphi \rangle}{\langle \psi | \varphi \rangle} A - \lambda \frac{\langle \psi | C \rangle}{\langle \psi | \varphi \rangle}. \end{aligned} \quad (4)$$

The coefficients of such a system constitute the so-called kinetic parameters, which are perfectly defined once the shape and the adjoint functions are defined.

As already pointed out, there is some freedom in the choice of the adjoint source. The selection of the problem-oriented adjoint source as the space- and energy-dependent cross section of the detector through which the local flux is measured may be physically advantageous for experimental interpretations. With this choice, the physical characteristics of the detector are accounted for. This model is denoted as *local* point kinetics (*lpk*) in the following. For other applications, in which the interest is more focused on the global behaviour of the system and thus the attention is concentrated on the fission process, the fission productivity $\nu\Sigma_f$ may be used, leading to a global point kinetic model (*gpk*). Of course, there is always the possibility to choose the critical adjoint as the weighting function, leading to a critical point kinetic equation (*cpk*).

Another important aspect in the generation of the lumped-parameter model concerns the choice of the shape function to be introduced in the factorization. Obviously, for a reactor departing from a criticality steady-state, the fundamental eigenfunction is naturally used, while for a deeply subcritical source-driven system at equilibrium the source-driven stationary distribution seems to be the most appropriate choice. However, a difficulty arises in the simulation of pulsed experiments, for which no neutrons are usually present in the initial system and no reference steady-state situation is approached during the experiment. Different kinetic models can thus be envisaged, by either using the critical shape, φ_c , or the source-driven shape, φ_s . All combinations of choices for the shape and for the adjoint are possible.

Summarizing the previous discussion, it is worth studying the performance of kinetic models obtained by the adoption of different shapes and weighting functions in the simulation of power transients and local flux signal evolutions, especially when the attention is focused on experimental analyses. Two shapes can be considered, the critical and the source-driven reference distributions. Furthermore, the weighting function can be chosen according to either the critical importance or the source-driven fission importance (the adjoint source is the system fission cross section), both retaining a global information, as well as a detector-tailored importance (the adjoint source is the detector cross section). In the following, some results are presented to highlight the features and the performance of the various possible models, which are quite numerous if one considers all the possible

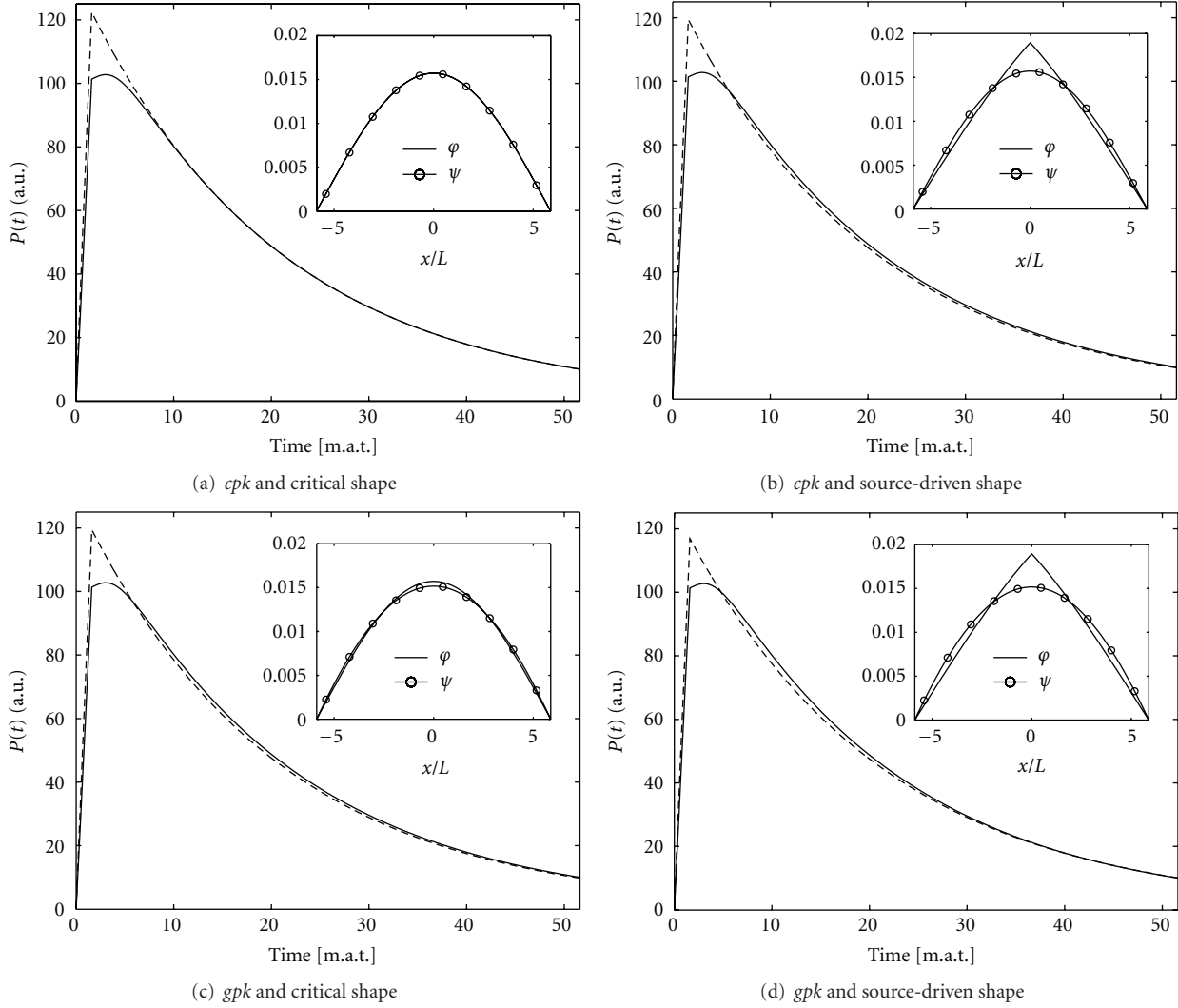


FIGURE 1: Power evolution following a source pulse in a subcritical system ($k_{\text{eff}} = 0.95$), simulated with different approaches to point kinetics: *cpk* and *gpk*. Solid line: reference; dashed line: point kinetics. The inset graphs represent the shape φ and the weight ψ adopted (m.a.t.: mean absorption time = $1/(\nu\sigma_a)$).

combinations. However, we restrict to presenting a limited number of cases, deemed to give some physical insight that may be useful to better understand the limits of a lumped-parameter model when used for experimental interpretations.

3. Application of Local and Global Point Kinetics to the Interpretation of Pulsed Experiments

In the following, comparisons between exact results for a pulsed source in a system described by one-group diffusion theory, assumed as the reference model, and the corresponding point kinetic model are presented. The system considered is characterized by the following physical parameters: neutron velocity $v = 10^7$ cm/s, diffusion coefficient $D = 1.5$ cm, diffusion length $L = 10$ cm, and slab thickness

$H = 117.5$ cm. The value of the infinite multiplication constant has been set in order to obtain the required k_{eff} , and two different subcriticality levels have been considered to highlight the effects of subcriticality. The source is localized and placed in the center of the system ($S(x) = \delta(x)$). In Figures 1–4, the power evolution following a source pulse of duration $\tau = 10 \mu\text{s}$ is presented, comparing the reference and point kinetic results, with different choices of the shape and weighting functions.

As can be seen in Figures 1 and 3, no relevant differences can be observed when adopting a critical or source-driven shape, and the adoption of a global (*gpk*) or critical (*cpk*) point kinetic model provides similar results in the reproduction of the power, with an average good quality, although the point models are not able to reproduce the behavior at short times, due to the presence of strong spatial effects in the propagation of the source pulse. On the other hand,

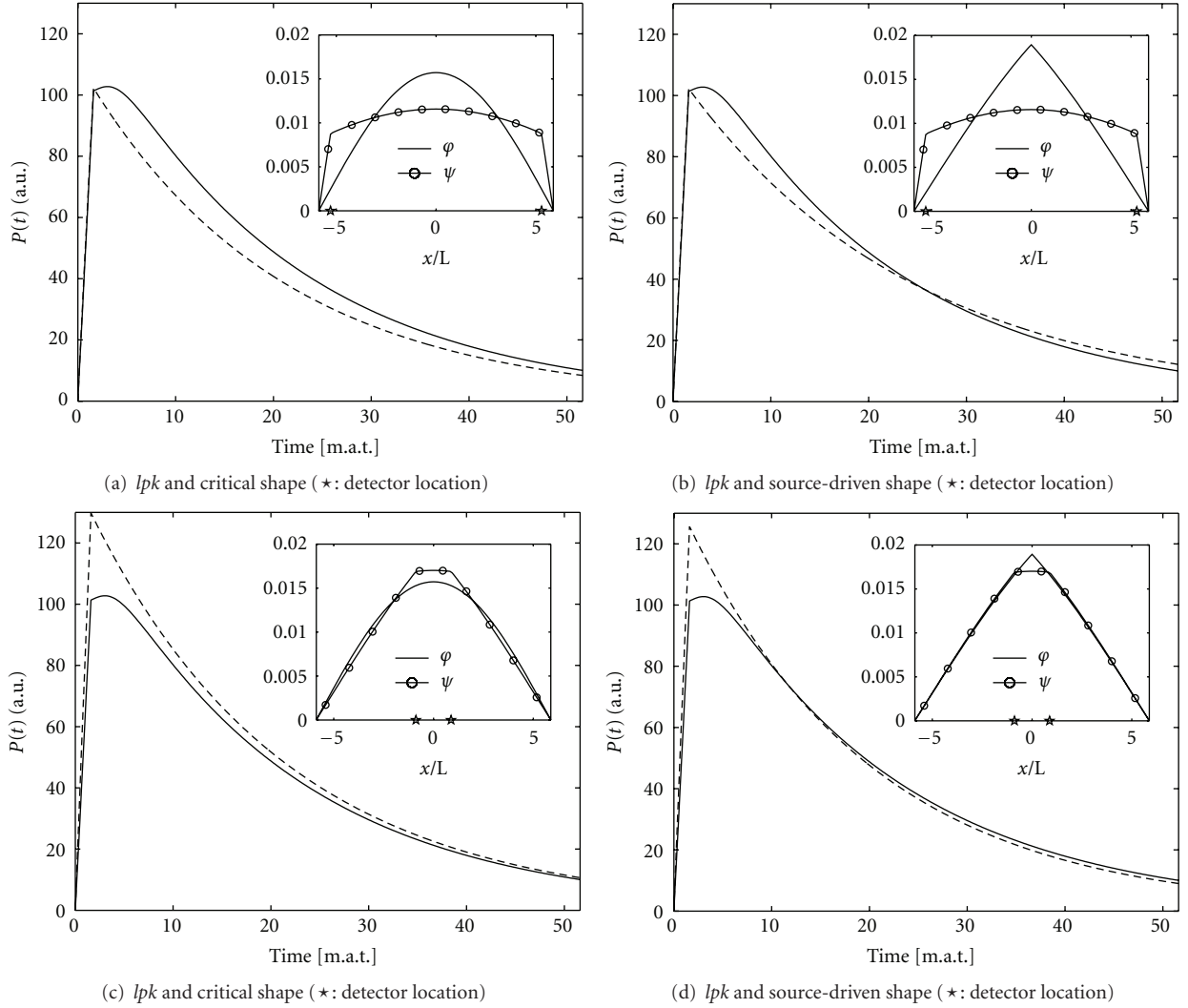


FIGURE 2: Power evolution following a source pulse in a subcritical system ($k_{\text{eff}} = 0.95$), simulated with a *lpk* approach, considering two different detector locations: first row, detector far from the source ($x_0 = 5.3L$); second row: detector close to the source ($x_0 = 0.9L$). Solid line: reference; dashed line: point kinetics. The inset graphs represent the shape φ and the weight ψ adopted.

the results obtained with the local point kinetics, presented in Figures 2 and 4, show larger discrepancies and are not suitable for the correct description of global quantities, such as the system power. It is thus interesting to compare the quality of the various point kinetic results in describing the response in the detector positions, close to the source as well as further away ($0.9L$ and $5.3L$). The results concerning the prediction of local fluxes are presented in Figures 5 and 6. To simplify the analysis of the results, the shape is adopted as the source-driven neutron distribution within the system, and the attention is focused on the type of point kinetic model that can be constructed by adopting different choices for the weight. In Figure 7, the graphs of the functions adopted as weights for this analysis are presented.

One can immediately notice how the quality of the point kinetic results is deteriorating when the source is far from the detector. On passing, it is worth also noticing that *lpk* model results are characterized by a better performance, especially

in the preservation of the areas, thus *lpk* looks more suitable if the area-ratio method [4] is to be used. In Table 1, the accuracy of the forecast of the areas below the pulse for different models with respect to the exact result is presented, showing how better results can be obtained by the *lpk* model. On the other hand, if the detector is very close to the source (see the left graphs of Figures 5 and 6), neutrons can reach the detector at the very early stage of the transient and, therefore, the contribution of higher-order harmonics can be relevant.

4. Time Modelization of the Effective Source

In the derivation of the lumped-parameter (point) model through a projection procedure, only an integration over phase space is performed, thus leaving the time behaviour of the source unchanged. Therefore, no propagation effects associated to the finite velocity of neutrons can be accounted for. Of course the signal from localized detectors is affected

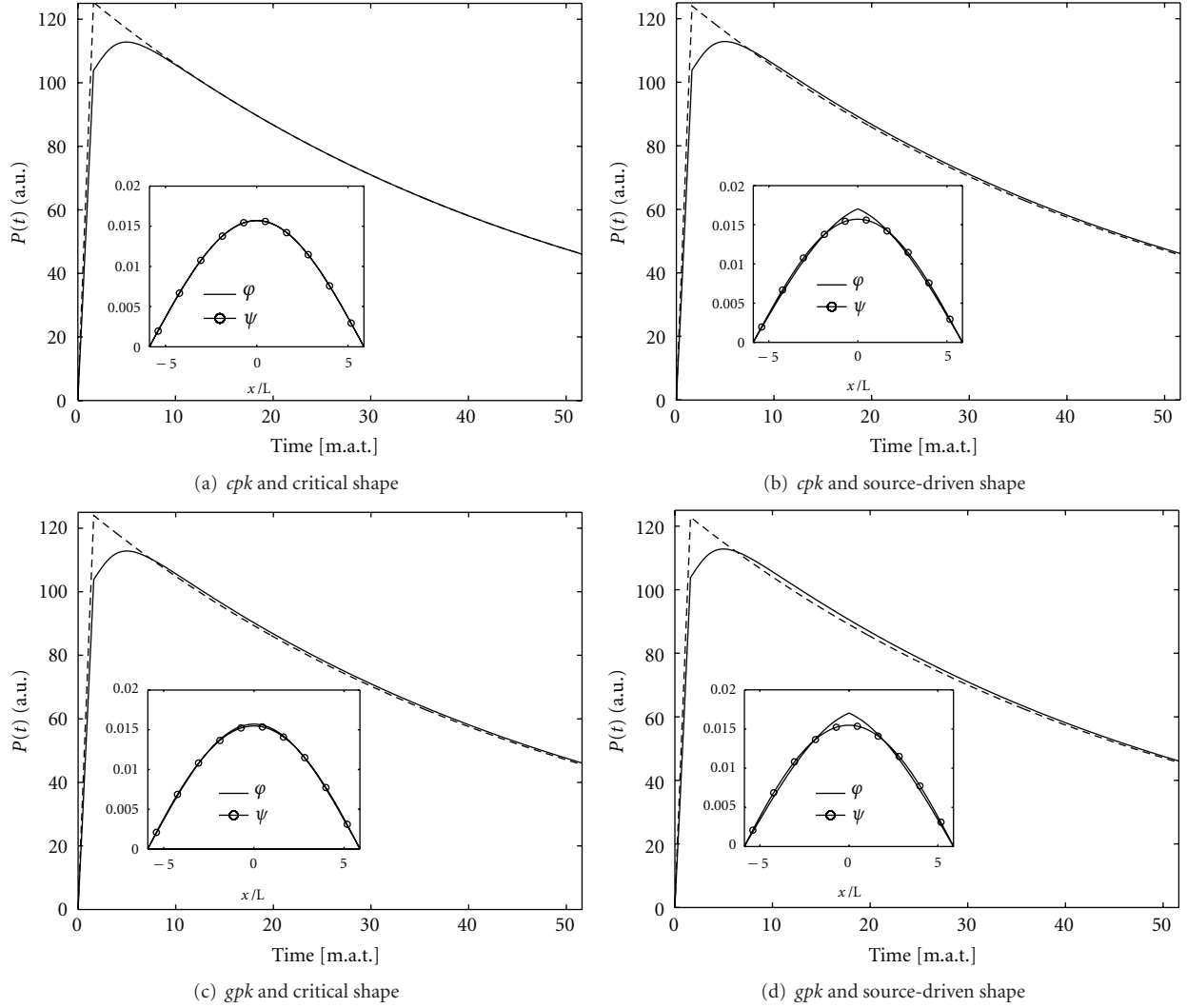


FIGURE 3: Power evolution following a source pulse in a subcritical system ($k_{\text{eff}} = 0.98$), simulated with different approaches to point kinetics: *cpk* and *gpk*. Solid line: reference; dashed line: point kinetics. The inset graphs represent the shape φ and the weight ψ adopted.

TABLE 1: Percentage relative error on the integral of the flux in the detector positions, as obtained by the different point kinetic models with respect to the reference solution. In bold the “best” results are evidenced.

PK model	$k_{\text{eff}} = 0.95$		$k_{\text{eff}} = 0.98$		
	$x_0 = 0.9L$	$x_0 = 5.3L$	$x_0 = 0.9L$	$x_0 = 5.3L$	
Source-driven shape	<i>lpk</i>	0.66	-2.29	0.12	0.29
	<i>gpk</i>	-0.92	1.22	-1.83	3.90
	<i>cpk</i>	-0.44	1.71	-1.27	4.49
Critical shape	<i>lpk</i>	0.17	1.71	-1.01	4.49
	<i>gpk</i>	-7.83	18.80	-4.48	11.25
	<i>cpk</i>	-5.56	21.72	-3.50	12.40

by the distance of the detector with respect to the source and the effect is of particular relevance when a highly localized source is considered. In these cases, one may study the

possibility to introduce in the effective source of the point model a suitable time delay.

Different options are considered to modify the time behaviour of the source in order to account for the time delay from the source to the detector. The delay may be assumed to be equal to the traveling time between the source and the detector or to an average displacement time on a suitable distribution, to be specified. A possible alternative is also the generation of the time behaviour by a convolution of the external source with the system response Green function. This idea is analogous to the practice of using the first-collision distribution for studying the response to a highly localized pulsed source in transport problems.

The procedure to modify the source behaviour to account for the finite time propagation of the neutron signal seems somewhat arbitrary. Its motivation is just to try to capture the physical phenomenon connected to the propagation of the neutrons from the source to the detector, and, as such, it is problem dependent. The introduction into the point

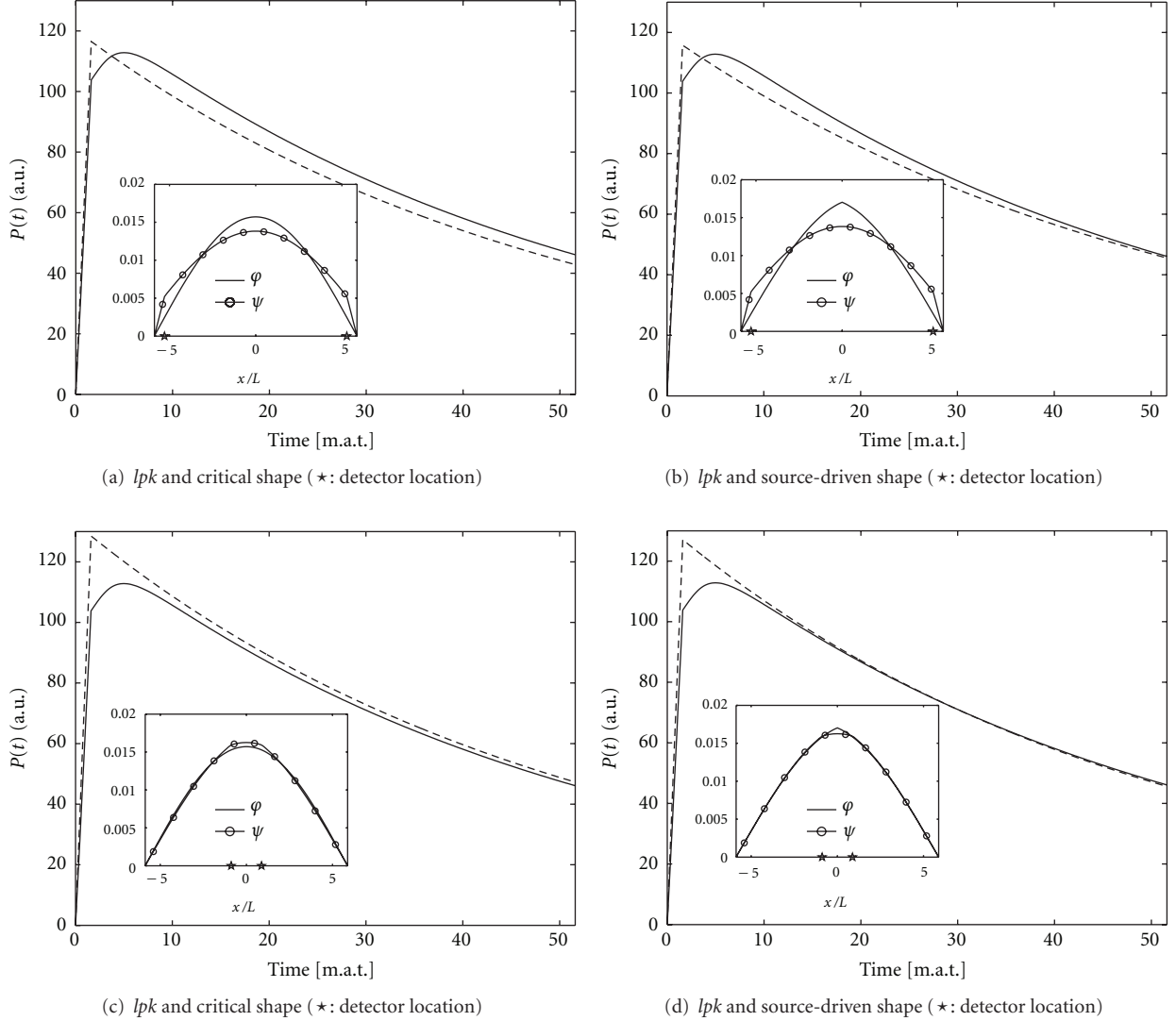


FIGURE 4: Power evolution following a source pulse in a subcritical system ($k_{\text{eff}} = 0.98$), simulated with a *lpk* approach, considering two different detector locations: first row, detector far from the source ($x_0 = 5.3L$); second row: detector close to the source ($x_0 = 0.9L$). Solid line: reference; dashed line: point kinetics. The inset graphs represent the shape φ and the weight ψ adopted.

model is mathematically unjustified and an attempt to make it more consistent is certainly required, which lies in future developments and extensions of the present work.

The possible options are summarized in the following. For the standard point model, the effective source is assumed to be defined through the projection operation of the reference balance model. Therefore, its time dependency is given by

$$S(t) = \frac{\langle \psi | S \rangle}{\langle \psi | \varphi \rangle}. \quad (5)$$

The time behaviour of the effective source may be modified when describing a detector at distance x_0 from the source by delaying the signal of the transit time for the neutrons between the source and the detector, that is, $\tau = x_0/v$ (modification 1). Of course, this amounts to assuming an irrelevant

contribution from the emitted neutrons from collisions taking place along the path from the source to the detector. In this case, the modified effective source \tilde{S} is defined by the following formula:

$$\tilde{S}(t) = S(t)u(t - \tau), \quad (6)$$

where u is the unitary Heaviside step function.

A further option involves the introduction of a delay time τ given by the average displacement time according to a given distribution, as

$$\tau = \int dt' f(x_0, t')t' \quad (7)$$

(modification 2). Alternatively, the source can be constructed as a convolution of the physical source on the proper Green

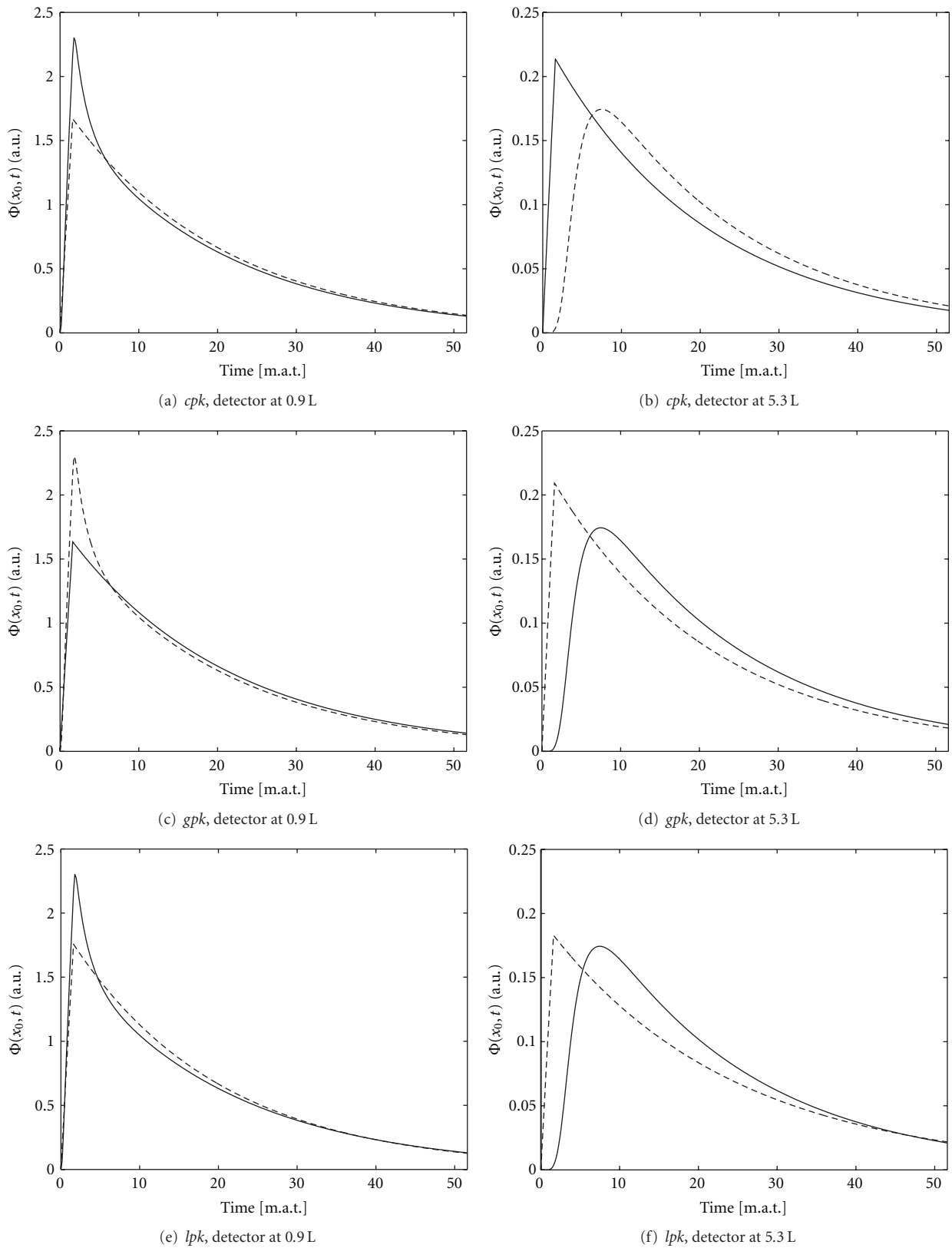


FIGURE 5: Evolution of the local flux following a source pulse in a subcritical system ($k_{\text{eff}} = 0.95$) for two detectors, at $x_0 = 0.9L$ (a, c, and e) and at $x_0 = 5.3L$ (b, d, and f), adopting different formulations of the point kinetic model. Solid line: reference; dashed line: point kinetics.

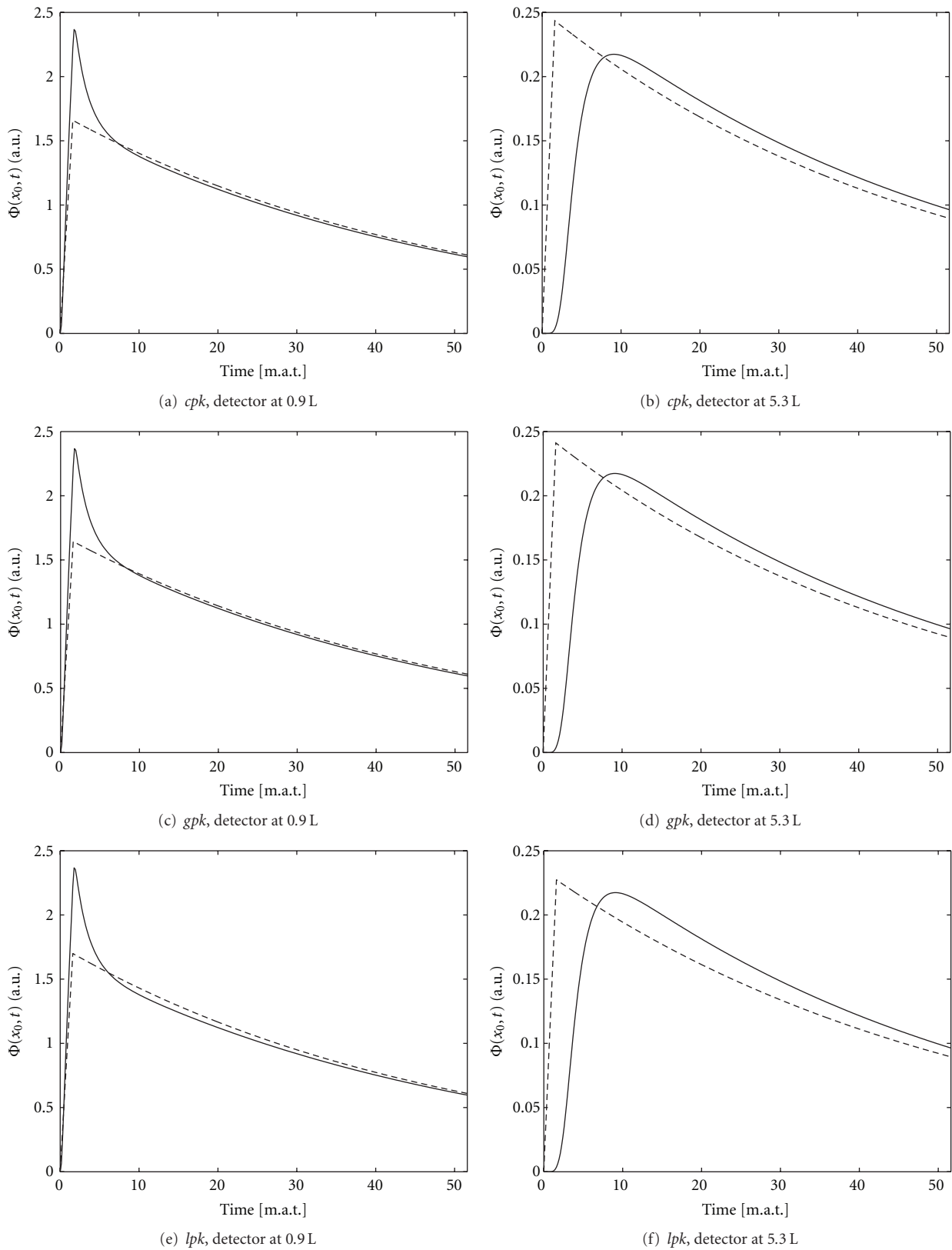


FIGURE 6: Evolution of the local flux following a source pulse in a subcritical system ($k_{\text{eff}} = 0.98$) for two detectors, at $x_0 = 0.9L$ (a, c, and e) and at $x_0 = 5.3L$ (b, d, and f), adopting different formulations of the point kinetic model. Solid line: reference; dashed line: point kinetics.

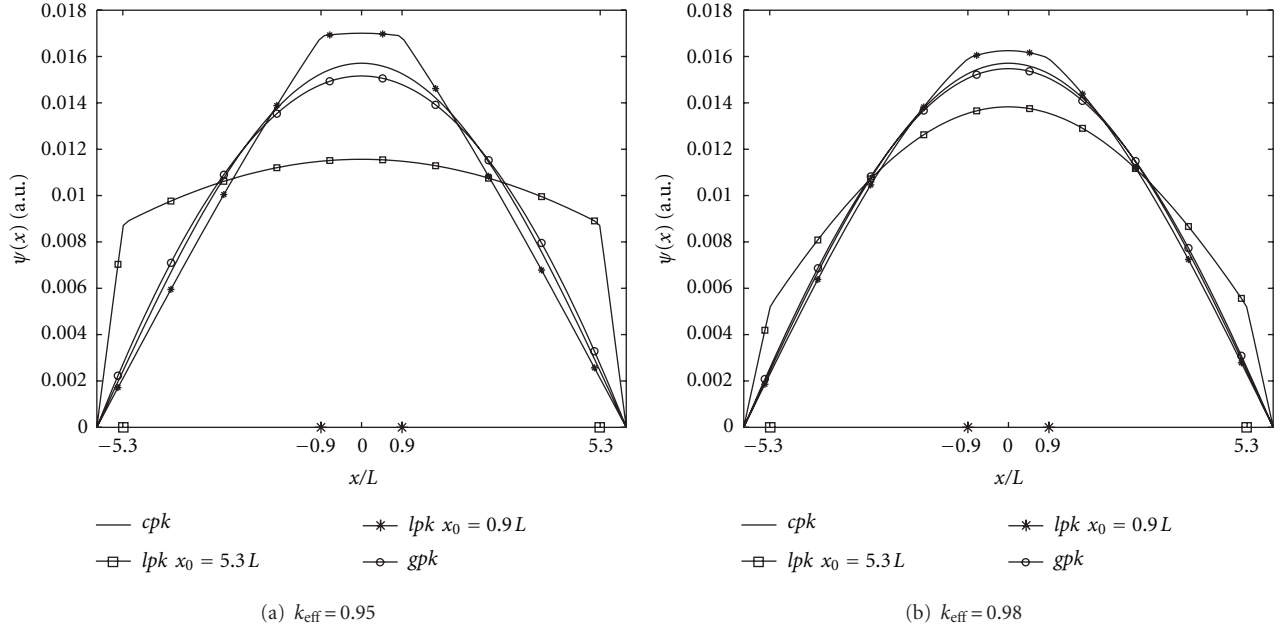


FIGURE 7: Weights adopted for the generation of the point kinetic models for the prediction of the local fluxes.

TABLE 2: Performance of *gpk* and *lpk* for the prediction of the system power during a transient induced by localized perturbations. Values of ΔP are computed as relative percentage errors with respect to the corresponding reference values at two different time instants along the transient ($t_1 = 1$ ms and $t_2 = 10$ ms).

	T1		T2		T3		
	t_1	t_2	t_1	t_2	t_1	t_2	
Exact	1.25	1.38	1.42	1.76	1.15	1.23	
Δgpk [%]	-1.68	-2.61	-2.35	-4.08	-0.44	-1.32	
Δlpk [%]	d_{11}	3.86	6.67	0.18	0.62	0.81	0.48
	d_{12}	0.27	0.28	2.42	4.95	0.44	-0.17
	d_{13}	-0.92	-0.35	-0.47	1.88	3.33	5.40
	d_{21}	0.54	0.41	-1.05	-2.77	0.17	-0.76
	d_{22}	-0.51	-1.19	0.09	-0.32	0.01	-0.93
	d_{23}	-1.55	-1.49	-1.74	-0.96	0.89	1.35
	d_{31}	-2.23	-5.85	-4.34	-12.09	-1.33	-4.06
	d_{32}	-1.42	-2.93	-1.76	-4.47	-0.57	-1.95
	d_{33}	-2.42	-2.72	-3.38	-3.83	-0.53	-0.73
	d_{41}	3.21	5.67	0.49	1.52	0.95	0.78
	d_{42}	0.80	1.28	2.11	4.54	0.59	0.12
	d_{43}	-0.64	0.73	-0.24	3.73	0.95	1.87

function of the problem (modification 3). This option amounts to the following choice:

$$\tilde{S}(t) = \int dt' S(t') G(x_0, t - t'). \quad (8)$$

Definition (8) provides a better physical description of the migration process of the particles. In Figure 8, time behaviors of the source adopted for the calculations are compared, considering the position of the two detectors as in the previous evaluations. Both the system characteristics and the duration of the source pulse are the same as in all other

calculations. The average displacement time is obtained using as a weighting distribution the Green function itself, after a proper renormalization in order to obtain a probability density function. The relevant modification in the time behavior of the source when a convolution with the Green function is adopted is evident. Figure 9 illustrates the reproduction of the response to a pulse with the above source assumptions for the two detectors (locations at 5.3 L and 0.9 L from the source). Good results can be obtained using the third modification for a signal far from the source and also a good simulation of the decaying portion of the

TABLE 3: Performance of gpk and lpk for the prediction of the flux in detectors located at x_α (see positions in Figure 10(b)) during a transient induced by localized perturbations. Values of $\Delta\varphi$ are computed as relative percentage errors with respect to the corresponding reference values at two different time instants along the transient ($t_1 = 1$ ms and $t_2 = 10$ ms).

		T1		T2		T3	
		t_1	t_2	t_1	t_2	t_1	t_2
$\frac{\varphi_1(x_1, t)}{\varphi_1(x_1, t = 0)}$	Exact	1.34	1.49	1.47	1.82	1.17	1.26
	Δgpk [%]	-8.88	-9.69	-5.56	-7.13	-2.20	-3.02
	Δlpk [%]	-3.75	-1.08	-3.11	-2.58	-0.97	-1.25
$\frac{\varphi_2(x_1, t)}{\varphi_2(x_1, t = 0)}$	exact	1.28	1.42	1.51	1.87	1.17	1.25
	Δgpk [%]	-4.30	-5.07	-8.16	-9.59	-1.63	-2.41
	Δlpk [%]	-2.40	-2.25	-3.68	-1.07	-0.76	-1.28
$\frac{\varphi_3(x_1, t)}{\varphi_3(x_1, t = 0)}$	exact	1.26	1.41	1.47	1.83	1.22	1.31
	Δgpk [%]	-3.14	-4.55	-5.39	-7.89	-5.97	-7.15
	Δlpk [%]	-2.39	-2.34	-3.57	-2.17	-2.40	-0.83
$\frac{\varphi_1(x_2, t)}{\varphi_1(x_2, t = 0)}$	exact	1.28	1.42	1.44	1.78	1.16	1.24
	Δgpk [%]	-4.53	-5.16	-3.72	-4.97	-1.18	-1.86
	Δlpk [%]	-2.37	-2.22	-2.44	-3.67	-0.57	-1.30
$\frac{\varphi_2(x_2, t)}{\varphi_2(x_2, t = 0)}$	exact	1.26	1.40	1.47	1.81	1.16	1.24
	Δgpk [%]	-3.16	-3.85	-5.25	-6.56	-0.98	-1.69
	Δlpk [%]	-2.01	-2.44	-2.89	-2.90	-0.53	-1.30
$\frac{\varphi_3(x_2, t)}{\varphi_3(x_2, t = 0)}$	exact	1.25	1.40	1.44	1.80	1.18	1.27
	Δgpk [%]	-2.19	-3.59	-3.68	-6.17	-2.63	-3.81
	Δlpk [%]	-2.06	-2.48	-3.07	-3.11	-1.32	-1.21
$\frac{\varphi_1(x_3, t)}{\varphi_1(x_3, t = 0)}$	exact	1.22	1.34	1.37	1.65	1.13	1.20
	Δgpk [%]	0.01	0.46	1.75	2.41	1.38	1.48
	Δlpk [%]	-0.55	-2.88	-0.33	-6.13	0.47	-1.34
$\frac{\varphi_2(x_3, t)}{\varphi_2(x_3, t = 0)}$	exact	1.25	1.38	1.43	1.76	1.15	1.23
	Δgpk [%]	-1.76	-2.31	-2.71	-3.80	-0.087	-0.69
	Δlpk [%]	-1.51	-2.63	-2.13	-4.18	-0.21	-1.32
$\frac{\varphi_3(x_3, t)}{\varphi_3(x_3, t = 0)}$	exact	1.24	1.38	1.41	1.76	1.16	1.24
	Δgpk [%]	-0.96	-2.50	-1.49	-4.26	-0.60	-1.89
	Δlpk [%]	-1.71	-2.62	-2.53	-4.01	-0.68	-1.31
$\frac{\varphi_1(x_4, t)}{\varphi_1(x_4, t = 0)}$	exact	1.33	1.48	1.48	1.83	1.18	1.26
	Δgpk [%]	-8.17	-9.03	-6.01	-7.67	-2.43	-3.30
	Δlpk [%]	-3.61	-1.30	-3.28	-2.28	-1.06	-1.23
$\frac{\varphi_2(x_4, t)}{\varphi_2(x_4, t = 0)}$	exact	1.29	1.43	1.51	1.86	1.17	1.25
	Δgpk [%]	-5.06	-5.87	-7.87	-9.37	-1.88	-2.69
	Δlpk [%]	-2.66	-2.10	-3.66	-1.22	-0.86	-1.26
$\frac{\varphi_3(x_4, t)}{\varphi_3(x_4, t = 0)}$	exact	1.27	1.42	1.48	1.86	1.18	1.27
	Δgpk [%]	-3.74	-5.43	-5.98	-8.94	-2.85	-4.27
	Δlpk [%]	-2.72	-2.19	-3.95	-1.52	-1.49	-1.17

curve is reached, which is needed for the application of several interpretation procedures. On the other hand, a little improvement can be obtained when the detector is very close to the source. In this case, it is important also to recall that the presence of high transport effects dominated by the uncollided fraction of the source neutrons makes the lumped-parameter and the whole source-delay formalism inapplicable.

5. Use of Local Point Kinetics for Transient Simulation

The potentialities of improvement adopting a point kinetic model with a problem-tailored weighting are now tested for the simulation of transients in a subcritical system. Results are compared with those produced using a standard global weighting, that is, assuming as adjoint source the fission

TABLE 4: Percentage relative error on the flux at position x_1 and time $t = 10$ ms during transient T1 with different localizations of the adjoint source for the definition of the lpk model adopted. In bold, the result obtained when the adjoint source is located where the detector is (spatially and energetically).

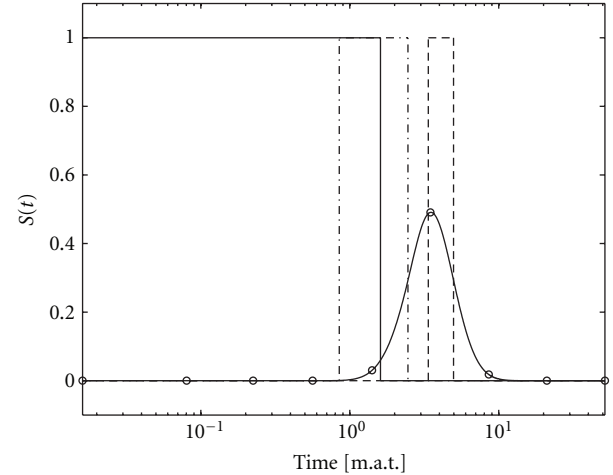
S^\dagger	$\Delta\phi_1$	$\Delta\phi_2$	$\Delta\phi_3$
d_{11}	-1.10	4.00	4.54
d_{12}	-7.00	-2.25	-1.72
d_{13}	-7.59	-2.87	-2.34
d_{21}	-6.89	-2.12	-1.59
d_{22}	-8.37	-3.68	-3.16
d_{23}	-8.65	-3.98	-3.46

productivity $\nu\Sigma_f(gpk)$. Spectral effects can also be important; hence results of a three-group calculation are now presented. The evolution is induced in a fast reflected one-dimensional slab structure (see Figure 10), with material characteristics as for the system studied in [7], by a local perturbation of the absorption cross section in each one of the corresponding energy group inside the core to investigate also spectral effects. The location of the perturbed region is specified in Figure 10(a).

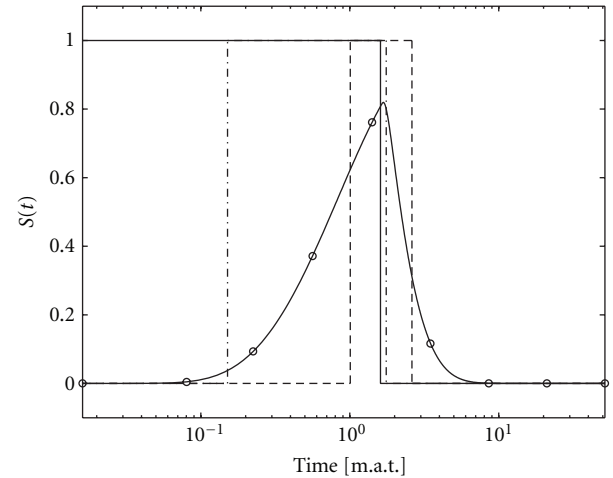
The features of the different point kinetic models can be clearly seen by observing Tables 2 and 3, where the differences between power level and local fluxes obtained with the use of gpk and lpk at two different time instants ($t_1 = 1$ ms and $t_2 = 10$ ms) during the transients are reported. All results are obtained by comparison with a reference produced by a full space-time solution. The system starts from an initial multiplication constant $k_{\text{eff}} = 0.975$, and three transients are considered (Tj, $j = 1, 2, 3$), where the index j indicates in which energy group the cross section perturbation is introduced. The reactivity insertions associated to each transient are 811 pcm, 1263 pcm, and 552 pcm, respectively. The detector $d_{\alpha g}$ is localized at position x_α and detects neutrons belonging to energy group g . The detectors are localized in the center of the perturbed region ($x_1 = 60.9$ cm), outside the perturbation within the fissile region ($x_2 = 71.5$ cm), in the lead zone close to the source ($x_3 = 82.1$ cm), and in the reflector ($x_4 = 41.9$ cm), see Figure 10(b).

Point kinetic models based on a global weighting always underestimate the power signal, as shown in Table 2. The performances of point models with a detector-based adjoint source, when adopted for the power prediction, provide results with different ranges of error, thus not evidencing a clear pattern. It is thus of interest to compare the performance of such models in the reproduction of the local flux signals, summarized in Table 3. It can be observed how lpk is usually providing a smaller error with respect to gpk when the adjoint source is located in the position where the flux is observed, since it can capture the physical information most effectively.

It is also of interest to see how the performance can be affected by a less proper choice of the detector. In Table 4, the attention is focused on the flux in the detector 1 (within the



(a) $x_0 = 5.3$ L



(b) $x_0 = 0.9$ L

FIGURE 8: Time behavior of the sources according to the modifications proposed. Solid: original case; dash-dotted: modification 1; dashed: modification 2; circles: modification 3.

perturbed region) and is simulated with different lpk models, placing the adjoint source in the perturbed region and in the correct energy range (first group), and then moving it to different spatial and spectral locations. The degradation of the quality of the results when the adjoint source moves further from the position of observation is quite evident.

At last, an evaluation of the reactivity term from lpk and gpk , compared to the subcriticality level in the system, is performed. The same configuration in three-group diffusion as in the previous calculations is considered, imposing different levels of subcriticality in order to test the performances for configurations close and far from criticality. In Table 5, the

TABLE 5: Error in pcm on the subcriticality level as obtained by the different point kinetic models adopted in the one-dimensional domain sketched in Figure 10. The direct shape is assumed to be the subcritical source-driven distribution.

Δgpk [pcm]		Δlpk [pcm]					
		d_{11}	d_{12}	d_{13}	d_{21}	d_{22}	d_{23}
$\rho_0 = -7526.9$	12.9	337.0	213.1	111.1	-262.4	-47.7	-55.2
		d_{31}	d_{32}	d_{33}	d_{41}	d_{42}	d_{43}
		-3742.5	-473.7	-202.7	462.9	304.7	244.3
$\rho_0 = -2564.1$	1.6	d_{11}	d_{12}	d_{13}	d_{21}	d_{22}	d_{23}
		d_{31}	d_{32}	d_{33}	d_{41}	d_{42}	d_{43}
		42.4	26.6	13.9	-32.8	-6.3	-7.0
		-458.0	-58.8	-25.2	58.4	38.3	30.7
$\rho_0 = -1010.1$	0.3	d_{11}	d_{12}	d_{13}	d_{21}	d_{22}	d_{23}
		d_{31}	d_{32}	d_{33}	d_{41}	d_{42}	d_{43}
		6.8	4.2	2.2	-5.2	-1.0	-1.1
		-72.3	-9.3	-4.0	9.3	6.1	4.9

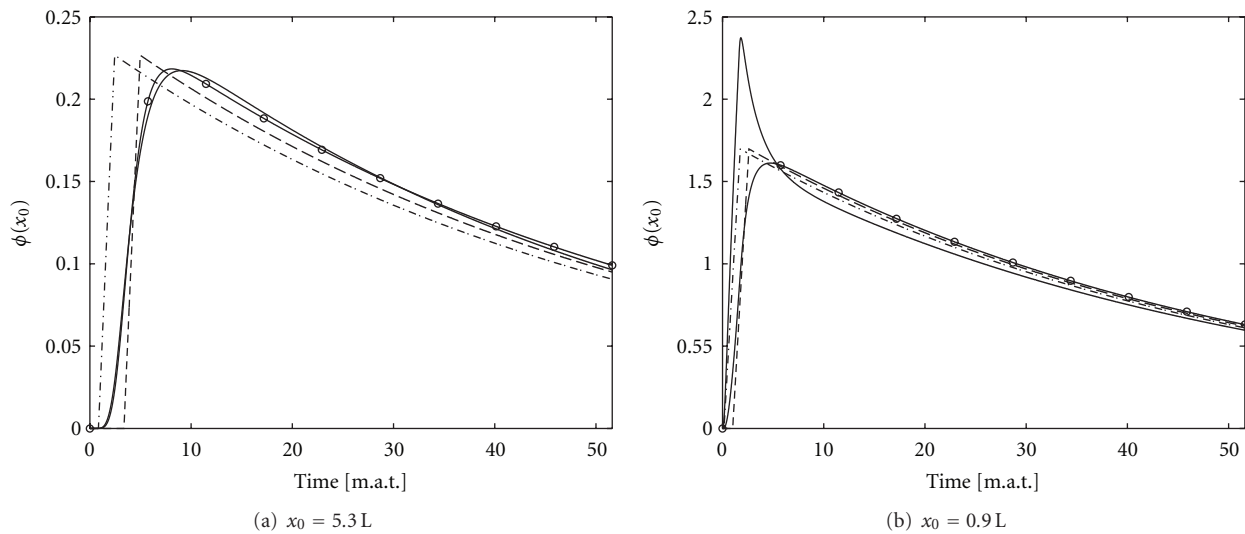


FIGURE 9: Local flux response to a source pulse obtained with point kinetics in association with a modified treatment of the source time behavior. Solid: reference; dash-dotted: modification 1; dashed: modification 2; circles: modification 3.

errors on ρ_0 in pcm (10^{-5}) are reported. As expected, systems closer to criticality are associated to smaller discrepancies, and the adoption of a global weighting for the prediction of the subcriticality level appears to be more effective. The performances of local detectors again show different trends. However, it can be noticed that, when the energy localization of the detector corresponds to the thermal group, a better quality in the results can be achieved. This is due to the larger amount of information associated to neutrons that, after being emitted by fission or by the external source at high energy, are slowed down within the system and have a “better knowledge” of the subcritical configuration. A similar reasoning explains why the results produced by the detector closer to the source (detector 3) are of lower quality: this position detects primarily neutrons directly from the source, with little information of the subcritical assembly.

6. Concluding Remarks

Point models that satisfactorily represent the kinetic behavior of the local flux evolution in a subcritical system can be developed using different neutron shapes and, as weighting function for the projection, the adjoint solution of a source-driven problem where the local detector is used as a source. A better physical representation of the source can be attained by introducing suitable delay functions in the effective source term.

The limits and shortcomings of possible kinetic models are discussed, illustrating results for some simple but physically representative configurations, in the effort to evidence specific sources of errors and the space for improvements. It is shown that the choice of a local detector-tailored weighting is the most appropriate for experimental flux measurement interpretation.

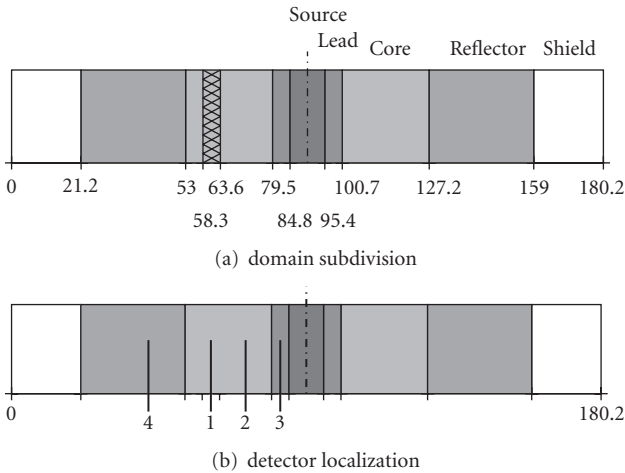


FIGURE 10: System domain adopted for the three-group calculations. The localization of the region where the cross section perturbations are introduced is highlighted (a), as well as the position of the four detectors (b).

Another important issue that is discussed concerns the proper treatment of the source term in the kinetic model, with special regards to its time behaviour. It is shown that the introduction of a suitable delay is necessary to adequately reproduce the system response.

In conclusion, the point model performs satisfactorily if local kinetic parameters are generated and if the source is properly delayed to account for propagation times inside the finite medium. In future works, the analysis of the point model presented in this work will be extended to more effective approaches, such as multipoint, with the objective to yield more accurate computational tools for kinetic experiment evaluations.

References

[1] R. Soule, W. Assal, P. Chaussonnet et al., “Neutronic studies in support of accelerator-driven systems: the MUSE experiments in the MASURCA facility,” *Nuclear Science and Engineering*, vol. 148, no. 1, pp. 124–152, 2004.

[2] C. M. Persson, A. Fokau, I. Serafimovich et al., “Pulsed neutron source measurements in the subcritical ADS experiment YALINA-Booster,” *Annals of Nuclear Energy*, vol. 35, no. 12, pp. 2357–2364, 2008.

[3] N. G. Sjöstrand, “Measurements on a subcritical reactor with a pulsed neutron source,” in *Proceedings of the International Conference on the Peaceful Uses of Atomic Energy*, vol. 5, United Nations, New York, NY, USA, 1956.

[4] N. G. Sjöstrand, “Measurements on a subcritical reactor using a pulsed neutron source,” *Archiv fr Physik*, vol. 11, pp. 233–246, 1956.

[5] I. Pázsit and C. Demazière, “Noise techniques in nuclear systems,” in *Handbook of Nuclear Engineering*, D. G. Cacuci, Ed., vol. 2, pp. 1631–1734, Springer, New York, NY, USA, 2010.

[6] P. Ravetto, M. M. Rostagno, and P. Vinai, “Inverse problem for the determination of the reactivity in pulsed experiments for subcritical systems,” *Transactions of the American Nuclear Society*, vol. 86, pp. 426–428, 2002.

[7] M. Carta, A. D’Angelo, V. Peluso et al., “Reactivity assessment and spatial time-effects from the MUSE kinetics experiments,” in *Proceedings of the International Conference: The Physics of Fuel Cycles and Advanced Nuclear Systems—Global Developments (PHYSOR ’04)*, pp. 657–669, Chicago, Ill, USA, April 2004.

[8] M. Becker, “A generalized formulation of point nuclear reactor kinetics equations,” *Nuclear Science and Engineering*, vol. 31, pp. 458–464, 1968.

[9] S. Dulla, P. Ravetto, M. M. Rostagno, G. Bianchini, M. Carta, and A. D’Angelo, “Some features of spatial neutron kinetics for multiplying systems,” *Nuclear Science and Engineering*, vol. 149, no. 1, pp. 88–100, 2005.

[10] S. Dulla, F. Cadinu, and P. Ravetto, “Neutron importance in source-driven systems,” in *Proceedings of the International Topical Meeting on Mathematics and Computation (M&C ’05)*, Avignon, France, 2005.

[11] S. Dulla, M. M. Rostagno, and P. Ravetto, “Models for the interpretation of local flux measurements in subcritical systems,” *Transactions of the American Nuclear Society*, vol. 93, pp. 568–570, 2005.

[12] A. F. Henry, *Nuclear-Reactor Analysis*, MIT Press, Cambridge, Mass, USA, 1975.

[13] L. N. Ussachoff, “Equations for importance of neutrons, reactor kinetics and perturbation theory,” in *Proceedings of the International Conference on the Peaceful Uses of Atomic Energy*, vol. 5, pp. 503–570, Geneva, Switzerland, 1955.

Research Article

Study of an ADS Loaded with Thorium and Reprocessed Fuel

Graiciany de Paula Barros,^{1,2} Claubia Pereira,^{1,2}
Maria A. F. Veloso,^{1,2} and Antonella L. Costa^{1,2}

¹Departamento de Engenharia Nuclear (DEN), Universidade Federal de Minas Gerais (UFMG),
Avenida Antonio Carlos 6627 Campus Pampulha, 31270-901 Belo Horizonte, MG, Brazil

²Instituto Nacional de Ciências e Tecnologia de Reatores Nucleares Inovadores/CNPq Rede Nacional de Fusão/FINER, Brazil

Correspondence should be addressed to Claubia Pereira, claubia@nuclear.ufmg.br

Received 15 November 2011; Revised 13 February 2012; Accepted 14 February 2012

Academic Editor: Alberto Talamo

Copyright © 2012 Graiciany de Paula Barros et al. This is an open access article distributed under the Creative Commons Attribution License, which permits unrestricted use, distribution, and reproduction in any medium, provided the original work is properly cited.

Accelerator-driven systems (ADSs) are investigated for long-lived fission product transmutation and fuel regeneration. The aim of this paper is to investigate the nuclear fuel evolution and the neutronic parameters of a lead-cooled accelerator-driven system used for fuel breeding. The fuel used in some fuel rods was $^{232}\text{ThO}_2$ for ^{233}U production. In the other fuel rods was used a mixture based upon Pu-MA, removed from PWR-spent fuel, reprocessed by GANEX, and finally spiked with thorium or depleted uranium. The use of reprocessed fuel ensured the use of $^{232}\text{ThO}_2$ without the initial requirement of ^{233}U enrichment. In this paper was used the Monte Carlo code MCNPX 2.6.0 that presents the depletion/burnup capability, combining an ADS source and kcode-mode (for criticality calculations). The multiplication factor (k_{eff}) evolution, the neutron energy spectra in the core at BOL, and the nuclear fuel evolution during the burnup were evaluated. The results indicated that the combined use of $^{232}\text{ThO}_2$ and reprocessed fuel allowed ^{233}U production without the initial requirement of ^{233}U enrichment.

1. Introduction

In recent years great interest has been given to accelerator-driven systems (ADSs). This is mainly because of their inherent safety features, their waste transmutation potential, and their capability to breed the required ^{233}U when the thorium fuel is used. ADSs are useful for recycling of americium, curium, neptunium, and plutonium. A great number of works on the ADS and the relative neutronics have been reported in the scientific literature [1–7]. Pioneers in this revival have been Furukawa et al. [8], Bowman et al. [9, 10], and Rubbia et al. [11, 12]. Very similar idea was first presented almost 60 years ago [13]. In an accelerator-driven system, an accelerator is coupled to a subcritical core loaded with nuclear fuel. The particles accelerated are injected into a spallation target that produces neutrons, which are used in the subcritical core for the fission chain maintenance.

Both critical reactors and subcritical accelerator-driven systems are potential candidates as dedicated transmutation systems. Critical reactors, however, loaded with fuel containing large amounts of MA have safety problems caused by

unfavorable reactivity coefficients and small delayed neutron fraction. Nevertheless, subcritical systems present criticality and safety advantages: they operate with a neutron source rate that can be increased to compensate for the negative reactivity or any variation during the operation. Therefore, research interest in spent nuclear fuel transmutation has focused on both accelerator-driven systems and fusion-driven systems. At DEN/UFMG we began about 2006 and some results were obtained [14–16]. In this work, the focuses are ^{233}U production and transuranic transmutation possibility in accelerator-driven systems.

The main characteristic of ADS (i.e., subcriticality) is particularly favorable and allows a maximum transmutation rate while operating in a safe manner. An advantage of accelerator-driven systems is that, since there is no criticality condition to satisfy, almost any fuel composition can be used in the system [17]. Moreover, ADS could transmute 99.9% of transuranics light-water-reactor- (LWR-) spent nuclear fuel [18].

Another fuel proposed for using in ADS is the thorium-based fuel. There are many reasons for the resurgence of

interest in the thorium fuel cycle nowadays. The thorium's abundance is about three times more than uranium abundance. Thorium-fueled reactor is also an attractive tool to produce long-term nuclear energy with low radiotoxicity waste [19]. The main issue verified in the usage of this fuel in subcritical systems is the need of initial enrichment (^{233}U), since the use of natural thorium (^{232}Th) is not feasible due to the very low values of achieved criticality.

Based on those questions, this work presents a preliminary study of ADS for simultaneous use of thorium fuel and reprocessed fuel. The simultaneous usage of thorium fuel and spent fuel allows one to get appropriate values of criticality without the need of enrichment of thorium and still can reduce radiotoxicity of spent fuel by transmutation. The proposal is the simulation of a core with some fuel elements of ^{232}Th and other elements based on fuel spent from LWRs. There was simulated a cylindrical core of 12.0 m^3 filled with a hexagonal lattice formed by 156 fuel rods, the fuel used in 36 rods was $^{232}\text{ThO}_2$, and the fuel used in the other 120 rods was reprocessed fuel spiked with thorium or depleted uranium. The reprocessed fuel was obtained from spent fuel discharged from the Brazilian PWR ANGRA-I, reprocessed by GANEX processes, and spiked with thorium or depleted uranium. Different percentages of ThO_2 or UO_2 were added to the reprocessed fuel and analyzed, as the use of only reprocessed fuel generates high criticality values. The neutron spectra were evaluated at BOL (Begin Of Life) and the criticality and the fuel evolution were investigated during ten years with the system operating at steady state, at 515 MW of thermal power. During this time, the ^{233}U production and the reprocessed fuel evolution were quantified.

MCNPX 2.6.0 code [20] was used to simulate the geometrical and operational characteristics of the system. For the simulation there was used a combination of spallation source (external source-SDEF) and kcode-mode for the calculation of initial k_{eff} and flux, describing in this way the real behavior of an ADS; that is, the initial criticality is the sum of neutrons produced by fission in the fuel and the neutrons produced by spallation in the target. During the burnup the code does not take into account the flux from external source, so the k_{eff} and fuel evolution results obtained are just approximations. Moreover, the k_{eff} results that were obtained during the burnup (kcode-mode) provide an insight of the necessary contribution of the external source during the operation period.

The isotopic composition of the reprocessed fuel used in this simulation was obtained using GANEX process (Group ActiNide EXtration) which is currently in testing phase [21]. The GANEX process developed by CEA for the reprocessing of Generation IV spent nuclear fuels is composed of two extraction cycles following the dissolution of the spent fuel. Once the uranium is selectively extracted from the dissolution solution by a monoamide solvent, the transuranic elements (Np, Pu, Am, and Cm) are separated from the fission products in a second cycle prior to the co-conversion step [22].

The GANEX first cycle recovers more than 99.99% of the total amount of uranium. In a second cycle neptunium, plutonium, americium, and curium are recovered altogether

in one liquid flow (actinide product) and the losses of transuranics in the different outputs and in the solvent were estimated at a value lower than 0.5% (neptunium essentially) at the end of the test, corresponding to a recovery yield of actinides higher than 99.5%. Nevertheless, the decontamination factors versus some lanthanides (especially Nd, Sm, and Eu) were much lower than expected and the mass of lanthanides in the actinide product was around 5% at the end [23].

2. Methodology

2.1. Computational Tool. The MCNPX 2.6.0 code was used to simulate the geometrical and operational characteristics of the system. Such version is quite interesting for the ADS evaluation because it describes the nuclear fuel evolution during the operation. For the calculation of the initial k_{eff} and flux there was used a combination of spallation source (external source-SDEF) and kcode-mode. The code does not take into account the flux from external source during the burnup, so the results obtained are just approximations.

The depletion/burnup capability is based on CINDER90. MCNPX depletion is a linked process involving steady-state flux calculations by MCNPX and nuclide depletion calculations by CINDER90. The code runs a steady-state calculation to determine the system eigenvalue, 63-group fluxes, energy-integrated reaction rates, fission multiplicity, and recoverable energy per fission (Q values). CINDER90 then takes those MCNPX-generated values and performs the depletion calculation to generate new number densities for the next time step. MCNPX takes these new number densities and generates another set of fluxes and reaction rates. The process repeats itself until after the final time step specified by the user [24].

2.2. System Parameters. Figures 1 and 2 show schematic views of the simulated ADS. The basic geometry includes the spallation target, a subcritical core, and the reflector. The accelerator tube has a radius of 1.5 cm, and the axial position is in the center of the target. The spallation source is represented by a neutrons source with a spectrum characteristic of spallation reactions. Such spectrum was generated, in a previous simulation, using a beam of 1-GeV protons with a parabolic spatial profile. There was used Bertini intranuclear cascade model for the transport of protons, neutrons, and charged pions. The parameters of this simulation were described in [15].

Due to its high neutron yield by spallation reactions there was used lead as spallation target. The Pb cylindrical target has 9.5 cm radius and 39 cm height. Lead was also used as coolant and as reflector. The use of lead as coolant offers many advantages like convective cooling, passive safety and small neutron absorption cross section [25].

Another advantage of the lead coolant is that it is not a neutron moderator. This is important because the protactinium effect, which limits the achievable values of k_{eff} , is less severe for harder spectra. For solid fuels, systems without moderator and based on thorium, smaller values of capture

TABLE 1: UO₂ fuel composition after 33.000 MW d/T.

Actinides		Fission Products			
Total weight fraction = 0.9785		Total weight fraction = 0.0215			
Nuclide	Weight fraction	Nuclide	Weight fraction	Nuclide	Weight fraction
²³⁴ U	1.546E-04	H	1.525E-06	Ag	2.386E-03
²³⁵ U	8.046E-03	Li	5.395E-09	Cd	3.267E-03
²³⁶ U	4.113E-03	Be	4.384E-09	In	6.975E-05
²³⁸ U	9.781E-01	C	7.707E-10	Sn	2.686E-03
²³⁷ Np	4.759E-04	Co	2.672E-17	Sb	8.428E-04
²³⁸ Pu	1.851E-04	Ni	9.566E-15	Te	1.413E-02
²³⁹ Pu	4.847E-03	Cu	8.460E-14	I	7.037E-03
²⁴⁰ Pu	1.657E-03	Zn	1.186E-09	Xe	1.527E-01
²⁴¹ Pu	1.558E-03	Ga	6.593E-10	Cs	8.153E-02
²⁴² Pu	5.888E-04	Ge	1.929E-05	Ba	4.294E-02
²⁴³ Am	1.126E-04	As	5.897E-06	La	3.566E-02
Others	1.620E-04	Se	1.635E-03	Ce	7.546E-02
	Total 1.000E+00	Br	6.294E-04	Pr	3.211E-02
	OBS.: "Others" include:	Kr	1.058E-02	Nd	1.120E-01
⁴ He	1.202E-06	Rb	9.934E-03	Pm	3.342E-03
²³⁰ Th	3.407E-09	Sr	2.512E-02	Sm	2.246E-02
²³³ U	2.069E-09	Y	1.339E-02	Eu	4.776E-03
²³⁷ U	5.860E-06	Zr	1.031E-01	Gd	2.583E-03
²³⁸ Np	7.797E-07	Nb	6.179E-04	Tb	8.146E-05
²³⁹ Np	4.923E-05	Mo	9.596E-02	Dy	4.039E-05
²⁴¹ Am	8.292E-05	Tc	2.262E-02	Ho	4.368E-06
²⁴² Am	1.526E-07	Ru	6.843E-02	Er	1.724E-06
²⁴² Cm	2.582E-05	Rh	1.275E-02	Tm	1.812E-09
²⁴⁴ Cm	2.960E-05	Pd	3.906E-02	Yb	3.676E-10
²⁴⁵ Cm	1.030E-06		Total 1.000E+00		

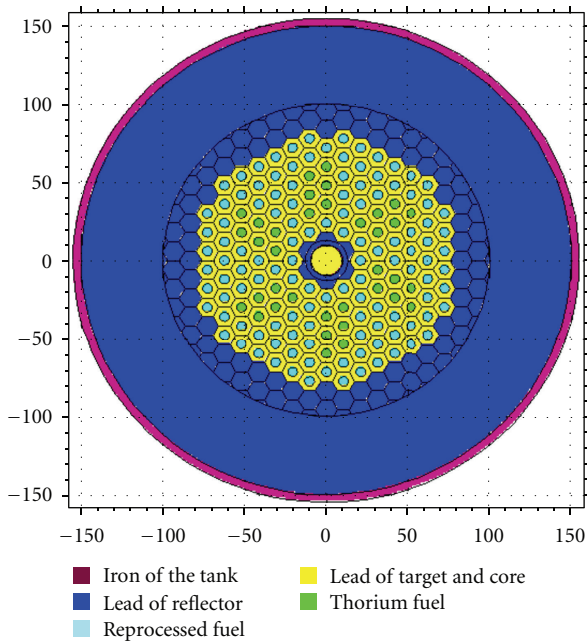


FIGURE 1: Horizontal cross section of the ADS simulated.

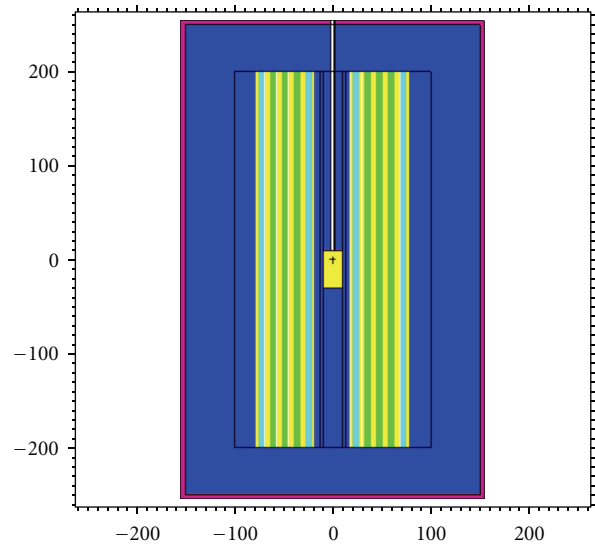


FIGURE 2: Vertical cross section of the ADS simulated.

cross sections of fission products will reduce the k_{eff} variation and produce a hardening (shift to higher energies) in the neutron energy distribution. So, the inventory of ²³³U is

TABLE 2: Fuel composition (normalized) after reprocessing.

Actinides	Weight fraction
^{234}U	$9.29E-07$
^{235}U	$4.83E-05$
^{236}U	$2.47E-05$
^{238}U	$5.88E-03$
^{237}Np	$2.72E-02$
^{238}Pu	$1.11E-02$
^{239}Pu	$2.91E-01$
^{240}Pu	$9.95E-02$
^{241}Pu	$9.36E-02$
^{242}Pu	$3.54E-02$
^{243}Am	$6.76E-03$
^{233}U	$1.20E-11$
^{237}U	$3.52E-08$
^{238}Np	$4.45E-05$
^{239}Np	$2.81E-03$
^{241}Am	$4.98E-03$
^{242}Am	$9.17E-06$
^{242}Cm	$1.55E-03$
^{244}Cm	$1.78E-03$
^{245}Cm	$6.19E-05$
Nd	$3.36E-01$
Sm	$6.75E-02$
Eu	$1.43E-02$

much larger in fast reactors (about 7 times), with the associated larger breeding times and inventory radiotoxicity [26].

The simulated core is a cylinder of 12.0 m^3 filled with a hexagonal lattice formed by 156 fuel rods. The fuel rod diameter is 6 cm, the pitch is 12 cm, and rod length is 400 cm. The fuel used in 36 rods is $^{232}\text{ThO}_2$. The fuel used in the other 120 rods is spent fuel discharged from reactor ANGRA-I, with initial enrichment of 3.1%. This fuel was burned in ORIGEN 2.1 code [27] for three cycles, with the burnup of approximately 11,000 MW d/t in each cycle, following the ANGRA-I power historic of real cycles 1, 2, and 3. The composition of the spent fuel used is shown in Table 1 [28], after remaining 5 years in a cooling pool.

After cooling by five years, the spent nuclear was submitted to GANEX reprocessing and the isotopic composition after the reprocessing is presented in Table 2. The amount of uranium after the reprocessing is 0.01% of the total amount of uranium in the burned fuel. In terms of actinides, neptunium, plutonium, americium, and curium are recovered with a loss of only 0.5% (neptunium essentially). The lanthanides contamination in the reprocessed fuel is around 5%. The isotopic composition presented in Table 2 was adjusted (with a computational program) for several percentages of thorium or depleted uranium added to the reprocessed fuel and the final composition (ThO_2 or UO_2 + reprocessed fuel) was normalized. The ratio between the number of thorium fuel rods and reprocessed fuel rods and the positions of the thorium fuel rods were determined to maximize the amount of reprocessed fuel and achieve k_{eff} values close to 1.

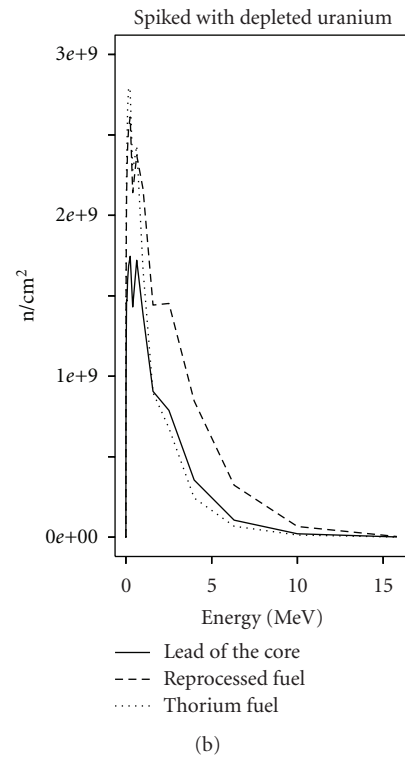
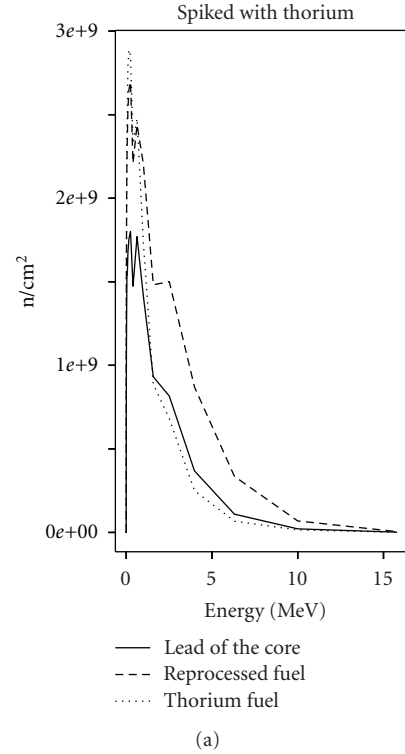


FIGURE 3: Neutron energy distributions in the (BOL).

The isotopic compositions used in the simulations with several percentages of thorium or depleted uranium added to the reprocessed fuel are shown in Tables 3 and 4.

2.3. *Computational Procedure.* For this simulation there was used a combination of ADS source (SDEF) and kcode-mode

TABLE 3: Fuel composition (normalized) for the reprocessed fuels spiked with thorium.

Actinides	Weight fraction fuel spiked with 60% of thorium	Weight fraction fuel spiked with 61% of thorium	Weight fraction fuel spiked with 62% of thorium
²³⁴ U	3.7145E-007	3.6216E-007	3.5287E-007
²³⁵ U	1.9331E-005	1.8848E-005	1.8365E-005
²³⁶ U	9.8820E-006	9.6349E-006	9.3879E-006
²³⁸ U	0.0023500	0.0022913	0.0022325
²³⁷ Np	0.010862	0.010591	0.010319
²³⁸ Pu	0.0044473	0.0043361	0.0042249
²³⁹ Pu	0.11646	0.11354	0.11063
²⁴⁰ Pu	0.039811	0.038816	0.037821
²⁴¹ Pu	0.037433	0.036497	0.035561
²⁴² Pu	0.014147	0.013793	0.013439
²⁴³ Am	0.0027054	0.0026377	0.0025701
²³³ U	4.8052E-012	4.6851E-012	4.5650E-012
²³⁷ U	1.4079E-008	1.3727E-008	1.3375E-008
²³⁸ Np	1.7797E-005	1.7352E-005	1.6907E-005
²³⁹ Np	0.0011237	0.0010956	0.0010675
²⁴¹ Am	0.0019923	0.0019424	0.0018926
²⁴² Am	3.6664E-006	3.5747E-006	3.4831E-006
²⁴² Cm	0.00062036	0.00060485	0.00058934
²⁴⁴ Cm	0.00071118	0.00069340	0.00067562
²⁴⁵ Cm	2.4747E-005	2.4128E-005	2.3510E-005
Nd	0.13455	0.13118	0.12782
Sm	0.026981	0.026307	0.025632
Eu	0.0057375	0.0055940	0.0054506
²³² Th	0.20000	0.20333	0.20667
O	0.40000	0.40667	0.41333

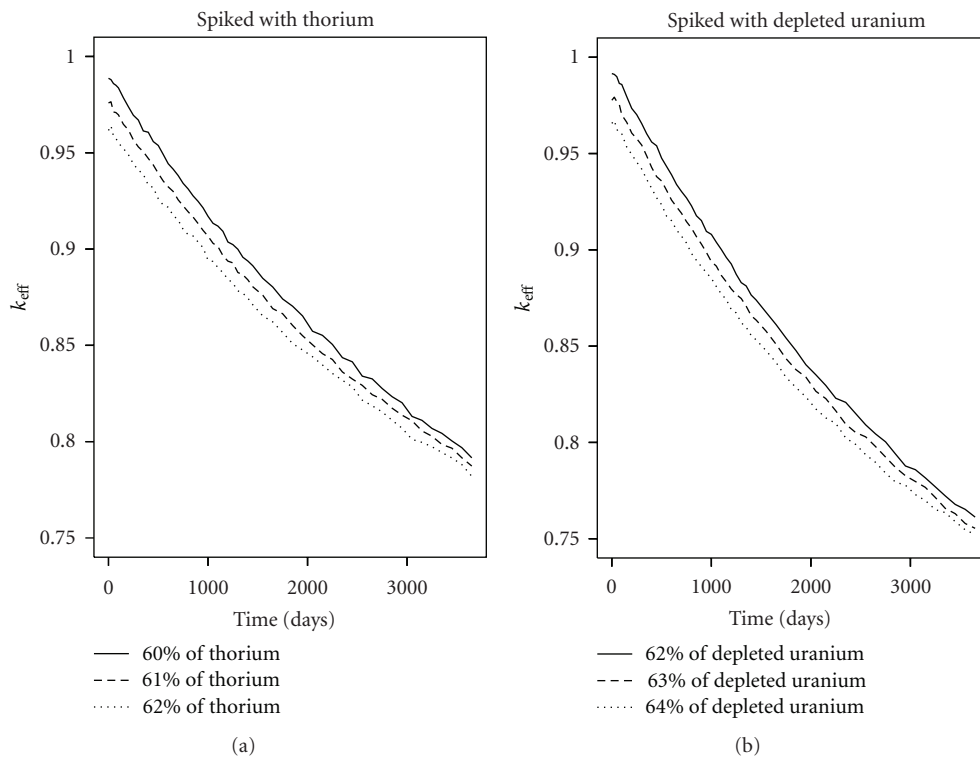


FIGURE 4: Multiplication factor (k_{eff}) evolution.

TABLE 4: Fuel composition (normalized) for the reprocessed fuels spiked with depleted uranium.

Actinides	Weight fraction fuel spiked with 62% of depleted uranium	Weight fraction fuel spiked with 63% of depleted uranium	Weight fraction fuel spiked with 64% of depleted uranium
²³⁴ U	3.5287E-007	3.4359E-007	3.3430E-007
²³⁵ U	1.8365E-005	1.7882E-005	1.7398E-005
²³⁶ U	9.3879E-006	9.1408E-006	8.8938E-006
²³⁸ U	0.0022325	0.0021738	0.0021150
²³⁷ Np	0.010319	0.010048	0.0097761
²³⁸ Pu	0.0042249	0.0041137	0.0040025
²³⁹ Pu	0.11063	0.10772	0.10481
²⁴⁰ Pu	0.037821	0.036826	0.035830
²⁴¹ Pu	0.035561	0.034625	0.033690
²⁴² Pu	0.013439	0.013086	0.012732
²⁴³ Am	0.0025701	0.0025025	0.0024348
²³³ U	4.5650E-012	4.4449E-012	4.3247E-012
²³⁷ U	1.3375E-008	1.3023E-008	1.2671E-008
²³⁸ Np	1.6907E-005	1.6462E-005	1.6017E-005
²³⁹ Np	0.0010675	0.0010394	0.0010113
²⁴¹ Am	0.0018926	0.0018428	0.0017930
²⁴² Am	3.4831E-006	3.3914E-006	3.2998E-006
²⁴² Cm	0.00058934	0.00057383	0.00055832
²⁴⁴ Cm	0.00067562	0.00065784	0.00064006
²⁴⁵ Cm	2.3510E-005	2.2891E-005	2.2272E-005
Nd	0.12782	0.12446	0.12109
Sm	0.025632	0.024958	0.024283
Eu	0.0054506	0.0053072	0.0051637
²³⁸ U	0.20625	0.20958	0.21291
²³⁵ U	0.00041333	0.00042000	0.00042667
²³⁴ U	2.0667E-006	2.1000E-006	2.1333E-006
O	0.41333	0.42000	0.42667

for calculation of initial k_{eff} and flux. The SDEF source was positioned on the center of the target. The burnup calculations were performed in kcode-mode using 53 time steps; the total simulated time was 10 years and the thermal power of operation throughout this period was 515 MW t. were performed simulations using reprocessed fuel spiked with thorium in different percentages and simulations using reprocessed fuel spiked with different percentages of depleted uranium.

3. Results

3.1. Neutronic Evaluation. In Figure 3 is shown the normalized neutron energy distribution (for the systems spiked with 62% of thorium and 62% of depleted uranium) in the BOL (beginning of life). Both spectra in the thorium fuel present their maximum around 150 keV and around 250 keV in the reprocessed fuel. Therefore, the reprocessed fuel neutron spectrum is harder than thorium fuel spectrum. That is result of the plutonium presence that emits fission neutrons with a harder spectrum. The spectra for the system loaded with fuel spiked with thorium are very similar to spectra for the

fuel spiked with depleted uranium. The spectrum in the lead of the core (coolant) presents a similar neutrons energy distribution to fuel spectra, but the number of neutrons available in the fuel is larger due to neutron production by fission reactions.

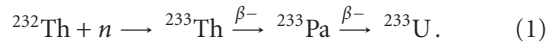
Figure 4 shows the multiplication factor (k_{eff}) as a time function for the systems loaded with ²³²ThO₂ (24 rods) and reprocessed fuel (132 rods) spiked with thorium (Figure 4(a)) and spiked with depleted uranium (Figure 4(b)). The percentages of thorium and depleted uranium in the reprocessed fuel were varied and the k_{eff} values obtained are represented in Figure 4. The percentages of thorium or depleted uranium were chosen in such a way that the values for the initial k_{eff} were close to 1, since a large variability on those percentages could lead to considerably low initial k_{eff} values.

From Figure 4 can be observed that after some years of operation the decrease in the k_{eff} value was smaller in the system which used reprocessed fuel spiked with thorium. That behavior indicates that the use of reprocessed fuel spiked with thorium allows an extension of the burnup without reloading fuel.

For the same percentage of thorium and depleted uranium (62%), the k_{eff} values for the system spiked with depleted uranium (k_{eff} variation of 0.991 to 0.761) were significantly higher than these for the system spiked with thorium (k_{eff} variation of 0.964 to 0.782), but the decrease in the k_{eff} for the system with depleted uranium was also higher.

The drop of the k_{eff} value observed in two cases is mainly due to the increased poisoning caused by the accumulation of fission products having large neutron capture cross sections and, of course, the constant energy generation by the system.

3.2. Thorium Fuel Evolution. Figure 5 describes the ^{232}Th , ^{233}Pa , and ^{233}U concentrations in the thorium fuel rods during the 10 years of operation for the systems spiked with 62% of thorium and 62% of depleted uranium. It can be verified that for the system spiked with thorium the concentration of the isotope ^{232}Th was reduced by about 17% (623 kg), for the system spiked with depleted uranium that was about 18% (644 kg). It is the result of the considerable capture cross section of that isotope, which allows the ^{233}U production. ^{233}U is formed when ^{232}Th captures a neutron, and it soon undergoes two beta decays:



A relevant question in the neutron spectrum choice is the protactinium effect. Protactinium captures neutrons (due to its large capture cross section) and, thus, decreases the reactivity and fuel regeneration. From Figure 5 can be observed that this isotope is formed in small scale in both systems. Furthermore, the protactinium effect is less severe for harder spectra like that.

Figure 5 also presents the ^{233}U concentration during the burnup, which is formed in large scale (~ 282 kg) for the system with reprocessed fuel spiked with thorium and (~ 284 kg) for the system spiked with depleted uranium. That ^{233}U production was due to ^{232}Th regeneration. Then these results show that the combined use of $^{232}\text{ThO}_2$ and reprocessed fuel allowed ^{233}U production without the initial requirement of ^{233}U enrichment.

3.3. Reprocessed Fuel Evolution. The long-term potential radiotoxicity of the spent nuclear fuel is mainly associated with transuranics (TRU) particularly Pu and MA: Am, Cm, and Np. These constitute a significant radiological source term over a very long period within a spent fuel [29]. Figures 6–9 show the concentration of those isotopes during the burnup.

In a standard uranium-uranium ($^{235}\text{U}_x$, $^{238}\text{U}_{1-x}$) fuel used in nuclear reactors, the isotope of neptunium, ^{237}Np , originates from ^{235}U , and the isotopes of americium, ^{241}Am and ^{243}Am , and curium, ^{242}Cm , ^{244}Cm , and ^{245}Cm , from ^{238}U as a result of nuclear reactions [30].

Plutonium is the major element for radiotoxicity and mass in the storage [31]. ^{238}Pu , which is generated from ^{237}Np , was produced in large scale in the system simulated (Figure 6), while ^{239}Pu and ^{241}Pu mass were reduced mainly due to fission reactions. ^{240}Pu is formed when ^{239}Pu captures

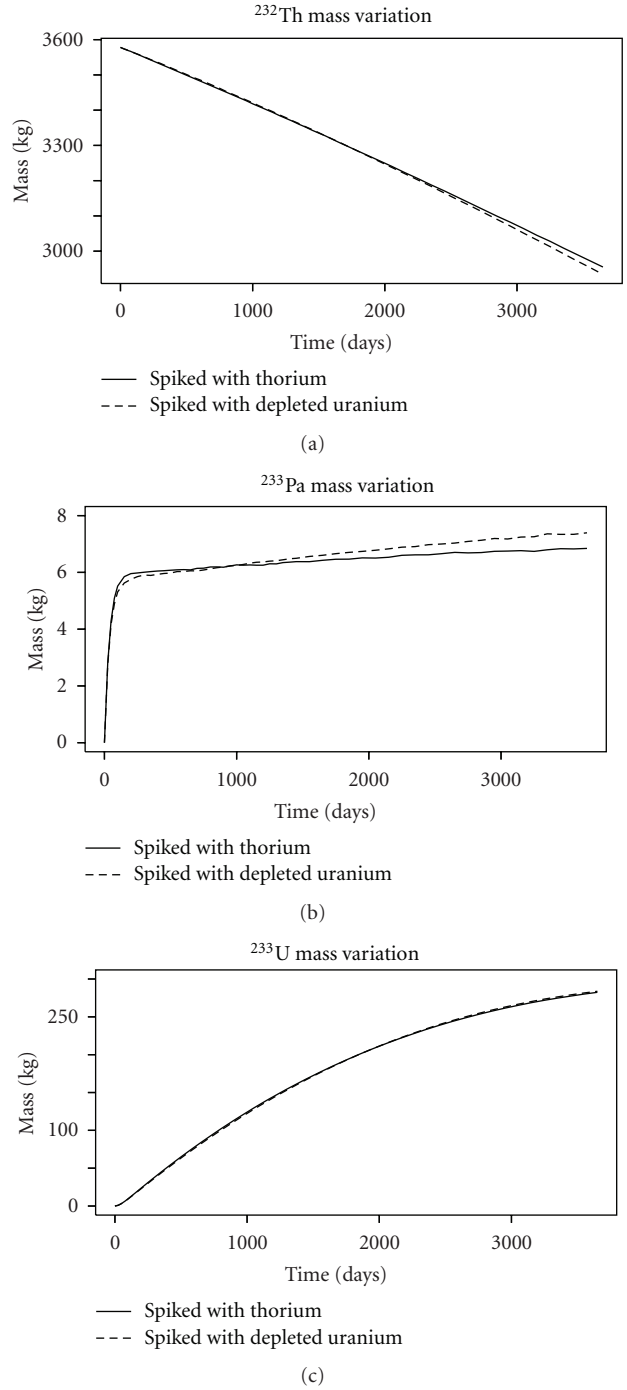


FIGURE 5: ^{232}Th , ^{233}Pa , and ^{233}U mass variations.

a neutron that justifies the high production of that isotope due to the reduced in ^{239}Pu . ^{242}Pu was formed in small scale. The greater plutonium production in the system spiked with depleted uranium was due to the greater uranium availability in this system that allows the ^{237}Np formation and consequently plutonium production.

Long-lived isotopes of americium produced are ^{241}Am and ^{243}Am . Americium is produced by β -decay of ^{241}Pu ($^{241}\text{Pu} \rightarrow ^{241}\text{Am}$) and (n, γ) reaction of

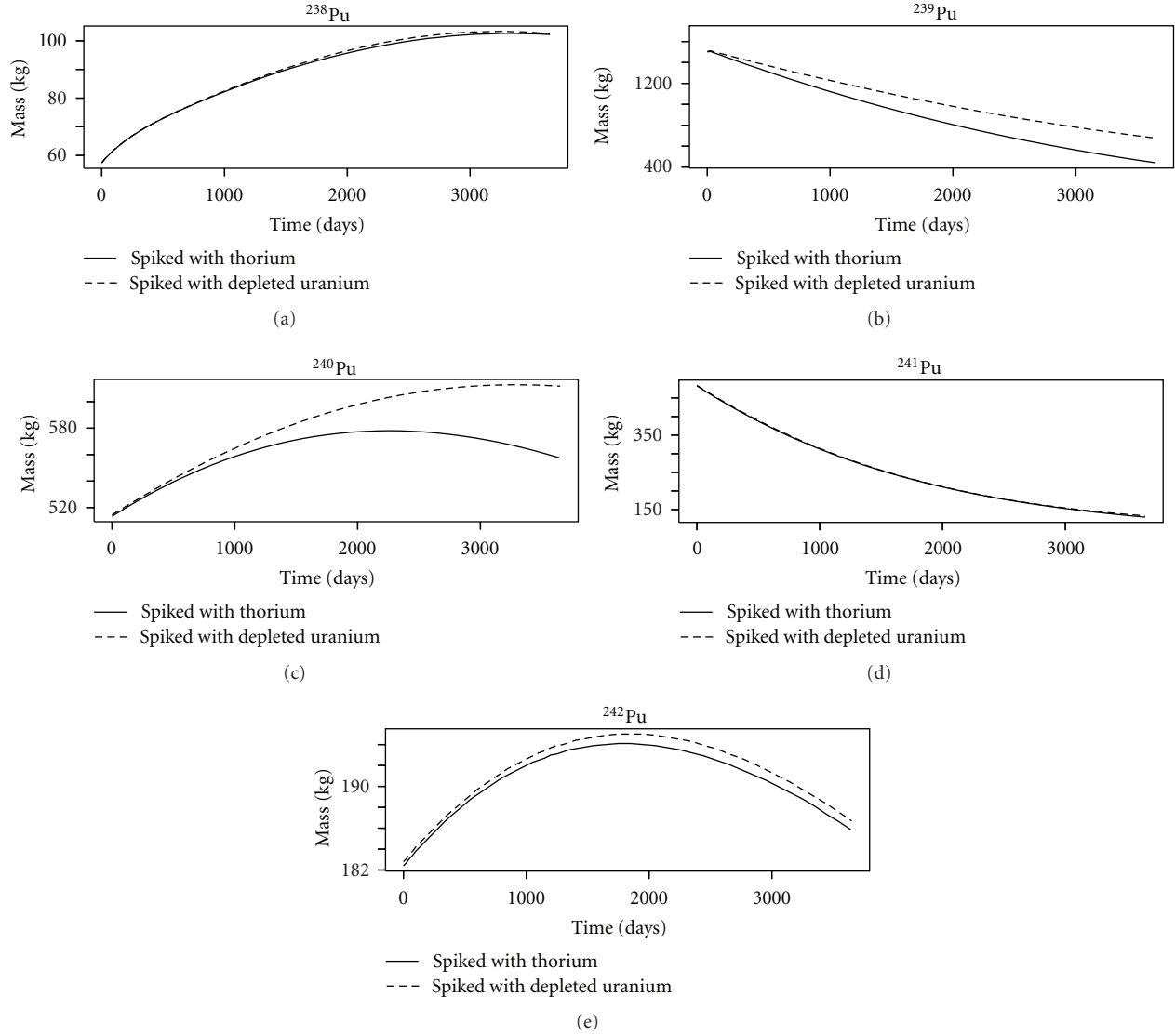
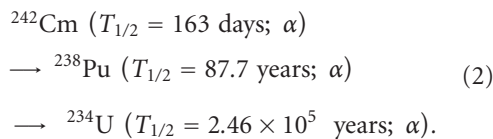


FIGURE 6: Plutonium mass variations.

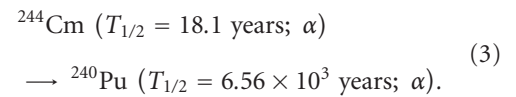
^{242}Pu ($^{242}\text{Pu} \rightarrow ^{243}\text{Am}$) during the operation. The mass variation of americium is shown in Figure 7; the difference between the americium productions in the two cases was very small.

Long-lived isotopes of curium produced are ^{242}Cm , ^{244}Cm , and ^{245}Cm . At that, isotope ^{242}Cm has a relatively short lifetime justifying its low production (Figure 8). The radioactive decay of ^{242}Cm proceeds as follows:

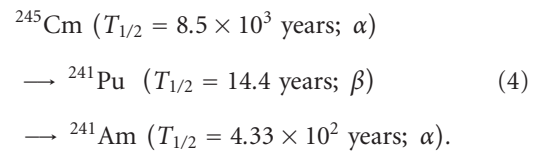


Curium is the most intensely radioactive of the actinides for both neutron emission and α -activity [32]. The most abundant of its isotopes is ^{244}Cm , which decays with a half-life of

18 years to form ^{240}Pu . Radioactive decay of ^{244}Cm occurs as follows:



The radioactive decay of ^{245}Cm to the nearest long-lived daughter nucleus proceeds as follows:



From Figure 8 can be observed increase in the masses of ^{245}Cm and ^{244}Cm . At long-term burnup of plutonium, there is the increase of radiotoxicity determined by accumulation of ^{244}Cm . The burnup of plutonium should be done by much

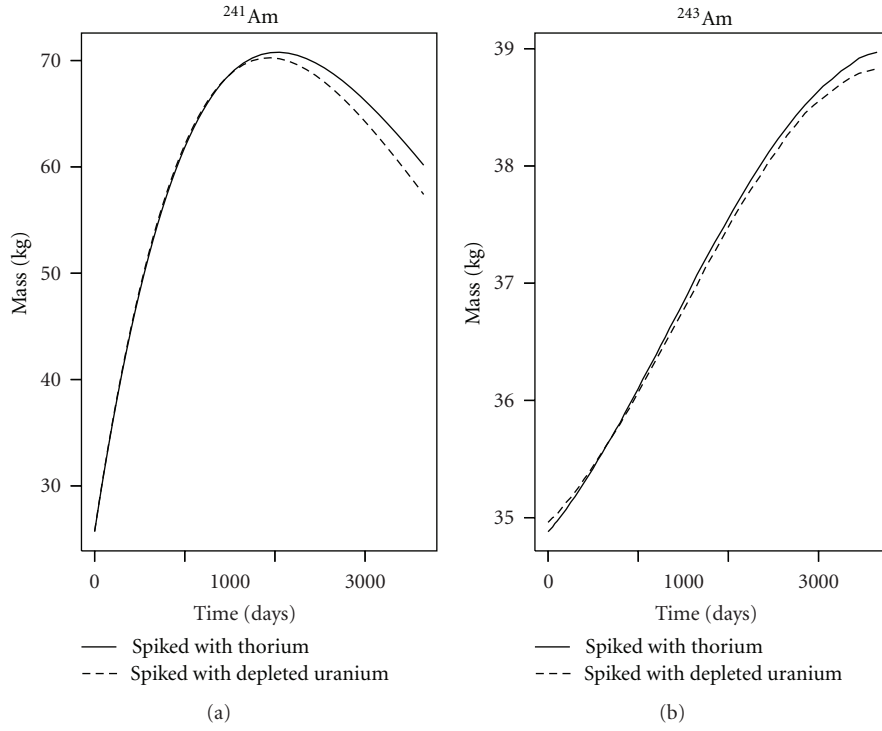


FIGURE 7: Americium mass variations.

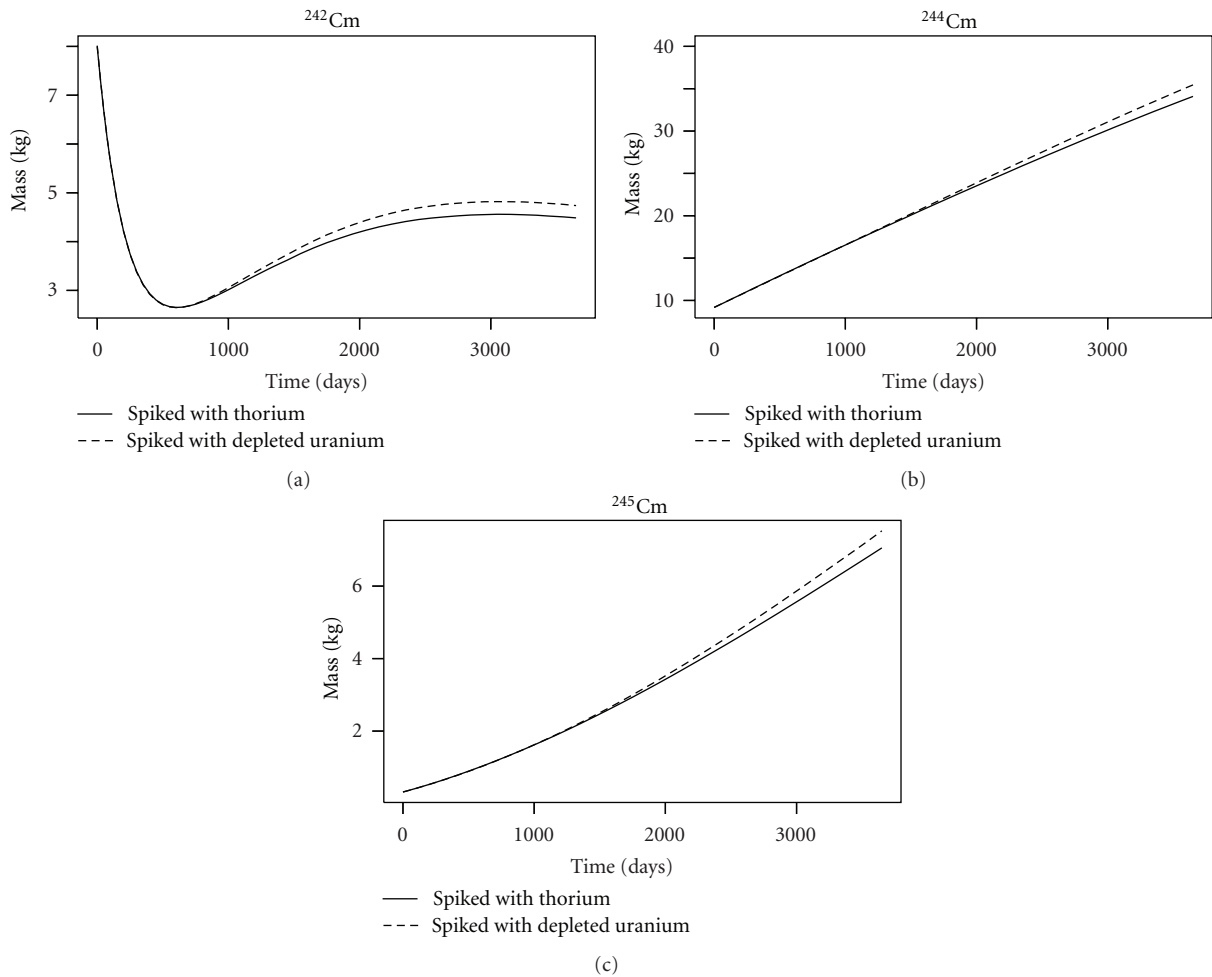


FIGURE 8: Curium mass variations.

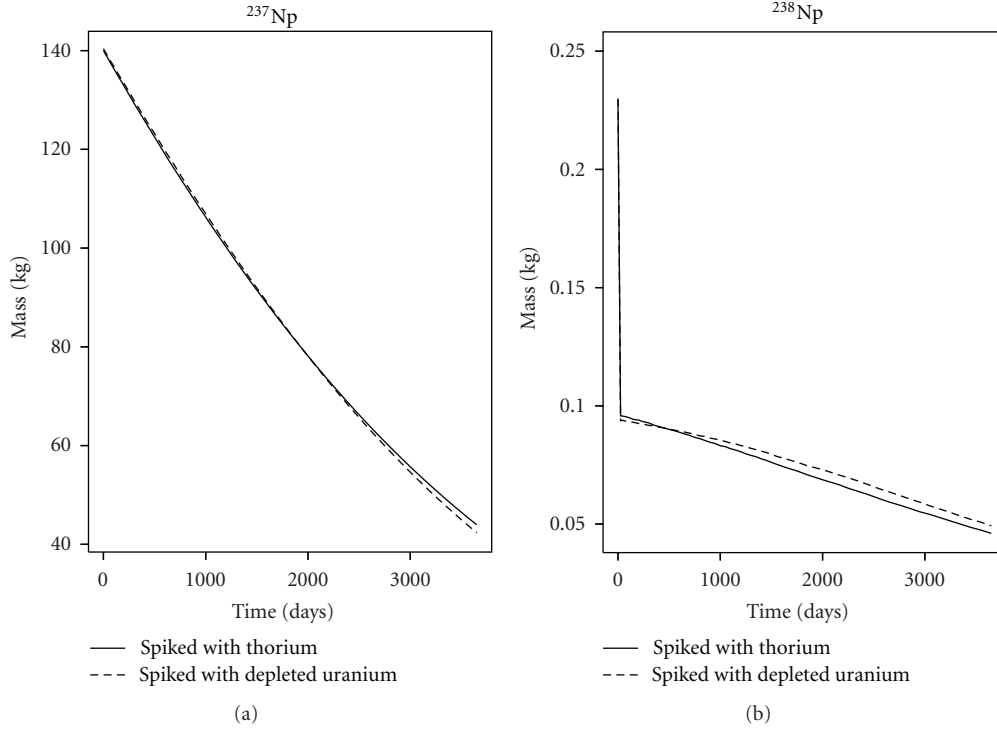


FIGURE 9: Neptunium mass variations.

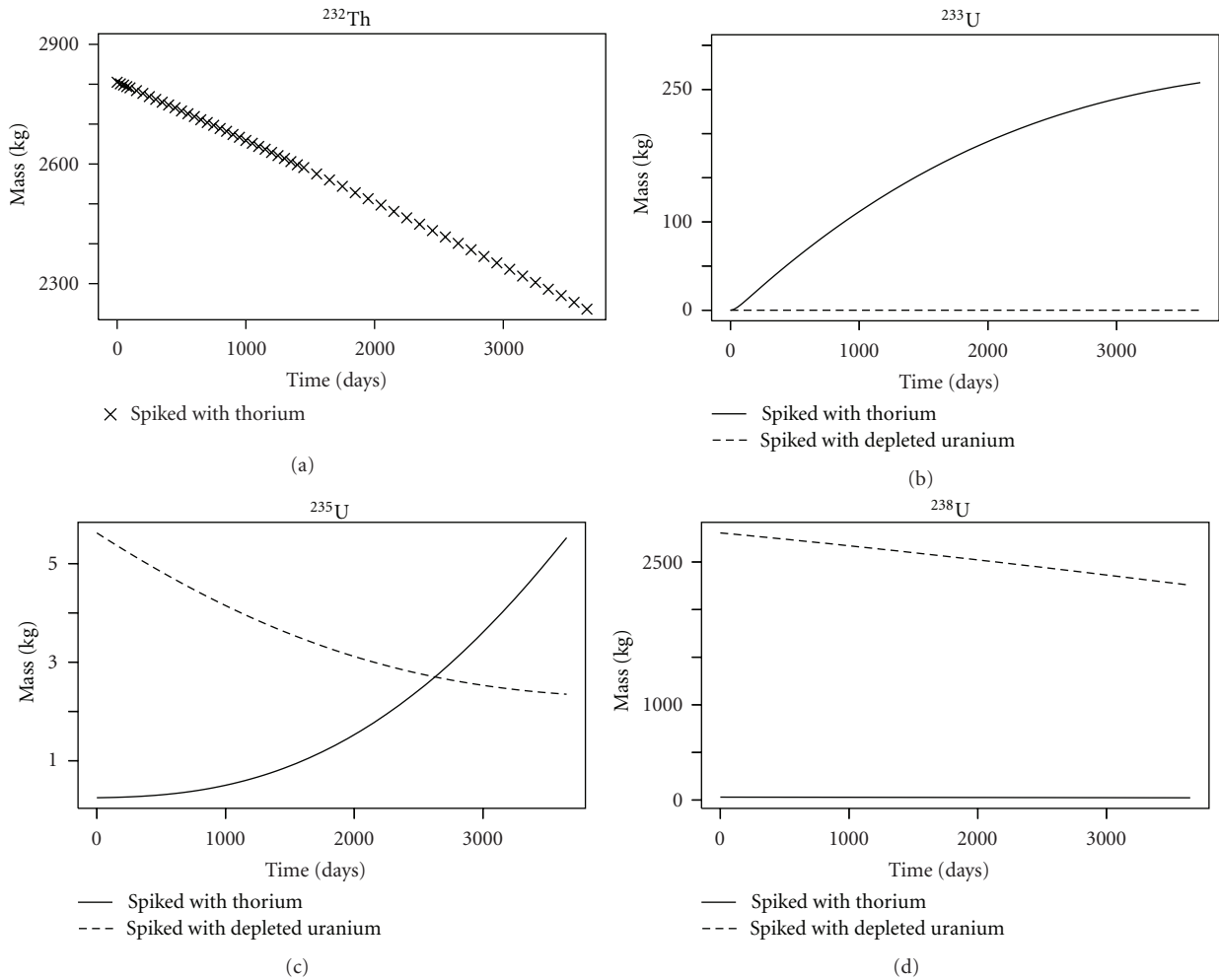


FIGURE 10: Thorium and uranium mass variation.

shorter lifetimes with intermediate processing and addition of new plutonium. Since ^{244}Cm half-life makes 18.1 years, one can organize a controllable storage of extracted curium [32]. The Cm mass evolution in the two cases was very similar.

Neptunium is produced by (n, γ) reaction of ^{235}U , $(n, 2n)$ reaction of ^{238}U , and α -decay of ^{241}Am . The most important Np isotope is ^{237}Np (half-life 2.14×10^6 years). The decrease observed in the ^{237}Np mass (Figure 9) is mainly due to ^{238}Np production by neutron capture. The very low concentration of ^{238}Np (Figure 9) is justified by the quick decay (2.117 days) to ^{238}Pu through β decay. Once more was not observed significant difference between the mass variations for each isotope in the two cases.

The large amount of ^{232}Th in the fuel spiked with $^{232}\text{ThO}_2$ results in a high ^{233}U production (~ 258 kg), as can be observed in Figure 10. That fuel regeneration potential appears with an advantage of the reprocessed fuel spiked with thorium. Figure 10 also shows the ^{235}U and ^{238}U mass variations.

4. Conclusions

The main conclusions indicated by the simulation presented in this work were as follow.

- (i) It is noteworthy that the code does not take into account the flux from external source during the burnup, so the k_{eff} and fuel results obtained are just approximations. Nevertheless, such approximated results are reasonable ones as long as the external source would not be sufficient to drive the system towards criticality, because the k_{eff} values obtained were substantial low during the operation period. The initial k_{eff} obtained ($k_{\text{eff}(\text{initial})} = \text{neutrons}_{\text{fission}} + \text{neutrons}_{\text{spallation}}$) were appropriate for an ADS and the k_{eff} obtained during the burnup ($k_{\text{eff}} = \text{neutrons}_{\text{fission}}$) provide an insight of the necessary contribution of the external source on the operation period.
- (ii) The insertion of reprocessed fuel in a $^{232}\text{ThO}_2$ system leads to harder neutron spectra due to the plutonium presence, facilitating the ^{233}U production. This is result of the protactinium effect reduction by hardening of the neutron spectrum.
- (iii) The reprocessed fuel evolution was very similar when that fuel was spiked with thorium or depleted uranium. However, the ^{233}U production appears with an advantage of the reprocessed fuel spiked with thorium. Furthermore, the decrease in the criticality was smaller in the system spiked with thorium that allows an extension in the burnup period.

References

- [1] "A Roadmap for developing ATW Technology," ANL, 99/16, 1999.
- [2] S. David, A. Billebaud, M. E. Brandan et al., "Fast subcritical hybrid reactors for energy production: evolution of physical parameters and induced radiotoxicities," *Nuclear Instruments and Methods in Physics Research, Section A*, vol. 443, no. 2, pp. 510–530, 2000.
- [3] D. G. Cacuci, "On the neutron kinetics and control of accelerator-driven systems," *Nuclear Science and Engineering*, vol. 148, no. 1, pp. 55–66, 2004.
- [4] K. Tsujimoto, T. Sasa, K. Nishihara, H. Oigawa, and H. Takano, "Neutronics design for lead-bismuth cooled accelerator-driven system for transmutation of minor actinide," *Journal of Nuclear Science and Technology*, vol. 41, no. 1, pp. 21–36, 2004.
- [5] B. Calgaro, B. Vezzoni, N. Cerullo, G. Forasassi, and B. Verboomen, "Wastes management through transmutation in an ADS reactor," *Science and Technology of Nuclear Installations*, vol. 2008, Article ID 756181, 6 pages, 2008.
- [6] H. Yapici, G. Genç, and N. Demir, "A comprehensive study on neutronics of a lead-bismuth eutectic cooled accelerator-driven sub-critical system for long-lived fission product transmutation," *Annals of Nuclear Energy*, vol. 35, no. 7, pp. 1264–1273, 2008.
- [7] A. A. Hamid, P. Baeten, B. de Didier, J. Heyse, P. Schuurmans, and J. Wagemans, "MYRRHA, a multipurpose hybrid research reactor for high-end applications," *Nuclear Physics News*, vol. 20, no. 1, pp. 24–28, 2010.
- [8] K. Furukawa et al., "The combined system of accelerator molten salt breeder (AMSB) and molten salt converter reactor (MSCR)," in *Proceedings of the Japan-US Seminar on Thorium Fuel Reactors*, Naora, Japan, 1982.
- [9] C. D. Bowman, E. D. Arthur, P. W. Lisowski et al., "Nuclear energy generation and waste transmutation using an accelerator-driven intense thermal neutron source," *Nuclear Inst. and Methods in Physics Research, A*, vol. 320, no. 1-2, pp. 336–367, 1992.
- [10] C. D. Bowman, "Accelerator-driven systems for nuclear waste transmutation," *Annual Review of Nuclear and Particle Science*, vol. 48, no. 1, pp. 505–556, 1998.
- [11] F. Carminati et al., "An energy amplifier for cleaner and inexhaustible nuclear energy production driven by a particle beam accelerator," *CERN/AT/93-47 (ET)*, 1992.
- [12] C. Rubbia et al., "Conceptual design of a fast neutron operated high power energy amplifier," *CERN/AT/95-44 (ET)*, 1995.
- [13] W. Lewis, Report AECL-968, 1952.
- [14] A. Araújo, C. Pereira, M. A. F. Veloso, A. L. Costa, and H. M. Dalle, "Flux and dose rate evaluation of iter system using MCNP5," *Brazilian Journal of Physics*, vol. 40, no. 1, pp. 58–62, 2010.
- [15] G. P. Barros, C. Pereira, M. A. Veloso, A. L. Costa, and P. A. Reis, "Neutron production evaluation from a ADS target utilizing the MCNPX 2.6.0 code," *Brazilian Journal of Physics*, vol. 40, no. 4, pp. 414–418, 2010.
- [16] C. Velasquez et al., "Axial neutron flux evaluation in a tokamak system: a possible transmutation blanketposition for a fusion-fission transmutation system," *Brazilian Journal of Physics*. In press.
- [17] The European Technical Working Group an ADS, "A European Roadmap for Developing Accelerator Driven System (ADS) for Nuclear Waste Incineration," 2001.
- [18] "Roadmap for developing Accelerator Transmutation of Waste (ATW) Technology," Tech. Rep. DOE/RW0-519, US Department of Energy.
- [19] Ismail, P. H. Liem, N. Takaki, and H. Sekimoto, "Performance of natural uranium- and thorium-fueled fast breeder reactors (FBRs) for ^{233}U fissile production," *Progress in Nuclear Energy*, vol. 50, no. 2-6, pp. 290–294, 2008.

- [20] D. Pelowitz, Ed., "MCNPX User's Manual," Version 2.6.0., Los Alamos National Security, 2008.
- [21] D. Warin, "Status of the French research program for actinides and fission products partitioning and transmutation," in *Proceedings of the GLOBAL Forum*, Tsukuba, Japan, 2005.
- [22] M. Miguirchian et al., "GANEX: adaptation of the DIAMEX-SANEX Process for the group Actinide separation," in *Proceedings of the Advanced Nuclear Fuel Cycles and Systems (GLOBAL '07)*, Boise, Idaho, USA, 2007.
- [23] D. Warin, "Future nuclear fuel cycles: prospect and challenges for actinide recycling," *Materials Science and Engineering*, vol. 9, pp. 1–6, 2010.
- [24] J. Hendricks et al., "MCNPX 2.6.0 Extensions," Los Alamos National Laboratory, LA-UR-08-2216, 2008.
- [25] H. Nifenecker, S. David, J. M. Loiseaux, and O. Meplan, "Basics of accelerator driven subcritical reactors," *Nuclear Instruments and Methods in Physics Research, Section A*, vol. 463, no. 3, pp. 428–467, 2001.
- [26] H. Nifenecker, S. David, J. M. Loiseaux, and A. Giorni, "Hybrid nuclear reactors," *Progress in Particle and Nuclear Physics*, vol. 43, pp. 683–827, 1999.
- [27] ORIGEN2, "User's Manual," ORNL/TM-7175, 1980.
- [28] S. Cota and C. Pereira, "Neutronic evaluation of the non-proliferating reprocessed nuclear fuels in pressurized water reactors," *Annals of Nuclear Energy*, vol. 24, no. 10, pp. 829–834, 1997.
- [29] A. Shelley, H. Akie, H. Takano, and H. Sekimoto, "Radiotoxicity hazard of U-free $\text{PuO}_2+\text{ZrO}_2$ and $\text{PuO}_2+\text{ThO}_2$ spent fuels in LWR," *Progress in Nuclear Energy*, vol. 37, no. 1-4, pp. 377–382, 2001.
- [30] "Production of minor actinides in thermal nuclear reactors and nonproliferation," 2011, http://www.partnershipforglobalsecurity.org/Documents/actinides_report1_eng.pdf.
- [31] "Transmutation of Americium and Curium: review of solutions and impacts," 2011, <http://www.oecd-nea.org/trw/docs/mol98/session4/SIVpaper1.pdf>.
- [32] "Conditions of Plutonium, Americium and Curium transmutation in nuclear facilities," 2011, <http://www.oecd-nea.org/pt/docs/iem/madrid00/Proceedings/Paper65.pdf>.

Research Article

Subcritical Multiplication Parameters of the Accelerator-Driven System with 100 MeV Protons at the Kyoto University Critical Assembly

Jae-Yong Lim, Cheol Ho Pyeon, Takahiro Yagi, and Tsuyoshi Misawa

Nuclear Engineering Science Division, Research Reactor Institute, Kyoto University, Asashiro-nishi, Kumatori-cho, Sennan-gun, Osaka 590-0494, Japan

Correspondence should be addressed to Cheol Ho Pyeon, pyeon@rri.kyoto-u.ac.jp

Received 9 November 2011; Revised 15 February 2012; Accepted 28 February 2012

Academic Editor: Piero Ravetto

Copyright © 2012 Jae-Yong Lim et al. This is an open access article distributed under the Creative Commons Attribution License, which permits unrestricted use, distribution, and reproduction in any medium, provided the original work is properly cited.

Basic experiments on the accelerator-driven system (ADS) at the Kyoto University Critical Assembly are carried out by combining a solid-moderated and -reflected core with the fixed-field alternating gradient accelerator. The reaction rates are measured by the foil activation method to obtain the subcritical multiplication parameters. The numerical calculations are conducted with the use of MCNPX and JENDL/HE-2007 to evaluate the reaction rates of activation foils set in the core region and at the location of the target. Here, a comparison between the measured and calculated eigenvalues reveals a relative difference of around 10% in C/E values. A special mention is made of the fact that the reaction rate analyses in the subcritical systems demonstrate apparently the actual effect of moving the tungsten target into the core on neutron multiplication. A series of further ADS experiments with 100 MeV protons needs to be carried out to evaluate the accuracy of subcritical multiplication parameters.

1. Introduction

The accelerator-driven system (ADS) is a hybrid technique combining a reactor core and an accelerator, which has been used worldwide in research and development of nuclear transmutation of minor actinides (MAs), long-lived fission products (LLFPs), and next-generation neutron sources. In ADS, a large number of high-energy neutrons are generated directly at a heavy metal target when high-energy protons produced by the accelerator are injected onto the target. The high-energy neutrons can be utilized for maintaining nuclear fission reactions in the reactor core and achieving the purposes of the introduction of ADS. The current research on ADS involved mainly an experimental feasibility study with the use of critical assemblies and test facilities: MASURCA [1–3], YALINA-booster and -thermal [4–6], VENUS-1 [7], and the Kyoto University Critical Assembly (KUCA) [8–14]. Moreover, numerical simulations [15–20] were executed by the deterministic and stochastic approaches for the evaluation of MAs and LLFPs in ADS. The new ADS test facility of GUINEVERE [21] is being commissioned

to start actual operation in subcritical states after the first critical experiments.

The Kyoto University Research Reactor Institute is pursuing an innovative research program (Kart & Lab.: Kumatori Accelerator-Driven Reactor Test Facility & Innovation Research Laboratory) to develop the fixed-field alternating gradient (FFAG) [22–24] accelerator and to establish a new neutron source by ADS in combination with KUCA and the FFAG accelerator. With the coupling of the KUCA core and the FFAG accelerator, the spallation neutrons generated by 100 MeV proton beams have been successfully injected into the uranium-loaded [25] KUCA core. In the first injection of spallation neutrons, the proton beam intensity and shape were low and poor, respectively, resulting in large statistical errors in the experiments, such as the reaction rate analyses. On the other hand, the spallation neutrons generated at the location of the tungsten target position were expected to make a reasonable contribution to neutron multiplication in the core region; however, the disadvantage of setting the target outside the core was low neutron generation in the core region by high-energy proton beams.

To resolve this drawback and enhance neutron multiplication, additional ADS experiments on the reaction rates were carried out by moving the tungsten target to another location in the subcritical core. Here, special note was taken of the effect of moving the target from the original location on subcritical multiplication parameters, including the neutron multiplication and the subcritical multiplication factor. The numerical analyses of the subcritical experiments were executed with the use of the Monte Carlo calculation code MCNPX [26] together with the nuclear data library JENDL/HE-2007 [27, 28]. The main objective of this study was to examine the accuracy of the subcritical multiplication parameters in the subcritical configurations of ADS by comparing the measured and calculated reaction rates. The preliminary (previous) experiments with high-energy neutrons generated by 100 MeV protons from the FFAG accelerator are shown in Section 2 and include descriptions of the core configuration; experimental and numerical results. The results of basic (additional) experiments on moving the target are presented in Section 3, and the conclusions are summarized in Section 4.

2. Preliminary ADS Experiments with 100 MeV Protons

2.1. Core Configuration. Among three cores designated A, B, and C at KUCA, A and B are polyethylene solid-moderated and solid-reflected cores, and C is a light water-moderated and light water-reflected one. The three cores are operated at a low mW power in the normal operating state, whereas the maximum power is 100 W. The preliminary ADS experiments were carried out in the A-core (Figure 1), which contains polyethylene reflector rods and three different fuel assemblies: normal, SV, and partial fuel assemblies (Figures 2(a), 2(b), and 2(c), resp.). The normal fuel assembly is composed of 36-unit cells and upper and lower polyethylene blocks about 591 and 537 mm long, respectively, in an aluminum sheath $54 \times 54 \times 1520 \text{ mm}^3$. For the normal and partial fuel assemblies, a unit cell in the fuel region is composed of a highly enriched uranium-aluminum fuel plate 1.59 mm (1/16"), and polyethylene plates 3.18 mm (1/8") and 6.35 mm (1/4"). The numeral 14 corresponds to the number of fuel plates in the partial fuel assembly used to reach the criticality mass. The horizontal dimensions of all fuel and polyethylene plates are $5.08 \times 5.08 \text{ mm}^2$ (2" \times 2").

The tungsten target located outside the core is not easily moved to the center of the core because control and safety rods are fixed in the core and function as the control driving system. The neutron guide composed of several shielding materials, including iron (Fe), boron (B), polyethylene, the beam duct, and a special fuel assembly with a void (SV, Figure 2(b)), are installed. In the neutron guide, the role of the SV assemblies is to direct the highest number possible of the high-energy neutrons generated in the target to the center of the fuel region, in order to improve neutron multiplication. Moreover, to collimate the high-energy neutrons, it was necessary to reduce the thermal component moderated in the reflector region before

their reaching the fuel region. This reduction was achieved by shielding unnecessary fast neutrons and by capturing parasite thermal neutrons. For deflecting unnecessary fast neutrons, the close vicinity in front of the target included the Fe block around the guide void to shield the fast neutrons from inelastic scattering. For capturing parasite thermal neutrons, polyethylene blocks containing 10 wt% B around the guide void were set around the Fe shielding near the target and in the two rows next to the assemblies. The rest of the neutron guide consisted of polyethylene assemblies and one void space. Details of the neutron guide were as described in [8, 9]. 100 MeV protons generated from the accelerator were injected into a subcritical system with the following parameters: 10 pA beam intensity; 30 Hz repetition rate; 100 ns pulsed width; 1.0×10^6 1/s neutron yield.

2.2. Experimental Analyses. In the subcritical experiments, gold (^{197}Au) and indium (^{115}In) foils were selected as normalization factors for monitoring reactor power in the core and neutron source generation at the target, respectively. The difference between the normalization factors in the core and at the target was attributable to the sensitivity of the thermal neutrons and the high-energy neutrons, respectively. The reaction rates of the ^{115}In wire (1.5 mm diameter and 750 mm long) in the core and the ^{115}In foil ($10 \times 10 \times 1 \text{ mm}^3$) at the target were normalized by those of the ^{197}Au foil (8 mm diameter and 0.05 mm thick) emitted by $^{197}\text{Au}(n, \gamma)^{198}\text{Au}$ reactions attached in the core center (O, 15; Figure 1), and of the ^{115}In foil emitted by $^{115}\text{In}(n, n')^{115\text{m}}\text{In}$ reactions attached at the original location of the target, respectively. The experimental error in each activation foil was estimated to be about 5%, including the statistical error of γ -ray counts and the full width at half maximum (FWHM) of the γ -ray spectrum peak. The experiments were carried out within subcriticality level 770 pcm ($0.77\% \Delta k/k$). Here, the subcritical state was attained by the full insertion of C1, C2, and C3 control rods and the full withdrawal of S4, S5 and S6 safety rods (Figure 1). The measured subcriticality was obtained from the combination of both the control and safety rod worth by the rod drop method and its calibration curve by the positive period method. In the KUCA core, the subcriticality was attained by the full insertion of all control and safety rods within 2,000 pcm ($0.20\% \Delta k/k$; $k_{\text{eff}} = 0.98$), and the representative subcriticality level around 3,000 pcm is achieved by the removal of fuel rods in the ADS experiments. When the representative subcriticality is obtained, as a result, the change in the core characteristics, including the control rod worth, the neutron flux shape and the neutron spectrum, is apparently observed in comparison with before and after the removal of fuel rods. Therefore, the ADS experiments were carried out within the subcritical level attained by inserting the control and safety rods to maintain the core characteristics from the viewpoint of reactor physics.

The effect of the subcritical multiplication parameters was evaluated by thermal neutron flux distribution estimated through the horizontal measurement of $^{115}\text{In}(n, \gamma)^{116\text{m}}\text{In}$ reaction rates by activation analysis of the In wire. The wire was set in an aluminum guide tube within the 3 mm

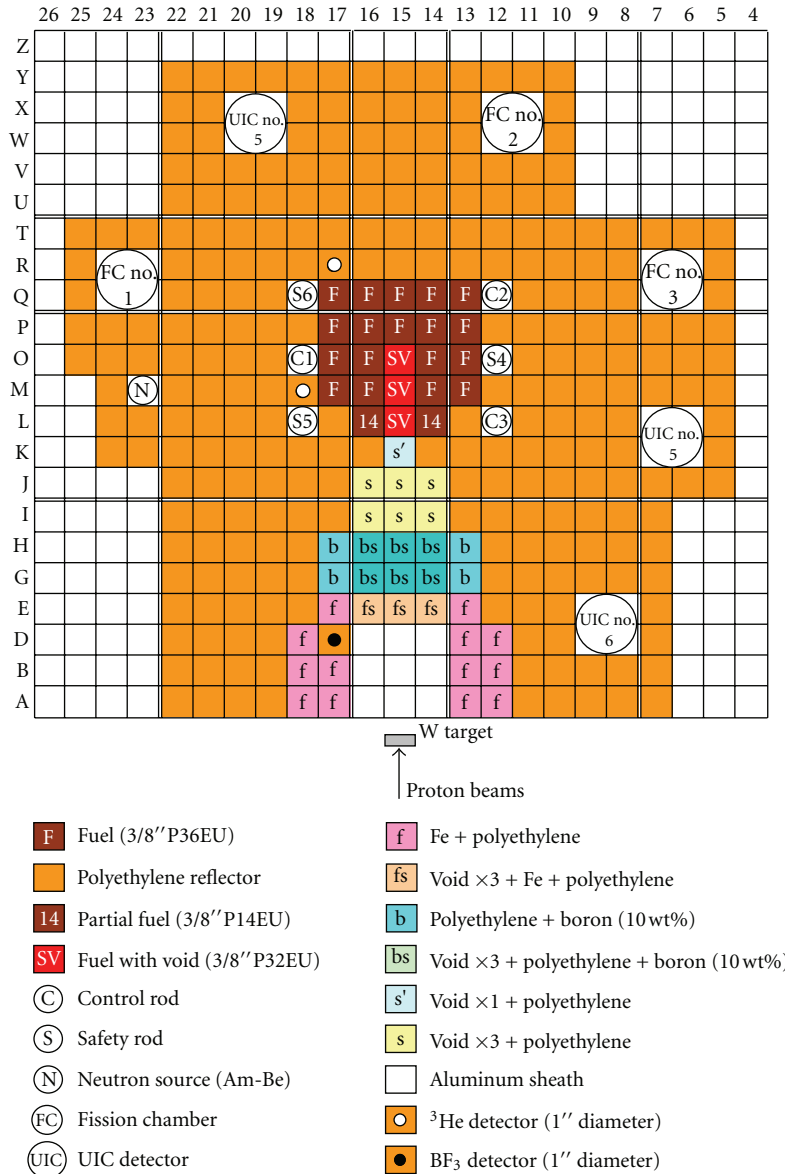


FIGURE 1: Top view of the KUCA A-core (A3/8''P36EU(3)) in the ADS experiments.

gap between rows 13 and 14 (Figure 1), from the front of the tungsten target to the center of the fuel region (13-14, A-P; Figure 1), at the height of the axial center of the fuel assembly. For comparison between the experiment and the calculation, normalization was based on reactor power: the ¹⁹⁷Au(*n*, γ)¹⁹⁸Au reaction rate set in the center of the core was measured. A global experimental error of about 5% was considered significant on reaction rate measurements of the In wire.

The subcriticality calculations were executed with the use of the Monte Carlo multiparticle transport code, MCNPX, in combination with nuclear data library JENDL/HE-2007. The irradiation foils and the In wire were included in the simulated geometry and transport calculation because the effects of their reactivity are not negligible; reaction rates were deduced from tallies taken in the reaction rate

experiments. Although better in the core region, an overall statistical error of 5% remained in the reaction rate in the present results. The results of eigenvalue calculations were obtained after 1,000 active cycles of 50,000 histories each. The deduced subcriticalities had statistical errors of 10 pcm (0.01% $\Delta k/k$). The fixed-source calculations were executed by a total of 1.0×10^8 histories, which led to a statistical error of less than 5% in the reaction rates.

The results of measured and calculated subcriticalities are presented in Table 1. A comparison between the experiments and the calculations demonstrated the ability of MCNPX calculations to reproduce the subcriticality level to within 2% of the C/E (calculation/experiment) value. A comparison made of the measured and the calculated reaction rate distributions to validate the calculation method demonstrated that the calculated reaction rate distribution

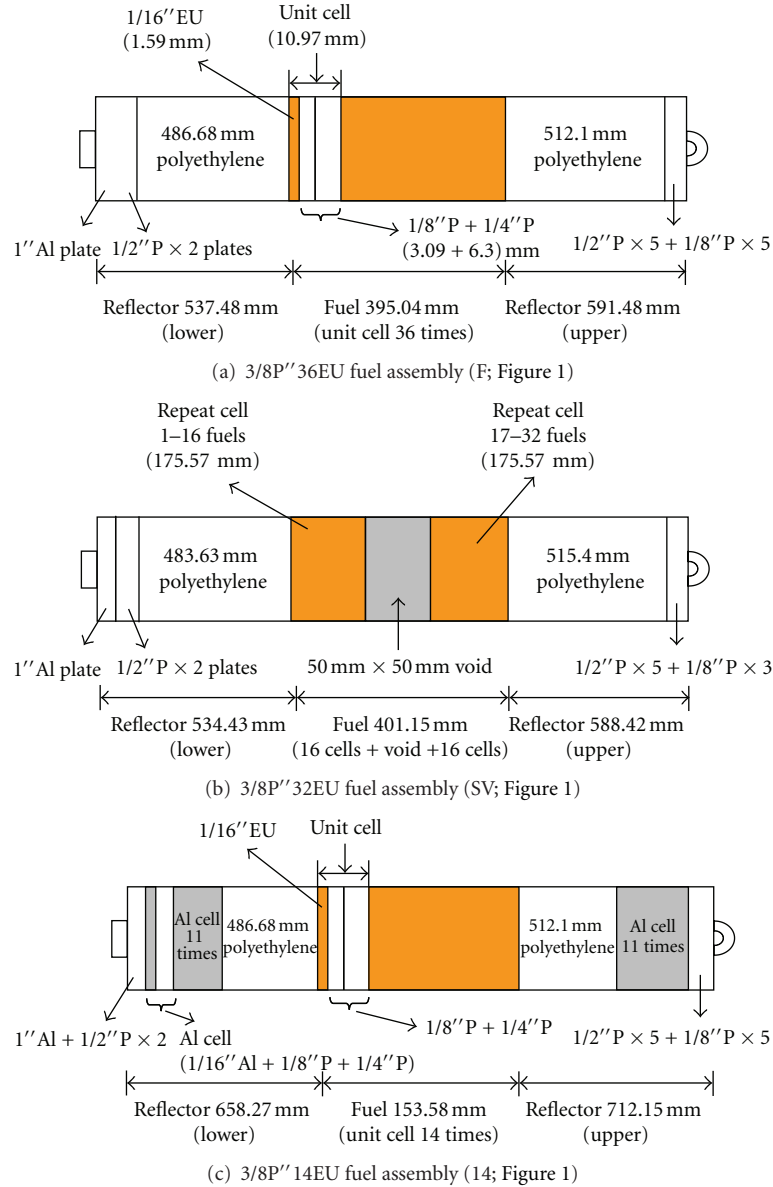


FIGURE 2: Schematic drawing of fuel assemblies in the A-core.

TABLE 1: Comparison between the measured and calculated subcriticalities obtained from the experiments (Figure 1) and calculations (MCNPX with JENDL/HE-2007).

Calculation (pcm)	Experiment (pcm)	C/E
773	760	1.02

(Figure 3) agreed approximately with the experimental one within the statistical errors in the experiments; however, the experimental errors were considerably larger than those of the calculations. These larger errors were attributable to the status of the proton beams, including the weak beam intensity and the poor beam shape at the target.

3. Basic ADS Experiments with 100 MeV Protons

The neutron spectrum analyses were conducted numerically for investigating anticipated high-energy neutrons at each location for the injection of the high-energy protons before the basic experiments, as shown in Figure 4. The high-energy neutrons were attained in front of target location (A, 15) and were dominant over the region of a few MeV neutrons of energy. The further the distance was from the tungsten target, including locations (E, 15), (J, 15), and (O, 15), the more thermalized the neutron spectrum is: this fact demonstrated that the high-energy neutrons generated at the location of the original target should be little affected upon neutron multiplication in the core, and the thermal neutrons

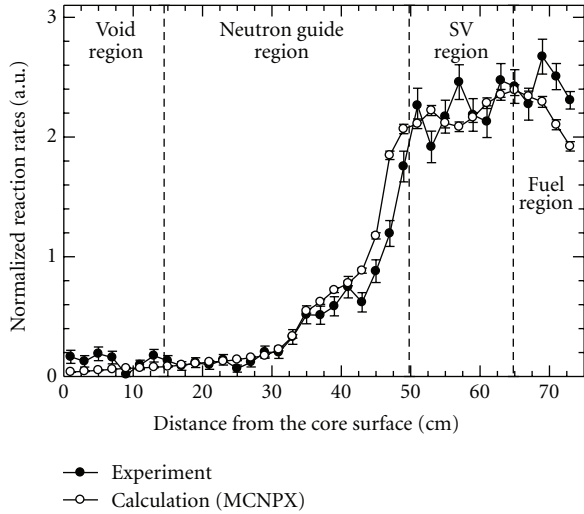


FIGURE 3: Comparison between the measured and calculated reaction rates of $^{115}\text{In}(n, \gamma)^{116\text{m}}\text{In}$ reactions along the region of (13-14, A-P; Figure 1).

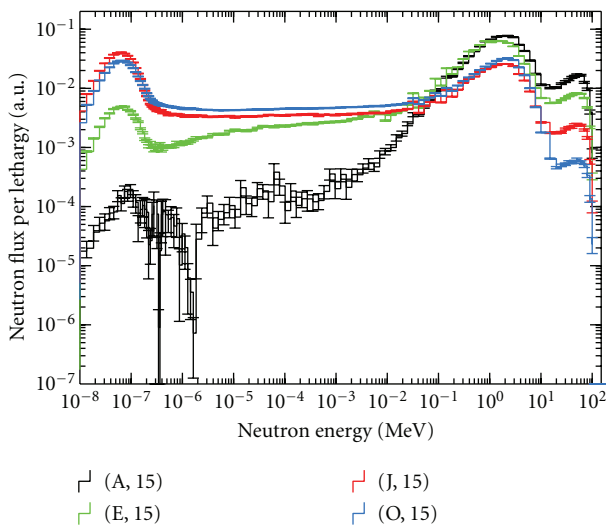


FIGURE 4: Comparison between neutron spectra at four points in the ADS experiments (Figure 1).

moderated in the reflector region were compared to be less than other locations.

For optimizing the effect of moving the target from its original location, additional experiments were carried out in the same core (Figure 5) as in a previous study described in Section 2: the composition of the neutron guide was made partly of lead (Pb) instead of Fe, thereby attaining neutron multiplication around the target region by the injection of high-energy neutrons into the shielding material, Pb. Also, the effect of moving the target was investigated through analyses of neutron multiplication, as in the previous study [29] at KUCA. In the experiments, the $^{115}\text{In}(n, \gamma)^{116\text{m}}\text{In}$ reaction rates were measured in the core region, and neutron multiplication was deduced by the reaction rate distribution, when the tungsten target was moved from the original location to another one close to the core center. Finally

TABLE 2: Comparison between the measured and calculated subcriticalities obtained from the experiments (Figure 5) and calculations (MCNPX with JENDL/HE-2007).

Case	Calculation (pcm)	Experiment (pcm)	C/E
(A, 15)	706	772	0.91
(G, 15)	659	737	0.89
(K, 15)	674	740	0.91

the actual effect of moving the target was examined by comparing the experimental and numerical analyses. As in Section 3, the experiments were carried out around subcriticality level 750 pcm ($0.75\%\Delta k/k$), and subcriticality was attained and then measured. Notably, the 100 MeV protons generated from the accelerator were injected into a subcritical system under the following parameters: 30 pA beam intensity; 30 Hz repetition rate; 200 ns pulsed width; 1.0×10^7 1/s neutron yield.

3.1. Subcriticality. The numerical calculations were executed with the use of MCNPX together with the JENDL/HE-2007 library. The numerical evaluation of subcriticality by JENDL/HE-2007 was in agreement with experimental data and within a relative difference of 10% (Table 2), whereas the accuracy of eigenvalue calculations was not good compared with the previous analyses presented in Section 2. By MCNPX, the eigenvalue calculations were executed for 5,000 active cycles of 10,000 histories. The subcriticalities in the eigenvalue calculations had statistical errors within 10 pcm ($0.01\%\Delta k/k$). Since the reactivity effects of activation foils and wire in the core are not negligible, they were included in the simulated geometry and transport calculations.

3.2. Reaction Rate Distribution. The calculated reaction rate was obtained by evaluating the volume tallies of activation foils. The statistical error of the reaction rates in the fixed-source calculations was within 5% after a total of 1.0×10^8 histories. The difference in the experimental results along region (13-14, A-P; Figure 5) is shown in Figure 6(a), by changing the location of the tungsten target to another one: in front of the original target (A, 15); between the target and the core (G, 15); in front of the fuel region (K, 15). From the experimental results in Figure 6(a), the reaction rate distribution was observed to be high in the SV and fuel regions, when the tungsten target was set at location (G, 15), although the core configuration of reaction rates varied in the SV and fuel regions. Comparison of the experimental and numerical results revealed the approximate reconstruction of the $^{115}\text{In}(n, \gamma)^{116\text{m}}\text{In}$ reaction rates by MCNPX with JENDL/HE-2007 shown in Figure 6(b), whereas the discrepancy was found to be in some regions of (G, 15) by the difference in experimental results in the core configuration.

3.3. Neutron Multiplication and Subcritical Multiplication Factor. Neutron multiplication M and subcritical multiplication factor k_s were experimentally and numerically analyzed on the basis of the accuracy in Section 3.2, related to

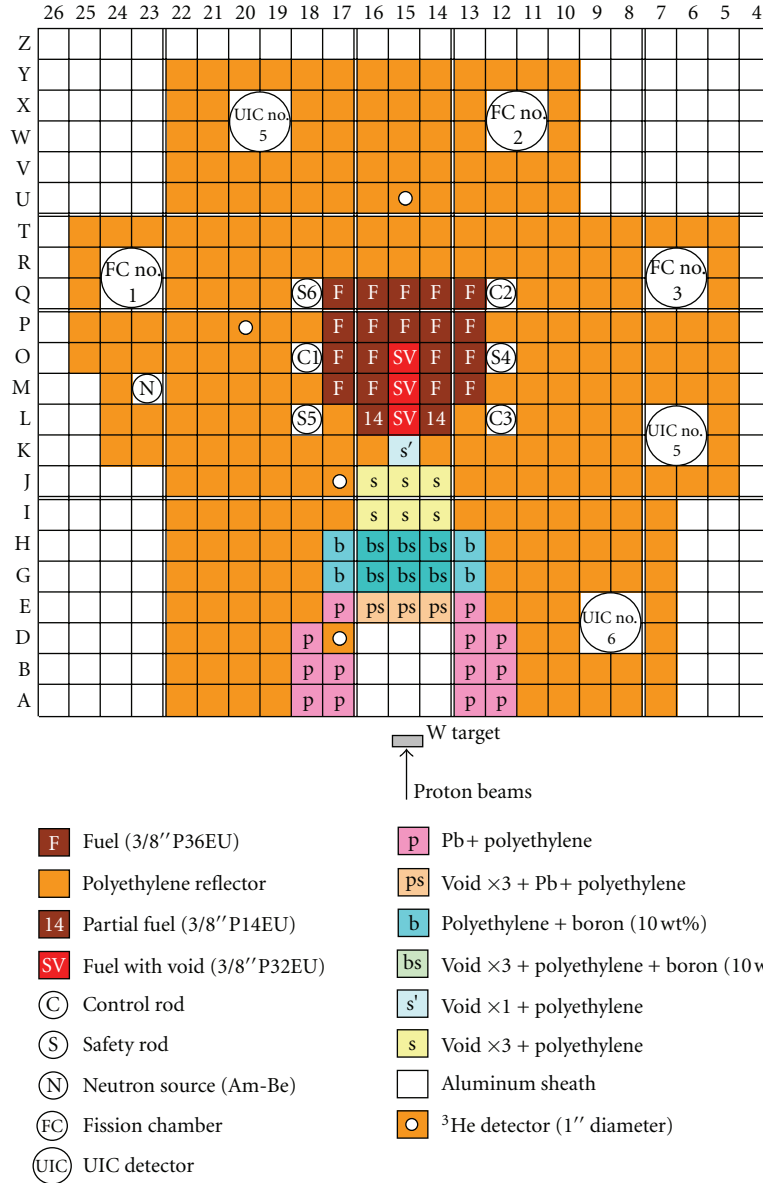


FIGURE 5: Top view of the KUCA A-core (A3/8''P36EU(3)) in the ADS experiments.

the subcritical multiplication parameters. The methodology of the theoretical basis used was as briefly described [29].

In the ADS study on the subcritical system, the neutron multiplication M is defined as the ratio of total fission neutrons F and the external neutron source rates S , to the rate of external neutron source as follows:

$$M = \frac{F + S}{S}. \quad (1)$$

The neutron multiplication M is also expressed by the subcritical multiplication factor k_s , which is defined as the ratio of the fission neutrons to the total neutrons in the system by the fission and source neutrons as follows:

$$M = \frac{1}{1 - k_s}. \quad (2)$$

In (1) and (2), k_s can be expressed by F and S as follows:

$$k_s = \frac{F}{F + S}. \quad (3)$$

Assuming that the fission reaction rate F is independent of one-dimensional (x -direction) in the thermal neutron field, the total fission neutrons can be expressed approximately by the In reaction rates R_{In} of $^{115}\text{In}(n, \gamma)^{116m}\text{In}$ reactions as follows:

$$F = \int_V \int_0^\infty \nu \Sigma_f(\underline{r}, E) \phi_s(\underline{r}, E) d\underline{r} dE \approx \int_a R_{In}(x, y_0, z_0) dx, \quad (4)$$

where V indicates the whole volume in the system, ν the average number of fission neutrons per fission reaction, Σ_f

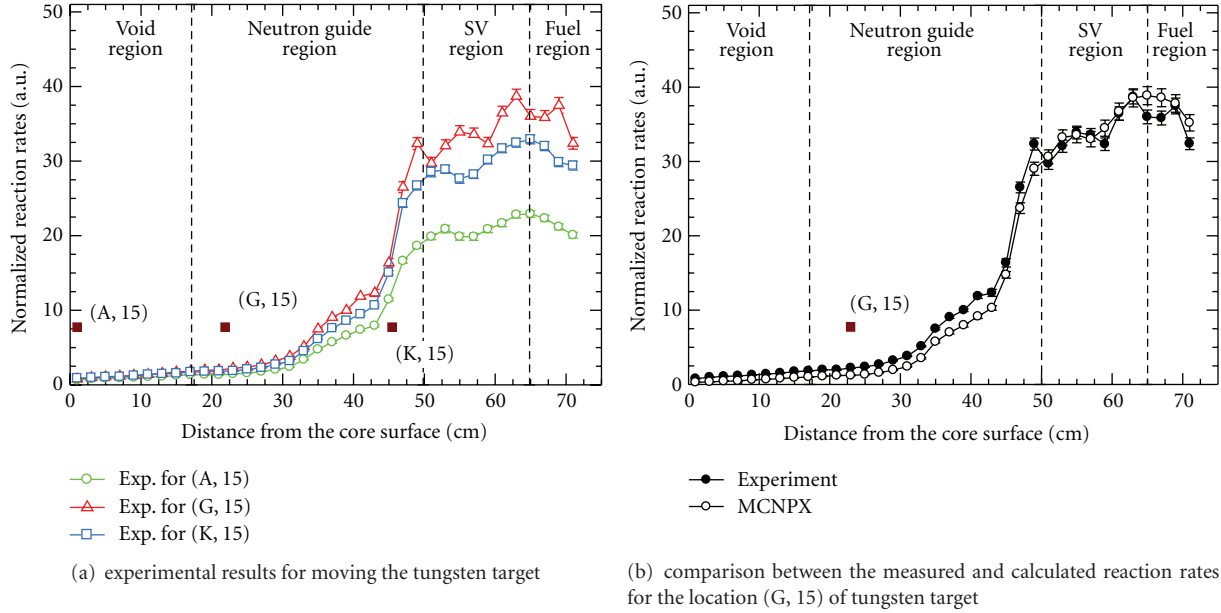


FIGURE 6: Reaction rates of $^{115}\text{In}(n, \gamma)^{116\text{m}}\text{In}$ reactions along the region (13-14, A-P; Figure 2) in the ADS experiments.

the fission cross-section, ϕ_s the neutron flux at position \underline{r} with energy E in the presence of an external source, and a the In wire along the fuel regions (SV and fuel regions; Figure 5) in the core. The external neutron source rate S can be expressed approximately by the In reaction rates $R_{\text{In}'}$ of $^{115}\text{In}(n, n')^{115\text{m}}\text{In}$ reactions in the same manner as that of (4) as follows:

$$S = \int_V \int_0^\infty s(\underline{r}, E) d\underline{r} dE \approx \int_{r_s} R_{\text{In}' }(\underline{r}) d\underline{r}, \quad (5)$$

where $s(\underline{r}, E)$ indicates the external neutron source rates at position \underline{r} with energy E , and r_s the position of external neutron source. The validity of approximation and the applicability of the methodology mentioned above have already been demonstrated in the previous study [29].

Finally, using (4) and (5), the neutron multiplication M and subcritical multiplication factor k_s in (1) and (3), respectively, can be expressed approximately as follows:

$$M \approx \frac{\int_a R_{\text{In}}(x, y_0, z_0) dx}{\int_{r_s} R_{\text{In}' }(\underline{r}) d\underline{r}} + 1, \quad (6)$$

$$k_s \approx \frac{\int_a R_{\text{In}}(x, y_0, z_0) dx}{\int_a R_{\text{In}}(x, y_0, z_0) dx + \int_{r_s} R_{\text{In}' }(\underline{r}) d\underline{r}}. \quad (7)$$

The measured reaction rates of the In wire (1.5 mm diameter and 750 mm long) emitted by $^{115}\text{In}(n, \gamma)^{116\text{m}}\text{In}$ reactions in the core were normalized by those of the ^{197}Au foil (8 mm diameter and 0.05 mm thick) emitted by $^{197}\text{Au}(n, \gamma)^{198}\text{Au}$ reactions attached at the core center (O, 15; Figure 5), and the reaction rates of the In foil ($10 \times 10 \times 1 \text{ mm}^3$) emitted by $^{115}\text{In}(n, n')^{115\text{m}}\text{In}$ reactions at moving the target were normalized by those of the ^{115}In foil ($10 \times 10 \times 1 \text{ mm}^3$) emitted by $^{115}\text{In}(n, n')^{115\text{m}}\text{In}$ reactions attached at

the original location of the target. The experimental error in each activation foil was estimated to be about 5%, including the statistical error of γ -ray counts and FWHM of the γ -ray spectrum peak. The calculated reaction rates of the In wire and the Au foil in the core were included in the simulated geometry and transport calculations and deduced from tallies taken in the fixed-source calculations. Also the calculated reaction rates of the In foil at the target was obtained by the same manner of the previous fixed source calculations, modeling the proton injection on the tungsten target.

The C/E value of the experiments and calculations of fission and source terms in (4) and (5), respectively, is shown in Table 3. Comparing with absolute values, the accuracy of fission term was within a relative difference of 20%, and that of the source term was well within the allowance for experimental error. The discrepancy between the measured and the calculated fission terms was caused mainly by the uncertainties of experimental values obtained from the reaction rates of the In wire especially in locations (G, 15) and (K, 15), because locations (G, 15) and (K, 15) were far from that of original target, and the proton weak and poor beams were in intensity and shape, respectively. As a result, it was considered that the In wire was not sufficiently activated to obtain the information on the thermal neutrons. As shown in Table 4, the neutron multiplication was considered to involve a large discrepancy caused by the evaluation of the C/E values of fission and source terms; inversely, the subcritical multiplication factor was considered fairly good in the evaluation of C/E values. The constant values of the measured and the calculated k_s demonstrated that the source term was not contributed largely to that of k_s , since the external source was located outside the core: the values of M and k_s in (1) and (2), respectively, were remarkably

TABLE 3: Comparison between the measured and calculated fission and source terms obtained from the experiments (Figure 5) and calculations (MCNPX with JENDL/HE-2007).

Case	Fission term F			Source term S		
	Calculation	Experiment	C/E	Calculation	Experiment	C/E
(A, 15)	46.37 ± 1.51	43.53 ± 0.27	1.07	0.04 ± 0.01	0.02 ± 0.01	1.70
(G, 15)	77.05 ± 2.50	67.34 ± 0.38	1.14	0.01 ± 0.01	0.02 ± 0.01	0.53
(K, 15)	68.55 ± 2.26	55.81 ± 0.29	1.23	0.03 ± 0.01	0.03 ± 0.01	1.14

TABLE 4: Comparison between the measured and calculated neutron multiplication and subcritical multiplication factor obtained from the experiments (Figure 5) and calculations (MCNPX with JENDL/HE-2007).

Neutron multiplication M			
Case	Calculation	Experiment	C/E
(A, 15)	$(1.15 \pm 0.04) \times 10^3$	$(1.83 \pm 0.05) \times 10^3$	0.63
(G, 15)	$(6.25 \pm 0.21) \times 10^3$	$(2.88 \pm 0.09) \times 10^3$	2.17
(K, 15)	$(2.04 \pm 0.09) \times 10^3$	$(1.88 \pm 0.05) \times 10^3$	1.08
Subcritical multiplication factor k_s			
Case	Calculation	Experiment	C/E
(A, 15)	0.99913 ± 0.00003	0.99945 ± 0.00001	1.00
(G, 15)	0.99984 ± 0.00003	0.99965 ± 0.00001	1.00
(K, 15)	0.99951 ± 0.00003	0.99947 ± 0.00001	1.00

dependent on that of F in (4), because of the location of the target outside the core. While the accuracy of the neutron multiplication was attributable to the experimental variation of reaction rates of the In wire, the actual effect of setting the tungsten target at location (G, 15) was found to be more significant than setting the target in the original location.

4. Conclusions

The ADS experiments with 100 MeV protons were carried out at KUCA to evaluate the subcritical multiplication parameters using the reaction rates. Comparison of the results of the experiments and the calculations by MCNPX with JENDL/HE-2007 revealed the following.

In the first injection experiments, the subcriticality C/E values of the experiments and the calculations were in fairly good agreement within a relative difference of 2%, and the calculated reaction rate distribution reconstructed the experimental one, although the proton beams were observed to be weak in intensity and poor in shape at the target. In the basic experiments, the notable effect of moving the target from the original location was clearly revealed in the analyses of the subcritical multiplication parameters for attaining further neutron multiplication in the core.

Further ADS study at KUCA needs to be conducted to investigate experimentally the effect of the subcritical multiplication parameters presented in this study, when the subcriticality and the neutron spectrum are varied. The present experimental data could be conducive to basic research of ADS, such as the verification of precision in numerical analyses by stochastic and deterministic approaches.

Acknowledgments

This work was supported by the ‘‘Energy Science in the Age of Global Warming’’ of the Global Center of Excellence (G-COE) program (J-051) of the Ministry of Education, Culture, Sports, Science and Technology of Japan. The authors are grateful to all the technical staff and students of KUCA for their assistance during the experiments.

References

- [1] R. Soule, W. Assal, P. Chaussonnet et al., ‘‘Neutronic studies in support of accelerator-driven systems: the MUSE experiments in the MASURCA facility,’’ *Nuclear Science and Engineering*, vol. 148, no. 1, pp. 124–152, 2004.
- [2] M. Plaschy, C. Destouches, G. Rimpault, and R. Chawla, ‘‘Investigation of ADS-Type heterogeneities in the MUSE4 critical configuration,’’ *Journal of Nuclear Science and Technology*, vol. 42, no. 9, pp. 779–787, 2005.
- [3] J. F. Lebrat, G. Aliberti, A. D’Angelo et al., ‘‘Global results from deterministic and stochastic analysis of the MUSE-4 experiments on the neutronics of accelerator-driven systems,’’ *Nuclear Science and Engineering*, vol. 158, no. 1, pp. 49–67, 2008.
- [4] C. M. Persson, A. Fokau, I. Serafimovich et al., ‘‘Pulsed neutron source measurements in the subcritical ADS experiment YALINA-Booster,’’ *Annals of Nuclear Energy*, vol. 35, no. 12, pp. 2357–2364, 2008.
- [5] Y. Gohar, G. Aliberti, I. Bolshinsky et al., ‘‘YALINA-booster subcritical assembly conversion,’’ *Transactions of American Nuclear Society*, vol. 101, pp. 39–40, 2009.
- [6] M. Tesinsky, C. Bergl of, T. B ack et al., ‘‘Comparison of calculated and measured reaction rates obtained through foil activation in the subcritical dual spectrum facility YALINA-Booster,’’ *Annals of Nuclear Energy*, vol. 38, no. 6, pp. 1412–1417, 2011.
- [7] H. H. Xia, ‘‘The progress of researches on ADS in China,’’ *ICFA Beam Dynamics Newsletter*, vol. 49, pp. 72–80, 2009.
- [8] C. H. Pyeon, Y. Hirano, T. Misawa et al., ‘‘Preliminary experiments on accelerator-driven subcritical reactor with pulsed neutron generator in Kyoto university critical assembly,’’ *Journal of Nuclear Science and Technology*, vol. 44, no. 11, pp. 1368–1378, 2007.
- [9] C. H. Pyeon, M. Hervault, T. Misawa, H. Unesaki, T. Iwasaki, and S. Shiroya, ‘‘Static and kinetic experiments on accelerator-driven system with 14 MeV neutrons in Kyoto University Critical Assembly,’’ *Journal of Nuclear Science and Technology*, vol. 45, no. 11, pp. 1171–1182, 2008.
- [10] C. H. Pyeon, H. Shiga, K. Abe et al., ‘‘Reaction rate analysis of nuclear spallation reactions generated by 150, 190, and 235 MeV protons,’’ *Journal of Nuclear Science and Technology*, vol. 47, no. 11, pp. 1090–1095, 2010.

- [11] C. H. Pyeon, H. Shiga, T. Misawa, T. Iwasaki, and S. Shiroya, "Reaction rate analyses for an accelerator-driven system with 14 MeV neutrons in the Kyoto university critical assembly," *Journal of Nuclear Science and Technology*, vol. 46, no. 10, pp. 965–972, 2009.
- [12] H. Taninaka, K. Hashimoto, C. H. Pyeon, T. Sano, T. Misawa, and T. Ohsawa, "Determination of lambda-mode eigenvalue separation of a thermal accelerator-driven system from pulsed neutron experiment," *Journal of Nuclear Science and Technology*, vol. 47, no. 4, pp. 376–383, 2010.
- [13] H. Taninaka, K. Hashimoto, C. H. Pyeon et al., "Determination of subcritical reactivity of a thermal accelerator-driven system from beam trip and restart experiment," *Journal of Nuclear Science and Technology*, vol. 48, no. 6, pp. 873–879, 2011.
- [14] H. Taninaka, A. Miyoshi, K. Hashimoto et al., "Feynman- α analysis for a thermal subcritical reactor system driven by an unstable 14 MeV neutron source," *Journal of Nuclear Science and Technology*, vol. 48, no. 11, pp. 1272–1280, 2011.
- [15] K. Tsujimoto, T. Sasa, K. Nishihara, H. Oigawa, and H. Takano, "Neutronics design for lead-bismuth cooled accelerator-driven system for transmutation of minor actinide," *Journal of Nuclear Science and Technology*, vol. 41, no. 1, pp. 21–36, 2004.
- [16] T. Sasa, H. Oigawa, K. Tsujimoto et al., "Research and development on accelerator-driven transmutation system at JAERI," *Nuclear Engineering and Design*, vol. 230, no. 1–3, pp. 209–222, 2004.
- [17] T. Sugawara, T. Iwasaki, T. Chiba, and K. Nishihara, "Development of dynamics code and proposal of start-up procedure for accelerator driven system," *Journal of Nuclear Science and Technology*, vol. 43, no. 1, pp. 20–31, 2006.
- [18] K. Nishihara, K. Iwanaga, K. Tsujimoto, Y. Kurata, H. Oigawa, and T. Iwasaki, "Neutronics design of accelerator-driven system for power flattening and beam current reduction," *Journal of Nuclear Science and Technology*, vol. 45, no. 8, pp. 812–822, 2008.
- [19] T. Sugawara, K. Nishihara, K. Tsujimoto, T. Sasa, and H. Oigawa, "Analytical validation of uncertainty in reactor physics parameters for nuclear transmutation systems," *Journal of Nuclear Science and Technology*, vol. 47, no. 6, pp. 521–530, 2010.
- [20] T. Sugawara, M. Sarotto, A. Stankovskiy, and G. Van Den Eynde, "Nuclear data sensitivity/uncertainty analysis for XT-ADS," *Annals of Nuclear Energy*, vol. 38, no. 5, pp. 1098–1108, 2011.
- [21] W. Uyttenhove, P. Baeten, G. Van Den Eynde, A. Kochetkov, D. Lathouwers, and M. Carta, "The neutronic design of a critical lead reflected zero-power reference core for on-line subcriticality measurements in accelerator driven systems," *Annals of Nuclear Energy*, vol. 38, no. 7, pp. 1519–1526, 2011.
- [22] M. Tanigaki, K. Takamiya, H. Yoshino, N. Abe, T. Takeshita, and A. Osanai, "Control system for the FFAG complex at KURRI," *Nuclear Instruments and Methods in Physics Research A*, vol. 612, no. 2, pp. 354–359, 2010.
- [23] T. Planche, E. Yamakawa, T. Uesugi et al., "Scaling FFAG rings for rapid acceleration of muon beams," *Nuclear Instruments and Methods in Physics Research A*, vol. 622, no. 1, pp. 21–27, 2010.
- [24] T. Planche, J.-B. Lagrange, E. Yamakawa et al., "Harmonic number jump acceleration of muon beams in zero-chromatic FFAG rings," *Nuclear Instruments and Methods in Physics Research A*, vol. 632, no. 1, pp. 7–17, 2011.
- [25] C. H. Pyeon, T. Misawa, J. Y. Lim et al., "First injection of spallation neutrons generated by high-energy protons into the kyoto university critical assembly," *Journal of Nuclear Science and Technology*, vol. 46, no. 12, pp. 1091–1093, 2009.
- [26] J. S. Hendricks, G. W. McKinney, L. S. Waters et al., *MCNPX User's Manual, Version 2.5.0*, LA-UR-05-2675, Los Alamos National Laboratory, 2005.
- [27] T. Fukahori, "JENDL high-energy file," *Journal of Nuclear Science and Technology*, vol. 2, supplement, pp. 25–30, 2002.
- [28] H. Takada, K. Kosako, and T. Fukahori, "Validation of JENDL high-energy file through analyses of spallation experiments at incident proton energies from 0.5 to 2.83 GeV," *Journal of Nuclear Science and Technology*, vol. 46, no. 6, pp. 589–598, 2009.
- [29] H. Shahbunder, C. H. Pyeon, T. Misawa, and S. Shiroya, "Experimental analysis for neutron multiplication by using reaction rate distribution in accelerator-driven system," *Annals of Nuclear Energy*, vol. 37, no. 4, pp. 592–597, 2010.

Research Article

Nuclear Level Density Parameters of $^{203-209}\text{Pb}$ and $^{206-210}\text{Bi}$ Deformed Target Isotopes Used on Accelerator-Driven Systems in Collective Excitation Modes

Şeref Okuducu,^{1,2} Nisa N. Aktı,³ Sabahattin Akbaş,³ and M. Orhan Kansu¹

¹Department of Physics, Faculty of Sciences, Gazi University, 06500 Ankara, Turkey

²Department of Physics, Faculty of Science and Arts, Bozok University, 66200 Yozgat, Turkey

³Institute of Science, Gazi University, Milas No 15 Street, Teknikokullar, 06500 Ankara, Turkey

Correspondence should be addressed to Şeref Okuducu, okuducu@gazi.edu.tr

Received 27 December 2011; Accepted 17 February 2012

Academic Editor: Alberto Talamo

Copyright © 2012 Şeref Okuducu et al. This is an open access article distributed under the Creative Commons Attribution License, which permits unrestricted use, distribution, and reproduction in any medium, provided the original work is properly cited.

The nuclear level density parameters of some deformed isotopes of target nuclei (Pb, Bi) used on the accelerator-driven subcritical systems (ADSs) have been calculated taking into consideration different collective excitation modes of observed nuclear spectra near the neutron binding energy. The method used in the present work assumes equidistant spacing of the collective coupled state bands of the considered isotopes. The present calculated results for different collective excitation bands have been compared with the compiled values from the literature for s-wave neutron resonance data, and good agreement was found.

1. Introduction

The knowledge of nuclear level densities is a crucial input in various fields/applications such as the creation of consistent theoretical description of excited nucleus properties and the nuclear reaction cross-section calculations for many branches of nuclear physics, nuclear astrophysics, nuclear medicine, and applied areas (medical physics, etc.) [1–14]. The neutron capture cross-sections, required for both design and nuclear model calculations in nuclear science and technologies, are approximately proportional to the corresponding level densities around the neutron resonance region. In nuclear medicine, the cross-section data obtained from nuclear level density approaches are needed to optimize production of radioactive isotopes for therapeutic purposes, for example, biomedical applications such as production of medical radioisotopes and cancer therapy and accelerator-driven incineration/transmutation of the long-lived radioactive nuclear wastes.

Recently, the accelerator-driven systems (ADSs), which are used for production of neutrons in spallation neutron source and can act as an intense neutron source in accelerator-driven subcritical reactors, and their neutronics have

been studied by many researchers [15–20]. Most of the studies were concerned with specific design concepts and the production of neutrons from spallation reactions. New accelerator-driven technologies make use of spallation neutrons produced in (p,xn) and (n,xn) nuclear reactions on high-Z targets. Through (p,xn) and (n,xn) nuclear reactions, neutrons are produced and moderated by heavy water in the target region and light water in the blanket region. These moderated neutrons are subsequently captured on ^3He , which flows through the blanket system, to produce tritium via the (n,p) reaction. Therefore, new nuclear cross-section data are needed to improve the theoretical predictions of neutron production, shielding requirements, activation, radiation heating, and material damage [21]. The design of ADS requires precise knowledge of nuclide production cross-sections in order to predict the amount of radioactive isotopes produced inside the spallation target (W, Pb, Bi, and other isotopes), may be liquid or solid [20–24]. However, the precision of models used to estimate production cross-sections is still far from the performance required for technical applications. An important applied field in the ADS systems, which is presently discussed, is the technical application of accelerator-driven subcritical reactors, of

nuclear collision processes for the energy production and the transmutation of nuclear waste in hybrid reactor systems.

Nuclear reactions calculations based on standard nuclear reaction models play an important role in determining the accuracy of various parameters of theoretical models and experimental measurements. Especially, the calculations of nuclear level density parameters for the isotopes can be helpful in the investigation of reaction cross-sections. In this manner, very sophisticated theoretical approaches have been developed to estimate total level densities of atomic nuclei, especially in the region of deformed heavy and light nuclei. However, in practice analytical expressions, which contain several parameters adjusted on scarce experimental data, are generally preferred [25].

The analytical expressions used for the nuclear level density calculations [2, 3, 5] are based on the Fermi gas model. The most widely used description of the nuclear level density is the Bethe formula, based on the thermodynamic relation between entropy and the average energy of a system considered in the framework of noninteracting particles of the Fermi gas. The traditional Bethe theory of the nuclear level density calculation, which uses the assumption that the individual neutrons and protons occupy a set of low energy levels in the ground state and fill up the higher individual states at any excitation energy, has been successfully used so far, with different contributions made to this model in the form of shell, pairing, deformation effects [4, 26–29], finite size effects [30], and thermal and quantal effects [31], as well as improvements in the determination of the spin cut-off factors [32]. However, such contributions do not take into account the collective effects, which may play a basic role in describing the nuclear level density of some deformed nuclides.

Calculations of all parameters of fission and fusion reactors, accelerator-driven systems, and other nuclear technology fields depend strongly on cross-section data. And, it is well known that nuclear level density parameters are of crucial importance for the cross-section. In light of the preceding knowledge in the present study, the nuclear level density parameters of deformed $^{203-209}\text{Pb}$ and $^{206-210}\text{Bi}$ target isotopes used on the ADS systems have been calculated by using different collective excitation modes of the observed nuclear spectra near the neutron binding energy and a simple model introduced in our previous works [6–12], in which the collective character of the nuclear excitations is available.

2. Theoretical View Point of the Nuclear Level Density

The above-mentioned Bethe theory gives also the dependence of the nuclear level density on the total angular momentum J of the nucleus. The expression used for the observable nuclear level density at any excitation energy U and momentum J can be written as [2, 3]

$$\rho(U, I) = \frac{\sqrt{\pi} \exp(2\sqrt{aU})}{12a^{1/4}U^{5/4}} \frac{(2I+1) \exp\left[-(I+(1/2))^2/2\sigma^2\right]}{2\sqrt{2\pi}\sigma^3}, \quad (1)$$

where a and σ are the level density parameter and spin distribution parameter, respectively. The parameters a and σ are defined by

$$a = \frac{\pi^2}{6} g(\varepsilon_F), \quad (2)$$

$$\sigma^2 = g(\varepsilon_F) \langle m^2 \rangle t. \quad (3)$$

Here, the parameter $g(\varepsilon_F)$ is the sum of the neutron and proton single-particle states density at the Fermi energy ε_F , $\langle m^2 \rangle$ is the mean square magnetic quantum number for single-particle states, and t is the nuclear thermodynamic temperature of an excited nucleus in the Fermi gas model. These factors are expressed as follows:

$$g(\varepsilon_F) = \frac{3}{2} \frac{A}{\varepsilon_F}, \quad \langle m^2 \rangle = 0, 146 A^{2/3}, \quad t^2 = \frac{U}{a}, \quad (4)$$

where A is the mass number of a nucleus.

The experimental observations cannot determine the different orientation of nuclear angular momentum J . Therefore, it is useful to obtain the observable level density, which has the form [3, 4]

$$\rho(U) = \sum_J \rho(U, J) = \frac{\sqrt{\pi} \exp(2\sqrt{aU})}{12} \frac{1}{a^{1/4} U^{5/4} \sqrt{2\pi}\sigma}. \quad (5)$$

Hence, substitute (2)–(4) into (5) to find the observable level density as

$$\rho(U) = \frac{a}{12\sqrt{2} \times 0.298 A^{1/3} (aU)^{3/2}} \exp(2\sqrt{aU}). \quad (6)$$

The level density parameters of the Bethe theory have been well established in a number of studies [3, 33, 34] on the s-wave neutron resonance for different mass nuclei. However, this theory does not take into account the collective effects of the nuclear particles in the excitation of the nuclei. On the other hand, the measured magnetic and quadrupole moments of the nuclei deviate considerably from the ones calculated using the single-particle shell model in which the closed shells forming the nuclear core play no part. In other words, the excited states and the magnetic and quadrupole moments are the results of collective motion of many nucleons, not just of those nucleons that are outside the closed shell. The collective motion of the nucleons may be described as a vibrational motion about the equilibrium position and a rotational motion that maintains the deformed shape of the nucleus.

3. Collective Excitation Modes of Deformed Nuclei

The existence of collective energy level bands of rotational and vibrational types can now easily be identified from nuclear spectra data [35] of many deformed nuclei. In the studies in [34, 36] the contribution of collective motion of nucleons to the energy level density has been considered. However, these studies naturally involve messy equations and

make the model complex for calculation of the nuclear level density parameters of deformed nuclei. A simpler description of collective model was first suggested by Rainwater [37] who made clear the relationship between the motion of individual nuclear particles and the collective nuclear deformation. Later a quantitative development of the nuclear collective model taking into consideration the collective motion of the nuclear particles was given by [30, 38–40]. Recently in considerable studies such as in [6–12], it has been attempted to identify the nuclear level density parameters in the region of some light and large deformed nuclei by the use of a simple model of nuclear collective excitation mechanism. Almost all data on the estimated level density parameters of these deformed nuclei are well identified on a base of collective rotational and collective vibrational bands such as ground state band, β band, octupole band, γ -band, and so forth.

Some deformed isotopes used on ADS systems have also stable deformation in their ground states. Such isotopes studied may rotate due to interactions with an external incident particle or emitting the particle. Rotational energy of an axially symmetric deformed even-even nucleus is given as [30]

$$E_{\text{rot}}(I, K) = \frac{\hbar^2}{2} \left[\frac{I(I+1)}{J_0} + \left(\frac{1}{J_3} - \frac{1}{J_0} \right) K^2 \right], \quad (7)$$

where I and K are the total angular momentum and its projection on the axis of symmetry, respectively, of a nucleus and J_3 and J_0 are moments of inertia about a symmetry axis and an arbitrary axis perpendicular to the symmetry axis, respectively. The authors of [30] have used the hydrodynamic moments of inertia restricting the deformed nuclear surface by a quadrupole term only. In this model one can admit $J_3 = 0$, which requires the value of K in (7) to be identically zero. Then, we come to the following rotational energy equation:

$$E_{\text{rot}} = \frac{\hbar^2}{2J_0} I(I+1), K = 0. \quad (8)$$

The above expression is in good agreement with the observed low-lying energy levels of the even-even large deformed nuclei, which are the values of angular momentum I , $I = 0, 2, 4, 6, \dots$. As mentioned above the energy level sequence in such a case is called ground state rotational band having positive parity.

In the following collective vibrational modes, we consider two modes, namely, the quadrupole and the octupole vibrational modes. The quadrupole mode, also called β -vibrational band, carries two units of angular momentum and even parity (0^+ , 2^+ , 4^+ , 6^+ , ...) while the octupole vibrational band carries two units of angular momentum and negative parity (1^- , 3^- , 5^- , 7^- , ...). Here, the β band is associated with vibrations that preserve the axis of symmetry and therefore is $K = 0$ band with the level sequence given by (8) and the band head $\hbar\omega_\beta$. Another excited band is often called the gamma band γ and is associated with the vibrations not preserving the symmetry axis and having the levels given by (7). The spin sequence of γ band with $K = 2$ is $I = 2^+, 3^+, 4^+, 5^+, \dots$

In such a case, in deformed odd- A isotopes simple identification of the observed nuclear levels is made on a base

of a strong coupling of a nucleon to an axially symmetric even-even deformed core. The rotational band with a given K value and spin sequence $I = K = \Omega, K+1, K+2, \dots$, where K and Ω are the projections of the total angular momentum and odd nucleon angular momentum, respectively, on the nuclear symmetry axis, has level spacing [41]

$$\Delta E(I, K) = E_{IK} - E_{K,K} = \frac{\hbar^2}{2J_0} [I(I+1) - K(K+1)]. \quad (9)$$

4. Calculation Method of Nuclear Level Density Parameter

The method used in this present study for calculation of nuclear level density parameters of some deformed target isotopes has been given in detail in the studies of [6–12]. Similarly, the mentioned method, in this study, can also be applicable to deformed target isotopes of interest.

In any case, the nuclear energy level density depending on the excitation energy, U , taking into account different excitation modes can be expressed in the following form:

$$\rho(U) = \sum_i a_i \rho_i(U), \quad (10)$$

where $\rho_i(U)$ is the partial energy level density at the excitation U for the i th excitation mode and a_i is the weighting coefficient satisfying the condition $\sum_i a_i = 1$. In the present work, we use a simple expression for the energy level density, which considered the collective excitation modes. Here, in our determination of the nuclear level density due to excitation bands the “equidistant” condition between energy levels, which is the important property of the observed energy spectrum of isotopes considered, should be satisfied. These properties can approximately be verified for the energies of the coupled state bands in deformed isotopes considered as being the ratios given by

$$R_1 : R_2 : R_3 : R_4 : \dots = 1 : r : 2r : 3r : \dots \quad (11)$$

Here, $R_1, R_2, R_3, R_4, \dots$ are the ratios of the sequential level energies to the appropriate energy unit of a corresponding band. When the above relation is satisfied, in our study, the nuclear level density formula introduced depending on the excitation energy U and energy unit ε_o for the i th excitation band can be represented as [6–12]

$$\rho_i(U, \varepsilon_{oi}) \cong \frac{\pi^2 a_{oi}}{24\sqrt{3}(a_{oi}U)^{3/2}} \exp\left(2\sqrt{a_{oi}U}\right), \quad (12)$$

which are fairly simple and contain only one parameter a_{oi} defined as

$$a_{oi} = \frac{\pi^2}{6\varepsilon_{oi}} \quad (13)$$

and represents a collective level density parameter corresponding to the i th band with the unit energy ε_{oi} . The

unit energies are $\varepsilon_{0GS} = E(2^+)$, $\varepsilon_{0\beta} = E(2^+) - E(0^+)$, and $\varepsilon_{0oct} = E(3^-) - E(1^-)$ for ground state, β , and octupole bands, respectively. Similarly, the other excitation bands can be included. In the even-even and odd- A isotopes it has been shown that the unit energy is either energy of the first excited state (for ground state bands) or the energy separation between the second and first excited states (for excited bands) of the corresponding band with the given projection of the total angular momentum K . For the applicability of (12) in our identification of the nuclear level density due to different excitation bands, the “equidistant” condition between energy levels should be satisfied. As mentioned before, these band energies clearly should, at least approximately, satisfy (11).

Now, the observable level density expressions of (6) and (12) can be compared which have similar dependence on the energy, although they have been obtained from different approaches. Equation (6) obtained from the Bethe theory has been based on a single-particle nuclear model, whereas (12) has been extracted from the symmetry properties of the nuclear spectra data expressed by (11). In the previous works [7–12], our approach has been successfully used in the classification of the level density parameters for different light and large deformed nuclei.

In the same way, in the present work, this approach takes into consideration the different collective excitation modes in deformed target isotopes that are interesting, and the nuclear level density parameters a_{oi} defined by (13) can easily be obtained from nuclear spectra data given in [36] regarding nuclear level spectra of collective rotational and collective vibrational bands. The theoretical obtained values for $^{203-209}\text{Pb}$ and $^{206-210}\text{Bi}$ isotopes with their different corresponding bands have been listed in Tables 1 and 2.

5. Results and Discussion

In the present paper, we have calculated the nuclear level density parameters of deformed target isotopes $^{203-209}\text{Pb}$ and $^{206-210}\text{Bi}$ used on ADS by using different collective excitation modes of observed nuclear spectra. It has been seen that the nuclear energy levels of different collective excitation bands (in particular, the bands given in Tables 1 and 2) in the investigated isotopes also approximately satisfy (11). Thus, (13) can be applied for determination of the corresponding level density parameters. The calculated values of the level density parameters due to different excitation bands and the compiled values of those parameters have been represented in Tables 1 and 2 for the deformed target isotopes considered. The demonstrated values of the parameters a are given in Tables 1 and 2. Figure 1 was compiled by Gilbert and Cameron [3], Baba [33], BSFG model [4], and Mughabghab and Dunford [42] and Figure 2 was compiled by Gilbert and Cameron [3] and Rohr [34] for s-wave neutron resonances near the neutron binding energy.

In Figures 1 and 2 we illustrate the comparison of the single-particle level density parameters a and the mass number with our calculated values of a_0 corresponding to the different bands for $^{203-209}\text{Pb}$ and $^{206-210}\text{Bi}$ deformed isotopes, respectively. From Figures 1 and 2, it is clear that the present values of the level density parameters a_0

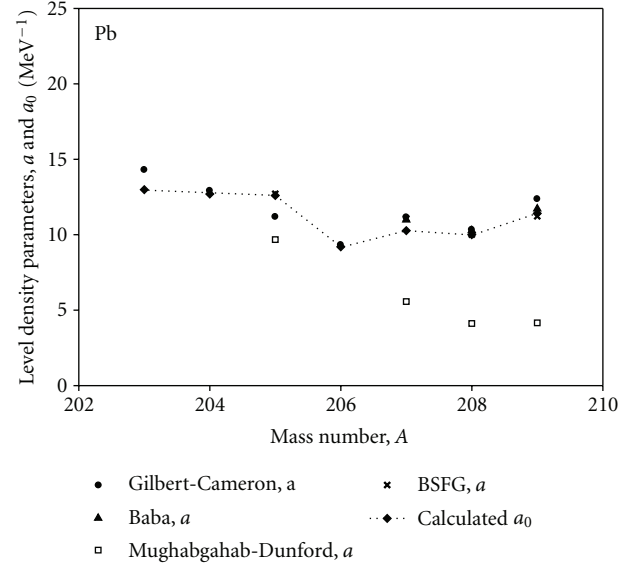


FIGURE 1: Mass dependence of the calculated nuclear level density parameters a_0 and those of the compiled values a for $^{203-209}\text{Pb}$ deformed isotopes.

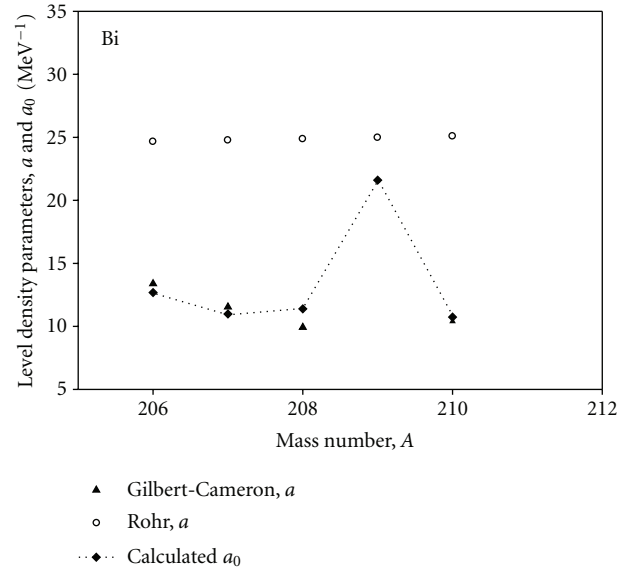


FIGURE 2: Mass dependence of the calculated nuclear level density parameters a_0 and those of the compiled values a for $^{206-210}\text{Bi}$ deformed isotopes.

calculated by (13) for these considered isotopes are well consistent with the compiled values of parameters a . As seen in Figure 1, the dominant bands in the population of $^{203-205}\text{Pb}$ deformed isotopes generally seem to be the well-known collective bands (especially ground state, octupole, and gamma vibrational bands; see also Table 1), as to $^{206-209}\text{Pb}$ deformed isotopes it seems to be the mixed bands (negative and positive parity bands). As clear from Figure 2, we can say that the calculated values a_0 for the mixed bands (negative and positive parity bands) of $^{206-210}\text{Bi}$ are generally good

TABLE 1: The calculated and compiled values of the nuclear level density parameters for $^{203-209}\text{Pb}$ isotopes.

Radionuclides	Gilbert and Cameron [3], a (MeV^{-1})	Baba [33], a (MeV^{-1})	Mughabghab-Dunford [42], a (MeV^{-1})	BSFG Egidy and Bucurescu [4], a (MeV^{-1})	Calculated a_0 (MeV^{-1})	Corresponding bands
^{203}Pb ₈₂					12.99	Ground state band
					21.04	Octupole vibration band
					27.39	Octupole vibration band
	14.29	—	—	—	2.22	Negative parity band
					1.96	Positive parity band
					17.94	Negative parity band
					7.30	Negative parity band
^{204}Pb ₈₂					1.83	Ground state rotational band
					19.85	Beta vibration band
					12.70	Gamma vibration band
					2.33	Gamma vibration band
					6.48	Gamma vibration band
					7.13	Beta vibration band
	12.91	—	—	—	9.33	Negative parity band
					4.67	Octupole vibration band
					20.57	Positive parity band
					7.04	Positive parity band
				9.54	Positive parity band	
				19.85	Beta vibration band	
				9.20	Beta vibration band	
^{205}Pb ₈₂					6.31	Octupole vibration band
					8.51	Octupole vibration band
					2.40	Positive parity band
	11.18	—	9.68	12.71	8.87	Negative parity band
					12.60	Octupole vibration band
					15.21	Octupole vibration band
					19.70	Positive parity band
^{206}Pb ₈₂					2.05	Ground state rotational band
					5.44	Beta vibration band
					8.80	Beta vibration band
					3.06	Gamma vibration band
					2.25	Gamma vibration band
	9.32	—	—	—	3.98	Gamma vibration band
					12.00	Gamma vibration band
					3.42	Negative parity band
					9.20	Negative parity band
					12.23	Negative parity band
				20.64	Positive parity band	

TABLE 1: Continued.

Radionuclides	Gilbert and Cameron [3], a (MeV ⁻¹)	Baba [33], a (MeV ⁻¹)	Mughabghab-Dunford [42], a (MeV ⁻¹)	BSFG Egidy and Bucurescu [4], a (MeV ⁻¹)	Calculated a_0 (MeV ⁻¹)	Corresponding bands
²⁰⁷ Pb ₈₂	—	10.98	5.57	11.08	2.88	Neutron hole states and ground state
					2.10	Single-neutron states G9/2, I11/2, J15/2, D5/2, S1/2, D3/2
					20.93	Positive parity band
					6.40	Negative parity band
					10.27	Positive parity band
					20.03	Positive parity band
					13.04	Positive parity band
					13.69	Positive parity band
					1.91	Negative parity band
					6.91	Positive parity band
²⁰⁸ Pb ₈₂					9.01	Positive parity band
					10.00	Positive parity band
					2.29	Negative parity band
					14.41	Octupole vibration band
		10.28	4.12	10.01	17.48	Octupole vibration band
					15.02	Octupole vibration band
					12.45	Octupole vibration band
					12.26	Octupole vibration band
					9.98	Octupole vibration band
					8.47	Octupole vibration band
²⁰⁹ Pb ₈₂					7.77	Negative parity band
					2.11	Ground state band
					36.52	Octupole vibration band
		11.72	4.16	11.22	9.69	Octupole vibration band
					16.43	Negative parity band
					11.41	Negative parity band
				3.25	Positive parity band	

TABLE 2: The calculated and compiled values of the nuclear level density parameters for $^{206-210}\text{Bi}$ isotopes.

Radionuclides	Gilbert and Cameron [3], a (MeV^{-1})	Rohr [34], a (MeV^{-1})	Calculated a_0 (MeV^{-1})	Corresponding bands
^{207}Bi 83	13.39	24.65	27.43	Ground state band
			14.41	Gamma vibration band
			12.68	Positive parity band
			3.60	Positive parity band
			11.64	Positive parity band
			2.76	Negative parity band
			10.96	Negative parity band
			5.17	Negative parity band
			5.83	Positive parity band
			1.66	Single-proton states: H9/2, F7/2, I13/2
^{208}Bi 83	11.54	24.76	22.51	Conf = ((206PB 2+), (P, 1H9/2))
			13.98	Conf = ((206PB 3+), (P, 1H9/2))
			10.39	Conf = ((P, 1H9/2 + 2, 0+), (P, NLJ, 1, 1+))
			1.83	(N, 3P1/2, -2, 0+))J + Conf = ((P, 1H9/2)
			2.45	(N, 1I13/2, -1) (N, NLJ, -1))
			6.27	Ground state band
			10.98	Negative parity band
			26.00	Negative parity band
			3.22	Positive parity band
			14.01	Positive parity band
^{209}Bi 83	9.92	24.86	25.96	Ground state band
			15.16	Positive parity band
			25.13	Positive parity band
			2.57	Positive parity band
			11.39	Gamma vibration band
			3.58	Gamma vibration band
			5.52	Negative parity band
			6.77	(208 PB 4-) (P, 1H9/2)
			20.93	(208 PB 5-) (P, 1H9/2)
			1.83	Single-proton states
32.89	(210 PO 0+) (P, NLJ, -1)			
^{210}Bi 83	10.40	25.08	14.84	Positive parity band
			32.09	Positive parity band
			21.60	Positive parity band
			11.73	Positive parity band
			2.03	Octupole vibration band
			35.31	Ground state band
			8.98	Negative parity band
			10.74	Positive parity band
			35.82	Negative parity band
			17.80	Negative parity band
7.85	Octupole vibration band			

dominant bands. The values of the calculated parameters of these bands are well consistent with those of the compiled data, in particular with the data of Gilbert and Cameron [3] for $^{206-210}\text{Bi}$.

6. Conclusions

On the basis of the above presented discussion we can conclude that the nuclear level density parameters of deformed target isotopes $^{203-209}\text{Pb}$ and $^{206-210}\text{Bi}$ used on the ADS can be identified by the use of collective vibrational bands taking into consideration the equidistant character of these bands including higher excitations. The nuclear energy level density at any excitation near the neutron binding energy may clearly have generally the same character such as collective rotational, collective vibrational, and intrinsic. Actually, as it has clearly been seen from Tables 1 and 2 and Figures 1 and 2, no dominant band alone is exactly responsible for identification of level density parameters a for the considered isotopes. Namely, the nuclear level density for such isotopes apparently should involve combination of partial level densities corresponding to the different bands, which is given by (10).

Consequently, we remark that the nuclear collective excitation modes are quite meaningful in order to obtain the level density parameters of different isotopes. The calculation of these parameters based on the properties of the measured nuclear low-lying level spectra should prove a productive area of study that should override the inherent experimental difficulties involved. Hence, at least such parameters can be useful in the design of an ADS system, which requires precise knowledge of isotopes production cross-sections in order to predict the amount of radioactive isotopes produced inside the spallation targets such as Pb and Bi isotopes.

Acknowledgment

This work has partially been supported by the project of Gazi University (BAP), Code no. 05/2010-28.

References

- [1] S. Shaleen, *Calculation of nuclear level densities near the drip lines*, Ph.D. thesis, Faculty of the College of Arts and Sciences of Ohio University, Physics and Astronomy, 2008.
- [2] H. A. Bethe, "An attempt to calculate the number of energy levels of a heavy nucleus," *Physical Review*, vol. 50, no. 4, pp. 332–341, 1936.
- [3] A. Gilbert and A. G. W. Cameron, "A composite nuclear-level density formula with shell corrections," *Canadian Journal of Physics*, vol. 43, pp. 1446–1496, 1965.
- [4] T. Von Egidy and D. Bucurescu, "Systematics of nuclear level density parameters," *Physical Review C*, vol. 72, no. 4, 2005.
- [5] A. V. Ignatyuk and N. Yu Shubin, "Role of collective effects in the systematics of nuclear level densities," *Soviet Journal of Nuclear Physics*, vol. 8, p. 660, 1969.
- [6] H. Ahmadov, I. Zorba, M. Yilmaz, and B. Gönül, "On the level density of even-nuclei in the regions of rare-earth and actinide elements," *Nuclear Physics A*, vol. 706, no. 3-4, pp. 313–321, 2002.
- [7] Ş. Okuducu and H. Ahmadov, "On the estimation of nuclear level density parameters in the region of some large deformed nuclei," *Physics Letters B*, vol. 565, no. 1-4, pp. 102–106, 2003.
- [8] Ş. Okuducu, E. Eser, and S. Sönmezoglu, "Analysis of the nuclear level-density parameters of some large deformed odd-A and odd-odd nuclei in the region of Rare Earth Elements," *Nuclear Science and Engineering*, vol. 154, no. 3, pp. 374–381, 2006.
- [9] Ş. Okuducu, S. Sönmezoglu, and E. Eser, "Calculation of nuclear level density parameters of some deformed light nuclei using collective excitation modes," *Physical Review C*, vol. 74, no. 3, Article ID 034317, 2006.
- [10] Ş. Okuducu, N. N. Akti, H. SaraÇ, M. H. Bölükdemir, and E. Tel, "Calculation of nuclear level density parameters of some light deformed medical radionuclides using collective excitation modes of observed nuclear spectra," *Modern Physics Letters A*, vol. 24, no. 33, pp. 2681–2691, 2009.
- [11] Ş. Okuducu and N. N. Akti, "Nuclear level density parameters of some largely deformed nuclei of medical radionuclides in low-lying collective excitation modes," *Kerntechnik*, vol. 75, no. 3, pp. 109–116, 2010.
- [12] Ş. Okuducu, N. N. Akti, and E. Eser, "The theoretical nuclear level density parameters of some deformed target radioisotopes 181–187 W and 196–204 Hg used on the accelerator-driven systems," *Annals of Nuclear Energy*, vol. 38, no. 8, pp. 1769–1774, 2011.
- [13] D. Bucurescu and T. Von Egidy, "Systematics of nuclear level density parameters," *Journal of Physics G*, vol. 31, no. 10, pp. S1675–S1680, 2005.
- [14] S. K. Kataria, V. S. Ramamurthy, and S. S. Kapoor, "Semiempirical nuclear level density formula with shell effects," *Physical Review C*, vol. 18, no. 1, pp. 549–563, 1978.
- [15] T. Takizuka, T. Nishida, M. Mizumoto, and H. Yoshida, "JAERI R&D on accelerator-based transmutation under OMEGA Program," in *Proceedings of the International Conference on Accelerator-Driven Transmutation Technologies and Applications*, pp. 64–73, Las Vegas, Nev, USA, 1994.
- [16] A. Boudard, F. Borne, F. Brochard et al., "Spallation study with proton beams around 1 GeV: neutron production," *Nuclear Physics A*, vol. 663-664, no. 1-2, 2000.
- [17] C. H. M. Broeders and I. Broeders, "Neutron physics analyses of accelerator-driven subcritical assemblies," *Nuclear Engineering and Design*, vol. 202, no. 2-3, pp. 209–218, 2000.
- [18] H. Yapici, G. Genç, and N. Demir, "Neutronic limits in infinite target mediums driven by high energetic protons," *Annals of Nuclear Energy*, vol. 34, no. 5, pp. 374–384, 2007.
- [19] I. Demirkol, E. Tel, A. Arasoğlu et al., "The neutron production cross sections for Pb, Bi, and Au targets and neutron multiplicity for nuclear spallation reaction induced by 20- to 1600 MeV protons," *Nuclear Science and Engineering*, vol. 147, no. 1, pp. 83–91, 2004.
- [20] A. Kaplan, E. Tel, E. G. Aydin, A. Aydin, and M. Yilmaz, "Spallation neutron emission spectra in medium and heavy target nuclei by a proton beam up to 140 MeV energy," *Applied Radiation and Isotopes*, vol. 67, no. 4, pp. 570–576, 2009.
- [21] E. G. Aydin, E. Tel, A. Kaplan, and A. Aydin, "Equilibrium and pre-equilibrium calculations of neutron production in medium-heavy targets irradiated by protons up to 100 MeV," *Annals of Nuclear Energy*, vol. 35, no. 12, pp. 2306–2312, 2008.
- [22] C. Rubbia and J. A. Rubio, "A Tentative Programme Towards a Full Scale Energy Amplifier," CERN/LHC/96-11 (EET), Geneva, Switzerland, 1996.

- [23] E. Tel, H. M. Şahin, A. Kaplan, A. Aydin, and T. Altinok, "Investigation of the properties of the nuclei used on the new generation reactor technology systems," *Annals of Nuclear Energy*, vol. 35, no. 2, pp. 220–227, 2008.
- [24] I. Demirkol, A. Arasoğlu, and E. Tel, "Neutron multiplicity with 1.0 and 1.2 GeV proton-induced spallation reactions on thin targets," *Chinese Journal of Physics*, vol. 46, no. 2, pp. 124–134, 2008.
- [25] S. Hilaire, "Energy dependence of the level density parameter," *Physics Letters B*, vol. 583, no. 3-4, pp. 264–268, 2004.
- [26] S. E. Woosley, *Theory and Applications of Moments Methods in Many-Fermion Systems*, Plenum, New York, NY, USA, 1980.
- [27] P. L. Huang, S. M. Grimes, and T. N. Massey, "Level densities for nuclei with $20 \leq A \leq 41$," *Physical Review C*, vol. 62, no. 2, pp. 240021–2400212, 2000.
- [28] T. Newton, "Shell effects on the spacing of nuclear levels," *Canadian Journal of Physics*, vol. 34, pp. 804–829, 1956.
- [29] T. Ericson, "Level density of degenerate Fermi systems," *Nuclear Physics*, vol. 8, no. C, pp. 265–283, 1958.
- [30] A. Bohr and B. Mottelson, *Nuclear Structure, Vol. II*, Benjamin, New York, NY, USA, 1969.
- [31] G. Puddu, P. F. Bortignon, and R. A. Broglia, "Nuclear level densities including thermal and quantal fluctuations," *Physical Review C*, vol. 42, no. 5, pp. R1830–R1833, 1990.
- [32] B. J. Dalton, S. M. Grimes, J. P. Vary, and S. A. Williams, *Theory and Applications of Moments Methods in Many-Fermion Systems*, Plenum, New York, NY, USA, 1980.
- [33] H. Baba, "A shell-model nuclear level density," *Nuclear Physics A*, vol. 159, no. 2, pp. 625–641, 1970.
- [34] G. Rohr, "New perspectives on the level density of compound resonances," *Zeitschrift für Physik A*, vol. 318, no. 3, pp. 299–308, 1984.
- [35] Nuclear Structure and Decay Data, National Nuclear Data Center. Brookhaven National Laboratory. ENSDF (Evaluated Nuclear Structure Data File), Upton, NY, USA, 2001.
- [36] A. V. Ignatyuk, K. K. Istekov, and G. N. Smirenkin, "Collective effects in level density, and the probability of fission," *Soviet Journal of Nuclear Physics*, vol. 29, pp. 450–454, 1979.
- [37] J. Rainwater, "Nuclear energy level argument for a spheroidal nuclear model," *Physical Review*, vol. 79, no. 3, pp. 432–434, 1950.
- [38] A. Bohr, "On the quantization of angular momenta in heavy nuclei," *Physical Review*, vol. 81, no. 1, pp. 134–138, 1951.
- [39] A. S. Davydov and G. F. Filippov, "Rotational states in even atomic nuclei," *Nuclear Physics*, vol. 8, no. C, pp. 237–249, 1958.
- [40] A. S. Davydov and A. A. Chaban, "Rotation-vibration interaction in non-axial even nuclei," *Nuclear Physics*, vol. 20, no. C, pp. 499–508, 1960.
- [41] J. P. Davidson, *Collective Models of the Nucleus*, Academic Press, New York, NY, USA, 1968.
- [42] S. F. Mughabghab and C. L. Dunford, "New approach for the determination of the nuclear level density parameters," in *Proceedings of the International Conference on Physics of Nuclear Science and Technology*, American Nuclear Society, Long Island, NY, USA, October 1998, Report BNL-NCS-65712, Brookhaven National Laboratory.

Research Article

Detector Dead Time Determination and Optimal Counting Rate for a Detector Near a Spallation Source or a Subcritical Multiplying System

V. Bécares and J. Blázquez

Division of Nuclear Fission, CIEMAT, Avenida Complutense 40, 28040 Madrid, Spain

Correspondence should be addressed to V. Bécares, vicente.becares@ciemat.es

Received 14 November 2011; Revised 10 February 2012; Accepted 14 February 2012

Academic Editor: Alberto Talamo

Copyright © 2012 V. Bécares and J. Blázquez. This is an open access article distributed under the Creative Commons Attribution License, which permits unrestricted use, distribution, and reproduction in any medium, provided the original work is properly cited.

The operation of accelerator-driven systems or spallation sources requires the monitoring of intense neutron fluxes, which may be billions-fold more intense than the fluxes obtained with usual radioactive sources. If a neutron detector is placed near a very intense source, it can become saturated because of detector dead time. On the contrary, if it is placed far away from the source, it will lose counting statistics. For this reason, there must exist an optimal position for placing the detector. The optimal position is defined as the one with the minimal relative uncertainty in the counting rate. In this work, we review the techniques to determine the detector dead time that can be applied with an accelerator-driven subcritical system or a spallation source. For the case of a spallation source, counting rates do not follow Poisson's statistics because of the multiplicity of the number of neutrons emitted by incident proton. It has been found a simple expression that relates the optimal counting rate with the source multiplicity and the uncertainty in the determination of the dead time.

1. Introduction

A strong interest in intense accelerator-driven neutron sources for different applications has grown in the last decades. Although a number of reactions is available for neutron production with accelerated particles (photoneutrons, D-Be...), preferred technology for these neutron sources is spallation, because it provides the highest neutron yield per unit of energy of the incident particles. Neutron spallation sources consist of a high-energy proton accelerator coupled to a high Z target. Typically, a 1000 MeV incident proton beam could produce ~ 50 nucleons per incident proton, approximately half of them neutrons [1]. In this way, very intense neutron fluxes can be obtained (over 10^{15} n/cm² s). Although current mode detectors are generally preferred for monitoring such high fluxes, pulse mode detectors are also of interest because of their ability to record information from the individual detector signals. However, if a pulsed mode detector is used to monitor such high fluxes, it can become saturated because of dead time effects.

An important application of spallation sources is to drive accelerator-driven systems (ADSs). An ADS consists of a subcritical reactor driven by an external spallation neutron source. The interest in these systems has risen since the 1990s [2–6] as it has been recognized their ability to reduce the volume and radiotoxicity of high-level nuclear waste. Operation of ADSs requires the monitoring of the neutron source intensity and the neutron flux within the reactor, for instance, to apply reactivity monitoring techniques such as the current-to-flux technique or pulsed neutron source (PNS) techniques [7–9]. Again, for this purpose, it is required to measure neutron fluxes high enough to likely cause saturation of the detectors used.

Therefore, the operation of both spallation sources and ADSs requires the monitoring of intense neutron fluxes that can cause detector saturation problems. Hence, a good characterization of the detector dead times becomes mandatory.

The measurement of dead times is usually accomplished using two constant-intensity neutron sources (the so-called

two-source method). However, in Section 2 we propose alternative techniques that are suitable to be directly applied to measurements in spallation sources or ADS, without the need of dedicated calibration experiments and that can provide a better characterization of the dead time of the detector system than the two-source method. These techniques have been applied to the experimental results obtained at the Yalina-Booster subcritical facility [10, 11] during the EUROTRANS [12] experimental campaign carried out in this facility.

Finally, the combination of the saturation effects at high counting rates and the poor statistics at low counting rates cause that there must be an optimal counting rate with a minimum relative uncertainty. The determination of this optimal counting rate for the case of an spallation process is complicated by the non-Poissonian nature of the spallation process. This problem will be addressed in Section 3.

2. Measurement of Dead Time

The dead time of a detector is defined as the minimum time interval that two consecutive counts must be separated in order to be recorded as two different events. The effect of having a dead time in a detector used to monitor counting rates is that the measured counting rates will be lower than the real ones. However, the real counting rate can be determined from the measured one if the dead time of the detector is known.

To obtain a formula for relating the real and the measured counting rates in a detector system affected by dead time, it must be taken into account that there are two fundamental behaviors for the dead time. They are referred as *paralyzable* and *non-paralyzable* [13, 14] (also called *extendable* and *non-extendable*, resp.). In a detector affected by paralyzable dead time, events that occur during the dead time of a previous one, and consequently not recorded, also produce a dead time. In other words, the effect of this last event can be regarded as extending the dead time of the previous one. On the contrary, in a non-paralyzable detector, events occurred during the dead time of a previous event are neither detected nor cause an additional dead time. For instance, fission chambers are affected by paralyzable dead time because a fission occurring during the time that the detector is ionized after a previous event also causes additional ionization, thus extending the dead time. On the contrary, some elements of the electronic chains can introduce a non-paralyzable dead time if they ignore the counts arrived during the time they are processing or recording a previous one.

The relationship of the real counting rates with the measured counting rates is well known for these two basic models. If we denote by N the real counting rate, by M the measured counting rate, and by τ the dead time and considering that the non-dead time disturbed distribution is Poissonian, M and N are related by

$$N = \frac{M}{1 - M\tau}, \quad (1)$$

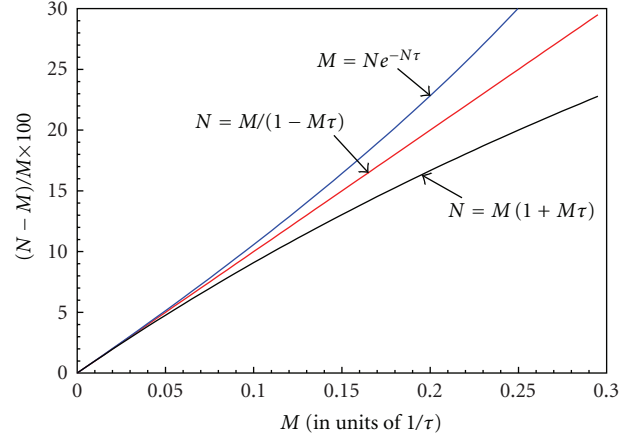


FIGURE 1: Relative value of the dead time correction for different counting rates considering (1), (2), and (3).

for the case of a non-paralyzable dead time, and by

$$M = Ne^{-N\tau}, \quad (2)$$

for the case of a paralyzable dead time.

These formulae are derived for an initially Poissonian process. This is the case of radioactive decay, but not the case of either fission or spallation. In the case of nuclear fission, the probability to have a fission in the immediate instants after a previous one is higher than that for the Poissonian process because of the secondary neutrons emitted in the fission process. In fact, the non-Poissonian nature of the fission process, constitutes the basis of the neutron noise techniques. Nevertheless, for dead time correction purposes the deviation from the Poisson distribution is small enough and the formulae derived for the Poisson process can be applied for fission. The spallation process is not a Poissonian process. This fact will be further discussed in Section 3.

In practice, however, these two models of dead time are idealized models, and actual detectors systems have neither a paralyzable nor a non-paralyzable dead time, but a combination of both. Furthermore, detector systems comprise additional elements (amplifiers, etc.) that add additional dead times to the dead time of the detector itself. Hence, it is common to study the behavior of *series arrangements of dead times*. Quite obviously, a series arrangement of dead times is only relevant when the first dead time is shorter than the following ones, because otherwise only the first dead time is to be taken into account. See, for instance, [14] for further details. Notice that for small dead time corrections, that is, if $\tau \ll 1/N$, both correction formula (1) and (2) can be approximated by the same first-order Taylor term:

$$N = M(1 + M\tau). \quad (3)$$

And therefore, first-order dead time corrections are independent on the model of dead time. The relative value of the dead time correction considering each one of (1), (2), and (3) for different counting rates is presented in Figure 1.

Several techniques are available for the experimental determination of dead times [13, 14]. The most simple one

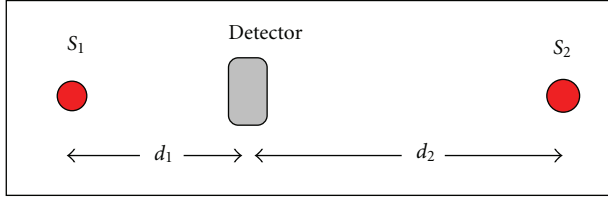


FIGURE 2: Two-source method.

is possibly the two-source method, described in Section 2.1. Beside these techniques, in this study we suggest another two techniques for dead time determination. The first technique (Section 2.2) is applicable with variable intensity sources such as spallation sources or ADSs. With the second technique (Section 2.3), the dead time is determined from the distribution of time intervals between consecutive detector counts.

2.1. The Two-Source Technique. The most usual technique to measure the dead time τ is the two-source technique [13, 15]. Let us consider that we have two sources S_1 and S_2 placed at distances d_1 and d_2 from the detector, as it is shown schematically in Figure 2.

In the absence of sources, the detector gets only the background radiation level B c/s. When the source S_2 is removed and only S_1 is present, the detector gets $N_1 + B$ c/s and detects M_1 c/s. Therefore, from (3),

$$N_1 + B = M_1(1 + M_1\tau). \quad (4)$$

Similarly, in absence of S_1 and with only S_2 present, we will have that,

$$N_2 + B = M_2(1 + M_2\tau). \quad (5)$$

And with both sources,

$$N_1 + N_2 + B = M_{12}(1 + M_{12}\tau). \quad (6)$$

Working out the dead time from these three equations,

$$\tau = \frac{M_1 + M_2 - M_{12} - B}{M_{12}^2 - M_1^2 - M_2^2}. \quad (7)$$

From the uncertainties in the right-hand side (Poisson statistics)'s it is immediate to estimate the uncertainty in the dead time. The background B has been included in case that sources are not intense enough. Usually, it can be neglected, but this simplification introduces a systematic error in the measurement.

2.2. Dead Time Determination Varying the Source Intensity. In an ADS or, more generally, in an accelerator-driven neutron source, the ability to change the accelerator intensity can be applied for detector dead time determination. Typically, the neutron flux measured at any point of the assembly is proportional to the source intensity. Therefore, if the detector used to measure the flux within the assembly is not affected by dead time, the measured counting rate in this detector

will be linear with the accelerator intensity; say $N = kI_A$. If it is affected by dead time, the measured counting rate in the detector will be related with the source intensity by an equation similar to (3):

$$kI_A = M(1 + M\tau) \implies \frac{I_A}{M} = \frac{1}{k} + \frac{\tau}{k}M. \quad (8)$$

Hence, from the linear fit of I_A/M to M , the dead time τ of the detector can be determined. This technique can be also applied using the counting rates in a second detector with a much lower sensitivity so that it is not affected by dead time, instead of the accelerator current I_A .

A variant of this technique using a single detector can be also applied in an ADS if the source-jerk technique is used for reactivity monitoring. The source-jerk technique [16–18] is based on the kinetic response of the neutron flux in the system to a sudden removal of the external source. In this case, the counting rate in the flux monitors experiences a fast decay due to the decay of the prompt neutrons followed by a much slower decay due to the delayed neutrons, in such a way that it can be considered that the counting rate ends in a constant level in the millisecond scale. This situation is shown in Figure 3, where the neutron level before the source removal is denoted by N_0 and the neutron level after the source removal (due to the slowly decaying delayed neutrons) is denoted by N_1 .

It can be obtained in the point kinetics model that the reactivity of the reactor (in units of dollars) is related with the ratio N_0/N_1 by the expression

$$\rho(\$) = 1 - \frac{N_0}{N_1} \implies N_0 = (1 - \rho(\$))N_1. \quad (9)$$

Equation (9) constitutes the basis of the source-jerk technique. If we consider that at the counting rate N_0 the detector is affected by dead time (at therefore it measures a counting rate M_0) but the counting rate N_1 is low enough not to be affected by dead time, we can write an expression similar to (8) replacing I_A by N_1 , M by M_0 , and k by $1 - \rho(\$)$:

$$\frac{N_1}{M_0} = \frac{1}{1 - \rho(\$)} + \frac{\tau}{1 - \rho(\$)}M_0. \quad (10)$$

Hence, if it is possible to operate the ADS with different values of the source intensity (and therefore of N_1 and M_0), we can use source-jerk experiments to determine both the reactivity of the assembly and the dead time of the detector. An example of the application of this technique to the experimental results in Yalina-Booster is presented in Figure 4.

However, the application of (8) or (10) for the determination of the detector dead time, either with two detectors with different sensibilities or with a single detector and the source-jerk technique, has been found to be limited in practice by a number of causes, including the presence of spatial and energy effects that make the point-kinetics model lose validity, source stability requirements before the source removal, and dynamical effects that may cause the reactivity to vary with the power level and thus with the source intensity.

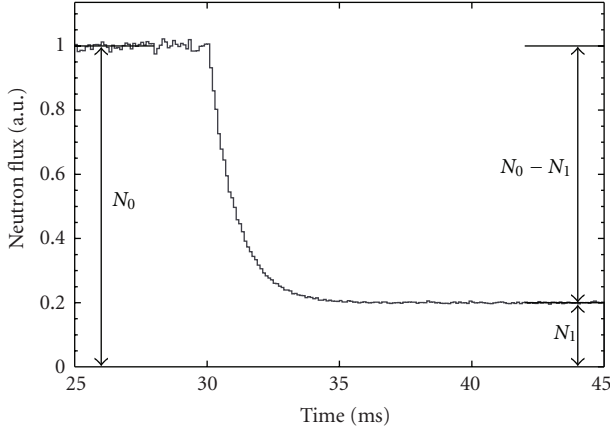


FIGURE 3: Graphical scheme of the source-jerk technique.

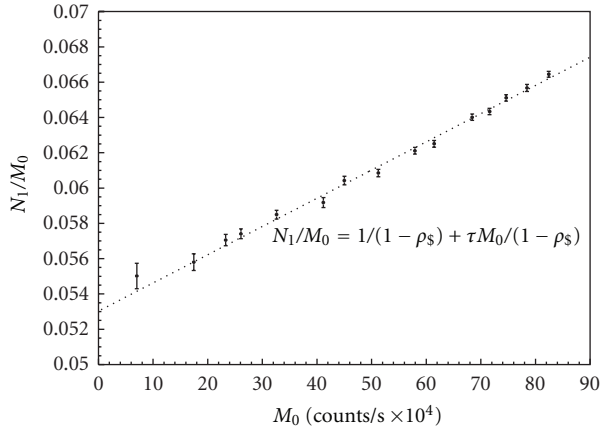


FIGURE 4: Example of the application of (10) to the source-jerk experiments at the Yalina-Booster subcritical facility.

2.3. Dead Time Determination from the Distribution of Time Intervals between Consecutive Counts. We have considered another technique to determine the detector dead time that requires a single detector and a single counting rate. This technique arises from the distribution of time intervals between consecutive counts. Modern data acquisition systems such as the one used during the EUROTRANS experiments at Yalina-Booster can register the times of individual detector signals instead of average counting rates. It is well known that for a Poissonian process the distribution of time intervals between consecutive counts (let us denote it by $I_1(t)$) takes the shape of a simple exponential. However, the presence of a dead time alters this distribution. Analytical formulae for this distribution are known for a long time for the cases of a simple paralyzable or non-paralyzable dead time [14]. For the non-paralyzable case this formula reads

$$I_1(t) = Ne^{-N(t-\tau)}, \quad \text{for } t > \tau; \quad (11)$$

while, for the paralyzable case

$$I_1(t) = N \sum_{j=1}^J \frac{1}{(j-1)!} [-N(t-j\tau)]^{j-1} e^{-jN\tau}, \quad (12)$$

where J is the largest integer below t/τ . For the case of a series arrangement of dead times, the determination of the analytical shape of $I_1(t)$ becomes cumbersome and the reader is referred to the bibliography [19, 20]. Nevertheless, the shape of $I_1(t)$ for complex arrangements of dead times can also be determined with Monte Carlo simulations. For this, we have implemented a program that generates events simulating an initial Poisson random process and then applies successively dead times of different types. Some results obtained with this program are presented in Figure 5. They are the cases of a purely paralyzable and non-paralyzable dead time, as well as the cases of series arrangements of two dead times: paralyzable/non-paralyzable and non-paralyzable/paralyzable. Normalization has been chosen so that $\int_0^{\infty} I_1(t) dt = 1$ for the unperturbed Poisson distribution; with this normalization $I_1(0)$ is equal to the counting rate of the unperturbed Poisson distribution. Notice the clear differences in the shape of $I_1(t)$ among these cases. This causes that the shape of $I_1(t)$ can be used to determine not only the value of the dead time of the system but also its nature (paralyzable or non-paralyzable) even in the presence of complex series of dead times.

An example of the application of this technique obtained in Yalina-Booster is presented in Figure 6. The determination of the value of the dead time was straightforward, but the determination of the type of dead time or if several types were present was impossible because of the presence of some ringing effects that are visible in the figure. Notice as well that (11) and (12) are derived for a strictly constant counting rate; variations of the source intensity in actual systems also alter these results.

3. Optimal Counting Rate with a Spallation Neutron Source

If the detector is placed very close to a spallation neutron source, it can become saturated; if it is placed too far away, statistical resolution is very small. From here it can be inferred that there must exist an optimal position in which the relative uncertainty of the counting rate is minimal. Let us consider the case of a non-paralyzable dead time. In this case, if we denote by $m = M\Delta t$ the number of counts in the detector in the interval Δt , we have from (1) that

$$N = \frac{m/\Delta t}{1 - \tau m/\Delta t}. \quad (13)$$

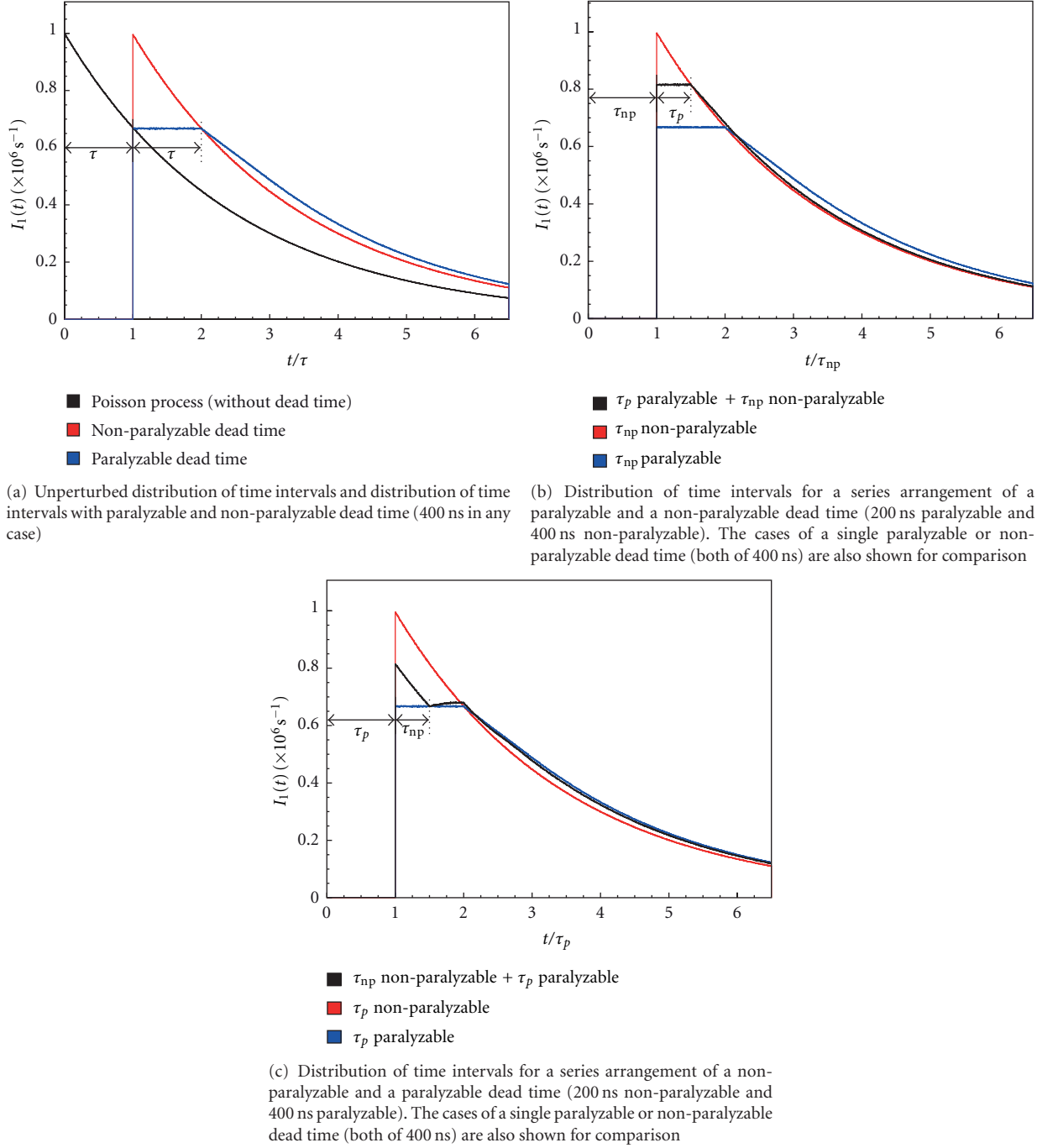
The uncertainty in N can be estimated from the variances:

$$\sigma_N^2 = \left(\frac{\partial N}{\partial m} \right)^2 \sigma_m^2 + \left(\frac{\partial N}{\partial \tau} \right)^2 \sigma_\tau^2. \quad (14)$$

Partial derivatives can be computed from (13) as follows

$$\frac{\partial N}{\partial m} = \frac{N}{m}(1 + \tau N), \quad \frac{\partial N}{\partial \tau} = N^2. \quad (15)$$

For a radioactive source, which follows a Poisson-like distribution of detection probabilities, we have that $\sigma_m^2 = m$,


 FIGURE 5: Distribution function $I_1(t)$ for intervals between adjacent random events (counting rate 10^6 counts/s, 10^9 counts in the simulation).

but a spallation source, because of the neutron multiplicity μ , the distribution of detection probabilities differs from the Poisson distribution. In a first approximation, we have that [21]

$$\sigma_m^2 = m(1 + D\mu), \quad (16)$$

where D is the Diven factor, which is close to the unity. Notice that if the neutron multiplicity is zero, the variance corresponds to that of a Poisson process. With these

conditions,

$$\sigma_N^2 = \frac{N^2}{m^2} (1 + \tau N)^2 m(1 + D\mu) + N^4 \sigma_\tau^2. \quad (17)$$

Replacing m by the first-order approximation $m \simeq N\Delta t(1 - N\tau)$ and approximating the first term in the right-hand side to the first order in $N\tau$, we find the following expression for the relative error in σ_N :

$$\varepsilon_N^2 = \left(\frac{\sigma_N}{N}\right)^2 = \frac{(1 + 3\tau N)(1 + D\mu)}{N \Delta t} + N^2 \sigma_\tau^2. \quad (18)$$

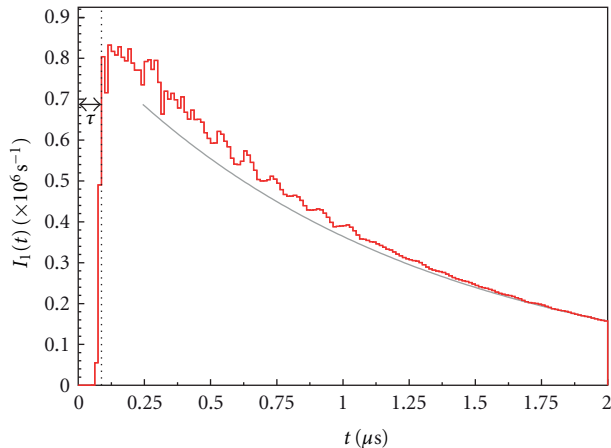


FIGURE 6: Example of the distribution of intervals between consecutive counts obtained from the Yalina-Booster experiments. Gray line represents the fit to an exponential (over a large range than the plotted interval).

The optimal counting rate is the one that minimizes the relative error ε_N :

$$\left. \frac{\partial \varepsilon_N^2}{\partial N} \right|_{N=N_{\text{op}}} = 0 \implies -\frac{1}{N_{\text{op}}^2} \left(\frac{1+D\mu}{\Delta t} \right) + 2N_{\text{op}}\sigma_\tau^2 = 0. \quad (19)$$

Working out N_{op} in this equation, we finally find that

$$N_{\text{op}} = \sqrt[3]{\frac{1+D\mu}{2\sigma_\tau^2\Delta t}}. \quad (20)$$

Typical values for the problem are given in Table 1. With these values, optimal counting rate is 1.05×10^5 (c/s). Correction by dead with these parameters is about 20%, in the limit of the first-order approximation (3). The only parameter one can change in (20) is Δt so if we choose 10 s instead of 1 s, the new optimal counting rate becomes 0.48×10^5 (c/s), and the correction is now 10%, low enough for using (3). Therefore, the detector must be placed at points with counting rates about 4×10^4 (c/s). Diven's factor can be taken as the unity without a large error in the computation of the optimal counting rate.

4. Conclusions

In addition to traditional techniques for dead time measurement, we propose in this work two alternative methods to determine detector dead times. The first of them can be applied with variable intensity sources, such as accelerator-driven neutron sources. This method consists in studying the relationship between the detector counting rate and the source intensity that results of the presence of dead time in the detector system. A variation of this technique can be applied measuring the counting rate in a second detector with a lower counting rate (i.e., with negligible dead time effects) instead of the source intensity. Another variation of this technique, which does not require either a second detector or knowing the source intensity, can be applied in an

TABLE 1: Multiplicity, Diven's factor dead time, and measurement time for a typical problem.

μ	D	τ (μs)	Δt (s)
20	1.1	2 ± 0.1	1

ADS making most of the results of the source-jerk technique, used to determine the reactivity of the system.

The second method we propose to determine the dead time of a detector system can be applied if the data acquisition system registers the times of individual detector events instead of counting rates. In this way the distribution of time intervals between consecutive counts can be obtained, from which the detector dead time can be determined. This method has the advantage of requiring no additional detector and only one counting rate. In addition, this method is in principle capable of determining the type of dead time (paralyzable or non-paralyzable) even in the case of complex arrangements of dead times.

Finally, we remark that neutrons produced in a spallation source do not follow the Poisson statistics because of the multiplicity in the neutron production. An expression has been found that relates the multiplicity, the measurement interval, and the variance of the detector dead time. This expression allows placing neutron monitors where the relative error is minimal.

Acknowledgments

The experiments at Yalina-Booster presented in this work were supported by the IP-EUROTRANS Contract no. FI6W-CT2005-516520 and the ENRESA-CIEMAT Agreement for the Transmutation Applied to High Level Radioactive Waste. The authors would like to acknowledge as well the personnel of different institutions involved at the EUROTRANS experimental campaign at Yalina-Booster, especially D. Villamarín (CIEMAT, Madrid), M. Fernández-Ordóñez (CIEMAT, Madrid) C. Berglöf (KTH, Stockholm), and finally, the support and dedication of the Yalina-Booster team at JIPNR-Sosny during the experimental campaign.

References

- [1] A. Letourneau, J. Galin, F. Goldenbaum et al., "Neutron production in bombardments of thin and thick W, Hg, Pb targets by 0.4, 0.8, 1.2, 1.8 and 2.5 GeV protons," *Nuclear Instruments and Methods in Physics Research, Section B*, vol. 170, no. 3, pp. 299–322, 2000.
- [2] H. Nifenecker, S. David, J. M. Loiseaux, and A. Giorni, "Hybrid nuclear reactors," *Progress in Particle and Nuclear Physics*, vol. 43, pp. 683–827, 1999.
- [3] A. Gandini and M. Salvatores, "The physics of subcritical multiplying systems," *Journal of Nuclear Science and Technology*, vol. 39, no. 6, pp. 673–686, 2002.
- [4] OECD-NEA, "Accelerator-Driven Systems (ADS) and fast reactors (FR) in advanced nuclear fuel cycles. A comparative study," Tech. Rep. NEA-3109, 2002.
- [5] OECD-NEA, "Physics and safety of transmutation systems—A status report," Tech. Rep. NEA-6090, 2006.

- [6] W. von Lensa, R. Nabbi, and M. Rossbach, “RED-IMPACT—impact of partitioning, transmutation and waste reduction technologies on the final nuclear waste disposal—synthesis report,” in *Schriften des Forschungszentrums Juelich—Reihe Energie & Umwelt*, vol. 15, 2008.
- [7] P. Baeten and H. A. Abderrahim, “Reactivity monitoring in ADS, application to the Myrrha ADS project,” *Progress in Nuclear Energy*, vol. 43, no. 1–4, pp. 413–419, 2003.
- [8] E. González-Romero, D. Villamarín, M. Embid et al., “The MUSE4 pulsed Neutron source experiments,” in *The Physics of Fuel Cycles and Advanced Nuclear Systems—Global Developments (PHYSOR '04)*, pp. 1399–1407, Chicago, Ill, USA, April 2004.
- [9] R. Soule, W. Assal, P. Chaussonnet et al., “Neutronic studies in support of accelerator-driven systems: the MUSE experiments in the MASURCA facility,” *Nuclear Science and Engineering*, vol. 148, no. 1, pp. 124–152, 2004.
- [10] V. Bournos et al., “YALINA-Booster benchmark specifications for the IAEA coordinated research projects on analytical and experimental benchmark analysis on accelerator driven systems, and low enriched uranium fuel utilization in accelerator driven sub-critical assembly systems,” IAEA Document, 2007.
- [11] H. Kiyavitskaya et al., “Experimental investigations at sub-critical facilities of Joint Institute for Power and Nuclear Research—Sosny of the National Academy of Sciences of Belarus,” in *Technical Meeting on Use of Low Enriched Uranium in Accelerator Driven Sub—Critical Assemblies*, Vienna, Austria, October 2005.
- [12] European Commission, Integrated Project EUROTRANS. Annex I—Description of Work. Contract no. FI6W-CT-2004-516520, 2005.
- [13] G. F. Knoll, *Radiation Detection and Measurement*, John Wiley & Sons, 3rd edition, 1999.
- [14] International Commission on Radiation Units & Measurements, “Particle counting in radioactivity measurements,” ICRU Report 52, 1994.
- [15] A. E. Profio, *Experimental Reactor Physics*, John Wiley & Sons, 1976.
- [16] G. R. Keepin, *Physics of Nuclear Kinetics*, Addison-Wesley, 1965.
- [17] K. O. Ott and R. J. Neuhold, *Introductory Nuclear Reactor Dynamics*, American Nuclear Society, 1985.
- [18] D. L. Hetrick, *Dynamics of Nuclear Reactors*, American Nuclear Society, 1993.
- [19] H. D. Choi, “Counting statistics distorted by two dead times in series which end with an extended type dead time,” *Nuclear Instruments and Methods in Physics Research, Section A*, vol. 599, no. 2-3, pp. 251–259, 2009.
- [20] H. D. Choi, “Counting statistics modified by two dead times in series,” *Nuclear Engineering and Technology*, vol. 43, no. 3, pp. 287–300, 2011.
- [21] Y. Yamane and I. Pázsit, “Heuristic derivation of Rossi-alpha formula with delayed neutrons and correlated source,” *Annals of Nuclear Energy*, vol. 25, no. 17, pp. 1373–1382, 1998.

Research Article

Development of a Secondary SCRAM System for Fast Reactors and ADS Systems

Simon Vanmaercke,¹ Gert Van den Eynde,¹ Engelbert Tijskens,² and Yann Bartosiewicz³

¹*Institute for Advanced Nuclear Systems, SCK.CEN, 200 Boeretang, 2400 Mol, Belgium*

²*Laboratory for Agricultural Machinery and Processing, Katholieke Universiteit Leuven, 30 Kasteelpark Arenberg, 3001 Heverlee, Belgium*

³*Institute of Mechanics, Materials and Civil Engineering, Catholic University of Leuven, 2 Place du Levant, 1348 Louvain-la-Neuve, Belgium*

Correspondence should be addressed to Simon Vanmaercke, simon.vanmaercke@sckcen.be

Received 15 November 2011; Accepted 14 February 2012

Academic Editor: Alberto Talamo

Copyright © 2012 Simon Vanmaercke et al. This is an open access article distributed under the Creative Commons Attribution License, which permits unrestricted use, distribution, and reproduction in any medium, provided the original work is properly cited.

One important safety aspect of any reactor is the ability to shutdown the reactor. A shutdown in an ADS can be done by stopping the accelerator or by lowering the multiplication factor of the reactor and thus by inserting negative reactivity. In current designs of liquid-metal-cooled GEN IV and ADS reactors reactivity insertion is based on absorber rods. Although these rod-based systems are duplicated to provide redundancy, they all have a common failure mode as a consequence of their identical operating mechanism, possible causes being a largely deformed core or blockage of the rod guidance channel. In this paper an overview of existing solutions for a complementary shut down system is given and a new concept is proposed. A tube is divided into two sections by means of aluminum seal. In the upper region, above the active core, spherical neutron-absorbing boron carbide particles are placed. In case of overpower and loss of coolant transients, the seal will melt. The absorber balls are then no longer supported and fall down into the active core region inserting a large negative reactivity. This system, which is not rod based, is under investigation, and its feasibility is verified both by experiments and simulations.

1. Introduction

One of the most important safety features of all reactor types is the ability of shutting down under all circumstances. This is in particular true for GEN IV reactors because they are designed to be safer than currently existing reactors thus also the ability to shut down the chain reaction must also be more reliable. In current PWR reactors shutting down the reactor can be accomplished in two completely independent and diverse methods. The first method is the insertion of safety and control bars by means of gravitation or other passive methods. The second method is the dissolution of the neutron absorbing boric acid into the primary water. For the liquid-metal- and gas-cooled GEN IV reactors (LFR, SFR, and GFR), the second method cannot be used because there are no liquid absorbers that can be dissolved in sufficient quantity in the liquid metal or gas, and even if such an

absorbent would exist, cleaning the liquid metal after a SCRAM would be very expensive. In a liquid-metal-cooled ADS, there are in principle two different ways to shut down the reactor. First the accelerator can be turned off, leading to a safe shutdown of the subcritical core. Second the reactor power can be lowered by decreasing the multiplication factor of the core by inserting negative reactivity. This is the same problem as inserting reactivity in a critical reactor. (Note that this only decreases the power level and thus is not as effective as in a critical reactor.) The problem is therefore relevant for both ADS and critical reactors.

This paper focuses on inserting negative reactivity in a liquid-metal-cooled core, using a diverse operating principle compared to control/safety rods. First it gives a short overview of the existing solutions to this problem. It finally presents a new concept that can be used in liquid-metal-cooled reactors and replaces the dissolution of a neutron

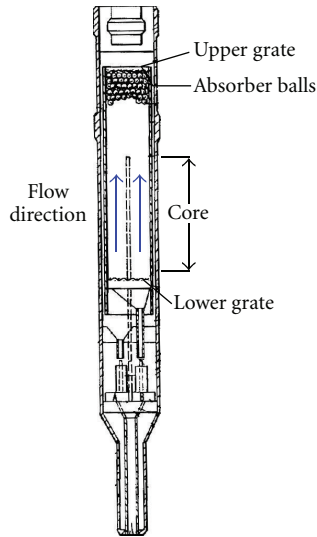


FIGURE 1: Conceptual drawing of the hydraulically suspended absorber balls secondary SCRAM system [1, 2].

absorber into the primary coolant. This concept is demonstrated by both simulations and experiments.

2. Overview of Existing Concepts

2.1. Hydraulically Suspended Absorber Balls. The hydraulically suspended absorber balls concept [1, 2] was designed by Rockwell International for use in sodium-cooled reactors. An illustration of this concept is shown in Figure 1. It uses spheres made of a neutron-absorbing material, tantalum, which are hydraulically suspended by the upward flow of the sodium coolant. In case this flow is interrupted, either by loss of coolant or by loss of flow, this upward force disappears and the tantalum spheres drop into the active core region. In this way they insert a negative reactivity shutting down the fission chain reaction. This system has the advantage of being self-actuating but can also be activated by a SCRAM system since it has a valve that can shut down the flow in case of SCRAM.

2.2. Liquid Absorber with Melt Seal. This concept, called LIM (lithium injection module) and illustrated in Figure 2, uses liquid lithium neutron poison in tubes. It was conceived for use in the Rapid and Rapid-L [3, 4] lithium-cooled reactor design concepts. These are self-controlling reactor concepts which do not require the intervention of an operator. An aluminum seal keeps a liquid poison (Li^6) above the active core region during normal operation. In case of overpower, loss of coolant, and loss of flow accidents, the seal temperature increases, and at approximately 650°C it melts, thus releasing the Li^6 into the active core region. This system is fully self-actuating, but it cannot be activated by a SCRAM system. The disadvantage of this system is that Li^6 is not a very good neutron absorber, is chemically reactive, and is quite expensive.

2.3. ALMR Ultimate Shutdown System. The American ALMR [5], advanced liquid metal reactor, also plans to have

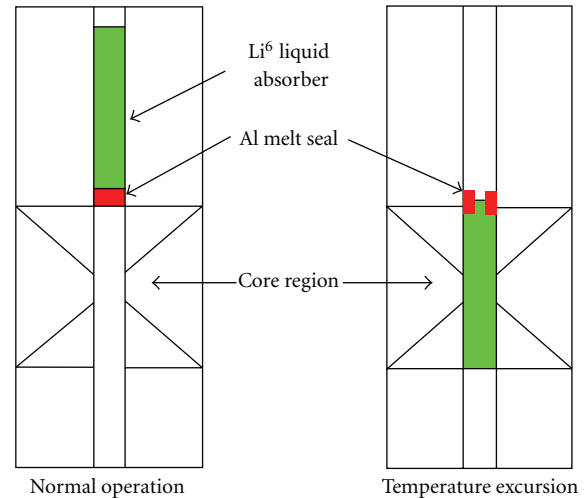


FIGURE 2: Liquid absorber concept with melt seal from [3].

a complementary shutdown system. This system also uses absorber spheres that are kept in a central channel above the core in normal operation by means of a seal. In case of SCRAM, the seal is ruptured by means of a mechanical device. With the seal ruptured, the balls are then free to flow in the active core region. This system is not self-actuating and requires a SCRAM signal.

2.4. Gas Expansion Modules. A self-actuating system for use in gas fast reactors (GFRs) was proposed, based on the gas expansion modules [6]. In this system a boron carbide rod is submerged into a liquid metal. The level of the liquid metal, and thus boron carbide rod, is controlled by the liquid metal vapor pressure in the system. In an anticipated transients without scram, temperatures will increase resulting in an increased vapor pressure, decreasing the level of the liquid metal and thus inserting the neutron absorbing boron carbide rod into the active core region. Although this system is self-actuating and even self-resetting, it has an operational similarity to the control rod-based systems.

2.5. Articulated Absorber Rod. A complementary SCRAM system using an articulated absorber was implemented in the German SNR-300 [7–9] reactor. The system consists of three absorber elements linked in a chain. When the reactor is scrammed, the chain is pulled up through the core by means of an accelerator spring. Due to the flexibility of the chain, the assembly will conform to a duct with a bow that is several times larger than the maximum bow calculated for the guide tube [7]. However, other blocking scenarios may arise, and the articulated absorber rod might in those cases be too similar to a conventional absorber rod.

3. Presented Concept

The concept that is presented in this paper aims at combining some of the strong points of the currently existing concepts. The presented concept is shown in Figure 3 [10]. It consists of a tube, with the same diameter as a fuel pin, in the central

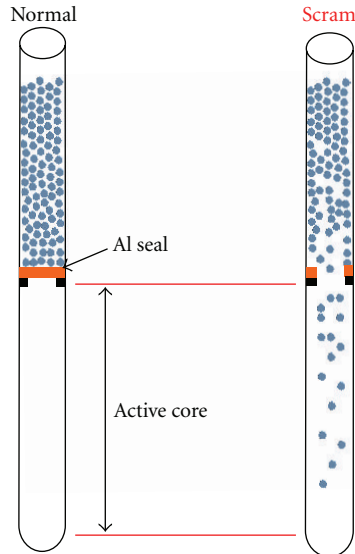


FIGURE 3: Presented concept for a secondary SCRAM system using absorber spheres and an Aluminum melt seal.

position of every fuel assembly. The tube is divided into two sections by means of aluminum seal similar to the melting seal in the LIM concept. In the upper region, above the active core, spherical neutron-absorbing boron carbide particles are placed. In case of overpower and loss of coolant transients, the seal will melt. The absorber balls are then no longer supported and fall down into the active core region inserting a large negative reactivity.

A solid absorber was selected here because liquid-absorbing materials are rare and their negative reactivity effect is much lower compared to solid absorbers such as tantalum and boron carbide. A solid absorber has however the disadvantage that the flow of solid particles is not as well understood as the flow of liquids. Therefore it is clear that the absorber particle flow will be an important aspect of study for this concept.

The concept is also self-actuating just like the hydraulically suspended absorber balls and the liquid insertion with melting seal. It is however mechanically simpler than the hydraulically suspended balls which might contribute to the overall reliability. Unlike the hydraulically suspended absorber balls, it is not resettable and the reaction times might be longer.

Because this system is placed in every assembly, it has a distributed character similar to the dissolution of boric acid, unlike the primary SCRAM system using absorber rods that are localized to a few fixed positions or the ALMR ultimate shutdown system that is situated only in the central channel. Due to the flow-like behavior of the absorber balls, it is less prone to failure due to channel deformation/blocking than the absorber rods even though this issue has to be investigated.

Given the newly presented concept, a few questions require an answer before it can actually be used.

- (i) Can it provide sufficient negative reactivity to shut down a reactor?

- (ii) Will the particle flow block by itself?
- (iii) What is the optimal diameter of the spheres?
- (iv) Will the particle flow block when in contact with the molten seal?
- (v) Will the system be fast enough?

The following sections will address most of these questions, although further research is still needed.

4. Neutronic Effectiveness

Two important requirements of a SCRAM system are first to be able to insert sufficient negative reactivity to shut down the reactor under all circumstances and second to have a minimal impact on the normal operation of the core.

These two requirements can be verified using static MCNPX [11] calculations. This has been done on a critical variant of the MYRRHA core [12]. MYRRHA is a lead-bismuth-cooled experimental accelerator-driven system.

In the reference subcritical core of MYRRHA, four fuel assemblies were added in order to obtain a critical core. In every assembly one fuel pin in the center was replaced with a SCRAM pin. These pins have been tested for their effectiveness with several materials. For every material the reactivity in normal operating case, where the absorber spheres are above the critical core, was compared to the scrammed case, where the absorber case was in the critical core region. This value yields the reactivity worth of the SCRAM system.

Also the normal case, where the spheres are above the critical core, was compared to a reference case, without the SCRAM system. This yields the reactivity influence of the system at normal operation.

The density for the sphere stacking is 61% of the theoretical density of the material that was used. This is the packing factor found in experiments when spheres are poured into a random stacking and conform to the value described in the literature [13]. Experiments have also shown that this packing factor is very constant, with maximal deviation of about 0.5% points.

Table 1 shows both the impact of the secondary SCRAM system on the normal operation, as well as the SCRAM worth. Most of the effect on normal operation is caused by removing the fuel as can be seen with very ineffective absorbers, such as natural lithium. By far the most effective absorber material is enriched boron carbide. Another interesting candidate is however tantalum; although its neutron worth is not very high, it has the advantage of being heavier than lead bismuth and would therefore work reliably even when the SCRAM channel would be flooded. As a first option, 90% enriched boron carbide is retained. When channel flooding proves to be an important issue, tantalum can be considered as a valuable alternative.

5. Absorber Particle Flow Study

The presented concept relies heavily on the flow of the absorber spheres to shut down the reactor. Since particle flows are less well understood than liquid flows, verification of the reliability of this principle is therefore vital. This

TABLE 1: Impact on normal operation and SCRAM worth for different neutron absorbing materials in per cent mille (pcm). For all materials except lithium, which is a liquid at the working temperatures, 61% of the theoretical density was used. Uncertainty on these values is about 150 pcm.

Absorber mat.	Density (kg/m ³)	Normal (pcm)	SCRAM (pcm)
Natural B ₄ C	1540	-789	-1178
90% B ¹⁰ B ₄ C	1540	-1368	-4565
Natural Li	530	-847	-18
90% Li ⁶	530	-931	-1869
Europium	3198	-840	-1132
Tantalum	10130	-876	-600

verification has been done both experimentally as well as with simulations. In a first instance, the particle flow is simulated alone without interaction of the molten aluminum seal. In a later stage the simulation of the seal will be done together with the particles giving a full simulation of the secondary SCRAM system. In this section only the results concerning the particle flow are discussed.

5.1. Simulation of Absorber Particles Flow Dynamics. The simulations are done using the DEMeter [14] general-purpose discrete element method (DEM) program, which is developed at the KU Leuven. The simulation scheme is shown in Figure 4.

The simulation starts with the particles in an initial position. The next step is to find all particles that are in contact with each other and compute the overlap they have. Based on this overlap and other parameters such as contact history, the normal and tangential forces are computed using a contact force model. All the normal and tangential forces working on a particle are then summed to one force and moment working in the center of gravity of the particle. Finally the forces are integrated to a new velocity and the velocity to a new particle position, and the scheme is repeated.

The choice of the selected normal and tangential force models is largely determinant in the accuracy of the simulation.

The normal contact force model is a Hertz-Kuwabara-Kono model [15, 16]:

$$F_n = \frac{4}{3} \sqrt{R_{ij}^{\text{eff}}} k \left(\xi^{3/2} + \frac{A_i + A_j}{2} \xi \sqrt{\xi} \right). \quad (1)$$

With k the contact stiffness and A the viscous normal damping parameter of particle i or j , the overlap between particle i and j is given by ξ , the effective radius R_{ij}^{eff} is computed as

$$R_{ij}^{\text{eff}} = \frac{R_i R_j}{R_i + R_j}. \quad (2)$$

The contact stiffness k is given by

$$k = \left(\frac{1 - \nu_i^2}{E_i} + \frac{1 - \nu_j^2}{E_j} \right)^{-1} \quad (3)$$

with E , ν , respectively, the Young modulus and the Poisson ratio.

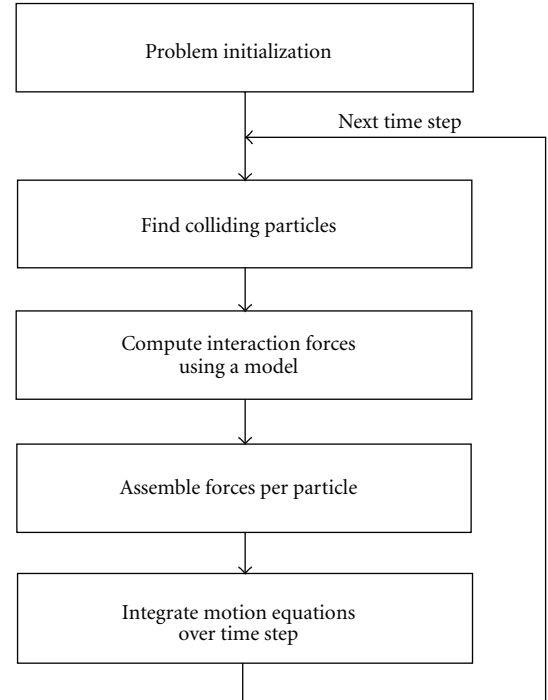


FIGURE 4: Scheme of the DEM simulation.

The tangential model is the Vu-Quoc tangential force model [17, 18]. This model is based on the Mindlin and Deresiewicz [19] theory for elastic frictional contact.

These models very accurately describe the forces between spheres in contact and require only physical constants to be known, being the Young modulus, viscous damping constant, and the static and dynamic Coulomb coefficients of friction μ_s and μ_d .

Due to the number of particles that amounts to several hundred thousands and the very small time steps required, the computational cost of the simulations is very high. To be able to complete the simulations in a reasonable time a, GPU- (graphics processing unit) based version of the DEMeter code was developed and used. This allowed for a speedup of 30 compared to the CPU-based version.

5.2. Experimental Investigation of Absorber Particle Flow Dynamics. The simulations done with the Demeter tool are compared to experiments. The experimental setup is shown

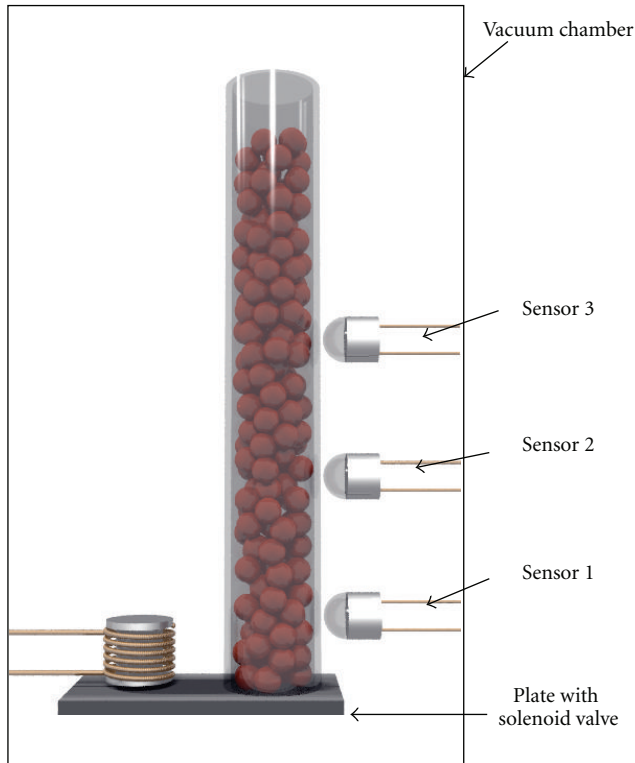


FIGURE 5: Schematic representation of the experiment.

in Figure 5 and consists of a 6 mm cylindrical glass tube filled with spherical “Ballotini” glass particles with a diameter of $500 \pm 30 \mu\text{m}$. The tube diameter is representative for the diameter of fuel rods used in the MYRRHA design.

The glass particles are kept in their initial position by a magnetic solenoid valve. The particle velocities are measured at three different heights (22 mm, 78 mm, 130 mm) from the bottom section of the tube. After the tube has been filled, the entire setup is completely enclosed in a vacuum chamber. This geometry is different from the real safety system, in the sense that the lower part of the tube is not present in the experiment. This has been done because it is much easier to do the experiments with the solenoid valve with this geometry. Additionally it is not expected that the lower part of the tube will have a significant influence on the particle flow. To measure the velocities of the particles, an optical flow method [20] has been selected. This has the advantage that the measurement does not influence the particle flow at all since it is nonintrusive. Optical flow measurement is a technique where images of the particle flow are taken at high frame rates. After capture, the frames are processed and subsequent frames are compared to each other to determine the magnitude and direction of the motion.

5.3. Results of the Particle Flow Analysis. For a tube filled to a height of 200 mm with glass spheres, the velocity evolution found both by experiments and simulations is shown in Figure 6. The experiment has been repeated 20 times in order to obtain an error estimation on the experiment. The velocities for the simulations are a cross-sectional average

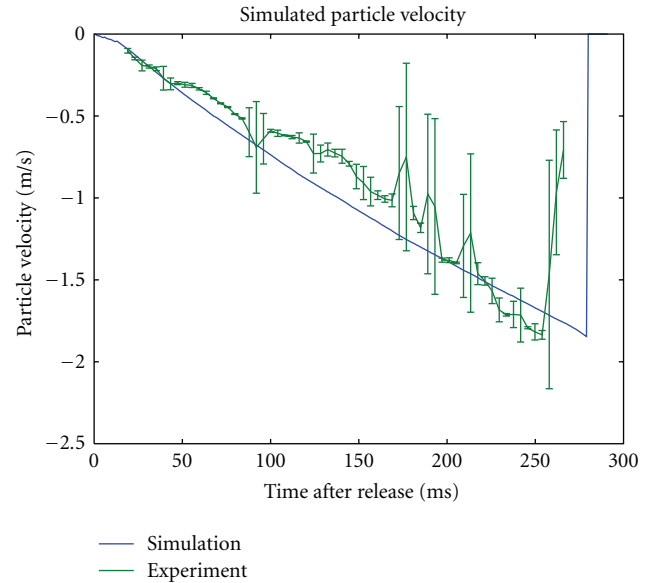


FIGURE 6: Glass sphere velocity measured at 22 mm above the bottom of the tube as a function of time.

of the particles that would be visible by the experimental sensor. On average 100 particles are taken into account for this averaging.

Surprisingly the experiments are highly repeatable, yielding very similar results. This can be seen in the generally small error bars plotted on Figure 6. The standard deviation on the total time needed to empty the tube is less than 3%. This feature is of course an advantage for a safety system. The change in error bar range is caused by the fact that the optical sensor sometimes is unable to track sufficient particles to yield an accurate velocity value. During periods with reduced particle density, this will increase the error bar drastically.

The particle velocity profile shown in Figure 6 is a simple acceleration of the particles as would be expected for particles in free fall mode. However, the particles are not in free fall mode; they do have interaction with the tube wall. This can be seen by the fact that the acceleration of the particles is not 9.81 m/s^2 but closer to 6 m/s^2 . These interactions thus cause an energy loss. This energy loss however appears to be quite independent of the particle velocity, proven by the straight line in the velocity profile of the particles.

At the end of the graph, it can be observed that the velocity suddenly drops back to 0 m/s. This is simply due to the fact that the tube has been emptied and that there are no more particles to measure. The simulations predict the experimental data quite well, with a maximal difference in predicted time needed to empty the tube of about 5%.

5.4. Ideal Particle Size. The diameter of the absorber spheres is one of the few remaining free parameters that still can be optimized. Other parameters such as tube diameter and tube wall thickness, are determined by the necessity of not influencing the normal thermal hydraulics of the reactor. The location of the seal is fixed at the top of the active core region.

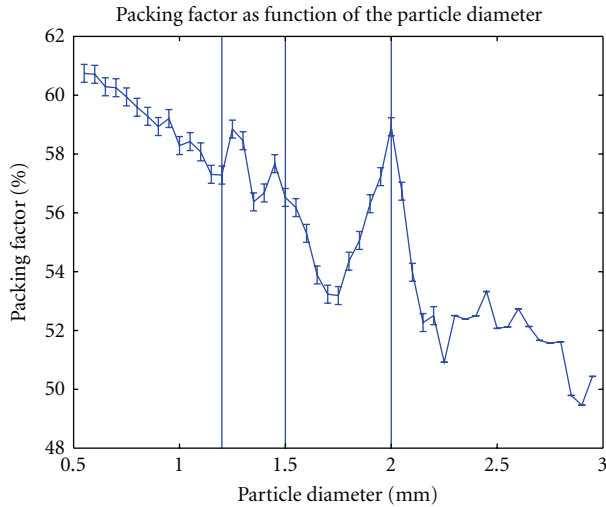


FIGURE 7: Packing factor of the particles in the tube as function of the particle diameter.

This is a logical choice because at that location temperatures will be the highest, leading to shorter reaction times.

The absorber sphere size can be optimized for several goals: firstly it should be the size with a very low probability for blocking, next it should flow as fast as possible, and finally a high packing factor is desirable since it will increase the neutronic efficiency.

When the particle size becomes too small $\leq 100\text{--}250\ \mu\text{m}$, it is no longer the gravity force combined with collision forces that dominate and determine the movement of the particles. Other forces such as electrostatic, air friction, and especially Van der Waals forces become dominant. The latter one is an attractive force and reduces the free flowing capabilities of the particles. On top of deteriorated flow properties and a seriously increased risk of flow blockages, the flow becomes less easily predictable by simulations, due to the difficult to model electrostatic, and Van der Waals forces.

Choosing particles that are very large such as $1/2$ or $1/3$ of the tube diameter is also disadvantageous for several reasons. First of all they have a relatively high risk of blocking. Simulations and experiments show that the risk of blocking might be as high as 90% for diameters larger than 1.8 mm, although this risk seems to be very sensitive to the diameter in this region. Additionally the flow with these particles is slower compared to smaller sphere flows as can be seen in Figure 8 where the particle velocity is plotted for several diameters. Finally they have a lower packing factor as can be seen in Figure 7 showing the packing fraction as a function of the diameter. The packing factor is a decreasing function of the particle size, which can be expected since the wall effect on the stacking becomes increasingly important.

For the proposed complementary SCRAM system, this limits the possible range for the particle size between $500\ \mu\text{m}$ and $1000\ \mu\text{m}$ or between $1/12$ th and $1/6$ th of the tube diameter. The exact choice here is not very important; it can be seen in Figure 8 that in this diameter range the particle

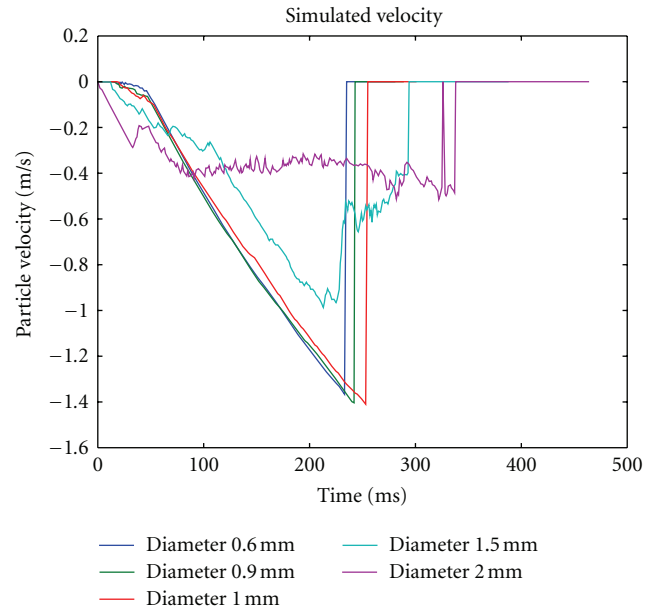


FIGURE 8: Simulated particle velocity measured at outflow section as a function of particle diameter.

flow velocities are very insensitive to a change in particle diameter. Also the packing factor is not very sensitive to the exact choice of the diameter as can be seen in Figure 7 where the difference in packing factor between $500\ \mu\text{m}$ and $1000\ \mu\text{m}$ is less than 3%. For the envisioned range of particle diameters between $500\ \mu\text{m}$ and $1000\ \mu\text{m}$, it was found impossible to find a single simulation that showed a blocking flow in over 3000 simulations. Also experimentally using $500\ \mu\text{m}$ spheres, not a single experiment showed a blocking flow in over 400 experiments.

6. Absorber Particle-Metal Seal Interaction

This section describes the modeling of the interaction of the absorber particles and the aluminum seal that keeps the particles above the seal during normal operation and melts during a transient.

6.1. Molten Seal Modeling. The melting dynamics of the aluminum seal is modeled using smoothed particle hydrodynamics (SPH) [21]. SPH is a Lagrangian particle method that does not require a computational mesh. It can be used to model a compressible fluid moving arbitrarily in three dimensions. SPH is very suitable to model free surface flows [22], and due to its particle-based nature, interaction with solid DEM particles can be easily implemented, which is the reason why this technique was selected to simulate the melting seal. The SPH equations for a liquid are obtained from the continuum equations of fluids dynamics by interpolating density, velocity, and so forth, from a set of points which may be disordered [23]. The standard smoothed particle hydrodynamics method is extended with an energy transport equation [24], a simple melt model for the seal, and a surface tension model [25].

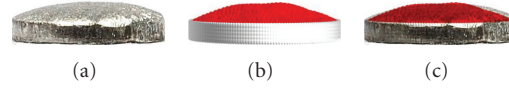


FIGURE 9: Comparison between experimentally obtained seal shape (a) and shapes predicted by the simulation (b), and an overlay of simulation and experiment (c).

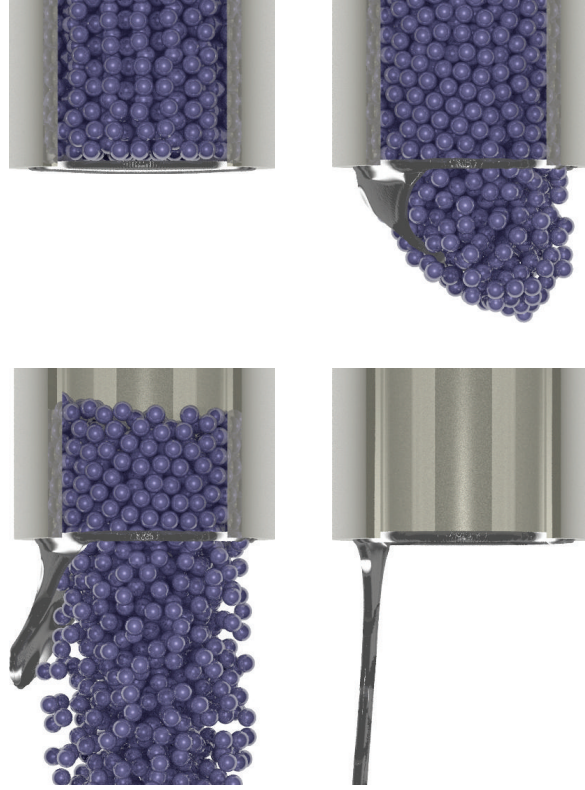


FIGURE 10: Combined seal and particle simulation with a 0.25 mm seal, rupturing under the weight of the particles.

It was found experimentally that aluminum seals with a thickness of 1 mm and a diameter of 6 mm do not flow when molten but are kept steady by the surface tension. The seal shape deforms slightly as can be seen in Figure 9 where the experimentally obtained shape of the molten seal is compared to the predicted shape by the simulation. In order to have a functional secondary SCRAM system, the seal thickness has been reduced to 0.25 mm.

6.2. Seal-Particle Interaction. The aluminum seal has mechanical interaction with the solid absorber spheres both before the activation, when the aluminum seal is supposed to keep the particle above the core, and during the activation, when liquid aluminum seal can possibly mix with the solid particles. During the possible mixing between the solid particles and the molten seal, the seal could resolidify and form a blocking particle-seal conglomerate.

Because no wetting interaction between the aluminum and the boron carbide was observed, it was deemed sufficient

to model the interaction using a Lennard-Jones potential barrier [26]:

$$\vec{F} = A \left[\left(\frac{\sigma}{d} \right)^{12} - \left(\frac{\sigma}{d} \right)^6 \right] \frac{(\vec{x}_1 - \vec{x}_2)}{d^2}, \quad (4)$$

where A is a strength parameter, scaling the Lennard-Jones force, d is the distance between points \vec{x}_1 and \vec{x}_2 , and σ is the distance at which the force is exactly zero, sometimes also called repulsion distance. If the distance between the two particles is shorter than σ , there is a repulsive force between the two particles; when the distance between the two particles is larger than σ , there is an attractive force that quickly drops off with increasing distance.

The combined particle/seal simulation with a 0.25 mm seal is shown in Figure 10. The outer surface of the secondary SCRAM system is supposed to have an instantaneous temperature increase from 450°C to 700°C or 50°C above the melting temperature of the aluminum seal. As can be seen, the particles rupture the liquid seal and are released into

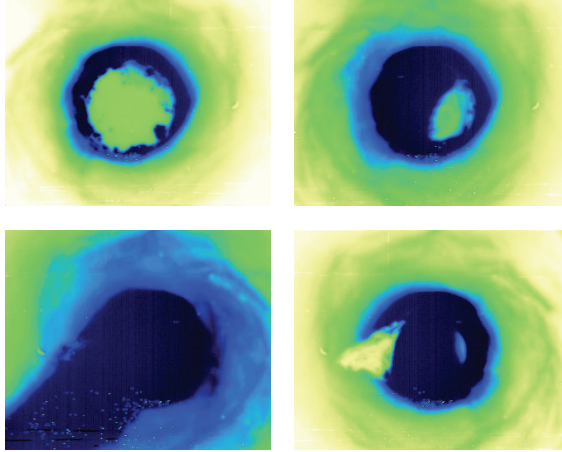


FIGURE 11: Combined experiment.

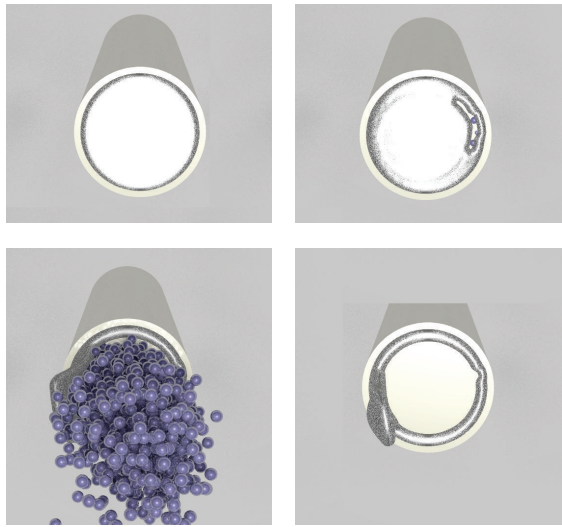


FIGURE 12: 0.25 mm seal bottom view.

the core. The release of the particles, shown in the second image in Figure 10, occurs after 450 ms. The seal remains attached to the tube itself during the release of the particles and remains there afterwards.

In order to validate these results, the combined experiment has been repeated with a 0.25 mm seal. An infrared image sequence of the experimental particle release is shown in Figure 11. For better comparison, the simulation with the 0.25 mm seal, shown in Figure 10, is shown again in bottom view in Figure 12. These experiments have been repeated 5 times with consistent results.

The fact that the seal remains attached to the tube both in experiments and simulations reduces the interaction probability of the particles and the molten seal and therefore increases the overall reliability of the system.

7. Conclusions

In this paper the need for a secondary method to insert negative reactivity in an ADS or critical variant of an ADS

prototype was explained. The currently proposed solutions for a reactivity insertion system have been summarized, and a new concept proposed. This concept uses spherical absorber particles that are placed in an empty tube with a similar diameter as a fuel pin. In normal operation they are kept above the active core region by means of an aluminum seal. In case of an accident, the temperature increases and melts the aluminum seal. This releases the particles into the active core region.

The flow of these particles is not as well understood as the flow of a liquid. Therefore this paper first addresses the flow of the absorber spheres, with both simulations as well as experiments. The flow was simulated with the discrete element method (DEM) and fits the experimental results well. Also, the ideal diameter range was determined to be between $500\ \mu\text{m}$ and $1000\ \mu\text{m}$ or between 1/12th and 1/6th of the tube diameter.

As a next step, the possible interaction between the solid absorber particle and the aluminum seal has been modeled. First the seal behavior has been simulated using the smoothed particle hydrodynamics (SPH) method, which has been extended with an energy transport equation, melt behavior, and surface tension model. This model has consequently been coupled to the particle simulation, and a combined simulation has been done. Using this model it was found that the time required to release the particles by melt of the seal in case that the outer surface of the system is 700°C is less than 500 ms. Also it was found that the liquid seal remains attached to the tube when molten and after release of the particles. This reduces the likelihood of interaction between the liquid aluminum and the particles and thus reduces blocking likelihood of the particles.

In the future unprotected and protected transients need to be done using a system code such as RELAP in order to verify that the proposed system is able to protect the reactor during these transients, without interfering with the primary SCRAM system.

References

- [1] R. K. Paschall and A. S. Jackola, "Hydraulically supported absorber balls iss (inherent shutdown system)—water loop testing, absorber column," Tech. Rep., Rockwell International, 1976.
- [2] E. R. Specht, R. K. Paschall, M. Marquette, and A. Jackola, "Hydraulically supported absorber balls shutdown system for inherently safe lmfbr's," in *Proceedings of the International Meeting on Fast Reactor Safety and Related Physics*, vol. 3, p. 683, 1976.
- [3] M. Kambe, H. Tsunoda, K. Mishima, and T. Iwamura, "RAPID-L operator-free fast reactor concept without any control rods," *Nuclear Technology*, vol. 143, no. 1, pp. 11–21, 2003.
- [4] M. Kambe and M. Uotani, "Design and development of fast breeder reactor passive reactivity control systems: LEM and LIM," *Nuclear Technology*, vol. 122, no. 2, pp. 179–195, 1998.
- [5] E. L. Gluekler, "U.S. Advanced liquid metal reactor (ALMR)," *Progress in Nuclear Energy*, vol. 31, no. 1-2, pp. 43–61, 1997.
- [6] M. J. Driscoll, M. A. Pope, and P. Hejzlar, "Self-actuated reactivity insertion device for GFR service," *Transactions of the American Nuclear Society*, vol. 89, pp. 573–576, 2003.

- [7] OECD, "Status of LMFBR safety technology improving the performance and reliability of protection and shutdown systems," OECD CSNI-R-69:0, 1983.
- [8] K. Marten and H. Hoffmann, "Fluid dynamic investigations of snr-300 absorbers of the first and second shutdown unit," Tech. Rep., Karlsruhe Nuclear Research Center, 1980.
- [9] F. H. Morgenstern, F. Brandl, V. Ertel, and A. Schoensiegel, "The plant protection system of the SNR-300," in *Proceedings of the IEEE International Meeting on Fast Reactor Safety Technology*, pp. 2602–2611, 1979.
- [10] S. Vanmaercke, G. van den Eynde, E. Tijskens, and Y. Bartosiewicz, "Design of a complementary scram system for liquid metal cooled nuclear reactors," *Nuclear Engineering and Design*, vol. 243, pp. 87–94, 2012.
- [11] D. B. Pelowitz, *MCNPX User Manual*, RSICC, 2005.
- [12] G. Van Den Eynde, E. Malambu, H. A. Abderrahim et al., "Neutronic design of the XT-ADS core," in *Proceedings of the International Conference on the Physics of Reactors (PHYSOR '08)*, vol. 3, pp. 2110–2115, 2008.
- [13] F. A. Dullien, *Porous Media: Fluid Transport and Pore Structure*, Academic Press, 1991.
- [14] P. Van Liedekerke, E. Tijskens, E. Dintwa, J. Anthonis, and H. Ramon, "A discrete element model for simulation of a spinning disc fertilizer spreader," *Powder Technology*, vol. 170, pp. 348–360, 2009.
- [15] N. V. Brilliantov, F. Spahn, J. M. Hertzsch, and T. Pöschel, "Model for collisions in granular gases," *Physical Review E*, vol. 53, no. 5, pp. 5382–5392, 1996.
- [16] G. Kuwabara and K. Kono, "Restitution coefficient in a collision between 2 spheres," *Japanese Journal of Applied Physics Part 1*, vol. 26, no. 8, pp. 1230–1233, 1987.
- [17] P. Franken, S. Francois, E. Tijskens, and G. Degrande, "A tangential force-displacement model for elastic frictional contact between the particles in triaxial test simulations," in *Proceedings of the International Conference on Particle-Based Methods Fundamentals and Applications*, Barcelona, Spain, 2011.
- [18] L. Vu-Quoc and X. Zhang, "Accurate and efficient tangential force-displacement model for elastic frictional contact in particle-flow simulations," *Mechanics of Materials*, vol. 31, no. 4, pp. 235–269, 1999.
- [19] R. D. Mindlin and H. Deresiewicz, "Elastic spheres in contact under varying oblique forces," *ASME Journal Applied Mechanics*, vol. 20, pp. 327–344, 1953.
- [20] B. D. Lucas and T. Kanade, "An iterative image registration technique with application to stereo vision," in *Proceedings of Imaging Understanding Workshop*, pp. 121–130, 1981.
- [21] V. P. Nguyen, T. Rabczuk, S. Bordas, and M. Duflot, "Meshless methods: a review and computer implementation aspects," *Mathematics and Computers in Simulation*, vol. 79, no. 3, pp. 763–813, 2008.
- [22] M. Becker and M. Teschner, "Weakly compressible sph for free surface flows," in *Proceedings of the Eurographics/ACM SIGGRAPH Symposium on Computer Animation*, 2007.
- [23] J. J. Monaghan, "Smoothed particle hydrodynamics," *Annual Review of Astronomy and Astrophysics*, vol. 30, no. 1, pp. 543–574, 1992.
- [24] J. J. Monaghan, H. E. Huppert, and M. G. Worster, "Solidification using smoothed particle hydrodynamics," *Journal of Computational Physics*, vol. 206, no. 2, pp. 684–705, 2005.
- [25] A. Tartakovsky and P. Meakin, "Modeling of surface tension and contact angles with smoothed particle hydrodynamics," *Physical Review E*, vol. 72, no. 2, Article ID 026301, pp. 1–9, 2005.
- [26] J. E. Jones, "On the determination of molecular fields. from the equation of state of a gas," *Proceedings of the Royal Society of London Series A*, vol. 106, pp. 463–477, 1924.

Research Article

Advanced Method for Calculations of Core Burn-Up, Activation of Structural Materials, and Spallation Products Accumulation in Accelerator-Driven Systems

A. Stankovskiy and G. Van den Eynde

Institute of Advanced Nuclear Systems, SCK·CEN, Boeretang 200, 2400 Mol, Belgium

Correspondence should be addressed to A. Stankovskiy, astankov@sckcen.be

Received 14 November 2011; Accepted 26 January 2012

Academic Editor: Alberto Talamo

Copyright © 2012 A. Stankovskiy and G. Van den Eynde. This is an open access article distributed under the Creative Commons Attribution License, which permits unrestricted use, distribution, and reproduction in any medium, provided the original work is properly cited.

The ALEPH2 Monte Carlo depletion code has two principal features that make it a flexible and powerful tool for reactor analysis. First of all, it uses a nuclear data library covering neutron- and proton-induced reactions, neutron and proton fission product yields, spontaneous fission product yields, radioactive decay data, and total recoverable energies per fission. Secondly, it uses a state-of-the-art numerical solver for the first-order ordinary differential equations describing the isotope balances, namely, a Radau IIA implicit Runge-Kutta method. The versatility of the code allows using it for time behavior simulation of various systems ranging from single pin model to full-scale reactor model, including such specific facilities as accelerator-driven systems. The core burn-up, activation of the structural materials, irradiation of samples, and, in addition, accumulation of spallation products in accelerator-driven systems can be calculated in a single ALEPH2 run. The code is extensively used for the neutronics design of the MYRRHA research facility which will operate in both critical and subcritical modes.

1. Introduction

SCK·CEN, the Belgian Nuclear Research Centre in Mol, is designing a Multipurpose Hybrid Research Reactor for High-tech Applications (MYRRHA) [1, 2]. The Accelerator-Driven System (ADS) concept has been chosen as a basis for this reactor, assuming that it can operate in both subcritical and critical modes (clearly without the accelerator running). The 600 MeV, 4 mA proton accelerator is coupled with the MOX-fueled core. The lead-bismuth eutectic (LBE) serves as coolant and spallation target to generate the source neutrons. To perform the neutronics design of such a system, dedicated codes must be used. The majority of neutronics codes used in the analysis of critical systems cannot be applied to calculations of ADS since multiparticle physics extending far beyond the energy range typical for nuclear reactors is involved.

The growth of computing power caused sustainable increase of the share of Monte Carlo codes in nuclear reactor and nuclear criticality research and development. These

Monte Carlo codes can provide the most accurate locally dependent neutronics characteristics in realistic 3D geometries of any complexity. Among them, only the general-purpose radiation transport code MCNPX [3, 4] is fully capable to treat ADS-related problems, since it tracks almost all particle types of nearly all energies. In the upper energy region (above 20 MeV) it relies on the model calculations using different intranuclear cascade, preequilibrium and equilibrium model combinations. However, recent progress in nuclear data library extensions to higher energies (up to 200 MeV) allows implementing evaluated nuclear data in neutronics analysis of ADS systems. These evaluated data are generally more precise than model calculations. Thus MCNPX coupled with nuclear data libraries is a powerful tool to perform steady-state particle transport calculations.

However, it has limited applicability to follow the evolution of the system neutronics characteristics in time. Its depletion module based on the CINDER90 code [5] can only be applied to fuel burn-up calculations in criticality

(KCODE) mode and not in the fixed source mode necessary to model ADS. In addition, the material activation and spallation products accumulation cannot be treated at all thus external depletion codes are required. Among such depletion codes oriented to calculate time behavior of nuclide inventories, the SNT code [6] and EASY-2007 code system [7] can be mentioned. The ADS core burn-up is reported to be studied with EVOLCODE [8, 9] and MCB [10] codes. However, to our knowledge, none of these codes is capable to simulate the behavior of ADS neutronics in time.

There is a noticeable progress in the development of reactor-oriented Monte Carlo depletion codes such as those mentioned above: MCNPX with CINDER'90 depletion capability, MCB, as well as Serpent [11], MURE [12], ACAB [13], MonteBurns [14], Casmo/Simulate [15], and other codes. The common principle of these codes is that a steady-state Monte Carlo calculation of neutron fluxes and spectra is followed by solving the system of first-order ordinary differential equations (ODEs) for a given time step using the reaction rates calculated from these fluxes and spectra. Then the nuclide concentrations are updated and passed to the Monte Carlo code for recalculation of fluxes and spectra, and so forth. This procedure repeats up to the end of the irradiation and/or decay history. As a rule, these codes wrap around general-purpose Monte Carlo radiation transport codes (MCNP [16], MCNPX) and depletion codes (ORIGEN [17, 18], CINDER'90). However, some of them use built-in depletion modules (MCB, Serpent). The method of coupling is often realized as a set of scripts which complicates its utilization by nonexperienced users.

The general-purpose burn-up code ALEPH merging MCNP(X) (any version of MCNP or MCNPX) Monte Carlo radiation transport and ORIGEN-2.2 [17] depletion codes is being developed at SCK-CEN since 2004 [19, 20]. Belonging to the same category of shells coupling Monte Carlo transport and "deterministic" depletion codes, ALEPH possess some unique features that distinguish it from other codes. The most important feature is full consistency of cross-section data. The same unionized cross section tables (i.e., cross sections are linearized on the same energy grid) for a given nuclide are used for Monte Carlo transport and subsequent depletion calculations. The reaction rates are calculated at the beginning of each time step using the fluxes and spectra provided by MCNP(X). ALEPH allows the user to change materials, temperature, and geometry after each time step to reflect the irradiation conditions. Finally, the code is easy to use since it requires only several extra cards in the MCNP(X) input deck. The validity of ALEPH has been confirmed for different types of problems [21–23].

However, since ALEPH invokes ORIGEN-2.2 to perform time evolution calculations, it retains all limitations inherent to ORIGEN-2.2. This concerns the accuracy of matrix exponential method to solve ODEs and the limited number of nuclear data involved. The application of the code is limited to (classical) reactor systems.

The new version of the code, ALEPH2 [24], is free from these limits and possess some other outstanding features which altogether make it a powerful and flexible tool to

perform time evolution analysis of various nuclear systems. It is fully applicable to ADS problems: core burn-up calculations, activation of structural materials, spallation product accumulation, and associated radiation source terms (decay heat release, heat generation by delayed photons, absorbed doses, neutron sources due to decay) can be calculated in a single code run which requires a few extra cards to MCNPX input deck. The features of the code especially important for ADS-related problems are described in Section 2 with the main focus on the method to perform depletion calculations. Section 3 describes the application of the code to the neutronics design of MYRRHA system and the conclusions are drawn in Section 4.

2. Basic Working Principles of ALEPH2

Two principal modifications have been made to ALEPH code: extending the nuclear data set and replacing ORIGEN-2.2 by built-in depletion module. Besides that, the predictor-corrector mechanism, calculation of heating during irradiation and decay, calculation of neutron sources due to decay, fuel management as well as some minor corrections to improve the code performance and facility of use were made.

2.1. Nuclear Data. One of two major improvements concerns nuclear data treatment. ORIGEN-2.2 is capable to treat only a limited number of reactions (radiative capture, fission, $(n, 2n)$, $(n, 3n)$, (n, p) , and (n, α)). However, the ADS problems require more extensive nuclear data treatment. The number of open reaction channels can be significantly higher and increases drastically for the problems involving energies beyond those characteristic to nuclear reactors. The auxiliary utility, ALEPH-DLG [20] wrapping around the NJOY code [25], was modified to be able to build the nuclear data library containing nuclide production cross sections up to 1 GeV. The library can be constructed for a set of temperatures from basic general-purpose evaluated data files like JEFF-3.1.1 [26, 27], ENDF/B-VII [28], or JENDL-4 [29]. Then it is extended to a higher number of nuclides and reactions per target nuclide by adding the data from the TENDL-2010 library [30]. TENDL-2010 contains ~2000 neutron files for the nuclides with half-lives greater than one second. The upper energy limit in these files is either 200 MeV for the majority of stable and important unstable nuclides or 60 MeV for short-lived isotopes. Actinides, however, have upper limit 20 MeV. The final step is an extension to higher energies using the HEAD-2009 activation data library [31]. The HEAD-2009 library contains neutron- and proton-induced data for 684 stable and unstable nuclides from C to Po in the primary particle energy range 150 MeV to 1 GeV.

Proton-induced reactions can play an important role in investigating the time behavior of spallation and activation products in an ADS. The capability to treat proton data was added to ALEPH. To summarize, the new library constructed by ALEPH-DLG consists of ~2000 neutron files and ~1200 proton files for individual nuclides with half-lives greater than a second. Files contain up to ~2000 reaction cross sections with upper energy limit 1 GeV.

Since the number of reactions for an individual nuclide can be rather high, significant efforts were directed to accelerate the cross section averaging over the spectrum produced by MCNP(X). The format of activation data storing (PENDF tapes generated by NJOY code) was found to be ineffective. It was changed to ACE (A Compact ENDF) dosimetry type [3, 4, 16] where only reaction cross sections are recorded. Tests have shown that the total time to get one-group averaged cross sections for most complex problem (involving all reactions for all nuclides in the library, i.e., about 460,000 neutron and proton induced reactions) is comparable to the time to process ~3000 neutron reactions for most complex problem handled by the previous version of ALEPH.

The previous version of ALEPH was updating only cross sections in the ORIGEN library at the beginning of each time step; moreover, the cross sections of reactions leading to metastable states remained unchanged. All other information, such as neutron fission product yields and radioactive decay data, was not updated. The ALEPH2 code is capable to use almost all special-purpose data supplied in basic libraries, namely, radioactive decay data (e.g., JEFF-3.1.1 radioactive decay file contains information for 3851 nuclides), total recoverable energy per fission of fissile nuclides, spontaneous neutron fission product yields, and direct neutron and proton fission product yields.

2.2. Depletion Algorithm. Assuming that the particle fluxes and spectra remain constant during the time step and locally in selected volume, the concentrations (atom densities) of nuclides y_i at the end of irradiation step can be obtained by solving the system of first-order linear differential equations with constant coefficients:

$$\frac{dy_i(t)}{dt} = \sum_j \lambda_{ji}^{tr} y_j(t) - \lambda_i^{tr} y_i(t), \quad (1)$$

or, in compact matrix form,

$$\frac{d\vec{y}}{dt} = \Lambda \vec{y}, \quad (2)$$

with the matrix coefficients being $\lambda_{ij} = \lambda_{ji}^{tr} - \lambda_i^{tr} \delta_{ij}$. Here λ_{ji}^{tr} is the transmutation (production) rate of nuclide i from nuclide j , and λ_i^{tr} is the disappearance rate of nuclide i . These rates are defined as follows:

$$\lambda_{ji}^{tr} = \sum_m \sigma_{ji}^m \varphi^m + \lambda_{ji}^d, \quad (3)$$

$$\lambda_i^{tr} = \sum_m \sigma_{R,i}^m \varphi^m + \lambda_i^d. \quad (4)$$

Here σ_{ji}^m is the energy-averaged production cross section of nuclide i from nuclide j in the reaction with incident particle m , φ^m is the average flux of type m particles, λ_{ji}^d stands for the decay rate of nuclide j into the nuclide i , $\sigma_{R,i}^m$ represents the energy-averaged reaction cross section of nuclide i transforming it into another nuclide, and λ_i^d

is the decay constant of nuclide i . In most cases $m =$ neutrons since only neutron reactions are considered, but when dealing with spallation products accumulation and activation of structural materials close enough to spallation target of accelerator driven system, the contribution of proton-induced reactions has to be taken into account.

As it was mentioned before, the previous version of ALEPH used the ORIGEN-2.2 depletion code [17] to obtain the nuclide concentrations at the end of irradiation step. The essence of the algorithm used by ORIGEN-2.2 is the matrix exponential method where the solution of (2) is obtained by truncating the power series for the exponential. The short-lived nuclides are assumed to decay instantly and are removed from the system. They are treated separately by a Gauss-Seidel iterative technique under the assumption of secular equilibrium of decay and production chains. The same method is used by the successor of ORIGEN-2.2, ORIGEN-S which is a part of the SCALE code system [18]. It is clear that the applied series expansion has a limited accuracy due to truncation and round-off errors. Moreover, due to some inherent workings of ORIGEN-2.2 it cannot be applied to the problems involving particle types other than neutron.

Modern computers, however, allow applying more precise methods of solving the systems of stiff first-order differential equations with constant coefficients. The common practice is to use the backward differentiation formulas (BDF methods) or implicit Runge-Kutta (IRK) methods. The IRK methods offer some important advantages over BDF. Being single step, the IRK methods do not suffer from systems discontinuities and changes in the order or time step. The IRK methods are also self-starting which means that the only starting values required are the initial conditions. However, the drawback is leading after the time discretization to larger and more complex sets of linear equations. Numerous tests have shown that the IRK method Radau IIA (3 stages, accuracy order 5) as implemented in RADAU5 solver [32] is more stable and faster than the BDF method applied in DLSODA solver [33, 34]. As a consequence the Radau IIA algorithm has been incorporated in ALEPH2. The details of implementation are given below.

2.2.1. Implementation. Implicit Runge-Kutta methods have been known to have a high order of solution accuracy and excellent stability properties in solving stiff ordinary differential equations (ODEs) [32, 35]:

$$\frac{dy(t)}{dt} = \mathbf{f}(t, \mathbf{y}(t)); \quad \mathbf{y}(t_0) = \mathbf{y}_0. \quad (5)$$

\mathbf{y} is unknown N -size vector of values (concentrations in case of depletion equations), and $\mathbf{f}(t, \mathbf{y}(t))$ is the N -size vector of functions of known form. In case of depletion equations, it is simply $\mathbf{f}(t, \mathbf{y}(t)) = \Lambda \mathbf{y}(t)$, and Λ is the effective reaction rate matrix.

If the time step is subdivided into m substeps with a fixed step size

$$h = \frac{t_1 - t_0}{m} \quad (6)$$

with the mesh points t_n , $n = 0, 1, \dots, m$, $t_m = t_1$, the implicit Runge-Kutta method is defined by

$$y_{n+1} = y_n + h \sum_{i=1}^s b_i f(t_n + c_i h, g_i). \quad (7)$$

Here

$$g_i = y_n + h \sum_{j=1}^s a_{ij} f(t_n + c_j h, g_j), \quad i = 1, \dots, s. \quad (8)$$

The stage number is denoted by s and a_{ij} , b_i , and c_i are parameters satisfying the conditions:

$$a_{ij} \neq 0, \quad \sum_{j=1}^s a_{ij} = c_i \quad \text{for } i = 1, 2, \dots, s, \quad \sum_{i=1}^s b_i = 1. \quad (9)$$

There are different IRK methods based on different sets of above parameters, the Radau IIA method being one of them. In this case, the parameters c_i for $i = 1, 2, \dots, s$ are selected as the zeros of Radau polynomial $(d^{s-1}/dt^{s-1})(t^{s-1}(t-1)^s)$. Parameters a_{ij} are obtained by solving the linear system

$$\sum_{j=1}^s a_{ij} c_j^{q-1} = \frac{c_i^q}{q}, \quad i = 1, \dots, s; \quad q = 1, \dots, s \quad (10)$$

and $b_i = a_{s,i}$ for $i = 1, 2, \dots, s$. Stage number s can be set to 1, 3, 5, or 7. The RADAU5 solver uses $s = 3$ thus its accuracy order is $2s - 1 = 5$ and it is considered as absolutely stable.

At each sub-step, the system (3) of rank sN has to be solved iteratively for the stage values $\{g_i\}_{i=1}^s$. To reduce round-off errors, it is often reformulated as

$$z_i = g_i - y_n, \quad (11)$$

where

$$z_i = h \sum_{j=1}^s a_{ij} f(t_n + c_j h, y_n + z_j), \quad i = 1, \dots, s. \quad (12)$$

Since the matrix of coefficients $A = (a_{ij})$ is nonsingular (as it can be seen from (10)), (12) can be rewritten in vector form

$$\begin{pmatrix} z_1 \\ \vdots \\ z_s \end{pmatrix} = A \begin{pmatrix} hf(t_n + c_1 h, y_n + z_1) \\ \vdots \\ hf(t_n + c_s h, y_n + z_s) \end{pmatrix}, \quad (13)$$

so that (7) becomes

$$y_{n+1} = y_n + \sum_{i=1}^s d_i z_i, \quad (14)$$

where the coefficients d_i are defined as

$$(d_1, \dots, d_s) = (b_1, \dots, b_s) A^T. \quad (15)$$

For $s = 3$, since $b_i = a_{s,i}$, the vector d is $(0, 0, 1)$.

The linear system with matrix

$$\begin{pmatrix} I - ha_{11} \frac{\partial f}{\partial y}(t_n + c_1 h, y_n + z_1) & \cdots & -ha_{1s} \frac{\partial f}{\partial y}(t_n + c_s h, y_n + z_s) \\ \vdots & \ddots & \vdots \\ -ha_{s1} \frac{\partial f}{\partial y}(t_n + c_1 h, y_n + z_1) & \cdots & I - ha_{ss} \frac{\partial f}{\partial y}(t_n + c_s h, y_n + z_s) \end{pmatrix} \quad (16)$$

must be solved to get the solution at the end of time step. The Jacobians in (12) are approximated as follows:

$$J = \frac{\partial f}{\partial y}(t_n + c_i h, y_n + z_i) \approx \frac{\partial f}{\partial y}(t_n, y_n). \quad (17)$$

It has to be noted that for the case of depletion equations the calculation of the Jacobians is straightforward since $\partial f / \partial y_i = \lambda_{ii}$. The simplified Newton iterations become

$$(I - hA \otimes J) \Delta Z^k = -Z^k + h(A \otimes I) F(Z^k) \quad (18)$$

$$Z^{k+1} = Z^k + \Delta Z^k.$$

Here the following notations are used:

(i) k th approximation to the solution $Z^k = (z_1^k, \dots, z_s^k)^T$;

(ii) increments $\Delta Z^k = (\Delta z_1^k, \dots, \Delta z_s^k)^T$;

(iii) function $F(Z^k) = (f(t_n + c_1 h, y_n + z_1^k), \dots, f(t_n + c_s h, y_n + z_s^k))^T$.

Thus each iteration requires $s = 3$ evaluations of f and the solution of a linear system with the dimension $3N$. Each linear system of dimension sN can be split into one real and one complex linear system of dimension N through a dimensionality reduction procedure [36]. As a result, the computing time of solving each related linear system is

sharply reduced. This dimensionality reduction makes the simplified Newton method efficient in the implementation of IRK methods. However, this method has poor convergence properties since it is only an approximation of the classic Newton-chord method [37]. Reducing the step size can accelerate the convergence rate of the simplified Newton method. RADAU5 automatically selects a sufficiently small step size of IRK to yield a fast rate of convergence.

The matrix $I - hA \otimes J$ is computed only once for all iterations for linear problems with constant coefficients (depletion problems belong to this category).

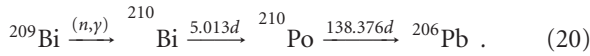
The step size is not a constant and changes according to the following relation [32]:

$$h_{\text{new}} = h_{\text{old}} \cdot \theta \left(\frac{\text{Tol}}{\|\text{Err}\|} \right)^{1/(s+1)}, \quad (19)$$

where $\|\text{Err}\|$ is error estimate, Tol is prescribed tolerance, and θ is model parameter ranging from 0.6 to 0.9 and usually being set to 0.9 if not too many step rejections occur.

2.2.2. Tests

(1) *Accuracy.* To test the accuracy of the RADAU5 solver applied to depletion calculations, a simple problem of calculation the ^{210}Po inventory accumulated in lead-bismuth eutectic coolant of MYRRHA after 90 days of irradiation has been investigated. Neglecting ^{210}Po production chains from lead isotopes (whose contribution into total ^{210}Po inventory is rather small), we focus on ^{210}Po production from neutron capture on ^{209}Bi through the chain:



The system (1) applied to this chain can be solved analytically for the given time step and initial concentration of ^{209}Bi using the classic Bateman solutions [38]

$$y_n = \frac{y_1(0)}{\lambda_n^{tr}} \sum_{i=1}^n \lambda_i^{tr} \alpha_i e^{-\lambda_i^{tr} t}, \quad (21)$$

where

$$\alpha_i = \prod_{\substack{j=1 \\ j \neq i}}^n \frac{\lambda_j^{tr}}{(\lambda_j^{tr} - \lambda_i^{tr})}. \quad (22)$$

The indexing here is according to (20) so that $i = 1$ is assigned to ^{209}Bi .

The numerical data used to obtain concentrations are summarized in Table 1. The values of average capture cross section on ^{209}Bi leading to the ground state of ^{210}Bi , neutron flux, and initial concentration of ^{209}Bi are typical for MYRRHA core. It has to be noted that the energy dependence of the branching ratio of (n, γ) reaction leading to ground and metastable states of ^{210}Bi has been taken into account, since only the ground state of ^{210}Bi decays to ^{210}Po .

For the calculations with RADAU5, $\lambda_{21} = -\lambda_{21}$, $\lambda_{32} = -\lambda_{22}$, $\lambda_{43} = -\lambda_{33}$, all other $\lambda_{ji} = 0$.

TABLE 1: Input parameters for calculation of ^{210}Po production.

i	Nuclide	$y(0)$, at/(b·cm)	λ_{ii} , s $^{-1}$
1	^{209}Bi	0.0165368	$-2.09 \cdot 10^{-11}$ *
2	^{210}Bi	0.0	$-1.60043 \cdot 10^{-6}$
3	^{210}Po	0.0	$-5.79554 \cdot 10^{-8}$
4	^{206}Pb	0.0	0.0

* Obtained by multiplying $\sigma = 0.0209$ b with $\varphi = 1 \cdot 10^{15}$ n/(cm 2 s).

For the calculations with ORIGEN-2.2, all the cross sections in ORIGEN-2.2 library were zeroed, except neutron capture cross section on ^{209}Bi . The considered decay chain was also separated from other chains in the decay library by zeroing decay constants to ensure full consistency with analytical solution at the level of input data. The results of comparison are shown in Table 2.

The calculations with RADAU5 were performed with two different tolerance values, Tol = 10^{-4} which was selected from numerous tests as ensuring the best quality at the reasonable speed when handling full matrix with $N = 3851$, and, for the sake of comparison, Tol = 10^{-10} which requires longer calculation time. As it can be seen from Table 2, ORIGEN-2.2 code cannot even provide accurate enough results for the small system of 4 equations. In contrast, RADAU5 has shown the outstanding quality. Thus, the obvious conclusion is that matrix exponential method of ORIGEN-2.2 cannot solve concentrations as accurately as RADAU5 does.

(2) *Speed.* RADAU5 has shown an excellent accuracy compared to matrix exponential method of ORIGEN-2.2, but at the cost of computational time which strongly depends on the size of matrix Λ with effective reaction rates. The comparison of RADAU5 (IRK method) and DLSODA (BDF method) is shown in Figure 1 as a function of matrix dimension N . The results were normalized to the CPU time required for ORIGEN-2.2 to solve the same number of equations. It has to be noted that ORIGEN is capable to treat only ~ 1700 nuclides.

The matrix exponential method of ORIGEN-2.2 has shown weak dependence on the size of the ODE system. Two precise numerical methods are competitive with ORIGEN only up to $N \sim 500$. In terms of nuclide inventory calculations, the calculations of structural materials activation can be done even faster than by ORIGEN. RADAU5 runs almost 2 times faster than BDF. This is an additional justification of our choice of proper method to solve system of ODE.

As it is mentioned in [35], poor convergence properties of the simplified Newton method may force the code to generate too small step sizes, which reduces the performance. Use of larger step sizes to solve an ODE system is one of main advantages of IRK. To retain this advantage, more effective iterative algorithms were proposed in [35] with better convergence properties than the simplified Newton method. The gain, as reported in [35], could be a reduction of the CPU time needed by a factor of two.

TABLE 2: Calculated nuclide inventories for $t = 90$ days and relative differences $((y_i^{\text{calc}} - y_i^{\text{anal}})/y_i^{\text{anal}})$ from analytical solution.

Nuclide	Analytical solution	ORIGEN-2.2		RADAU5, Tol = 10^{-4}		RADAU5, Tol = 10^{-10}	
	at/(b·cm)	at/(b·cm)	diff, %	at/(b·cm)	diff, %	at/(b·cm)	diff, %
^{209}Bi	$1.65341e-2$	$1.65341e-2$	$-7.68e-5$	$1.65341e-2$	0.0	$1.65341e-2$	0.0
^{210}Bi	$2.15920e-7$	$2.16954e-7$	$4.79e-1$	$2.15847e-7$	$-3.38e-2$	$2.15920e-7$	$-4.63e-11$
^{210}Po	$2.02059e-6$	$1.99902e-6$	1.07	$2.02067e-6$	$3.75e-3$	$2.02059e-6$	0.0
^{206}Pb	$4.50804e-7$	$4.74951e-7$	5.36	$4.50801e-7$	$-5.75e-4$	$4.50804e-7$	$-3.55e-10$

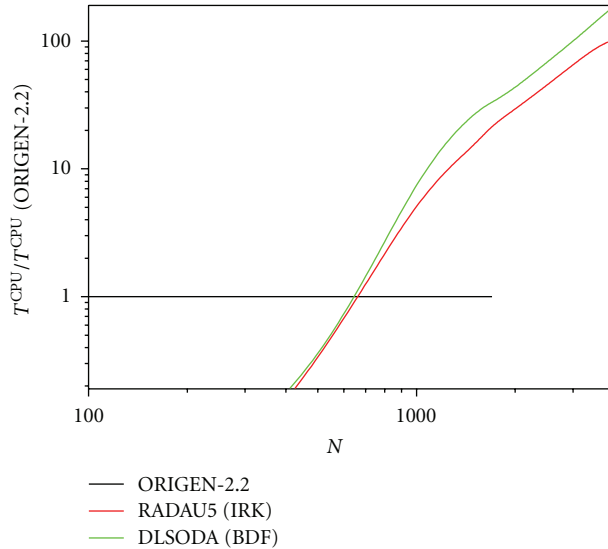


FIGURE 1: Elapsed CPU time as a function of the number of ODE equations.

But this improvement, once implemented, will not significantly influence the total calculation time for typical depletion problems. Usually, Monte Carlo steady-state particle transport calculation at the beginning of time step requires much more CPU performance than subsequent generation of matrix with effective reaction rates and solving the ODEs. The typical calculation time distribution among ALEPH modules required to complete one burn-up step of MYRRHA sub-critical core is shown in Table 3.

To reduce the impact of the RADAU5 solver on the total calculation time, especially for the problems with a huge number of irradiated materials, a simple parallelization was recently implemented when each material is treated separately in its own parallel task. The CPU wall time share shown in Table 3 is reduced to ~ 30 sec.

To summarize, the speed-up of RADAU5 is subject for future work, in view of implementation of nuclear data uncertainty propagation algorithms which are also in our high-priority to-do list for future ALEPH2 development. However, even now for typical ADS problems involving numerous materials (fuel, clad, structural materials, LBE spallation target, and coolant, etc.) ALEPH2 thanks to the RADAU5 solver provides very accurate nuclide inventories at an almost negligible CPU time compared to the total CPU time needed for the Monte Carlo simulation. Moreover, the

TABLE 3: CPU time share between ALEPH modules to calculate one irradiation step (90 days) of MYRRHA subcritical core. The MCNP(X) calculations have been performed on 64 CPU cluster using Open MPI. The number of irradiated materials is 11 (so that the reaction rates generator and the RADAU5 solver were called 11 times). Full matrix for $N = 3851$ nuclides is used.

	CPU wall time, s	Fraction, %
MCNPX fluxes and spectra, rsd 0.1%	$3.58e + 6$	99.988
ALEPH generation of average cross sections	19.3	$5.4e-4$
ALEPH solving ODE by RADAU5	312.5	$8.7e-3$
(or ALEPH solving ODE by ORIGEN-2.2)	(14.7)	($4.1e-4$)
Total		100

uncertainties on the nuclide concentrations at the end of time step are associated with nuclear data uncertainties and Monte Carlo statistical uncertainties only and not with the depletion calculations.

2.3. Predictor-Corrector Algorithm. The previous version of ALEPH did not use any predictor-corrector mechanism. A predictor-corrector mechanism aims to increase the macro time steps by using intermediate information. It should be noted that for the same macro time steps taken, the predictor-corrector method will obviously slow down the code since additional steady-state Monte Carlo calculations of fluxes and spectra are required. So if the macro time steps are kept the same, the option with predictor/corrector will increase the accuracy of the calculation at the cost of more CPU time. In case the required accuracy is fixed, the predictor/corrector will allow increasing the macro time steps, reducing the total number of macro time steps for the full irradiation history simulation. Of course, the best option from the quality/performance point of view remains the fine binning of irradiation history; however it is not always possible to properly define it. This situation is somehow similar to the variance reduction technique inside a Monte Carlo code itself: the best variance reduction is simply higher statistics, but for some problems such increase is not feasible.

In order not to severely overburden memory consumption, the number of Monte Carlo calculations per step using predictor-corrector is limited to 2. This means that the fluxes and spectra are calculated at the beginning of time step, and

then the concentrations are obtained at the half of the time step. Using these concentrations, the fluxes and spectra are recalculated and finally the concentrations at the end of time step are computed on the basis of new fluxes and spectra. The ALEPH2 code decides whether to apply predictor-corrector or not by comparing the nuclide concentrations and reaction rates at the beginning and end of time step.

A new and unique feature of ALEPH2 is the possibility of using the time-dependent matrix coefficients when solving the system of ODEs by the RADAU5 method. Since the function $\mathbf{f}(t, \mathbf{y}(t))$ in the right-hand side of (5) can be of arbitrary form, the coefficients λ_{ij} can in general be time-dependent. This allows to better reflect the realistic irradiation conditions. Starting from the second macro step, when the matrix coefficients are computed for 3 time points ($t = 0$, $t = 1/2\tau$ and $t = \tau$, here τ denotes time step length), ALEPH2 uses the linear extrapolation of the matrix coefficients and RADAU5 solver computes the nuclide concentrations using these linearly time-dependent reaction rates. The implementation of this feature is currently in the test phase.

2.4. Calculation of Photon Heating. The calculation of heating caused by photons is divided in two steps. When ALEPH2 calculates regular tallies of particle flux and spectra, it appends the photons to the list of transported particles and computes the flux and spectrum of prompt gammas. By folding the heating numbers (kerma factors) from nuclear data files with photon spectra, it computes the local heating caused by prompt photons. After that, ALEPH2 creates an additional MCNP(X) photon-only problem with the source of photons built from the information on nuclide concentrations at the beginning of time step and associated decay gammas. Nuclides are assumed to be uniformly distributed inside the material of interest. If the user has provided the cylindrical mesh covering the problem geometry with irradiated materials, the photon source is distributed similarly to the MCNP(X) power law “-21”. The additional calculation of photon-only problem usually does not increase significantly the total calculation time required for the given irradiation step. Using again the photon heating numbers, ALEPH2 computes the delayed photon heating and then sums up the two contributions—prompt and delayed—to get total photon heating.

2.5. (α, n) Neutron Source. Another major improvement of the code concerns the possibility to calculate the neutron source due to (α, n) reaction. It has to be noted, however, that this option can work with the MCNPX code only since it requires the simulation of alpha particle transport which is not compatible with MCNP code family.

The code generates the dependent source distribution of alpha particles at the beginning of each decay step (if requested by the user) in a similar way as it does for delayed photons described above. The energy distribution and intensity of this source depends on the material composition in the cells containing materials to be followed. Then the calculation of alpha particle-only problem is launched at the

beginning of each decay step. The alpha particle flux and spectrum is tallied. It has to be noted again that ALEPH2 optimizes the source and physics parameters in such way that the MCNPX calculation completes quickly so that the total ALEPH2 calculation time remains almost unaffected. After the completion of spectrum calculation, the neutron source is computed using (α, n) reaction cross section library generated from TENDL-2010 library data [30].

This feature allows calculating the decay neutron source in a much more precise way than it is realized in ORIGEN-2.2 and ORIGEN-S.

2.6. Termination by Burn-Up Tracers Concentration. In the majority of problems the irradiation history cannot be explicitly known. Experimentally, one uses so-called burn-up tracers like Neodymium to estimate the burn-up in energy produced per heavy metal mass. For researchers working with this experimental data, it is important to be able to end the irradiation history, or better simulation history, when one or more of these tracers have reached a certain concentration corresponding to the experimentally measured values. This option has been added to ALEPH2. The user has either the ability to define a weighted sum of selected isotopes which has to converge with a certain precision (minimization of the deviation of the weighted sum) or to create a “virtual” tracer consisting of a sum of different isotopes.

2.7. Other Improvements. Besides major improvements some minor corrections were done, such as the possibility to simulate fuel management by allowing material, temperature, density replacement, and fuel assembly permutation at each desired time step.

The code possess the very useful capability to perform criticality calculations as complementary to the main fixed source calculation in the problems such as core burn-up of an ADS. This allows the user to better optimize the core shuffling, for instance. However, for these applications the calculation time approximately doubles since an additional Monte Carlo calculation is required.

Next, the improved version of the code contains significantly lower number of commands which have to be added to the standard MCNP(X) input deck than its predecessor. This reduces the complexity of running ALEPH2 and the probability for users to make errors.

3. Myrrha Neutronics Calculations

ALEPH2 is currently one of the main tools to perform neutronics design of the MYRRHA fast spectrum research facility. As it was mentioned throughout the paper, the sub-critical (and critical) core burn-up, test materials irradiation performance, activation of structural materials, spallation products accumulation, radiation source terms—all these quantities—can be calculated (and are being calculated) with ALEPH2. In this section, the examples of sub-critical core burn-up calculations and spallation products analysis are shown.

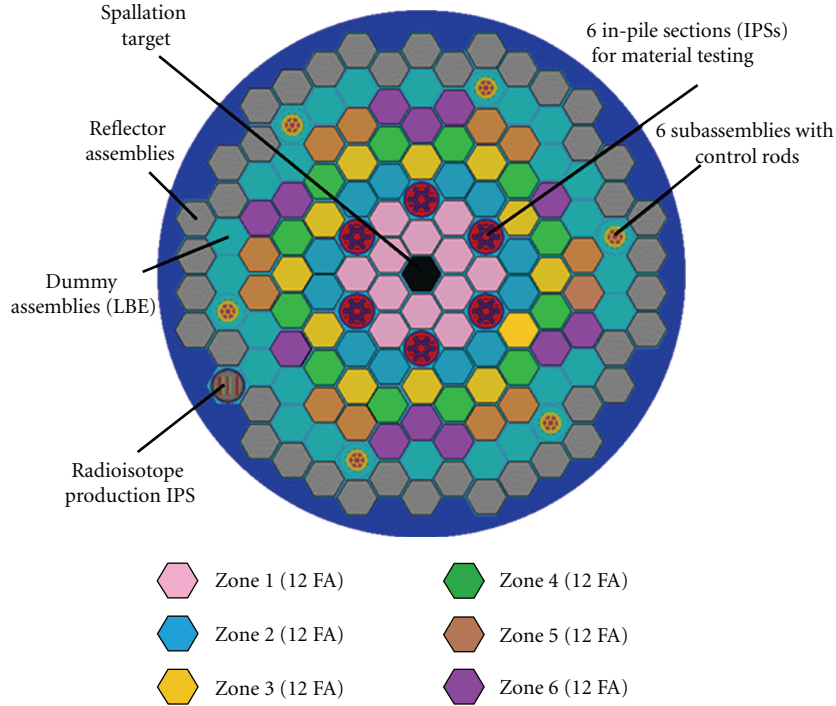


FIGURE 2: MYRRHA sub-critical core with 72 FA collected in 6 groups 12 FA each according to average neutron flux values.

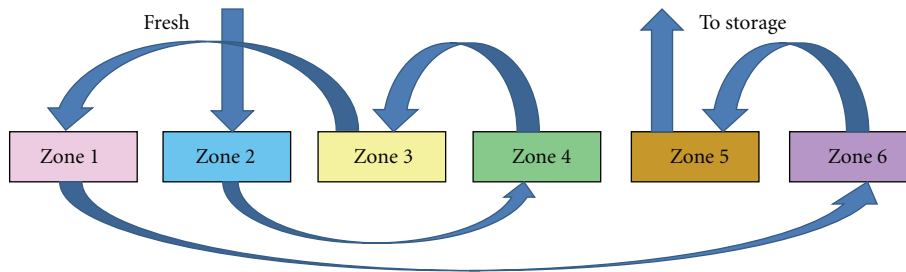


FIGURE 3: Mixed reshuffling scheme.

3.1. Core Burn-Up with Mixed Shuffling. A possible irradiation scheme envisages batches of three 90-day irradiations with two 30-day beam-off periods for maintenance between irradiations and long 90-day maintenance period after three irradiations. Current facility design implies only a limited number of interventions to increase the proton beam current in order to compensate reactivity losses. In the ALEPH2 model, the beam current was increased in the middle of the cycle (45 days) to compensate the reactivity loss. However, the limitations on the beam current and on the maximum clad temperature do not allow to achieve high burn-up values without fuel reshuffling. That's why several reshuffling strategies have been investigated with ALEPH2 code. Since ALEPH2 allows permuting or changing materials, the modeling of the reshuffling procedure becomes very simple in ALEPH2. The beginning-of-life (BoL) core consists

of 58 fresh fuel assemblies (FAs) and is characterized by effective neutron multiplication factor $k_{\text{eff}} \sim 0.965$. The fuel assemblies are grouped in six groups in order to minimize the flux variations between assemblies in the group. During first five maintenance periods, 2 to 4 assemblies with fresh fuel are added so that the core shown in Figure 2 is built with 72 FA (6 groups of 12 FA each). The central assembly hosts the spallation target structures. Besides that, there are shown 6 in-pile sections (IPSS) for test materials irradiations and one assembly hosting the irradiation device for production of radioisotopes. Control rods are in upper positions and are not assumed to be inserted in the core during normal operation.

The reshuffling strategy aimed at minimizing the reactivity swing during the cycle and reducing the radial power factor because the sub-critical cores with the source in

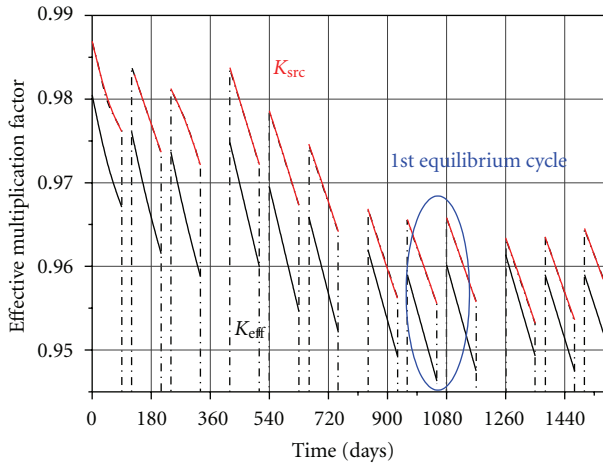


FIGURE 4: Evolution of effective neutron multiplication factor K_{eff} and external source neutron multiplication factor K_{src} .

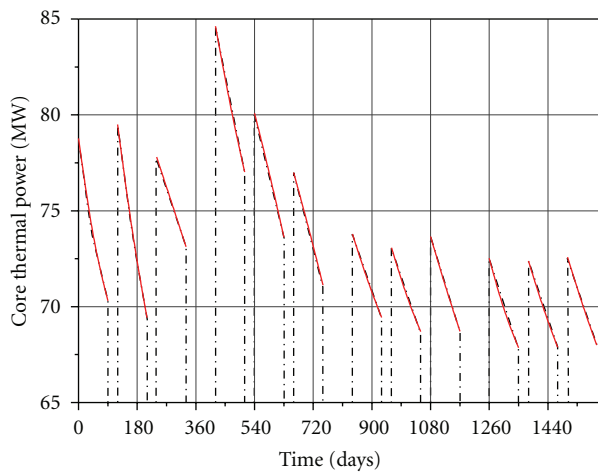


FIGURE 5: Evolution of total thermal power release.

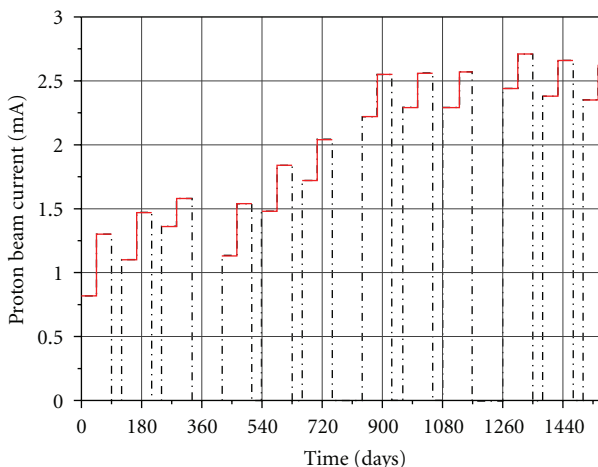


FIGURE 6: Evolution of proton beam current.

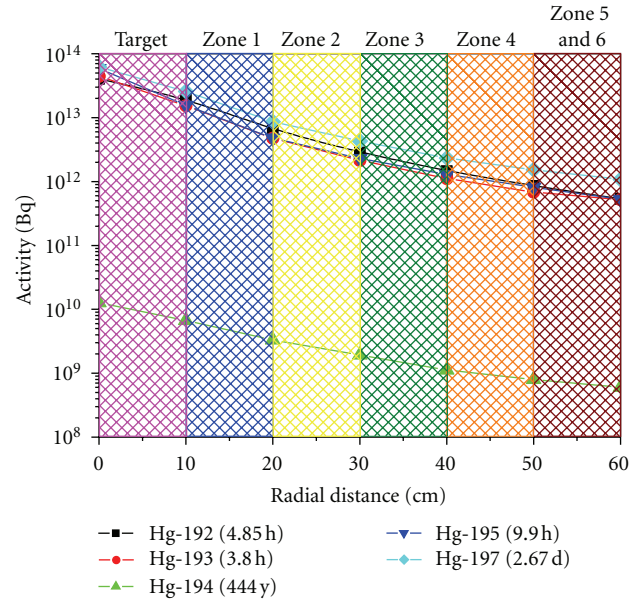


FIGURE 7: The radial dependence of Hg isotopes activity. Rings 1 to 6 denote the fuel assembly groups corresponding to Figure 2.

the center are characterized by a more steep flux gradient in the radial direction. A sensitivity analysis allowed to select the reshuffling scheme shown in Figure 3.

In this scheme, fresh fuel at the beginning of each cycle (BoC) is always inserted in Zone 2. Then, at each reshuffling, it subsequently goes to Zone 4, then Zone 3, Zone 1, Zone 6, and during the last irradiation cycle it resides in Zone 5. Results of main neutronics parameters calculations with ALEPH2 are shown in Figures 4, 5, and 6.

The system reaches equilibrium in ~ 3 years. The reshuffling scheme chosen allows keeping the power almost the same at the beginning of each cycle. The reactivity swing during the equilibrium cycle, ~ 1100 pcm, appears to be much less than that for the core loaded with fresh fuel (~ 1700 pcm). This is clearly a result from the optimization in positioning the fuel assemblies with different burn-up level.

3.2. Spallation Products Accumulation—A Mercury Example.

An important question to be answered is whether the confinement of the spallation source in a separate loop is worthwhile from the viewpoint of containing spallation and high-energy fission products. In order to analyze this, the specific case of mercury (with the very long-lived isotope ^{194}Hg) was studied.

The presence of Hg (all isotopes) has been evaluated for both the spallation volume and the volume of LBE circulating in the core. In the LBE composed of lead and bismuth, an impurity level of 1.734 mg/kg of mercury (natural occurring isotopes) has been assumed.

The different mercury yields, that is, atoms of Hg produced per proton coming from the accelerator, have been calculated. A distinction has been made in yields coming from proton-induced reactions and neutron induced reactions. The numerical values are given in Table 4.

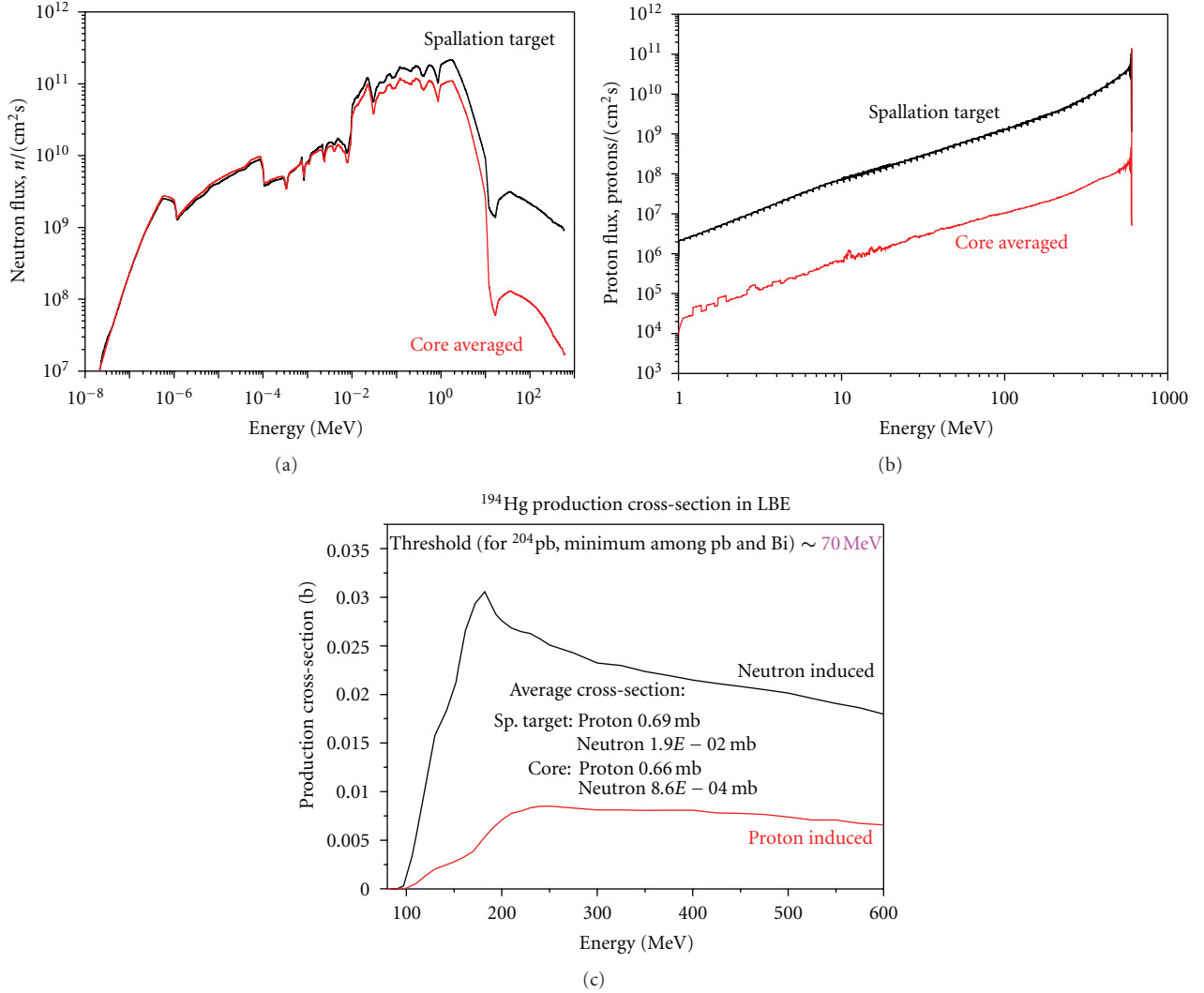


FIGURE 8: Neutron (a) and proton (b) energy spectra averaged over spallation target and core volumes. Neutron- and proton-induced ^{194}Hg production cross section from lead and bismuth isotopes (c).

Since ALEPH2 calculates neutron- and proton-induced production cross sections by averaging over the corresponding particle spectra, the yields shown in Table 4 were derived from ALEPH2 output using the relation

$$Y^m = V \cdot \gamma_{LBE} \sigma^m \phi_{MCNPX}^m, \quad (23)$$

where Y^m is the given nuclide yield due to reactions caused by particle type m , expressed in atoms per source proton, V is the scoring volume, γ_{LBE} represents the atomic density of LBE in atoms/(b·cm), σ^m stands for the energy-averaged production cross section (b) of the given nuclide by particle type m , and $\phi_{MCNPX}^m(E)$ is the MCNPX flux tally of particles m , expressed in particles per cm^2 per source proton. As it can be seen from this table, the relative contribution of proton-induced reactions is only about 25% both in the spallation target volume and in the core region. The rest is produced by neutrons (which in turn are produced in spallation target).

TABLE 4: Hg yield in atoms per source proton.

	Spallation target volume	Core volume
Hg yield due to protons (at/p)	0.032	0.036
Hg yield due to neutrons (at/p)	0.102	0.110
Total Hg yield (at/p)	0.134	0.146

Table 5 summarizes the different origins of mercury present in the spallation target and core volume after 90 days of irradiation at 2.5 mA, which corresponds to 70 MW of thermal power release at the equilibrium cycle. It is clear that the majority of the mercury is produced outside the spallation target volume.

The evolution of activity with distance to the core center is shown in Figure 7 for several radioactive mercury isotopes, ranging from short-lived to long-lived ^{194}Hg whose activity

TABLE 5: Origin of mercury in the LBE at the end of 90-day irradiation cycle.

	Spallation target volume	Core volume	Total
Hg as impurity (g)	0.56	25.62	26.18
Mass of Hg due to spallation (g)	5.28	5.74	11.02
Combined mass initial and spallation (g)	5.84	31.36	37.20

after 90 days of irradiation is rather low but will remain the main contributor to the activity of the irradiated LBE for thousands of years.

Figure 7 clearly shows that the presence of high-energy tail in neutron spectrum will produce mercury isotopes even in the periphery of the core. The thresholds of most of the neutron- and proton-induced reactions leading to production of mercury isotopes from lead and bismuth isotopes are typically 60–80 MeV. Neutron- and proton-spectra in the spallation target and core as well as ^{194}Hg production cross sections from neutron and proton-induced reactions on LBE isotopes are plotted in Figure 8 for illustration purposes. The cross sections are those used by ALEPH2; they have been generated from TENDL-2010 and HEAD-2009 libraries. Figure 8 confirms that spallation reactions will occur elsewhere (although with less intensity than in spallation target) where particles with energies above production threshold are present.

4. Conclusions

Two principal features of ALEPH2 Monte Carlo depletion code, an extensive nuclear data library and a state-of-the-art numerical solver for the Bateman equations, make this tool flexible and powerful. The nuclear data library covers neutron- and proton-induced reactions, neutron and proton fission product yields, spontaneous fission product yields, radioactive decay data and, total recoverable energies per fission. The numerical solver applied is an implicit Runge-Kutta method of the RADAU IIA family. The versatility of the code allows using it for time behavior simulation of various systems ranging from single pin models to full-scale reactor models, including specific facilities as accelerator-driven systems. The core burn-up, activation of the structural materials, irradiation of samples, and, in addition, accumulation of spallation products in accelerator-driven systems can be calculated in a single ALEPH2 run. The associated source term values, including decay heat release caused by particular radiation type, (α, n) and spontaneous fission neutron sources, absorbed doses, are calculated in much more precise way compared to other codes. All these features make ALEPH2 superior over other Monte Carlo depletion codes. The code is extensively used for the neutronics design of the MYRRHA research facility which will operate in both critical and sub-critical modes.

References

- [1] H. Ait Abderrahim, “MYRRHA, a new future for nuclear research. DRAFT-2 pre-design file,” Report R 4234, SCK·CEN, 2006.
- [2] “Independent evaluation of the MYRRHA project,” MIRT Report, OECD-NEA-6881, 2009.
- [3] D. B. Pelowitz, Ed., “MCNPX user’s manual, version 2.6.0,” Tech. Rep. LA-CP-07-1473, 2008.
- [4] D. B. Pelowitz et al., “MCNPX 2.7.C extensions,” Tech. Rep. LA-UR-10-00481, Los Alamos National Laboratory, 2010.
- [5] W. B. Wilson, T. R. England, and P. Möller, “A Manual for CINDER’90, Version 06.1 Codes and Data,” Advanced Fuel Cycle Program, 2006.
- [6] Y. A. Korovin, A. Y. Konobeyev, P. E. Pereslavtsev et al., “The code for the calculation of nuclide composition and activity of irradiated materials,” *Journal Yadernye Konstanty*, vol. 3-4, p. 117, 1992.
- [7] R. A. Forrest, “The European Activation System: EASY-2007 Overview,” UKAEA FUS 533, 2007.
- [8] E. Gonzalez, M. Embid, R. Fernandez et al., “EVOLCODE: ADS combined neutronics and isotopic evolution simulation system,” in *Proceedings of the International Conference (MC ’99)*, p. 963, Madrid, Spain, 1999.
- [9] F. Álvarez-Velarde, P. T. León, and E. M. González-Romero, “EVOLCODE2, a combined neutronics and burn-up evolution simulation code,” in *Proceedings of the 9th Information Exchange Meeting on Actinide and Fission Product P&T*, NEA/OECD, Nîmes, France, 2007.
- [10] J. Cetnar, “General solution of Bateman equations for nuclear transmutations,” *Annals of Nuclear Energy*, vol. 33, no. 7, pp. 640–645, 2006.
- [11] J. Leppänen, “Serpent Progress Report 2009,” VTT-R-01296-10, VTT Technical Research Centre of Finland, 2010.
- [12] O. Meplan et al., MURE, MCNP Utility for Reactor Evolution—User Guide—Version 1.0, IPNO-09-01, IPN Orsay, 2009.
- [13] N. García-Herranz, O. Cabellos, J. Sanz, J. Juan, and J. C. Kuijper, “Propagation of statistical and nuclear data uncertainties in Monte Carlo burn-up calculations,” *Annals of Nuclear Energy*, vol. 35, no. 4, pp. 714–730, 2008.
- [14] D. L. Poston and H. R. Trellue, “User’s Manual, version 2.0 for MONTEBURNS version 1.0,” Tech. Rep. LA-UR-99-4999, Los Alamos National Laboratory, 1999.
- [15] M. Edenius, K. Ekberg, B. H. Forsen, and D. Knott, “CASMO-4: A Fuel Assembly Burn-up Program User’s Manual,” Studsvik/SOA-95/1, Studsvik, 1995.
- [16] T. E. Booth and X-5 Monte Carlo Team, “MCNP—a general monte carlo N-particle transport code, version 5, volume II: user’s guide,” Tech. Rep. LA-CP-03-0245, Los Alamos National Laboratory, 2003.
- [17] A. G. Croff, “A user’s manual for the ORIGEN2 computer code,” Tech. Rep. ORNL/TM-7175, Oak Ridge National Laboratory, 1980.
- [18] I. C. Gauld et al., “Origen-S: SCALE system module to calculate fuel depletion, actinide transmutation, fission product buildup and decay, and associated radiation source terms,” SCALE-6 User Manual, ORNL/TM-2005/39, vol.2, sect. F7, 2009.
- [19] W. Haeck and B. Verboomen, “ALEPH 1.1.2—a monte carlo burn-up code,” BLG-1003, SCK·CEN, Brussels, Belgium, 2006.
- [20] W. Haeck and B. Verboomen, “ALEPH-DLG (Data Library Generator)—creating a general purpose validated application

- library for MCNP(X) and ALEPH,” BLG 1002, SCK·CEN, Brussels, Belgium, 2005.
- [21] W. Haeck and B. Verboom, “An optimum approach to Monte Carlo burn-up,” *Nuclear Science and Engineering*, vol. 156, no. 2, pp. 180–196, 2007.
- [22] A. Schubert, P. Van Uffelen, J. van de Laar, C. T. Walker, and W. Haeck, “Extension of the TRANSURANUS burn-up model,” *Journal of Nuclear Materials*, vol. 376, no. 1, pp. 1–10, 2008.
- [23] D. Chandler, R. T. Primm, and G. I. Maldonado, “Validation of a Monte Carlo based depletion methodology via High Flux Isotope Reactor HEU post-irradiation examination measurements,” *Nuclear Engineering and Design*, vol. 240, no. 5, pp. 1033–1042, 2010.
- [24] A. Stankovskiy, G. Van den Eynde, and T. Vidmar, “Development and validation of ALEPH Monte Carlo burn-up code,” in *Proceedings of the International Workshop (NEMEA-6 '10)*, pp. 161–169, Krakow, Poland, October 2010, NEA/NSC/DOC(2011)4.
- [25] R. E. MacFarlane and D. W. Muir, “The NJOY nuclear data processing system, Version 91,” Tech. Rep. LA-12740-M, Los Alamos National Laboratory, 1994.
- [26] A. Santamarina et al., “The JEFF-3.1.1 nuclear data library,” JEFF Report 22, NEA No. 6807, OECD, 2009.
- [27] A. J. Koning et al., “The JEFF-3.1 nuclear data library,” JEFF Report 21, NEA No. 6190, OECD, 2006.
- [28] M. B. Chadwick, P. Obložinský, M. Herman et al., “ENDF/B-VII.0: next generation evaluated nuclear data library for nuclear science and technology,” *Nuclear Data Sheets*, vol. 107, no. 12, pp. 2931–3060, 2006.
- [29] K. Shibata, O. Iwamoto, T. Nakagawa et al., “JENDL-4.0: a new library for nuclear science and engineering,” *Journal of Nuclear Science and Technology*, vol. 48, no. 1, pp. 1–30, 2011.
- [30] A. J. Koning and D. Rochman, “TENDL-2010: reaching completeness and accuracy,” JEFF-DOC 1349, 2010.
- [31] Y. A. Korovin, A. A. Natalenko, A. Y. Stankovskiy, S. G. Mashnik, and A. Y. Konobeyev, “High energy activation data library (HEAD-2009),” *Nuclear Instruments and Methods in Physics Research A*, vol. 624, no. 1, pp. 20–26, 2010.
- [32] E. Hairer and G. Wanner, *Solving Ordinary Differential Equations. Stiff and Differential-Algebraic Problems*, vol. 14 of *Springer Series in Computational Mathematics*, 2nd edition, 1996.
- [33] A. C. Hindmarsh, “ODEPACK, a systematized collection of ODE solvers,” in *Scientific Computing*, R. S. Stepleman et al., Ed., pp. 55–64, North-Holland, Amsterdam, The Netherlands, 1983.
- [34] L. R. Petzold, “Automatic selection of methods for solving stiff and nonstiff systems of ordinary differential equations,” *Journal on Scientific and Statistical Computing*, vol. 4, pp. 136–148, 1983.
- [35] D. Xie, “An improved approximate Newton method for implicit Runge-Kutta formulas,” *Journal of Computational and Applied Mathematics*, vol. 235, no. 17, pp. 5249–5258, 2011.
- [36] W. Liniger and R. Willoughby, “Efficient integration for stiff systems of ordinary differential equations,” *SIAM Journal on Numerical Analysis*, vol. 7, no. 1, pp. 47–66, 1970.
- [37] S. González-Pinto, J. I. Montijano, and S. Pérez-Rodríguez, “Implementation of high-order implicit Runge-Kutta methods,” *Computers and Mathematics with Applications*, vol. 41, no. 7-8, pp. 1009–1024, 2001.
- [38] H. Bateman, “Solution of a system of differential equations occurring in the theory of radioactive transformations,” *Proceedings of the Cambridge Philosophical Society, Mathematical and Physical Sciences*, vol. 15, pp. 423–427, 1910.

Research Article

A Fast Numerical Method for the Calculation of the Equilibrium Isotopic Composition of a Transmutation System in an Advanced Fuel Cycle

F. Álvarez-Velarde and E. M. González-Romero

Centro de Investigaciones Energéticas, Medioambientales y Tecnológicas (CIEMAT), Avenida. Complutense 40. Ed. 17, 28040 Madrid, Spain

Correspondence should be addressed to F. Álvarez-Velarde, francisco.alvarez@ciemat.es

Received 15 November 2011; Accepted 30 January 2012

Academic Editor: Alberto Talamo

Copyright © 2012 F. Álvarez-Velarde and E. M. González-Romero. This is an open access article distributed under the Creative Commons Attribution License, which permits unrestricted use, distribution, and reproduction in any medium, provided the original work is properly cited.

A fast numerical method for the calculation in a zero-dimensional approach of the equilibrium isotopic composition of an iteratively used transmutation system in an advanced fuel cycle, based on the Banach fixed point theorem, is described in this paper. The method divides the fuel cycle in successive stages: fuel fabrication, storage, irradiation inside the transmutation system, cooling, reprocessing, and incorporation of the external material into the new fresh fuel. The change of the fuel isotopic composition, represented by an isotope vector, is described in a matrix formulation. The resulting matrix equations are solved using direct methods with arbitrary precision arithmetic. The method has been successfully applied to a double-strata fuel cycle with light water reactors and accelerator-driven subcritical systems. After comparison to the results of the EVOLCODE 2.0 burn-up code, the observed differences are about a few percents in the mass estimations of the main actinides.

1. Introduction

The implementation of the advanced technologies of partitioning and transmutation (P&T) depends on the particular topics that energy policy makers of a country or region choose to optimize because of its singular constraints or motivations. Each of the different possible P&T configurations, that is, the advanced fuel cycle scenarios, will have different objectives that can impact technology choices and performance expected from such systems.

However, the full potential of any P&T policy can be exploited only if the advanced fuel cycle strategy is utilized for a minimum time period of about a hundred years [1, 2]. During this period of time, the irradiated fuels of the advanced reactors are reprocessed to obtain the useful elements for their later recycling as part of the new fresh fuel, in an iterative procedure along successive cycles. The fuel isotopic composition will evolve along a number of cycles, approaching progressively an equilibrium composition,

defined as the long-term state reached after infinite cycle iterations.

The calculation of the equilibrium isotopic composition of a transmutation system in an advanced fuel cycle is a matter of special interest since this composition is often used as representative of the nuclear reactor through the whole fuel cycle [3, 4].

In this paper, we describe a fast numerical method for the calculation of the equilibrium isotopic composition in a zero-dimensional approach, taking advantage of the Banach fixed point theorem [5] for the demonstration of uniqueness and existence of a solution. The method is based on the division of the fuel cycle in successive stages: fuel fabrication, storage, irradiation inside the transmutation system, cooling, reprocessing, and incorporation of the external material into the new fresh fuel. The fuel isotopic composition is represented by an isotope vector and will be modified by each fuel cycle stage that is described in a matrix formulation. The

fuel cycle is hence represented as a contractor mapping over the fuel composition vector.

With the aim of validating the methodology, a simulation of the fuel cycle with the advanced burn-up code EVOLCODE 2.0 [6, 7] has been performed, checking that the isotopic composition has successfully reached the equilibrium and discussing the range of the possible deviations.

2. Computational Tool

EVOLCODE 2.0 is an in-house development to solve the burn-up problem, that is, the coupled problem of neutron transport and isotopic evolution. Its cycle data flow is shown in Figure 1.

The neutron transport stage is solved by the MCNPX code [8], allowing an important degree of the heterogeneity description in the reactor core model. The isotope evolution stage can be solved by the ORIGEN code [9] or by ACAB [10]. The user selects some geometrical regions or cells inside which neutronic properties and material composition are considered constant. For each of these cells, EVOLCODE 2.0 creates one-group effective cross-section libraries using the neutron flux energy spectrum provided by MCNPX in such a way that the whole calculation is faster than allowing MCNPX to do the job. Then, one ORIGEN execution is made independently for each cell providing the isotopic evolution of the materials. The ORIGEN executions are made using the neutron flux and materials at the beginning of the time step. In case that the averaged reactor power (estimated by the ORIGEN simulation) is not equal to the desired value or if its variation along the time step is large (causing a large uncertainty in the final results [7]), then the predictor/corrector method is activated to fix it. This whole procedure is repeated for several successive irradiation steps (or cycles) to reach the total burn-up specified by the user.

3. Double-Strata Fuel Cycle Scenario

One of the proposed advanced fuel cycle scenarios for waste reduction is the so-called double-strata scenario, whose scheme is shown in Figure 2. This fuel cycle has been studied in detail in the frame of different projects [11, 12] and consists in two separated strata or stages, one dedicated to energy production and the other dedicated to waste consumption.

In this particular specification of the double-strata scenario, the first stratum of the fuel cycle consists in the irradiation of UO_2 in light water reactors (LWRs) and the later advanced Purex reprocessing of the irradiated fuel for the Pu reutilization, only once, as MOX, again in LWR. Recovered MA coming from the first partitioning process and Pu and MA coming from the reprocessing of the MOX irradiated fuel are reutilized as fuel for the accelerator-driven subcritical system (ADS) in the second stratum. This second stratum is based on a fast spectrum ADS, which operates with continuous recycling of the main actinides (U, Pu, Np, Am, and Cm). This recycling is supposed to be a pyrometallurgical process.

4. ADS Fuel Isotopic Composition

The isotopic composition of the ADS fuel depends on the LWR park since the LWR recovered material (from both UO_2 and MOX reprocessed fuels) becomes a part of the ADS fuel content in each new ADS irradiation (a 15% approximately). The other part of the ADS fuel comes from the pyro-reprocessing of the preceding ADS irradiated fuel. In different cycles, the ADS fuel isotopic composition would change (and being consumed), but maintaining similar ADS operating conditions and a constant additional supply per cycle of actinides from the first LWR-stratum, the fuel approaches an equilibrium (as it is demonstrated below) in which the fuel isotopic composition of each cycle is equal to the following one.

The iterative second stratum of this fuel cycle scenario can be divided in a succession of stages: fuel fabrication, storage, irradiation inside the ADS, cooling, reprocessing, and incorporation of the external material (from the first stratum) into the new fresh fuel. Each process can be described in a matrix formulation as an operator over the fuel composition vector V_n , obtained just before the n th ADS irradiation. Vectors and matrices length is determined by the total number of different isotopes considered in the problem. This number of isotopes is equal to $M = 26$ in this study (the detailed list is shown in Table 1), although a larger value of M has been used in other problems. If V_{n+1} is the fuel composition vector before the $(n + 1)$ th ADS irradiation, it is related to V_n following the expression

$$V_{n+1} = D_s R D_c A V_n + V_{\text{ext}} = C V_n + V_{\text{ext}}, \quad (1)$$

where A is the matrix operator representing the irradiation inside the ADS, D_c represents the cooling decay time after the irradiation (two years in this scenario), R is the reprocessing operator, D_s represents the storage time before irradiation (one year), V_{ext} is the material incorporation from the first stratum (taken at the moment just before the beginning of the ADS irradiation), and $C = D_s R D_c A$. Since the fuel composition vector can be expressed as $V = F(V) = C V + V_{\text{ext}}$, the process fulfils the requirements of the Banach fixed point theorem, and therefore there is a solution vector $V = F^n(V)$ under the requirement that $F(V)$ is a contractor mapping, that is, if there is a constant $0 < k < 1$ such as

$$\|F(V') - F(V)\| \leq k \|V' - V\|, \quad (2)$$

where the symbol $\|\cdot\|$ represents the norm of the operator. Applying $F(V) = C V + V_{\text{ext}}$, this inequality can be written as

$$\|C(V' - V)\| \leq k \|V' - V\|, \quad (3)$$

which is satisfied if $|C| < 1$. In order to prove that this condition is satisfied, we must analyze the norm of each of the matrix operators appearing in the definition of C . The norm of the decay operators D_s and D_c is equal to the unity because they only change one isotope into another leaving the total amount of material unchanged (being precise, it might be smaller than the unity as some decay products are not included in the dimensions of the composition vector).

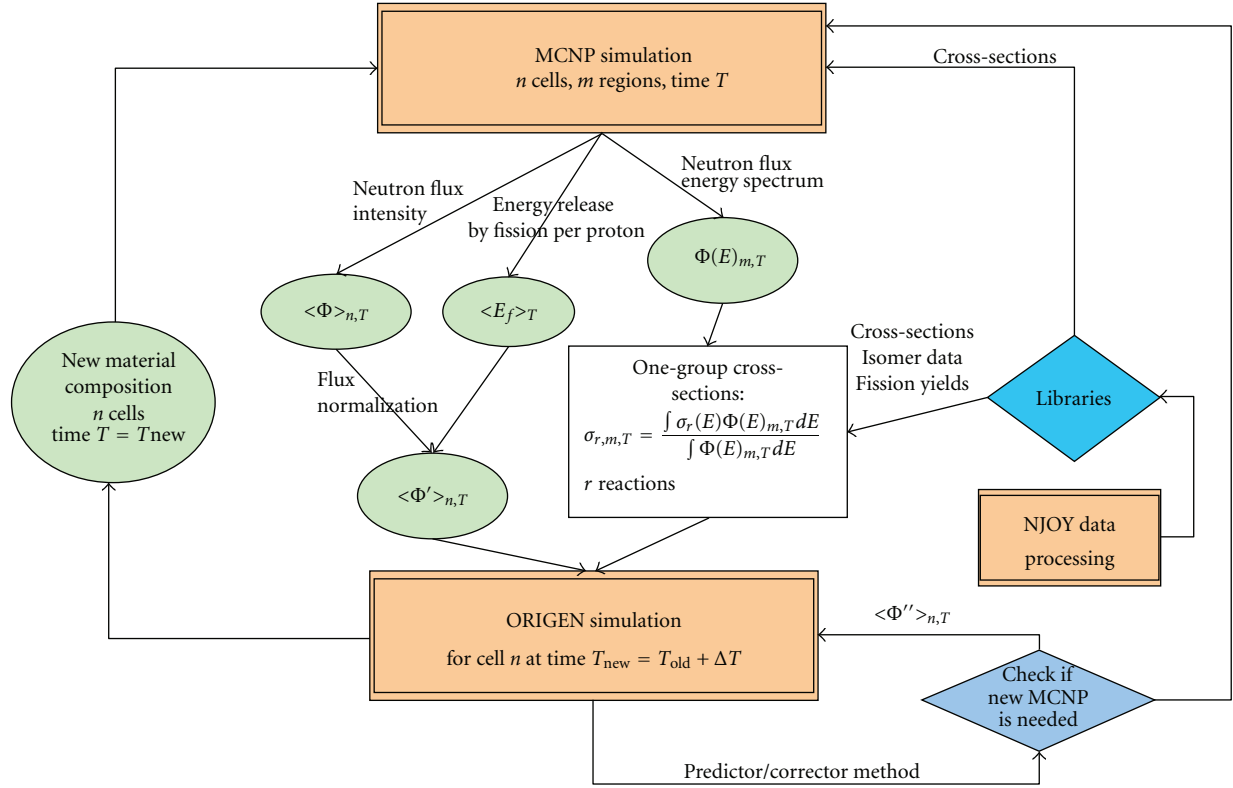


FIGURE 1: EVOLCODE 2 cycle data flow scheme.

The reprocessing operator, R , is a diagonal matrix having a constant diagonal value smaller than the unity (reprocessing recovery factor of 0.999) for the reprocessing isotopes (only the reprocessing elements U, Pu, Np, Am, and Cm have been considered), hence $|R| < 1$. Finally, the norm of the irradiation matrix A is strictly smaller than the unity because it represents consumption of heavy material (approximately a 15% for this ADS burn-up). This can be easily shown when the norm is defined as the maximum $|A_{ij}|$ and demonstrated for other definitions. For all these reasons, $|C| < 1$, therefore this process fulfils the Banach fixed point theorem and there exists a unique solution of the equation of the type $V = F^n(V_0)$, for an arbitrary V_0 .

Coming back to the previous notation, we can find the solution directly from the equilibrium equation $V_{n+1} = V_n = V_{\text{eq}}$; hence the expression of the fuel composition vector can be written as

$$V_{\text{eq}} = CV_{\text{eq}} + V_{\text{ext}}. \quad (4)$$

The solution of this equation is

$$V_{\text{eq}} = (1 - C)^{-1}V_{\text{ext}}. \quad (5)$$

In order to reach this solution, it is necessary to calculate D_c , D_s , A , R , and V_{ext} in a matrix formulation from the data of the problem. The operator R is represented by a diagonal matrix with a constant value of 0.999, as mentioned above. V_{ext} is a vector containing the contribution of the LWR stratum so it can be provided after solving the first

noniterative stratum of the fuel cycle. The operator A can be represented by the generic evolution of a nuclear system under irradiation. The generic evolution of the isotopic composition vector $V(t)$ can be described in the zero-dimensional approximation as

$$\frac{dV(t)}{dt} = E \cdot V(t), \quad \text{with } E = XS \cdot \Phi + \text{DEC}, \quad (6)$$

where XS is the cross-section matrix, DEC is the radioactive decay matrix, and Φ is the averaged neutron flux. Operators D_c and D_s can be obtained in case that $\Phi = 0$. The formal solution of this coupled linear system of equations of constant coefficients is

$$V(t) = e^{E \cdot t} \cdot V(0). \quad (7)$$

In the base of eigenvectors of the matrix E , this solution can be written as

$$A = e^{E \cdot t} = U \begin{pmatrix} e^{au_1 t} & 0 & \dots & 0 \\ 0 & e^{au_2 t} & \dots & 0 \\ \dots & \dots & \dots & \dots \\ 0 & 0 & \dots & e^{au_M t} \end{pmatrix} U^{-1}, \quad (8)$$

where $U(eu_1, eu_2, \dots, eu_M)$ is the matrix of the eigenvectors eu_i associated with the eigenvalues au_i . The calculation of the eigenvalues and eigenvectors needed to compute the exponential and the inversion of the $(1-C)$ matrix has

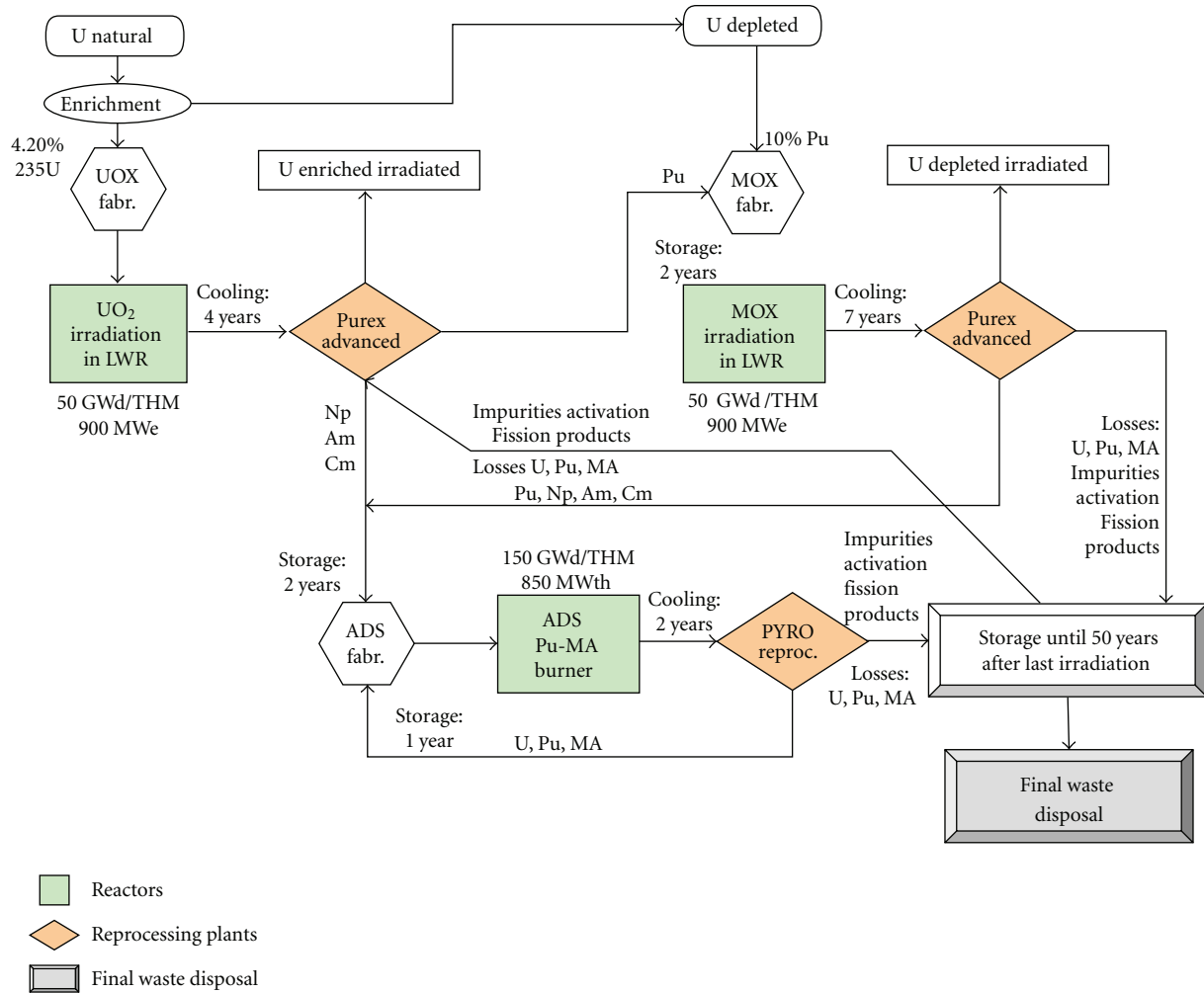


FIGURE 2: Scheme of the double-strata fuel cycle scenario with LWR and ADS.

been a difficult problem because of the large numerical instabilities involved in the manipulation of these large matrices. However, the easy access to arbitrary precision arithmetic, made recently available in popular computer codes as Maple [13] and Mathematica [14], allows using brute force and direct methods of solving these problems. For our case, it was necessary to set the arithmetic precision to 70 decimal digits to obtain the required stability. In spite of this condition, the eigenvectors computed had to be regularized by discarding very small imaginary components ($|\text{Im}(e_{u_i})| < 10^{-25} |\text{Re}(e_{u_i})|$). The process was implemented with the Maple program, where efficient procedures for the calculation of eigenvalues, eigenvectors, and matrix inversions were readily available. The typical calculation time is few minutes in a modern PC.

In order to estimate the flux level and the one-group zero-dimensional equivalent cross-sections, a fully detailed transport simulation was performed. In this simulation, the exact geometry, the required total power, and an initial guess of the equilibrium composition of the reactor materials were used. Careful weighting had to be used in the procedure of averaging the cross-sections over the whole reactor volume,

which was divided in different cells with isotopic evolution. For every one of these cells, one set of one-group effective cross-sections were calculated using the EVOLCODE 2.0 simulation system. The final reactor-averaged cross-sections were calculated weighting the different one-group cross-sections of each fuel cell by its fuel mass. The initial guess of the fuel composition was set to the same vector as the vector of actinides from the external refuelling, V_{ext} .

Since the initial ADS fuel composition, chosen for the calculation of matrices XS and Φ , is different from the final equilibrium composition, this method of calculation of the equilibrium isotopic composition of the ADS fuel introduces an error in the results. An iterative process can be carried out to increase the precision of the method. Once the equilibrium isotopic composition is calculated using the previous noniterative method, the resulting isotopic composition can be used as the initial ADS fuel content and a new set of cross-sections/neutron flux could be obtained with EVOLCODE 2.0. Then, the method is repeated in order to obtain a more precise value of the equilibrium isotopic composition. The new procedure can be successively performed until the isotopic composition of a certain

TABLE 1: Equilibrium isotopic composition of the ADS fuel, before the irradiation, for cycles n and $(n + 1)$. Units are tonnes of initial heavy metal in the ADS.

Isotope*	ADS fresh fuel equilibrium composition for the n th cycle estimated with the matrix equation method (t)	ADS fresh fuel composition for the $(n + 1)$ th cycle estimated with EVOLCODE 2.0 (t)	Ratio (EVOLCODE 2-Method)/EVOLCODE 2(%)
U234	$3.677E - 02$	$3.794E - 02$	3.08%
U235	$9.303E - 03$	$9.330E - 03$	0.29%
U236	$1.296E - 02$	$1.302E - 02$	0.48%
U238	$7.171E - 05$	$7.245E - 05$	1.03%
Np237	$1.554E - 01$	$1.553E - 01$	-0.09%
Pu238	$2.791E - 01$	$2.792E - 01$	0.04%
Pu239	$4.084E - 01$	$4.067E - 01$	-0.42%
Pu240	$1.204E + 00$	$1.208E + 00$	0.36%
Pu241	$2.476E - 01$	$2.417E - 01$	-2.44%
Pu242	$5.432E - 01$	$5.441E - 01$	0.16%
Am241	$2.338E - 01$	$2.386E - 01$	2.00%
Am242m	$1.313E - 02$	$1.348E - 02$	2.59%
Am243	$2.166E - 01$	$2.166E - 01$	0.01%
Cm242	$2.183E - 04$	$2.165E - 04$	-0.83%
Cm243	$1.958E - 03$	$1.853E - 03$	-5.68%
Cm244	$1.835E - 01$	$1.801E - 01$	-1.92%
Cm245	$5.300E - 02$	$5.266E - 02$	-0.64%
Cm246	$3.430E - 02$	$3.428E - 02$	-0.04%
Cm247	$9.439E - 03$	$9.370E - 03$	-0.74%
Total	$3.643E + 00$	$3.643E + 00$	

*The short-lived isotopes U-237, U-239, Np-238, Np-239, Pu-243, Am-242, and Am-244 were also used in the calculations.

iteration is deviated less than a limit value from the previous iteration. Nevertheless, one iteration is typically enough to achieve precisions acceptable for fuel cycle studies.

5. Results

The isotopic composition of the different stages of the iterative stratum of the fuel cycle has been calculated using the matrix equation method. Table 1 shows the initial (BOL, beginning of life, before the irradiation) ADS fuel isotopic composition (in terms of actinides), calculated as the solution of the equation for V_{eq} described in the previous section. Moreover, the isotopic composition of the ADS fuel at BOL has also been calculated for the following cycle V_{n+1} by means of the advanced burn-up code EVOLCODE 2.0 for checking purposes.

The deviation between the equilibrium isotopic compositions obtained from the matrix equation method and from the irradiation (and the successive decay and reprocessing as indicated in the fuel cycle scenario) using EVOLCODE 2.0 can be seen in the fourth column in Table 1. These deviations, due to the different accuracy of both methods, are smaller than 3% for all actinides (with significant contributions to the total mass) except for Cm-243, with 5.7% difference.

The objective of the fuel cycle scenario will define the maximum allowed deviation between one cycle and the following one and also the final decision concerning the necessity of a second iteration on the matrix equation method if the equilibrium isotopic composition has not been reached. For instance, for a fuel cycle scenario where the objective is the study of a representative set of the different (primary and secondary) waste streams, the obtained equilibrium isotopic composition is a good approximation so no iterative calculations are needed.

6. Conclusions

A fast numerical method, based on an arbitrary precision arithmetic solution to the matrix equations, for the calculation in a zero-dimensional approach of the equilibrium isotopic composition of a transmutation system in an advanced fuel cycle has been developed and successfully applied to a double-strata fuel cycle with LWR and ADS.

The observed differences between the matrix equation method and the EVOLCODE 2.0 results for the successive cycle are smaller than a few percents in the mass estimations of the main actinides. The precision of the calculation can be improved, if needed, by performing a second iteration on the

matrix equation method, using the one-group cross-sections of the ADS with the equilibrium composition obtained in the first iteration.

References

- [1] E. M. González-Romero, H. A. Abderrahim, C. Fazio et al., “Rational and Added Value of P&T for Waste Management Policies”, Deliverable 1.1, PATEROS project, EU 6th FP FI6W-Contract number 036418, 2007.
- [2] OECD Nuclear Energy Agency, *Advanced Nuclear Fuel Cycles and Radioactive Waste Management*, Nuclear Development, NEA/OECD No. 5990, Les Moulineaux, France, 2006.
- [3] “RED-IMPACT synthesis report,” Tech. Rep. 978-3-89336-538-8, Forschungszentrum Julich, Berlin, Germany, 2008.
- [4] OECD Nuclear Energy Agency, “Nuclear fuel cycle transition scenario studies. status report,” Tech. Rep. 6194, Nuclear Development, NEA/OECD, Les Moulineaux, France, 2009.
- [5] S. Banach, “Sur les opérations dans les ensembles abstraits et leur application aux équations intégrales,” *Fundamenta Mathematicae*, vol. 3, pp. 133–181, 1922.
- [6] F. Álvarez-Velarde, P. T. León, and E. M. González-Romero, “EVOLCODE2, a combined neutronics and burn-up evolution simulation code,” in *Proceedings of the 9th Information Exchange Meeting on Actinide and Fission Product P&T*, OECD Nuclear Energy Agency, Nîmes, France, 2007.
- [7] F. Álvarez-Velarde, *Development of a computational tool for the simulation of innovative transmutation systems*, Ph.D. thesis, University of Córdoba, Andalusia, Spain, 2011.
- [8] J. S. Hendricks, G. W. McKinney, H. R. Trellue et al., *MCNPX, Version 2.6.b*, LA-UR-06-3248, Los Alamos National Laboratory, Los Alamos, NM, USA, 2006.
- [9] A. G. Croff, “ORIGEN2: a versatile computer code for calculating the nuclide compositions and characteristics of nuclear materials,” *Nuclear Technology*, vol. 62, pp. 335–352, 1983.
- [10] J. Sanz, O. Cabellos, and N. García-Herranz, *ACAB Inventory Code for Nuclear Applications: User’s Manual V.2008*, NEA-1839/02, 2008.
- [11] OECD Nuclear Energy Agency, “Accelerator-driven systems (ADS) and fast reactors (FR) in advanced nuclear fuel cycles. A comparative study,” Tech. Rep. number, Nuclear Development, NEA/OECD, Les Moulineaux, France, 2002.
- [12] L. Boucher, “Detailed description of selected fuel cycle scenarios,” Deliverable 1.4, RED-IMPACT Project, EU 6th FP FI6W-CT-2004-002408, 2007.
- [13] M. B. Monagan, K. O. Geddes, K. M. Heal et al., *Maple 13 Advanced Programming Guide*, Maplesoft, Waterloo, ON, Canada, 2009.
- [14] S. Wolfram, *The Mathematica Book*, Wolfram Media, Champaign, Ill, USA, 5th edition, 2003.